A DEM numerical modelling approach to simulating size segregation of media in a stirred mill and effects on grind characteristics

by

Sievers, WJ

A thesis submitted to the University of Cape Town as fulfillment of the requirement for the degree of Master of Science in Chemical Engineering

MSc dissertation

2024-06-16

UNIVERSITY OF CAPE TOWN
IYUNIVESITHI YASEKAPA • UNIVERSITEIT VAN KAAPSTAD

A DEM numerical modelling approach to simulating size segregation of media in a stirred mill and effects on grind characteristics

Wilco John Sievers
SVRWIL001

Supervisors

Dr Maximilian Richter

Prof Aubrey Mainza

Dr Sherry Bremner

Department of Chemical Engineering
University of Cape Town
South Africa

ABSTRACT

Comminution is an important operation in the minerals processing industry. In both traditional and stirred mills, single-sized grinding beads are used, along with multiple passes through the mills, to achieve a sufficient size-reduction ratio. It is plausible to expand the size reduction capabilities of a mill using multiple-sized grinding beads in the mill. For this study, the discrete element method (DEM) was used to simulate dry size-segregated systems in a vertical stirred mill. These size-segregated systems were evaluated at different impeller speeds and weight distributions. The dry systems were susceptible to the *Brazilian nut effect*. Furthermore, it was found that excessive impeller speeds did not subsequently increase the overall collision modulus. The overall modal collision intensity for particle collisions was maximised between 350 rpm and 500 rpm where sufficient mixing and impeller speed were facilitated. At excessive speeds beyond 700 rpm the collision modulus plateaued. Excessive addition of smaller particles reduced the total energy applied to particle-particle collisions which also reduced the overall systems collision modulus. The results presented in this study could be considered as an introduction to dry size-segregated media in a vertical stirred mill.

Keywords: DEM, vertical stirred mill, size-segregated, impeller speeds, weight distribution, grind characteristics

Declaration of authenticity

This thesis/dissertation has been submitted to the Turnitin module and I confirm that my supervisor has seen my report and any concerns revealed by such have been resolved with my supervisor.

ACKNOWLEDGEMENTS

I would like to acknowledge that this thesis could not have been completed without the help of my friends and family throughout the years.

I would like to acknowledge Prof Aubrey Mainza, Dr Maximilian Richter and Dr Sherry Bremner for providing me the opportunity to further my education and skills. The skills developed during the completion of this thesis will actively be used to improve the quality and standard of my work moving forward.

I would like to thank my family, Ernst Sievers, Linda Sievers and Annalien Thomas, for their support both financially and emotionally throughout this ordeal. Listening to my ramblings about problems and decisions that would never affect them, must have been draining. Nevertheless, they always gave me honest advice and encouragement.

I would like to thank my friends, Eduard Barnard, Shaun Badenhorst and Conru Boshoff, for listening to my mad ramblings and playing games to make life a little lighter when troubles arose during the research.

Special thanks go to Divine Ssebunya, for being an angel. Without her, this thesis would not be half as good as it is. She helped to greatly expand my knowledge and competency regarding the understanding and manipulation of data generated by DEM. Her wit and humour is remarkable.

Finally, I would like to thank the UCT Brewing team for all the free beers and brewing sessions we had together.

Contents

List of Figures

List of Tables

Nomenclature

β	rate of segregation	$revolutions^{-1}$
Δt	integration time step	s
Δt_c	critical time step	s
δ	particle overlap	m
ϵ	voidage fraction in grinding chamber	$--$
$\epsilon_{i,J}$	energy loss fraction of *i*	$--$
$\hat{P}$	estimated power uncertainty	W
μ	coefficient of friction	$--$
ν_i	poison's ratio of *i*	$--$
ω	angular speed	$rad \cdot s^{-1}$
ϕ	percentage of particle population	$\%$
π	pi	3.142
ρ	density of the relevant subject	$kg \cdot m^{-3}$
ρ_B	bulk density of grinding media	$kg \cdot m^{-3}$
ρ_m	density of grinding media	$kg \cdot m^{-3}$
σ	deviation	$--$
τ	torque	$N \cdot m$
Θ	ratio of total collision energy loss relative to mass	$J \cdot kg^{-1}$
Υ	ratio of total collision energy loss of particles	$--$
$\vec{v}$	vector velocity	$m \cdot s^{-1}$
ξ	energy consumed	J
A	segregation limit	$nr\ of\ particles$
C_n	normal damping coefficient	$kN \cdot s \cdot m^{-1}$
C_t	tangential damping coefficient	$kN \cdot s \cdot m^{-1}$
d_p	particle diameter	m
E^*	effective young's modulus	GPa

E_i	young's modulus of *i*	GPa
e_n	coefficient of restitution	$--$
$e_{i,J}$	energy of *i*	J
f	penetration factor	$--$
F_n	normal force	kN
F_t	tangential force	kN
G	shear modulus	Pa
G^*	effective shear modulus	Pa
I	segregation intensity	$nr\ of\ particles$
k_i	spring stiffness of *i*	$kN \cdot m^{-1}$
k_n	normal spring stiffness	$kN \cdot m^{-1}$
k_t	tangential spring stiffness	$kN \cdot m^{-1}$
KE_i	kinetic energy of *i*	J
m^*	normalised mass	kg
m_i	mass of *i*	kg
ME_i	mechanical energy of *i*	J
N	number of particles	$--$
n	stirrer speed	rpm
N_c	number of particle collisions	Hz
N_{gm}	number of grinding media particles	$--$
n_{rev}	stirrer revolutions	rpm
P_i	power of subject i	W
PE_i	potential energy of *i*	J
R^*	equivalent radius	m
t_i	time of the *i*	s
T_R	rayleigh time step	s
T_r	residence time	s

$Tot_{E,loss,i}$	Total energy loss of a single collision of subject *i*	J
u_i	mean of subject *i*	$--$
v_n	relative normal velocity	$m \cdot s^{-1}$
v_t	relative tangential velocity	$m \cdot s^{-1}$
V_{gc}	volume of grinding chamber	$kg \cdot m^{-3}$
$V_{i,norm}$	normalised velocity of *i*	$m \cdot s^{-1}$
v_{max}	maximum particle velocity	$m \cdot s^{-1}$
$W_{i,avg}$	average watt usage of *i*	W
2D	two dimensional	
3D	three dimensional	
CAD	computer aided design	
CFD	computational fluid dynamics	
CMR	centre for minerals research	
DEM	discrete element method	
EDEM	altair's discrete element method simulation software	
FEM	finite element method	
GHG	greenhouse gas	
HDD	hard disk drive space	
MS	mono-sized / uniform	
NE	collision normal energy loss	J
nr	number	
PC	personal computer	
Q1	15th percentile of the box plot of *i*	
Q2	median value box plot of *i*	
Q3	75th percentile of the box plot of *i*	
RSD	relative standard deviation	
SAM	sala agitated mill	

SMD	stirred media detritor	
SPH	smooth particle hydrodynamics	
SV	size-varied	
TE	collision tangential energy loss	J
UCT	university of cape town	
wt	weight	

1 Introduction

Comminution is an important operation in the mining, pharmaceutical, cement and waste treatment industries. It allows for the recovery of minerals in subsequent downstream processes by exposing the minerals *via* size reduction (Weerasekara et al. 2013). As such, comminution plays an important role in the quality of subsequent downstream products (Shrivastava et al. 2011; Scientific 2012; Lisso 2013; Little 2016; Mkurazhizha 2018). Additionally, comminution is one of the more energy intensive operations in the mineral processing industry (Mishra 2003a,b; Santhanam and Dreizin 2012; Wills and Finch 2015; Somani et al. 2017). Thus, it is important that efficient grinding of ores is facilitated. Failing to do so leads to loss in productivity, profitability and quality of products. Furthermore, inefficient grinding results in increased energy consumption which also leads to more greenhouse gas (GHG) emissions (Ntsele and Allen 2012).

In the mining industry it has become difficult to effectively liberate ore from host bodies. This is due to declining ore grades that is coupled with complex ore structures (Yager 2004; Dominguez and Valero 2013; Lisso 2013; Neingo and Tholana 2016). Due to the depletion of high-yielding and easy-to-process ores, low grade and finely disseminated ores have become the major source of metals. In the past it was considered uneconomical to liberate and mine such ores. The only practical way of liberating the resources is to grind the ore into a fine or ultra-fine standard (Francis 2014). The relationship between size reduction and power consumption is exponential, meaning that significantly more energy is required for little size reduction in the fine grinding region (Ntsele and Allen 2012; Santhanam and Dreizin 2012).

To combat the increasing challenges of liberating minerals from low grade and finely disseminated ores, new grinding technologies need to be implemented for fine grinding applications. However, the mineral processing industry has been reluctant to implement new grinding technologies, and fine grinding applications are no exception (Jankovic 2003; Lisso 2013; Francis 2014).

The reluctance to implement the new technology may be due to uncertainties surrounding such equipment (Sinnott et al. 2006; Jankovic 2008; Radziszewski and Allen 2014). Not fully understanding the flow and grinding events inside new milling technology can lead to unsuccessful troubleshooting and inefficient operation.

Fortunately, the improvement of computer processing capabilities has enabled scientists and engineers to simulate comminution circuits and processes with success (Mishra 2003a; Cleary 2004; Sinnott et al. 2006; Luding 2008; Weerasekara et al. 2013). This is done by using computational methods such as the discrete element method (DEM), computational fluid dynamics (CFD), the finite element method (FEM) and smooth particle hydrodynamics (SPH). There are simulation software dedicated to approximating flow in particulate systems through the use of DEM. Available software are OpenFOAM, LIGGGHTS, CFDEMcoupling, Rocky and Altair's DEM simulation software EDEM (Kloss et al. 2012).

DEM coupled with fluid dynamics allows for the approximation and predictions of media flow, mixing, power draw, force networks, particle trajectories and many other phenomena within a particulate system. DEM describes the motion of each individual particle with special treatment for eventual collisions. DEM is reliable due to its principles originating from the fundamental laws of physics (Mishra 2003a; Kloss et al. 2012; Thornton 2015). Thus, it is possible to investigate, instantiate, prove and improve events and theories in comminution technologies using DEM.

When high reduction ratios are sought, multiple grinding operations are used which can lead to excessive or superfluous grinding (Lisso 2013). One possibility for improved operating conditions and energy efficiency is the use of size-segregated grinding media in stirred detritors. Mills generally tend to use uniform-sized grinding media that is eroded over time, resulting in a size-segregated system with mixed efficiencies. The implementation of a clearly defined size-segregated media could help define and expand the operational bounds of a stirred mill and should help improve the size reduction ratio of a singular stirred mill operation.

1.1 Hypotheses

For the thesis the following hypotheses are presented:

1. The collision modulus of a specific granular system is maximised when a high degree of mixing and speed is maintained because when a particulate size is properly dispersed throughout the bulk media the contacts and the intensities thereof are maximised which would in turn facilitate the maximum potential breakage events.

2. There exists an optimal impeller speed that would maximise the interparticle collision intensities for either large particle collisions or small particle collisions because at different impeller rotation speeds different degrees of mixing would be maintained, that would influence how the particles are dispersed throughout the mill and in turn the types of contacts facilitated and in turn the potential breakage that a system may facilitate.
3. Optimal weight distributions of the two size-class bulk media would favor a majority of large particles and a minority of small particles because large particles would facilitate the transfer of energy from impeller to charge body more effectively than smaller particles, based on the larger particles inertia and cross sectional area.

1.2 Key questions

1. For a size-segregated media mixture is the maximum collision mode facilitated at lower impeller speeds or increased impeller speeds?
2. What is the optimal media distribution that would facilitate the maximum collision modes?
3. Does the degree of mixing have a beneficial effect on the collision modulus, and in turn grinding efficiency, of the system?
4. How does size-segregated media influence the collisions in the mill? Does the addition of different sized grinding beads improve the collision mode of an existing system?
5. What aspects of granular flow agitated by low impeller speeds would be good for comminution purposes?
6. What aspects of high impeller speed action would be detrimental for comminution of the granular media in stirred mills?

1.3 Research objectives

The proposed study focuses on the simulation and estimation of optimal operating conditions for a vertical stirred mill. Particular emphasis is placed on the grinding media and collision modulii in the stirred mill. Size-segregated media has been implemented in conventional grinding technologies, such as tumbling and ball mills, but it has not been emphasised or well documented in the newer stirred milling technologies.

The effects and implications of differently sized grinding media on the efficiency of a process will be further documented. To achieve this, the following sub-objectives were formulated:

- Establish if the simulations experience artifacting. If the simulations do experience artifacting, what aspects of the data does the artifacting affect or change? If the artifacting does influence the data, to what degree does it compromise it?
- Establish the degree of mixing and segregation that the particles experience with different impeller rotation speed and weight distributions. Furthermore, establish the influence the different impeller speeds, weight distributions and degree of mixing has on the collision modulus of the system.
- Estimate the optimal grinding media weight distribution that would benefit the maximum collision modulus.
- Estimate the impeller rotation speed that would benefit the maximum collision modulus.

1.4 Scope

This thesis considers differently sized grinding media in a vertical stirred mill. The research is based solely on the numerically generated simulation and results of a simulated vertical stirred mill that involved different particle weights and sizes. The thesis takes into account mono-sized and size-mixed vertical stirred mill systems. The thesis accounts for the weight distribution of the size-mixed systems as well as the impeller agitation speed of the system.

This thesis does not consider how the addition of liquid, or water, to the size-mixed system would influence the particle dynamics and grinding performance. This thesis serves as an introduction to a size-mixed particle system, adding more variables and complexities such as liquid simulation would go beyond an introductory scope of the thesis. The addition of liquid can further be investigated in future work. This thesis does not investigate how the material, or rather weight and density, of different size-mixed beads would influence the dynamics of the system. Furthermore, this thesis does not investigate nor simulate particle breakages.

1.5 Thesis structure

The structure of the thesis is as follows

Chapter 1 gives a brief introduction to the current situation regarding grinding and the current problem statement. It further provides the research objectives and hypothesis.

Chapter 2 provides a literature review of the relevant subjects pertaining to the student's master's thesis. This involves a brief introduction and illustration of mills within the mining industry, the computational methods used to generate the data, the types of breakages, and other variables affecting the grinding action.

Chapter 3 elaborates on the equipment used in this study, as well as the simulation set-ups. It further discusses how the relevant data was produced and processed.

Chapter 4 contains the results, discussions and evaluations pertaining to the investigated simulations and experiments. The chapter contains subsections that pertain to the degree of simulation artifacting, the influence of impeller speed on particle collisions and grinding performance, as well as the influence of the particle weight distribution on grinding performance.

Chapter 5 contains the final recommendations and conclusions.

2 Literature review

Chapter 2 gives a brief introduction and history to the types of mills used within the industry, the principals of grinding, how breakages are achieved, the computing techniques evaluated for this paper, notable variables that affect comminution performance and interesting characteristics of size segregated media.

2.1 Grinding

Grinding is the result of compression and collision based impacts of objects. Grinding is an operation that occurs in multiple industries. These include the pharmaceutical, paint, chemical and mineral processing industries. Depending on the characteristics and requirements of the feed and product, different grinding media and operating conditions are then implemented accordingly (Jankovic 2003; Lisso 2013).

In the mining industry efficient mineral liberation is emphasised (Neingo and Tholana 2016). To liberate ore effectively, multiple grinding stages punctuated by flotation devices are implemented. If these grinding operations are applied haphazardly it could lead to over grinding. Over grinding of feed materials is not trivial due to the exponential relationship between power consumed and size reduction (Wang and Forssberg 2007; Ntsele and Allen 2012). It is important not to grind as fine as possible, but as economically and efficiently as possible. This means grinding until the required size reduction ratio is achieved, and not more. With reduced ore quality and grade, fine and ultra-fine grinding is implemented for improved mineral liberation (Larson et al. 2011; Lisso 2013).

The size and standard for fine media differs from industry to industry. In the mineral processing industry fine grinding is considered to be products that are less than $30\,\mu m$ (Jankovic 2003). Although advances in flotation technology allows for suitable recovery of ore, floating particles that are $\leq 10\,\mu m$ and $\geq 106\,\mu m$ leads to difficulties in recovering minerals (Gaudin and Malozemoff 2002). There are a myriad of reasons for inefficient recovering of ores. One of the main reasons being that there are milling factors that are unaccounted for in the kinetics of flotation. Thus, the type of mill used has ramifications on the minerals recovered (Varinot et al. 1997; Gaudin and Malozemoff 2002; Jankovic 2008).

New grinding technologies are being implemented in the mineral industry in order to facilitate fine grinding. Stirred mills are among the newer grinding technologies that are being implemented for fine grinding applications. These new mills will not replace conventional tumbling mills (Wang and Forssberg 2007; Rule 2011). Stirred mills are used to circumvent the shortcomings of the traditional tumbling mills.

2.2 Tumbling mills

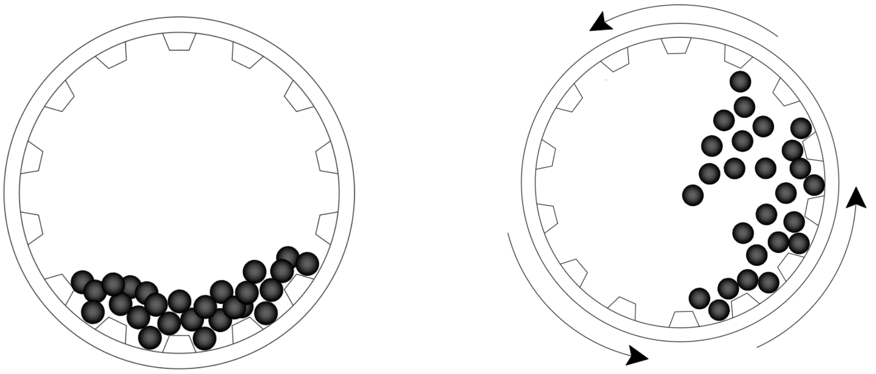

(a) Front view of tumbling mill at rest

(b) Front view of tumbling mill during motion

Figure 1: Simplistic illustration of a tumbling mill

Tumbling mills are used extensively in the mining industry (Wang and Forssberg 2007; Sun et al. 2009). A tumbling mill is a cylindrical mill laid horizontally with grinding media loaded into it. When in operation the mill carries the grinding media up to a point which then promotes one of two actions to occur: either cataracting or cascading (Mishra and Rajamani 1992; Sun et al. 2009).

Cataracting occurs when media are raised up to a certain point, termed a shoulder, and are then thrown out of the of the mill's surface where it then follows a parabolic path downward. This promotes intense impacts on the ore. The impact further promotes fracture formation in particles, as well as impact breakages (Varinot et al. 1997).

Cascading occurs when media are raised up a to certain point and then allowed to descend along the surface of the charge ramp. Ore is ground with the media rolling downwards. This promotes impact and cleavage breakages (Mishra and Rajamani 1992; Sun et al. 2009).

It is believed that tumbling mills are dominated by impact breakages depending on the speed and the media fill of the mill (Gao and Forssberg 1995). Tumbling mills are most suitable for the size reduction of larger, more coarse, ores (Varinot et al. 1997; Shi et al. 2009). However, it is known that tumbling mills are not particularly efficient as their power consumption is high and their size reduction efficiency is low (Flavel and Rimmer 1981; Shi et al. 2009). The efficiency of tumbling mills is dependent on ensuring that media and ore collisions utilise the full impact to propagate cleavage and fracture based breakages. These breakages are further elaborated on in Section 2.5.

More energy is lost and expended as particles become smaller. There are numerous reasons for this occurring. One reason can be attributed to fine particles facilitating a cushioning effect which reduces any meaningful collisions between the grinding media and ore (Orumwense 1992). Another reason is that more energy is required to break smaller particles with less flaws available for crack propagation (Wang and Forssberg 2007; Thornton 2015). A further problem is that power used to facilitate collisions can be converted and wasted into other forms of energy. The power applied can be converted into kinetic energy that can be used to deform or damage the available media, ore and equipment (Rajamani et al. 2000; Santhanam and Dreizin 2012). Particle breakage behaviour is strongly dependent on both the microscopic and macroscopic structure of the colliding particles (Antonyuk et al. 2006).

Thus, tumbling mills cease to be economically viable when used for fine grinding (Sinnott et al. 2006; Jankovic and Sinclair 2006; Shi et al. 2009; Ntsele and Allen 2012; Mazzinghy et al. 2017).

Figure 2: Tumbling mills in industry (Westpro 2021)

2.3 Stirred mills

Stirred milling is best suited for fine grinding applications. Shear based breakages play a more predominant role in stirred mills than in tumbling mills. There are multiple types of stirred mills, as shown in Table 1.

Table 1: Types of stirred mills available (Ndimande et al. 2019)

Stirred mill	Orientation	Agitator type	Type
Tower mill	Vertical	Helical screw	Gravity-induced
Vertimill	Vertical	Helical screw	Gravity-induced
Isamill	Horizontal	Rotor discs	Fluidised stirred mill
Sala agitated mill (SAM-mill)	Vertical	Pins	Fluidised stirred mill
Detirator (Stirred media mill)	Vertical	Impeller	Fluidised stirred mill

Vertical mills benefit from a simple design. A basic stirred mill consists of a grinding chamber filled with grinding media and an agitator in the centre of the mill's volume. The different types of stirred mills in operation differ mainly in orientation, available power intensity, agitator design, agitator speed and media separation.

A stirred mill can be operated with a dry or wet feed (Wang and Forssberg 2007). Wet grinding is preferred as it improves the separation of fines in the milling chamber (Sinnott et al. 2006).

Gravity-induced mills are slow-stirred mills that use high-density grinding media. The agitator rotates slowly to allow the grinding media and feed to settle under gravity. The slow motion of the agitator ensures that the grinding media and slurry particles stay in contact for a prolonged period of time. This enables efficient transfer of energy supplied into attrition and abrasion based breakages.

Fluidised mill types use high rotational speeds to enable the suspension and complete mixing of the grinding media and slurry particles. Fluidisation encourages the grinding media and slurry particles to collide and interact consistently. This further encourages attrition and abrasion based breakages.

Proper consideration needs to be taken when implementing a stirred mill. Though the stirred mills result in efficient grinding action, the feed requirements and grinding media, among other operating variables, need to be taken into account. This should promote proper usage of stirred mills, as energy supplied has been used with varying degrees of efficiencies (Stender et al. 2004).

The reasons for stirred milling being better suited and more energy efficient for fine grinding than tumbling mills, can be simplified to the following:

- There is more active volume used for grinding as opposed to an open volume in a tumbling mill (Stender et al. 2004).
- Stirred mills use reduced or smaller grinding media. The reduced media size results in an increased ”contact area” used for grinding. The reduced media size promotes abrasion and attrition breakages which results in a reduced product size.
- It requires less energy to rotate an agitator as opposed to an entire chassis of a tumbling mill loaded with materials (Somani et al. 2017).
- The design of stirred mills promotes shearing. Shearing results in increased abrasion breakages which promotes fine products (Jankovic 2008; Francis 2014).

Though stirred mills are the optimal technology for fine grinding, they are still susceptible to energy dissipation and loss. A majority of the energy supplied is dissipated through multiple events (Kwade and Schwedes 1997; Stender et al. 2004; Cleary et al. 2006; Yang et al. 2006).

These events include, but are not limited to:

(a) The wear and deformation of grinding media;

(b) The wear and deformation of equipment;

(c) Slip occurring when high stress events are facilitated;

(d) Fine particles and fluids damping and reducing stress and impact events;

(e) Ore and particles dissipating energy through friction;

(f) Energy being converted in to multiple forms and then reduced in said forms.

All mills are susceptible to the aforementioned energy dissipation mechanisms. The effectiveness of each mechanism is dependent on the mill used (Sinnott et al. 2006; Santhanam and Dreizin 2012).

2.3.1 Tower mill

The Tower mill was originally manufactured and developed in Japan. It is a low speed stirrer that uses a helical screw to displace feed during operation.

The motion of the helical screw type agitator, coupled with grinding media, ensures that the breakage mechanisms are enforced by attrition and abrasion breakages. However, a reasonable degree of slipping is experienced in Tower mills (Sinnott et al. 2006). This is due to high stress energy experienced by particles close to the agitator (Stender et al. 2004). Mills with a screw type agitator have an upper limit with regards to the rotational speed.

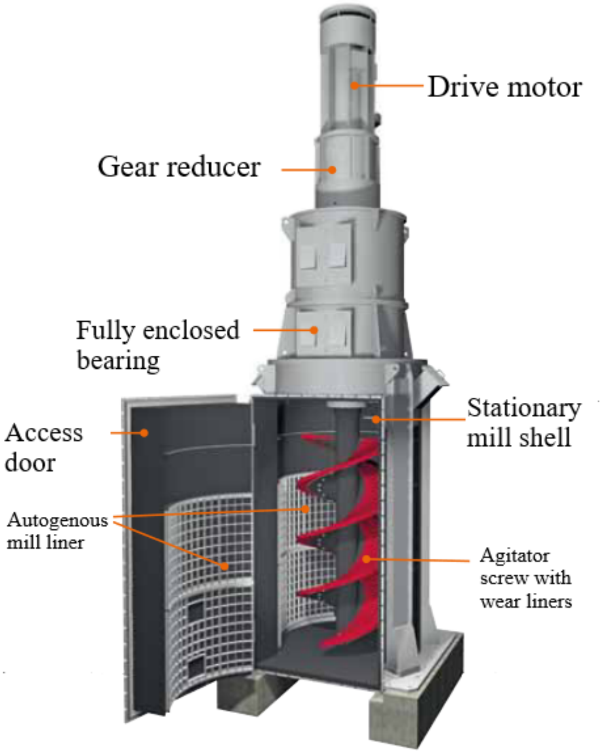

Figure 3: Illustration of a Tower mill (EIRICH 2018)

The size reduction of a Tower mill is limited to 20 µm to 35 µm. As such this type of mill applied in closed circuits in order to improve energy efficiency and size reduction (Lisso 2013).

2.3.2 Isamill

The Isamill is a high speed stirred mill developed by Mount Isa Mines in collaboration in collaboration with Netzsch Feinmahltechnik of Germany. It was developed in order to facilitate fine grinding.

The mill is a horizontally orientated mill with perforated disc stirrers. The discs operate at high speeds in order to fluidise the feed. This promotes efficient grinding and breakage events (Lisso 2013).

Figure 4: Illustration of an Isamill in industry(IsaMill 2021)

An additional advantage of the Isamill is that it can use fine grinding media, resulting in increased grinding events. The grinding chamber is maintained between 1 bar to 2 bar in order to maintain an even distribution of grinding events (Gaudin and Malozemoff 2002).

The Isamill has a unique product separator that prevents grinding media leaving the mill with the product.

The power requirement for horizontal stirred mills mills is usually an order of magnitude higher than that of vertical mills (Sinnott et al. 2006).

2.3.3 Stirred Media Detritor (SMD)

The SMD is a mill developed by Metso minerals. The mill is vertically orientated and contains a pins impeller. The ”pins-impeller” imparts high energy motion on the charge, increasing media particle interactions. This consequently improves grind efficiency and increases power consumption (Stender et al. 2004; Sinnott et al. 2006).

Pin mills are operated at higher speeds than screw type agitators. Thus, the mill’s power draw is higher and more sensitive to feed conditions and characteristics (Sinnott et al. 2006).

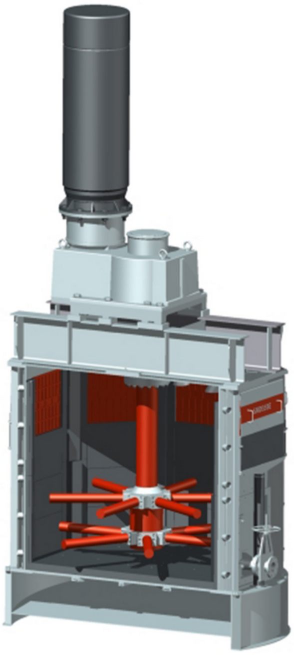

Figure 5: SMD with its agitator (Metso 2021a)

The SMD has numerous advantages. The mill is fairly versatile as it comes in a multitude of sizes. It can accommodate a wide range of feed conditions such as solids concentration, density and feed rate. It does not require any additional equipment such as compressors, slurry seals or cooling systems to effectively operate. This, in turn, leads to low maintenance costs (Ntsele and Allen 2012; Lisso 2013).

For a tower mill, and a pin mill, size reduction energies would be dominated by attrition and abrasive wear (Sinnott et al. 2006).

2.3.4 Vertical Stirred Mill

Similar to the SMD, the Vertimill is developed by Metso minerals. The Vertimill has similar advantages as the SMD. Particular emphasis is placed on its low maintenance costs and energy efficiency (Lisso 2013).

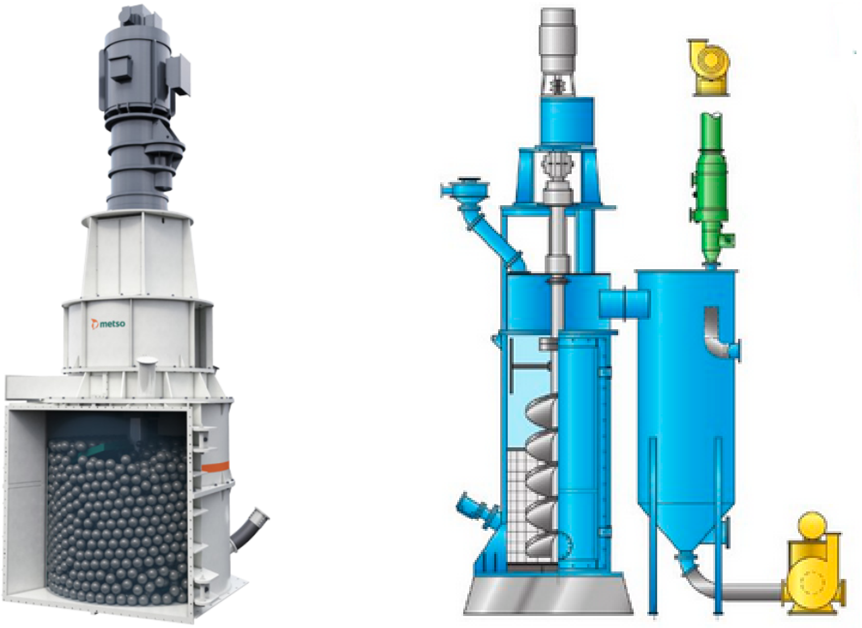

(a) Vertimill with its milling chamber exposed (Metso 2021a)

(b) Side view of a Vertimill with its pump (Metso 2021b)

Figure 6: Vertimill

2.4 Methods to approximate particulate flow

2.4.1 Eulerian approach

There are two approaches to modelling the particulate phase. There is the ”continuum approach” and the ”discrete approach”. The Eulerian approach approximates granular media as a continuum.

It has been established that granular media can be approximated as a continuum under the correct conditions (Pähtz et al. 2019; Morrison et al. 2016; Ding et al. 2002, 2001b). Furthermore, granular media has been approximated as a non-Newtonian fluid with some success (Zheng et al. 1995).

Approximating and understanding a simple, dilute or dense particulate flow is difficult and complex (Pähtz et al. 2019; Ding et al. 2001a). Particulate flow has different motions and flow regimes depending on the solids fraction, liquid temperature and coagulation of particles. An example of this is how the gas phase would have a significant impact on the motion of smaller particles under more turbulent conditions. (Ding et al. 2001a).

The equations and principles used in the Eulerian approach is based on the conservation of mass and momentum formula illustrated in Equation 1.

$$\frac{\partial \rho}{\partial t} + \nabla \cdot (\rho \vec{v}) = 0 \tag{1}$$

These equations are used to further derive new continuity expressions, based on the systems conditions at hand (Ding et al. 2001b,a). Simplifying assumptions are applied to reduce the complexity of the approximated systems.

The final approximation of the motion of solids in a system is the combination, approximation and incorporation of boundary conditions, particle profiles and characteristics into the conservation of mass and momentum equations. Discontinuities, assumptions, outliers and specific elements of the operating conditions further change the non-linearity, validity and form of the resulting motion equations.

A conservation model of the continuum approach is only valid for its defined flow regime and operating conditions. Unfortunately, the continuum approach does not adequately account for any anomalies or outliers in a heterogeneous population of particles. Thus, a continuum approach will not be used to simulate the particulate media.

2.4.2 Discrete approach

The discrete approach, also known and referenced as the discrete element method or distinct element method hereafter, is a robust and computationally intensive method of modelling particulate flow.

The DEM was first developed by Cundall and Strack (1979) to investigate the behaviour of stacked spheres and discs in the 2D-plane. It has since been expanded into the 3D space. DEM allows for greater accuracy and troubleshooting of mineral and comminution processes through modelling. It describes the motion of each individual particle, with special treatment for interactions with regards to system boundaries and other particles. These interactions are solved using Newton's equations of motion.

DEM is computationally intensive. This is due to it requiring a small time step to integrate over. The resulting simulation time step needs to be set lower than the critical value (Mishra 2003a). This is done in order to ensure that no excessive particle or boundary overlap occurs during the collisions. Should excessive overlap occur, unrealistic and skewed results would be produced. This enables DEM to simulate and capture relevant phenomena (Mishra 2003a; Cleary 2004; Kloss et al. 2012). The critical time step, Δt_c, is based on the characteristic natural frequency of a spring-mass oscillation system. The critical time step, Δt_c, is estimated using the mass of a relevant object, m_i, the spring dampening coefficient, k_i, with Equation 2.

$$\Delta t_c = 2\pi\sqrt{\frac{m_i}{k_i}} \tag{2}$$

For EDEM, the simulation software used in this paper, the critical time step is estimated as a fraction of the Rayleigh time step, T_R. This is done using the density of the media, ρ_b the diameter of the interacting particle, d_p, the shear modulus, G, and the poison's ratio, ν of the material. The estimation of T_R is illustrated Equation 3.

$$T_R = \frac{\pi(\frac{d_p}{2}\sqrt{\frac{\rho_m}{G}})}{0.1631\nu + 0.8766} \tag{3}$$

Multiple forces can be accounted for in a DEM model (Luding 2008). Particulate forces such as van der Waals forces as well as external forces, that are dependent on the surrounding operations and conditions of a system, can be accounted for. An example of an external force would be an unbalanced rotor of the mill, dissipating energy through vibration due to it being loose (Beinert et al. 2015). It is difficult to account for every force acting on the system. Thus, often times in simulations certain forces and conditions are not accounted for as they can be described as negligible or excessive. This leads to the simulations representing or approximating ideal or simplified systems. This results in certain operating conditions that are estimated *via* simulations, such as power draw, to be lower than the actual values.

There are various types of contact models available for use. The linear spring-dashpot model and the Hertz-Mindlin contact models are among the most popular models used (Mishra 2003a; Kulya 2008; Boikov et al. 2018).

2.4.2.1 Linear spring-dashpot model

In a linear spring-dashpot model, the interactions between the particles are assumed to be a linear spring and a dashpot. The linear spring-dashpot contact model is simple due to its parameters remaining constant throughout a simulation. It makes use of the soft contact formulation, where particles are permitted to overlap. The overlap is then used to estimate a force acting on the relevant particle.

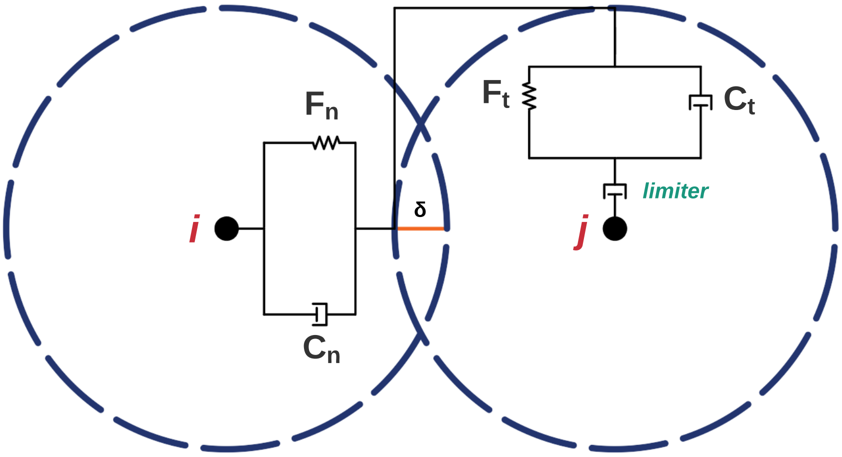

Figure 7: Linear spring-dashpot model

The normal force, F$_n$ is estimated using Equation 4. The normal spring stiffness, k_n, accounts for repulsion between the particles as they overlap, δ. The amount and rate of overlap gives rise to the normal contact force.

There is an inverse proportional relationship between the spring stiffness and the particle overlap.

$$F_n = k_n\delta + C_n v_n \tag{4}$$

k_n is dependent on the specific particles interacting with one another. In the case of the linear spring-dashpot model, a reliable value for k_n can be estimated by limiting the contact and overlap of particles during interaction (Misra and Cheung 1999; Mishra 2003a). This is illustrated in Equation 5, where the maximum absolute particle velocity, v_{max}, and penetration factor, f, are used to estimate the contact stiffness for a particle.

$$k_n = \frac{f m_i v_{max}}{d_p^2} \tag{5}$$

The normal damping coefficient, C_n, accounts for energy dissipation between collisions in the normal direction (Walton 1984). This in turn approximates energy dissipation throughout a system, which is mentioned in Section 2.3. C_n is heavily dependent on the coefficient of restitution, e_n. This is shown in Equation 6.

$$C_n = -2ln(e_n)\sqrt{\frac{k_n m^*}{\pi^2 + ln^2(e_n)}}. \tag{6}$$

The coefficient of restitution is defined as the ratio of the velocities of a particle, before and after a collision. The coefficient of restitution is not a material property. It is primarily dependent on the angle of impact, the shapes that are colliding, the sizes and of the colliding bodies, and the impact velocities thereof (Mishra and Rajamani 1992). There are numerous methods that can be used to estimate e_n (Thornton 2015). Generally e_n lies between zero and one.

The tangential force, F_t, is calculated incrementally. This is done as to account for slip occurring. Should slip occur, the tangential force would then be limited to μF_n. This adheres to the Mohr-Coulomb law (Kulya 2008). The tangential force accounts for shear based and friction forces acting on the particle.

$$F_t = min(\mu F_n, \sum_i k_t v_{t,i} \Delta t + C_t v_{t,i}) \tag{7}$$

An alternative form of Equation 7 is shown in Equation 8.

$$F_{t,i} = min(\mu F_n,\ F_{t,i-1} + k_t v_{t,i} \Delta t + C_t v_{t,i}) \tag{8}$$

The reason for the linear spring-dashpot model's popularity is that it gives reliable results within a relatively short time frame (Cleary 2004; Thornton 2015). It does however have a big flaw. It accounts for collisions in an unphysical manner (Kulya 2008). The result is that simulation data, from grinding circuits that are dominated by impact based breakages, are less reliable compared to grinding circuits that are dominated by shear based breakages.

2.4.2.2 Hertz-Mindlin contact model

In order to avoid the complicated equations and relations of Mindlin and Deresiewicz (1953), researchers combined the no-slip model of Mindlin (1949) with Hertzian contact theory to provide a non-linear contact model.

This model is more realistic compared to the linear spring-dashpot model. It adjusts parameters according to the colliding bodies overlap and materials (Kulya 2008; Thornton 2015).

The effective Young's modulus, E^*, and equivalent radius, R^*, of two particles colliding are used to adjust the spring stiffness and damping coefficient. The formulas used to estimate E^* and R^* are shown in Equations 9 and 10. The normalised mass, m^*, follows a similar formula shown in Equation 9.

$$\frac{1}{R^*} = \frac{1}{R_1} + \frac{1}{R_2} \tag{9}$$

$$\frac{1}{E^*} = \frac{1-\nu_1^2}{E_1} + \frac{1-\nu_2^2}{E_2} \tag{10}$$

$$\frac{1}{G^*} = \frac{2(2+\nu_1)(1-\nu_1)}{E_1} + \frac{2(2+\nu_2)(1-\nu_2)}{E_2} \tag{11}$$

The normal spring stiffness, k$_n$, is estimated using Equation 12. The tangential spring stiffnesses, k$_t$, is estimated using Equation 13.

$$k_n = \frac{4}{3} E^* \sqrt{R^* \delta} \tag{12}$$

$$k_t = 8G^* \sqrt{R^* \delta}. \tag{13}$$

The theory developed by Mindlin and Deresiewicz (1953) has been effectively used to give useful estimations of the shear contact stiffness (Kulya 2008). Consequently the normal damping coefficient, C$_n$, and tangential dampening coefficient, C$_t$, are dependent on the springs stiffnesses. This is shown in Equations 14 and 15.

$$C_n = \frac{ln(e_n)}{\sqrt{ln^2(e_n) + \pi^2}} \sqrt{5k_n m^*} \tag{14}$$

$$C_t = \frac{ln(e_n)}{\sqrt{ln^2(e_n) + \pi^2}} \sqrt{\frac{20}{6} k_t m^*} \tag{15}$$

The normal force, F$_n$, and tangential force, F$_t$ are estimated using the relative velocities. This is shown in Equations 16 and 17.

$$F_n = -k_n \delta_n + C_n v_n^{rel} \tag{16}$$

$$F_t = min(\mu F_n,\ k_t \delta_t + C_t v_t^{rel}). \tag{17}$$

Estimating the model parameters for each individual collision leads to increased computation time. The Hertz-Mindlin model gives accurate estimations, should the initial model data be configured correctly.

2.4.2.3 Boxing

DEM tracks all elements and contacts within a system. In a single time-step, with a system that has N particles, the number of contacts the DEM has to check is

$$\text{possible contacts} = \frac{N(N-1)}{2}. \tag{18}$$

As the number of particles increase, the possible collisions that are tracked in each time-step becomes excessively big. In order to optimise the DEM code and reduce time spent searching for possible collisions ”boxing” is implemented (Mishra 2003a).

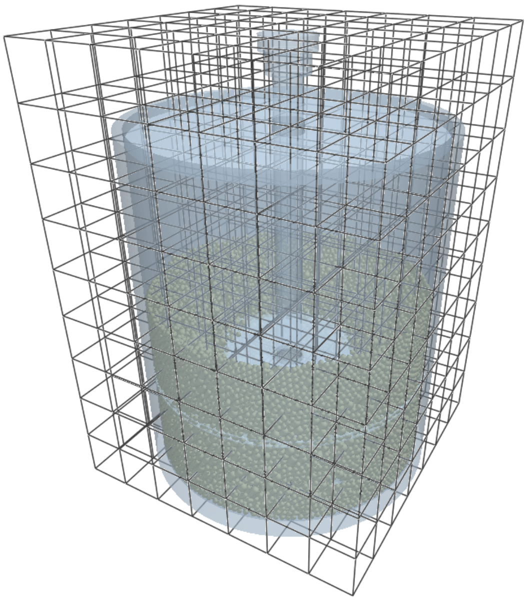

Figure 8: An illustration of boxing implemented in EDEM

Time spent searching for contacts is reduced by breaking sections of the system into localised cubes or squares, depending on whether the simulation is 3D or 2D. In the cubes, only local particles are taken into account when checking for collisions. This excludes any elements or particles outside the cube. If the cubes are sufficiently small the external forces can be accounted for through the course of a simulation. Though if the cubes are too large, certain phenomena or observations may be accentuated.

Complications are known to arise with boxing when working with non-spherical particles (Mishra 2003a). Complications can arise when coupling a DEM simulation with computational fluid dynamics (CFD). The CFD is dependent on how the boxing is implemented (Thornton 2015).

2.5 Breakages

Breakages in stirred mills occur *via* abrasion, cleavage and fracture. These breakages are more commonly known as impact, compression and abrasion based breakages. The different contact types (impact, tolling, torsion, shearing) do not exist separately, but in combined forms (Beinert et al. 2015).

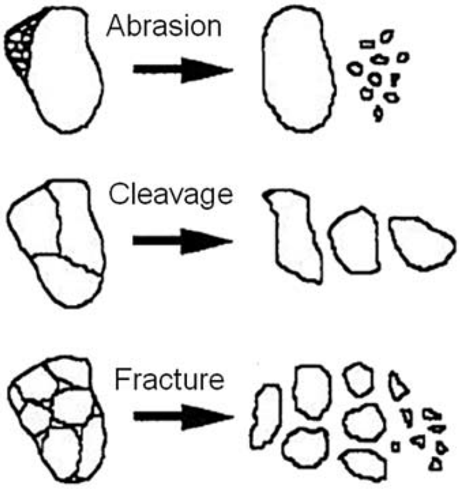

Figure 9: Mechanisms of breakages adopted from Varinot et al. (1997)

- Abrasion occurs when stress is applied along the tangential axis of the particles. Thus, shear-based strain promotes abrasion. Abrasion promotes bimodal particle size distribution.
- Cleavage occurs when intense stress and compression is applied on a particle over an extended time period. This produces fragments that are $50\,\%$ to $80\,\%$ smaller than the initial particle size.
- Fractures are promoted when rapid intense stresses are applied on the particle. Impact-based stresses promote this breakage. Fractures are not created by impacts; however, existing fractures are further emphasised by impacts.

2.6 Variables affecting grinding action

2.6.1 Stirrer speed

The stirrer speed affects the power input and collision efficiency intensity of a mill (Jankovic 2008; Edwards 2016; Ndimande et al. 2019). The influence of the stirrer is dependent on the type of mill used. In general, the impeller is used to facilitate charge motion in a mill. This, in turn, leads to differential velocities between adjacent particles which results in high shear rates in stirred mills (Jankovic 2008). The stirrer speed also affects the generalised motion and speed of grinding media and ore in the mill.

It is hypothesised that there is an optimal stirrer speed for a specific feed (Fadhel and Frances 2001; He and Forssberg 2007; Shrivastava et al. 2011). Below the optimum speed the stress events are insufficient for enabling proper breakages. Above the optimum speed excess agitation results in energy wastage. For gravity-induced mills lower stirrer speeds are favoured for reduced power consumption and energy efficiency (Jankovic 2008). For fluidised mills higher stirrer speeds are favoured for efficiency (Jankovic 2003, 2008; Shrivastava et al. 2011). These mills are highlighted in Table 1. The higher the stirrer speed, the more susceptible and sensitive the power consumption is to feed conditions.

2.6.2 Residence time

Proper consideration needs to be taken when altering the feed residence time in a mill. Low residence time allows for insufficient breakages to be facilitated. Prolonged periods of grinding do not result in a significant increase in the size reduction ratio of a grinding operation. The grinding media diameter and agitator speed have appreciable impacts on the required residence time, T_r, of ore in the mill (Szegvari et al. 1999).

$$T_r \propto \frac{d_p^3}{\sqrt{n}} \tag{19}$$

As particle size is reduced the particle strength is increased. This is due to there being reduced flaws in the particles structure and increased hardness in smaller particles (Thornton 2015). Thus, more intense stress events are required to break smaller particles. As such, over long grinding periods, energy is wasted as breakage events are reduced. Grinding efficiency is only appreciable in short periods of grinding action.

2.6.3 Feed

2.6.3.1 Feed size

There is a proportional relationship between initial and final particle sizes (Shrivastava et al. 2011). Coarse sizes need to be reduced *via* impact and compression based breakages. This in turn creates faults in the structures that can promote abrasion and attrition for fine grinding. Thus, the selection of grinding media size is dependent on the feed top size (Thornton 2015).

The size and shape of the powders and ore influence the flow and compaction of the feed. Smaller particles dissolve more quickly which leads to higher suspension viscosities (Scientific 2012).

2.6.3.2 Feed rate

The feed rate refers to the slurry mass or dry ore mass fed into the mill per unit time. The feed rate consequently influences several aspects of the mill. These aspects include, but are not limited to, the residence time, power draw and product production rate (Lisso 2013).

Stirred mills are often times operated at low tonnages compared to tumbling mills. High feed rates can result in negative operating conditions. High feed rates can reduce residence time. This can result in an uneven distribution of media, or feed, in the mill which reduces grinding efficiency (Jankovic 2008). At lower feed rates proper size reduction will occur, at the expense of increased residence time and increased power draw.

There may be an optimum feed rate. This feed rate may largely be dependent on the grinding media particle size, stirrer speed and mill volume (residence time).

2.6.3.3 Solids concentration

The solids concentration refers to the mass, or volume, fraction of ore fed to a mill with water as an additive. The fluid in a slurry feed is added to help with transportation and particle separation in downstream processes.

At low solids concentrations, collisions and breakages cannot be properly facilitated. This may be due to the fluid providing a cushion effect, reducing impact intensities. With a reduced solids concentration, there is a reduced probability of an ore sample being trapped between grinding media which would facilitate a breakage or collision (Lisso 2013; Edwards 2016).

At high solids concentrations flow complications may arise. An increase in solids leads to an increase in power requirement for transportation and agitation purposes (Edwards 2016). An increase in solids concentration can be beneficial as more solids leads to more collisions, improving grinding efficiency (Lisso 2013; Edwards 2016)

Any fluctuations in the slurry's solid concentration will lead to non-equilibrium distribution of slurry spacing. This leads to large swings in the kinetic and potential energy, which produces varying and exaggerated power draw (Thornton 2015).

Slurry mass fraction does not have a drastic impact on the final product size. Reduced solids leads to reduced contacts, collisions and energy dissipation (Frances et al. 1996; Cho et al. 1996). Reduced energy dissipation results in increased collision efficiency (He et al. 2004). These two effects dampen each other out.

Thus, there is an optimum solid concentration for grinding in a selected mill.

2.6.4 Grinding media

2.6.4.1 Density

The grinding media in a mill facilitates a specific size reduction ratio and energy transfer for breakages. Szegvari et al. (1999) and Graves and Boehm (2007) investigated the ideal characteristics of grinding media in the industry. These properties can be summarised as

- High hardness;
- Relatively low friction coefficient;
- No risk of contamination for downstream processes;
- Affordable;
- High surface stability; and
- Consistent in size.

High hardness and surface stability is important for grinding media to resist wear.

A direct proportional relationship exists between power consumed and media density (Zheng et al. 1995). Furthermore, the elasticity of the grinding media is inversely proportionate to density (Graves and Boehm 2007). The elasticity of a particle greatly affects the energy transfer efficiency during collisions (Lichter and Davey 2006; Shrivastava et al. 2011).

Balancing density to satisfy grinding efficiency, power consumption and media lifetime is important. Currently zirconia based ceramics are the ideal grinding media, providing high strength and fracture toughness without an overbearing density (Graves and Boehm 2007; Edwards 2016). A concern of this media is that it is susceptible to rapid wear when it eventually occurs. This in turn introduces undesired contaminants in the products.

A low friction coefficient is preferred to a high friction coefficient. Increased media friction would lead to excessive heat generation, energy dissipation and mill wear.

Density also plays a role in particle dynamics and mixing (Poux et al. 1991). Campbell and Bauer (1966) reported that a size-segregated mixture with a density ratio of 3:1 would result in an appreciable change in the mixing and segregation of a system.

2.6.4.2 Loading

It is known that the amount of collisions, N_c, that happen at any given time step is directly proportional to the amount of particles present in the system (Beinert et al. 2015; Shrivastava et al. 2011). This relationship is illustrated by Equation 20 and then simplified in Equation 21.

$$\frac{N_c}{\Delta t} \propto n\frac{V_{gc}(1-\epsilon)}{d_p^3 \times \frac{\pi}{6}} \tag{20}$$

Media loading and size have a meaningful impact on the number of effective collisions and power consumption (Cho et al. 1996; Jankovic 2008; Lisso 2013; Edwards 2016).

$$n\frac{V_{gc}(1-\epsilon)}{d_p^3 \times \frac{\pi}{6}} = n \times N_{gm} \tag{21}$$

Jayasundara et al. (2011) noted that there is an optimum media loading. Limitations need to be taken into account when attempting to estimate the optimal loading. The feed rate, available volume and power cost are limitations in this instance. Though the media loading is sensitive to feed conditions, it is not overly sensitive (Shrivastava et al. 2011).

2.6.4.3 Size and distribution

Particle size influences many properties in comminution. One of the more important properties it influences is the time at which steady state of fragmentation and re-agglomeration is reached, as well as the size reduction ratio (Fruhstorfer et al. 2014). For a specified feed size and required size reduction, there is an optimum grinding media size and load (Jankovic 2003; Wang and Forssberg 2007; Jayasundara et al. 2011). The selection of grinding media size is largely dictated by feed size, required product size and feed material (Edwards 2016; Maruf Hasan 2016).

The grinding media size determines the likelihood of particle breakage (He and Forssberg 2007; Beinert et al. 2015). With an increase in grinding media size, the contacts per time decrease as seen in Equation 20. Larger grinding media propagates impact and compression based breakages more effectively than smaller grinding media (Varinot et al. 1997; Jankovic 2003; Sun et al. 2009; Edwards 2016). The larger grinding media are thus better suited for coarser and larger sized feeds as opposed to smaller size grinding media. This is illustrated in Figure 10.

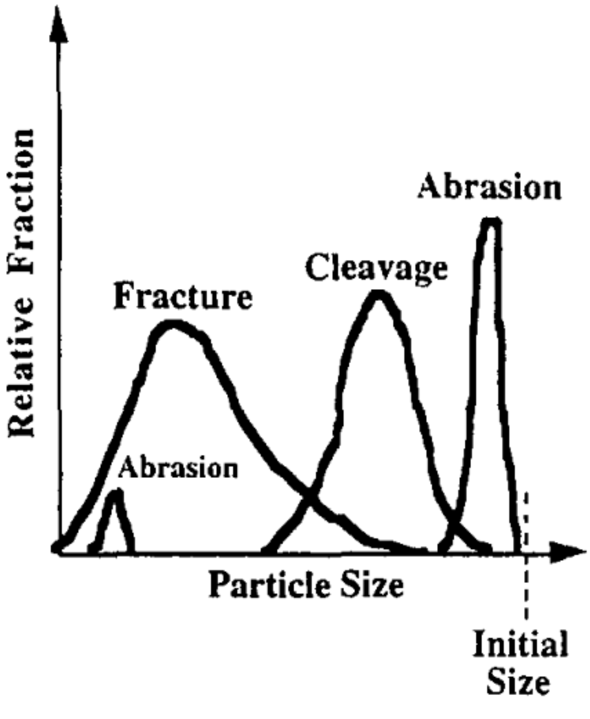

Figure 10: Dominant breakage mechanisms according to particle size distribution, adopted from Varinot et al. (1997)

Smaller sized grinding media propagate abrasion based breakages more effectively for fine grinding. Smaller size media is not well suited for coarse and larger sized feeds. The media can fail to sufficiently apply stresses that cause breakages to larger particles (Lisso 2013).

Bilgili et al. (2004) and Bayel (2019) reported that the use of size segregated media improves grinding performance in traditional tumbling mills. Simba and Moys (2014) also used different shaped grinding media in lab scaled grinders. In these experiments it was concluded that the shapes, used in combination with one another, still retained their original benefits. This effect could extend to size segregated grinding media.

Open volume between larger particles is reduced when using a bimodal distribution for grinding media. Small grinding media reduces the total available voidage between larger particles. Furthermore, smaller media increases the specific surface area and number of particles available in the system.

The bimodal packing should be able to reduce the maximum particle diameter after grinding (Fruhstorfer et al. 2014). However, the optimum operating conditions are subject to change when having a size segregated grinding media (Bayel 2019). Thus, a size-segregated particle distribution would not ultimately result in initial success.

Unfortunately, the size-segregated media might accelerate the wear of one another. The wear of grinding beads is determined by the structure and hardness of the beads as well as the hardness and shape of ground material (Becker and Schwedes 1999; Jankovic 2008). The wear of particles can be minimised by choosing the grinding media material accordingly (Fruhstorfer et al. 2014).

Coarse grinding media are more susceptible to wear than finer media (Bayel 2019). The wear of said media can further result in the contamination of downstream processes (Edwards 2016).

2.6.4.4 Shape

In comminution, grinding is dictated by spherical media. This is likely due to the simplistic, abundant and easy to manufacture nature of the spherical media. This simplistic shape allows it to be easily adapted into DEM modelling.

In reality, grinding media is non-uniform. The size and shape of media continuously changes due to breakages and wear mechanisms (Lameck et al. 2006). The wearing and breakage result in smooth, non-spherical ball shapes with pronounced cavities, porosity holes or angles (Vermeulen 1989). The worn down media can result in different grinding dynamics, stress distributions, energy distributions and efficiencies (Sinnott et al. 2011). Alternative media shapes such as cylpebs, conipebs and boulpebs have their own advantages (Cloos 1983).

Table 2: Benefits of media shape

Spherical shapes	Alternative shapes
Increased packing efficiency	Reduced production cost
Simple design parameters	Reduced porosity produced on casting
No inherent resistances in transportation	Increased area for contact

Media shape has an appreciable influence on the power draw, media packing, shear flows and mixing in a mill (Lameck et al. 2006; Sinnott et al. 2011). In the industry it is accepted that non-spherical debris from grinding media result in reduced grinding performance (Sinnott et al. 2011).

2.7 Notable characteristics of size segregated media

Size segregation can be both a desirable, as well as a non-desirable trait of granular media, depending on the context of the unit operation. In tumbling mills size segregation is common due to wear of grinding media and addition of new media.

Size segregated media gives rise to new phenomena in tumbling mills that are less pronounced, or absent, in mono-sized systems. Phenomena such as the *Boycott-* , *Leidenfrost-* and *Brazilian nut effect* effects are noteworthy. The degree to which size segregation occurs is dependent on the mill's operating conditions, with the mill rotation speed having a pronounced effect on the degree of segregation (Soni and Mishra 2016; Soni et al. 2016).

Grinding would be enhanced if the mill agitated the grinding media to allow for uniform size and contact distribution (Soni and Mishra 2016).

2.7.1 Boycott effect

The *Boycott effect* allows for faster settling of granular media in a container if the container is inclined at an angle. The accepted reason for this is that when the container is at an inclined angle, the supernatant will rise to the top and generate a convective layer over the granular media, further improving the speed at which the supernatant rises (Duran and Mazozi 1999).

2.7.2 Leidenfrost effect

The *Leidenfrost effect* allows for coarse particles, in a size segregated granular mixture with hexagonal packing, to rise to the top, supported by a dilute gaseous layer of fast acting particles underneath. This effect is only possible when specific conditions are met (Eshuis et al. 2005). This effect is possible when sufficient energy is supplied for agitation, there are enough particles, and the collisions are fairly elastic in nature.

2.7.3 Brazilian nut effect

Similar to the *Leidenfrost effect*, this effect allows for coarse particles to rise to the top of a granular mixture when it is subjected to mechanical agitations. The *Brazilian nut effect* can be become negligible, or even prevented, if the agitation occurs at low ambient air pressure (Wen et al. 2014).

The *Brazilian nut effect* is undesirable in tumbling mills, as it leads to coarser particles collecting or segregating in the mill (Breu et al. 2003). When particles are segregated, or clumped together, any mechanical energy that is imparted onto one group does not properly propagate outward to the rest of the particulate media (Soni et al. 2016; Ma et al. 2023).

At lower grinding speeds larger particles collect atop smaller particles in a tumbling mill. Uniform distribution of particles and contacts was achieved at intermediate grinding speeds of between 65 % and 85 % of the critical speed of a tumbling mill. At higher speeds the *Brazilian nut effect* is reversed, with smaller particles collecting on top of larger particles (Soni and Mishra 2016).

2.8 Summary

An introduction to grinding and mills is given in this section. Types of grinding mills used within the mining industry are highlighted. Two methods of approximating particulate media are discussed. This includes the Eulerian approach and discrete approach. The methods by which the discrete element method simulates particulate media is further illustrated. Additionally the variables that affect grinding action in a mill are mentioned in this section. Notable characteristics, or peculiarities, of size-segregated media are also mentioned.

3 Experimental procedures

In this chapter the methods and techniques used to generate and compute data within this study are discussed. A brief overview is provided of the equipment and simulation setup, the equipment and software afforded to the student, the coding principles used to manipulate and filter data, and a brief overview of the simulations performed and steps followed.

3.1 Personal computer (PC)

A stand-alone computer was used to perform the simulations in this study. The specifications of the computer used are given in Table 3. The PC and specified components were selected with the intent of processing and generating data from EDEM effectively and fast.

Table 3: PC specifications

Component	Specification
RAM	32 GB
CPU	AMD Ryzen 9 5900X 12 - Core Processor
GPU	NVIDIA GeForce RTX 3060
HDD	930 GB

The recommenced specifications for EDEM are listed in Table 4. The CPU of the PC is in line with modern standards of high-end hardware (Hardware 2022; UserBenchmark 2022). In terms of single thread performance, the Ryzen 9 5900X's is superior to an Intel Xeon E5 series. A particular highlight is the Ryzen 9 5900X's ability to perform multithreading. Multithreading allows for concurrent, or parallel, execution of threads. This allows for large data to be segmented and then processed simultaneously. This significantly improves the performance and speed of demanding programs or data.

Table 4: Requirements for EDEM (Col 2023)

Component	Minimum	Recommended
RAM	8 GB	32 GB or more
CPU	Intel Core i7 or AMD Ryzen 7 (8+ cores)	Intel Core i9 or AMD Ryzen Threadripper (16+ cores)
GPU	NVIDIA GeForce GTX 960 or AMD Radeon R9 270	Any modern GPU from either AMD or NVIDIA
HDD	4 GB (for software) +100 GB (for data handling)	1000 GB

The PC contains enough storage space for the data that can be generated by EDEM, as well as sufficient RAM for the fast processing required by the data and system being studied. A modern RTX 3060 series video graphics card was used in the computer.

3.2 Simulation parameter set up

The Hertz-Mindlin (no slip) contact model was used for the simulations in this study. This contact model was discussed and illustrated in Section 2.4.2.2. The materials present in the simulations were glass, high density poly ethylene (HDPE) and steel. The simulation material properties for the aforementioned materials is shown in Table 5. The impeller used in the simulations was based on an impeller in the Center for Minerals Research (CMR) lab, which is coated in HDPE and thus approximated as HDPE. This impeller was used in tandem with steel containers. The only available glass grinding media was 5 mm and 8 mm beads.

The parameters and constants that were used for this model were sourced from previous theses from the University of Cape Town (UCT) that used similar equipment and material setups. The material properties for HDPE and glass were sourced from (Bremner 2016). The parameters were based on previous literature sources that evaluated it with a multitude of different parameter set ups. The steel used was approximated AISI 4140 Alloy Steel (UNS G41400) (AZOMaterials 2022).

The simulation parameters for the glass particles interacting with glass, and HDPE materials, were sourced from Hromnik (2013). The simulation parameters from Hromnik (2013) were estimated from the physical properties of the materials. The parameters for glass interacting with steel was sourced from Malahe (2012). The parameters were sourced from previous established literature sources. The resulting simulation parameters are shown in Table 6.

Table 5: Material properties

	HDPE	Steel	Glass
Density (ρ)	940 kg $\cdot$ m^{-3}	7850 kg $\cdot$ m^{-3}	2500 kg $\cdot$ m^{-3}
Poisson's ratio (ν)	0.4200	0.2850	0.2000
Shear modulus (G)	7.0 $\times$ 10^{8} Pa	8.0 $\times$ 10^{10} Pa	6.4 $\times$ 10^{10} Pa

Table 6: Simulation parameters

Subject	Interacting subject	Parameter	Value
Glass	Glass	Coefficient of restitution	0.6600
		Static friction coefficient	0.1540
		Rolling friction coefficient	0.0100
	HDPE	Coefficient of restitution	0.5500
		Static friction coefficient	0.3200
		Rolling friction coefficient	0.0100
	Steel	Coefficient of restitution	0.8500
		Static friction coefficient	0.3060
		Rolling friction coefficient	0.0100
Gravity	Particles	–	9.8070 m $\cdot$ s^{-1}

3.3 Simulation equipment set up

This subsection includes the geometry, particles and factory setups for the simulations and goes into further detail regarding particle spawn rates and geometry placements.

The dimensions of the geometries used within EDEM are shown in Figure 11. This equipment was created using a 3D computer aided drawing (CAD) program named Autodesk Inventor Professional 2022. A student trial for this CAD software is freely available to students of UCT.

A lab scaled vertical stirred mill was selected to be investigated. There is little information, or studies done, on dry grinding applications of vertical stirred mills. Fewer of the available vertical stirred mill studies focused on size-mixed grinding media.

The vertical stirred mill used was based on an available lab-scaled stirred mill inside the Centre for Minerals Research (CMR) laboratories. The stirred mill design did not lend itself to continuous operation. Its design allowed for batch operations.

The equipment used in EDEM was set to be at the centre point of the simulation space. This was done as tangential velocities are estimated relative to the Z-axis. The impeller, grinding chamber and lid's centre points were set to be at the centre point of the simulation space.

The absolute bottom of the grinding chamber was set to be Z = 0 mm. This results in the grinding chamber floor reaching a height of 10 mm. The absolute bottom of the impeller was set to be 30 mm, which is 20 mm above the grinding chamber floor. The lid shape was used to prevent particles from escaping the simulation. The shape of the lid was also used as a virtual factory to spawn particles into the simulation. Particle spawn rates and impeller agitation speeds were adjusted as needed for the relevant simulations.

The methods by which the simulations were planned and approached are shown in Figure 12. The important decisions are depicted in the diamonds of the flow chart. At the diamonds decision making points either the operating conditions, such as the impeller speeds, or the simulation basis, such as the weight distribution, were adjusted as needed.

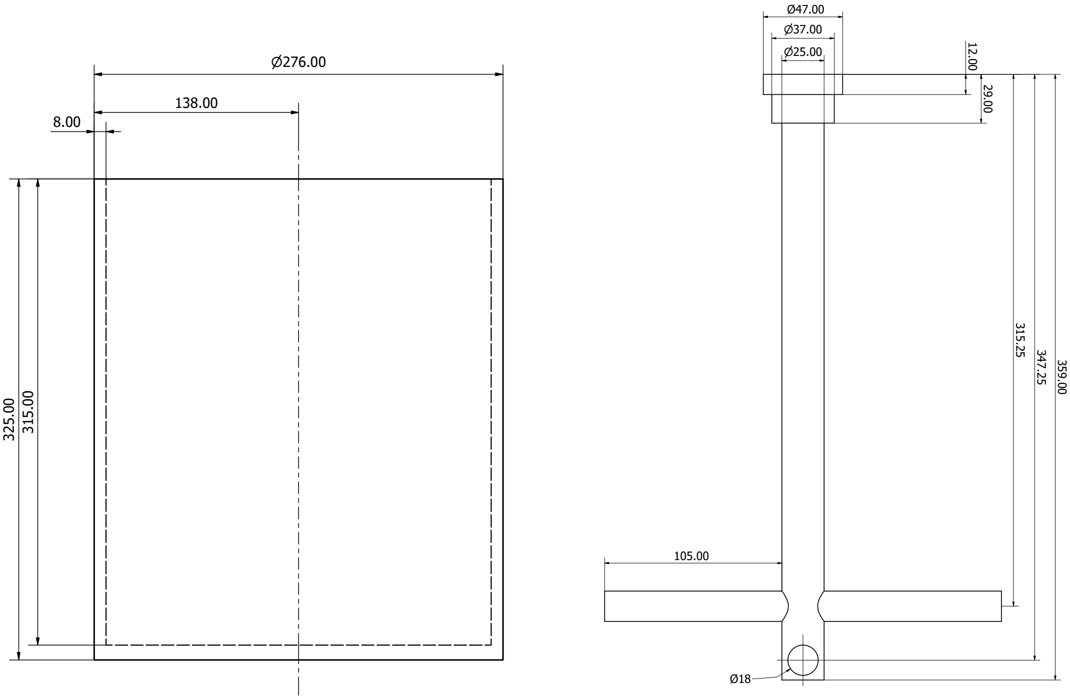

(a) Grinding chamber **(b)** Impeller

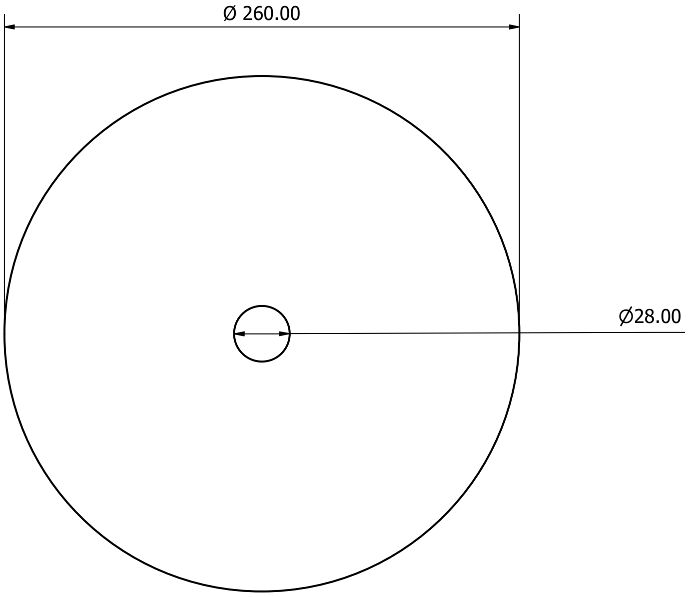

(c) Lid (thickness = 10 mm)

Figure 11: Dimensions of equipment used within simulations

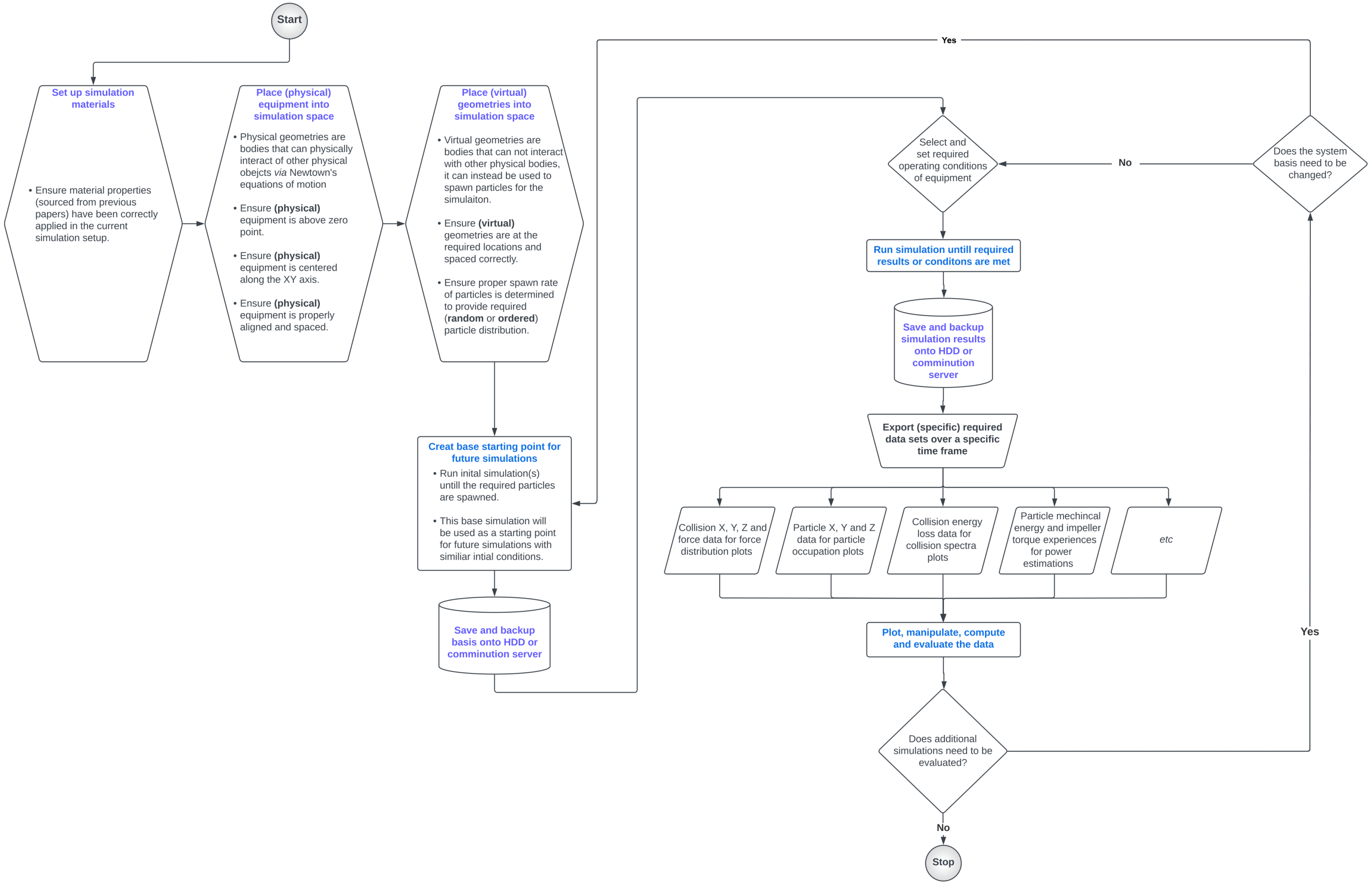

Figure 12: Flow chart illustrating the approach to simulation set up and parameter investigation

3.4 Data preparation

3.4.1 Computing data according to spacial distributions

Matlab 2021a was the main programming language used to compute the results. It further allows for boolean indexing, which is a helpful tool for filtering and grouping of multiple data sets (EducativeTeam 2022).

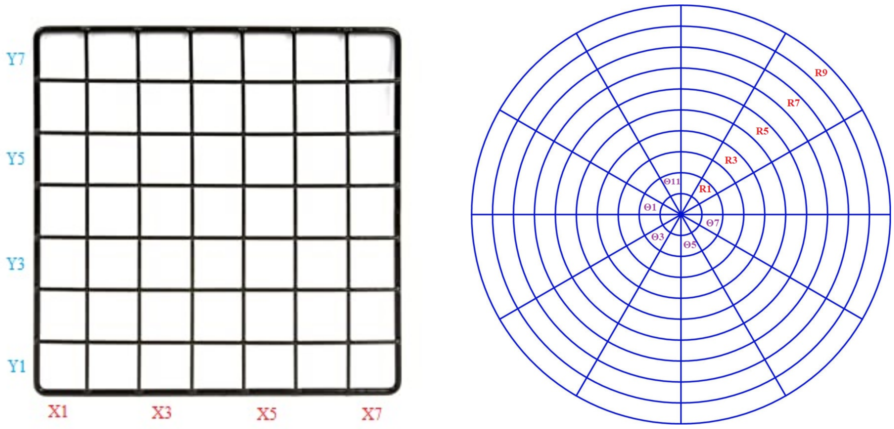

(a) Axial grid **(b)** Cylindrical grid

Figure 13: Different grids used for data analysis in the simulation space

For instance, one can group and compute the average force or energy loss experienced by a particle or collision at a specific point in space, determined by a grid cell. Different types of grids can allow for selective filtering and estimation of data. For example, filtering and estimating the energy dissipation between X_1 and X_3 will give different results when filtering and estimating the data between θ_1 and θ_2 in the cylindrical system. The two different types of grids used in this study, such as the axial and cylindrical grid, are shown in Figure 13. An axial coordinate can be converted into a cylindrical coordinate using Equations 22 and 23.

$$R = \sqrt{X^2 + Y^2} \tag{22}$$

$$\theta = \arctan(\frac{Y}{X}) \tag{23}$$

The Z-value for both sets of coordinate systems remains the same. Using the different coordinate systems, different results can be computed and presented in the form of graphs. Grouping values according to their XYZ, or RθZ locations. Summating the number in such a local space allows for the construction of an occupation profile of the collisions or particles in that space. Averaging the values in a specific space allows for the construction of concentration profile. Multiplying the concentration profile with the occupation profile of the relevant subjects can be done to create an illustration of the average distribution of the subject throughout that space.

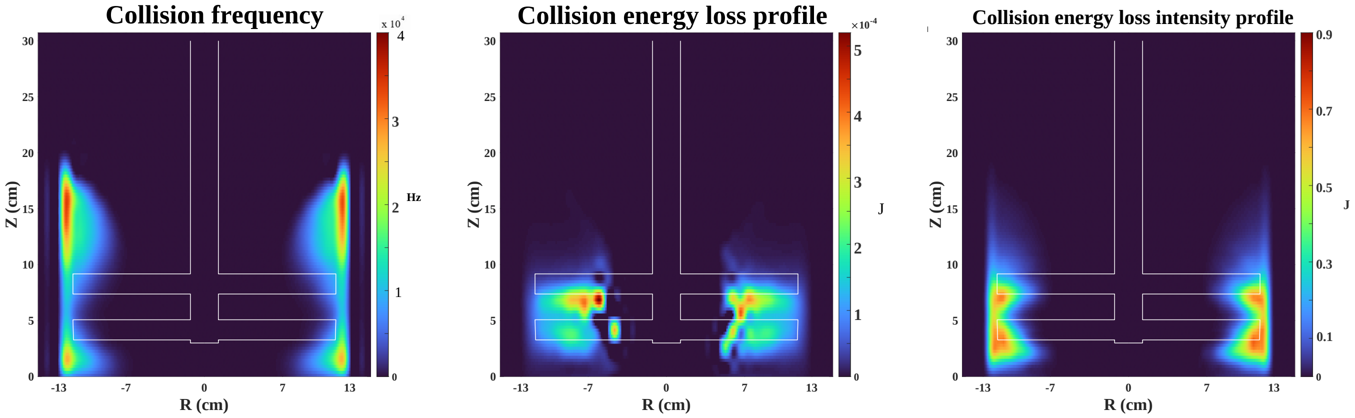

(a) Occupation profile **(b)** Concentration profile **(c)** Intensity profile

Figure 14: Illustration of how a pseudo colour plot is constructed

An illustration of the above mentioned data analysis method is shown in Figure 14. An occupation profile of the collision frequency is constructed in Figure 14a.The majority of the collisions occur above and below the impeller pins. The energy loss of the collisions, filtered and averaged according to the cylindrical grid, is used to produce the energy loss concentration profile in Figure 14b. The majority of the intense energy loss collisions can be seen around the impellers. Multiplying the concentration profile, Figure 14b, with the occupation profile, Figure 14a, results in the energy loss intensity profile in Figure 14c. Here it can be seen that a most of the energy loss is concentrated at the edges of the container.

In order to get a more generalised illustration of the select subject, the data needed to be time averaged. This entailed all the collisions and particles over multiple time steps to be accumulated in a single data structure, with the final filtered or computed value being averaged according to the number of time-steps used to generate the original data structure.

Furthermore, the occupation profile could be used to generate a percentage occupation of the particles. This could be done by dividing the time averaged particles spacial occupation values with the total number of occurrences, and then plotting the percentage value thereof.

3.4.2 Computing collision spectra

The collision spectra was used to characterise the collisions of a particulate system (Ndimande et al. 2019; Cleary et al. 2006; Morrison and Cleary 2004). In DEM the energy dissipation rate of tangential and normal based interactions can be computed for individual collisions and particles such as particle-particle, particle-environment, and so forth.

The collision energy spectra provided an opportunity to understand and optimise the overall collision energy dissipation within the mill. Understanding the changes in collision spectra according to operating conditions could allow for better evaluation of how the collision energies were utilised within the system (Cleary et al. 2006).

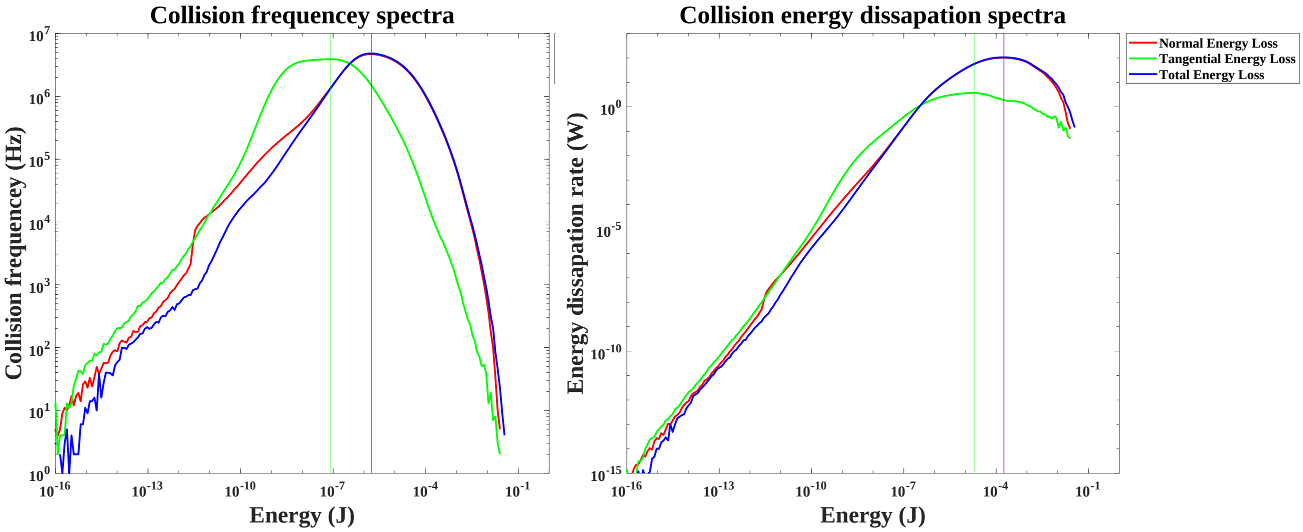

(a) **(b)**

Figure 15: Illustration of the collision spectra of the mono-size particle simulation with EDEM 2.5 in Section 4.1

A collision spectra was produced by taking the collision intensities of a specific energy loss within a select collision energy range. Summating the amount of data points within that energy range provided the collision frequency plot shown in Figure 15a. However, summating the energies within that bandwidth gave rise to the energy dissipation rate of the collisions, shown in Figure 15b. The average energy dissipation rate could also be computed using the average of the energy range and multiplying the average energy loss with the collision frequency.

When evaluating the collision spectra, both the collision energy range and the modal peaks were used to evaluate the performance of the collisions.

3.5 Simulation scope

The objective of the work in this thesis was to estimate the optimal operating conditions of a size-mixed system and to introduce the expected trends and tendencies of a size-mixed system. To this end four experiments were performed. These experiments involved:

Experiment 1 investigated the degree and tendency of simulation artifacting. In this setup two simulations were performed; one simulation had the particles with a uniform size throughout, whilst the other simulation allowed for the particles to have a normal distribution with a predetermined deviation.

Experiment 2 investigated the influence and tendencies of impeller agitation speed on the size segregated particulate system. Here four simulations were performed, with the exact same initial particle mixing setup for each simulation. In the different simulations the impeller rotation speed was changed for each run. The impeller agitation speeds evaluated were 200 rpm, 350 rpm, 500 rpm and 700 rpm. These speeds were selected to evaluate the results when the particles were fluidised, semi-fluidised and fully fluidised.

Experiment 3 investigated the influence of the particle weight distribution on the grind characteristics of the system. To this end, five different particle weight distributions were evaluated and four new simulations were performed. The different weight distributions were 100 wt% 5-mm particles, 25 wt% 8-mm and 75 wt% 5-mm particles, 50 wt% 8-mm and 50 wt% 5-mm particles, 75 wt% 8-mm and 25 wt% 5-mm particles and 100 wt% 8-mm particles.

Experiment 4 investigated the degree of particle segregation with different weight distributions. For this experiment an additional simulation was performed with three different sized particles. These three particle sizes simulated in the additional simulation were 3-mm, 5-mm and 8-mm. The three particle sizes were simulated with equal weight ratio's. The degree of particle segregation at different weight distributions, from experiment 3, were evaluated with the 3 particle system.

3.6 Summary

The methods used to generate and process data are discussed in this section. Furthermore, the equipment used and the set up thereof are elaborated on in this section. Additionally the variables that are used in the DEM simulation are given.

4 Results and discussions

4.1 Size-varied investigation

4.1.1 Initial setup

A preliminary experiment was performed to investigate the significance of particle radius variation in a simulation. DEM simulations are an approximation of the real world, where simplifying assumptions are made. This leads to possible issues where complex or stringent simulation conditions may result in digital artifacts (Iordache et al. 2010). Digital artifacting occurs when data and simulations setups result in questionable, or unrealistic, data being produced.

Two simulations were performed for this experiment. Two particle populations were generated with a random packing order in separate grinding chambers. For the first population, the particle diameters for the $5\,\mathrm{mm}$ and $8\,\mathrm{mm}$ particles remained uniform. For the second population, a standard Gaussian model was applied to the particles. The particle sizes were taken as the mean of the specific distribution with a $10\,\%$ standard deviation based on the particle diameter. This resulted in smaller particles having a narrower range than that the larger particles. The resulting particle probability distribution is shown in Figure 16b. A total of 3 kg of 5 mm and 8 mm particles was generated in the uniform-sized and size-varied simulations. This resulted in the size-varied simulation having less particles than that of the uniform-sized simulation. A summary of the number of particles is shown in Table 10.

The impeller and grinding chamber, as shown in Figure 11a and Figure 11b, were used for these simulations. The simulation parameter setup in Section 3.2 is adopted here. The particles were simultaneously spawned with random locations to approximate a well-mixed system. A resulting random particle packing can be seen in Figure 16a.

4.1.2 Simulation set up and data capture

The set up for the media was simulated over 5.00 seconds. The first 1.60 seconds were used for particle generation. In this time frame the particles were allowed to come to rest before the impeller started its rotation clockwise. After settling, the impeller rotation was accelerated to 500 rpm over 1.00 second. After the rotation speed had been achieved, 2.40 seconds was dedicated to the collection of particle and collision data.

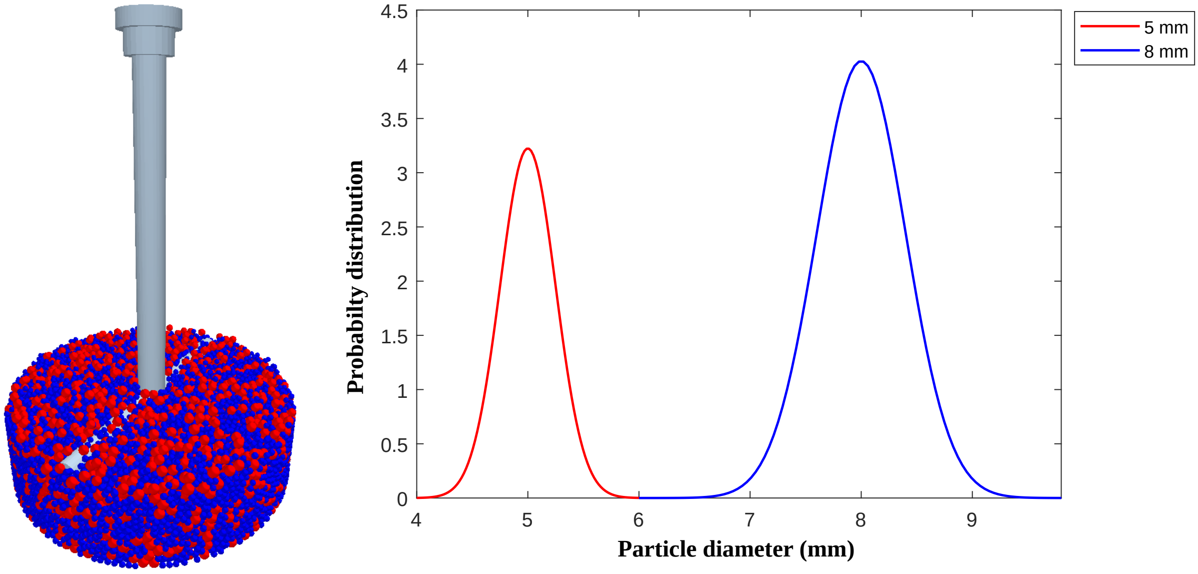

(a) Particle packing **(b)** Initial particle size distribution

Figure 16: Simulation investigation setup

The 1.00 second time period of acceleration achieved approximately ≈ 4.2 revolutions of the impeller. The 2.40 seconds dedicated to data collection corresponded to 20 revolutions of the impeller.

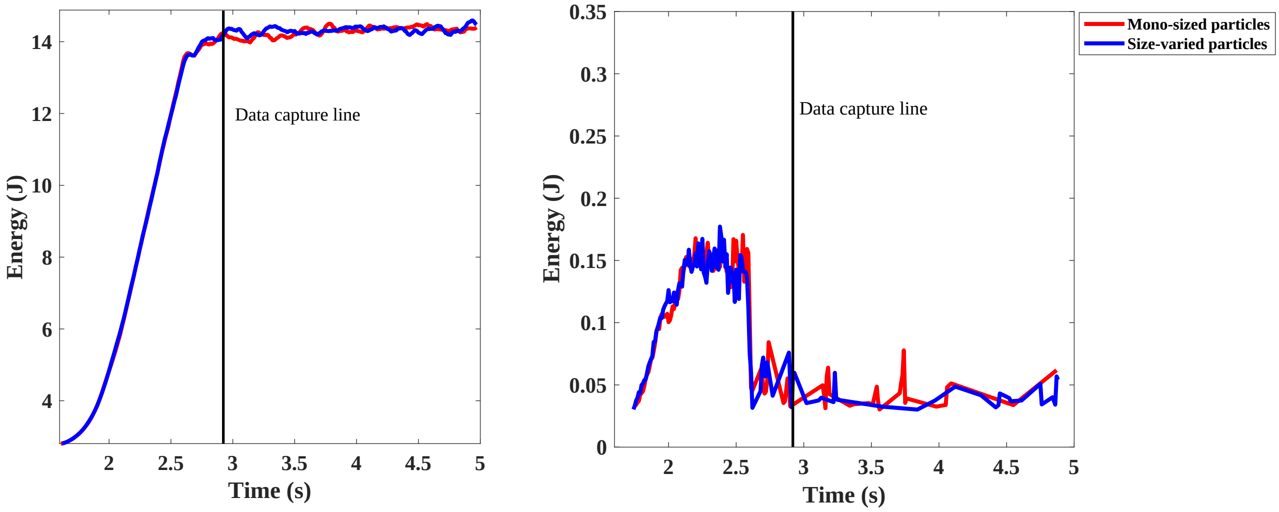

(a) Particle Mechanical Energy **(b)** Change in Particle Mechanical Energy

Figure 17: Resulting particle mechanical energy

The systems reached steady state from 2.90 seconds onwards. At this time the change in total mechanical energy becomes negligible, as seen in Figure 17b. The reduced change in total mechanical energy indicates that the system had stabilised, reaching a steady state. This can be seen in Figure 17b. The approximation of total mechanical energy is shown in Equation 24.

$$\sum Mechanical\ Energy = \sum PE_{particles} + \sum KE_{particles} \tag{24}$$

The data for analysis was captured from 2.90 seconds and onwards, unless otherwise stated or indicated. The residence time for the particles inside the grinding chamber can be approximated as the duration of the simulation.

4.1.3 Particles

4.1.3.1 Spatial distributions

The illustrations in Figure 18 are time averaged depictions of particle occupation in the systems. Here, an RθZ-grid was applied over the grinding chamber. In this grid the total particles occupation was averaged according to the total time steps in the local grid box.

The 5 mm particle occupation profiles are shown in Figures 18a and 18b. It can be seen that a significant portion of the 5 mm particles tended to collect at the top and bottom ends of the particulate system. The 5 mm particles tended to collect at the edges of the floor of the grinding chamber, as well as atop the particulate mixture at R = 13.0 cm and Z = 16.0 cm. This can be seen in Figures 18a and 18b.

The majority of the 8 mm particles tended to collect just above the impeller pins near the grinding chamber walls, at R = 13.0 cm and between Z = 8.0 cm and Z = 14.0 cm. This is somewhat similiar to the 5 mm particles, as a portion of the 8 mm particles tended to collect above the impeller pin. This can be seen in Figure 18c and 18d. It appears that the top 5 mm particles were collecting above the 8 mm particles. The portion of 8 mm particles that collected above the impeller pins appears to be more significant in the mono-sized particle population than the size varied population. This can be with the more pronounced red highlight of particle occupations in Figure 18c compared to Figure 18d.

There are multiple mechanisms that enabled the particles to collect above the impeller pins. The particles collected at the edges of the grinding chamber due to it being centrifuged outwards. With agitation smaller particles have improved flowability compared to larger particles. Thus, when the impeller pins create available space at the grinding chamber bottom, pushing particles outwards and upwards, the smaller particles are the first to occupy it while significant portion of the larger particles are moved upwards. The available particles that then occupy the lower spaces in turn support the larger and smaller particles above the impeller pins. This is similiar to what Soni and Mishra (2016) observed where smaller particles would fill available cavities that formed during agitation, further allowing the larger particles to rise up.

Inspecting the velocity profiles of the particles in Figures 18e and 18f, it can be seen that the highest particle speed was located near the impeller pins. Furthermore, the speed was reduced the further away the particles were from the impeller. The velocity profiles of the mono-sized and size-varied particles do not differ significantly from one another.

In the mono-sized velocity profile, in Figure 18e, trails of different velocity speeds can be seen in the top right corner of the image. These trails were the result of infrequent particles shooting upwards and creating the relevant profile. This occurrence was inconsistent in timing and occurrence.

The degree to which the particles separate does not change substantially between the mono- and size-varied systems. There does appear to be a higher degree of particle collection for the mono-sized particle population as opposed to the size-varied particles at the top end of the particulate mixture. This can be seen in Figures 18a through to 18d where the mono-sized colours are more intensive than that of the colours of the size-varied particles. This discrepancy is not incredibly apparent. This discrepency is further illustrated and discussed in Section 4.1.5. It is important to note that there were more particles in the mono-sized system compared to the size-varied system, which contributed to more accentuated observations being made. This was due to the Gaussian weight distribution. Other than the differences in particle occupations, there were no other apparent differences in the way the particles tended to collect in the system.

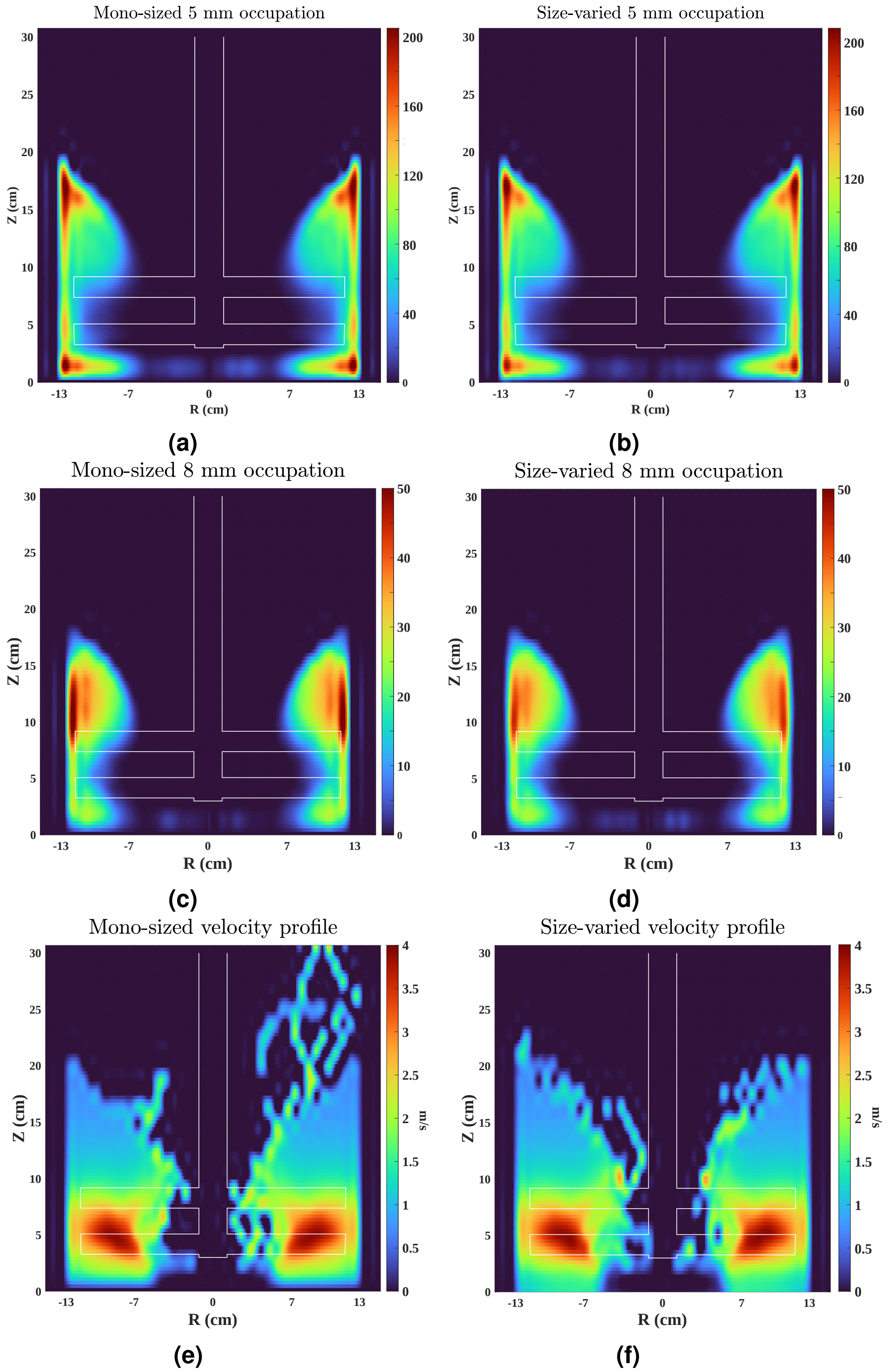

(a) (b) (c) (d) (e) (f)

Figure 18: Particle occupation and velocity profiles

4.1.3.2 Particle motion

The general particle motion for mono-sized and size-varied simulations were largely the same. In Figure 19 the normalised motion of particles is depicted. The radial velocity,V_r, which is the speed at which a particle moves either outwards or inwards relative to the centre of the grinding chamber, was normalised using Equation 25. Similarly the axial velocity,V_z, which is the speed at which particles move either upwards or downwards, was normalised using Equation 26.

$$V_{r,norm} = \frac{|V_r|}{\sqrt{V_r^2 + V_z^2}} \tag{25}$$

$$V_{z,norm} = \frac{|V_z|}{\sqrt{V_r^2 + V_z^2}} \tag{26}$$

The normalised time averaged radial and axial velocities were used to plot the quiver plot. Note that the speeds of the particles are not uniform throughout, as shown in Figure 18.

The angular rotation speed of the particles, V_θ, was not included in the following depictions as it would have further reduced the legibility of the graphs. The normalised radial and axial velocities, coupled with the particle velocity profiles in Figure 18, gave enough relevant information regarding the general particle motion in a clockwise manner.

In Figures 19a and 19b the particle vector fields of the mono-sized 5 mm and 8 mm particles are shown. Similarly, in Figures 19d and 19e the particle vector fields of the size-varied 5 mm and 8 mm particles are shown. In all the cases illustrated the vectors shown in red depict upwards motion, while those in blue depict downward motion.

In Figures 19c and 19f the 5 mm and 8 mm vector fields were superimposed on each other. The 8 mm particles are depicted in a soft green, whilst the 5 mm particles are depicted in a dark red.

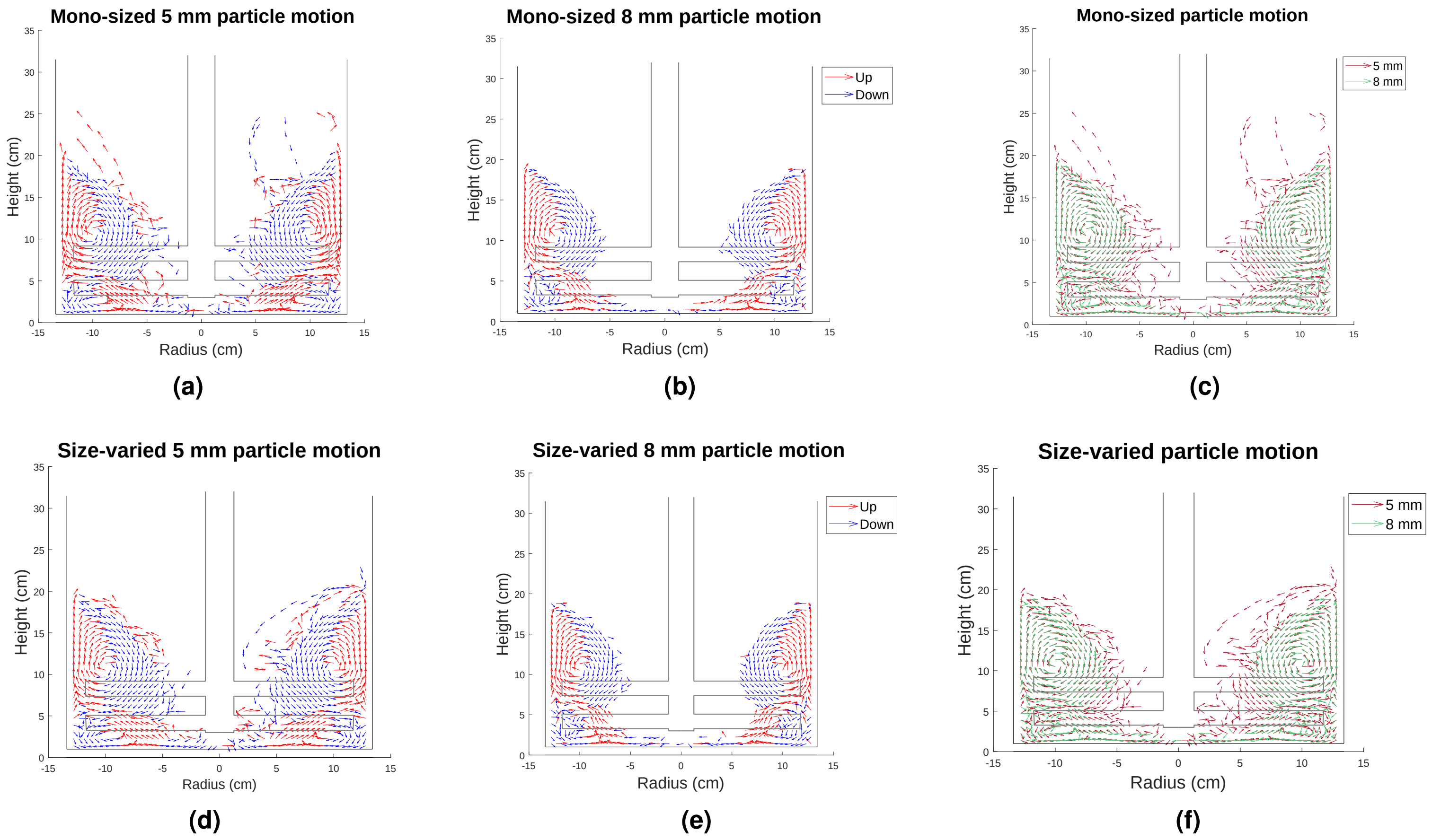

Figure 19: Normalised particle vector fields

As the particles achieved steady state and fluidised it follows a vortex like motion. This can be seen in Figure 19. The particles tended to move upwards and outwards at the edges of the container above the top impeller pin. Afterwards the particles appeared to cascade downwards to the bottom peripheries, before collecting again to join the initial rise.

Near the peak height, a particle would start to slow down, which resulted in an accumulation or stagnation of particles above the impeller pins and bulk of the particulate media. The smaller particles had increased flowability, relative to the larger particles; as such they tended to be the dominant particle accumulating at the top layer. The light mass of the smaller particles enabled it to receive momentum, or kinetic energy, more easily from colliding particles near the impeller pins. This energy was then directed upwards, due to the established particle motion.

The layer may have different implications depending on the particle. The larger 8 mm particles did not segregate as drastically as the 5 mm particles, tending to group together just above the impeller pins. This can be seen in Figure 18c. Perhaps the formation of the smaller particle collection above the larger particles cushioned or hindered the larger particles from accumulating or moving upwards, resulting in it gaining the majority of the intense collisions near the impeller pins.

According to the collective particle motion shown in Figures 19c and 19f, both the 8 mm and 5 mm particles followed the same general vortex-like motion. It does appear that there was more turbulent motion, for the smaller particles, near the bottom of the grinding chamber. This may be due to the particle motion force carrying the particles to a section where a large number of particles had already collected. This accumulation could then force the particles to move elsewhere in a more turbulent fashion. The smaller particles tended to cover a larger area in the quiver plot than the larger particles, illustrating their increased flowability.

4.1.3.3 Particle energies and momentum

The kinetic and potential energies of the uniform-sized and size-varied particles are shown in Figure 20a. The momentum experienced by the relevant particles is depicted in Figure 20b.

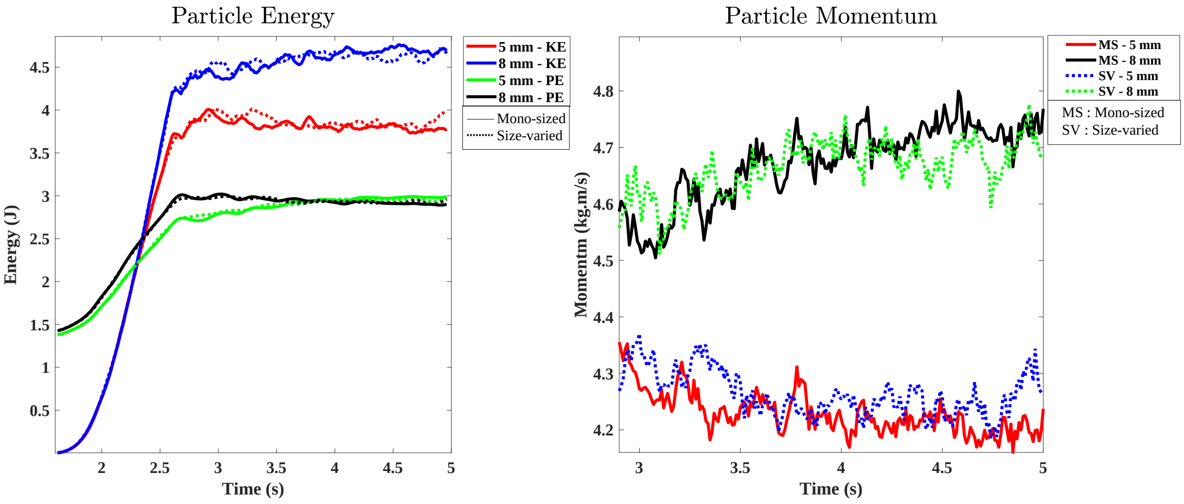

(a) (b)

Figure 20: Total particle energy and momentum in the system at 500 rpm impeller rotation speed

It can be seen from Figure 20 that the 8 mm particles have higher kinetic energy and as well as momentum than the 5 mm particles. This was likely due to the 8 mm particles being more closely located around the impeller than that of the 5 mm particles. The spatial occupation of the particles is indicated in Figure 18.

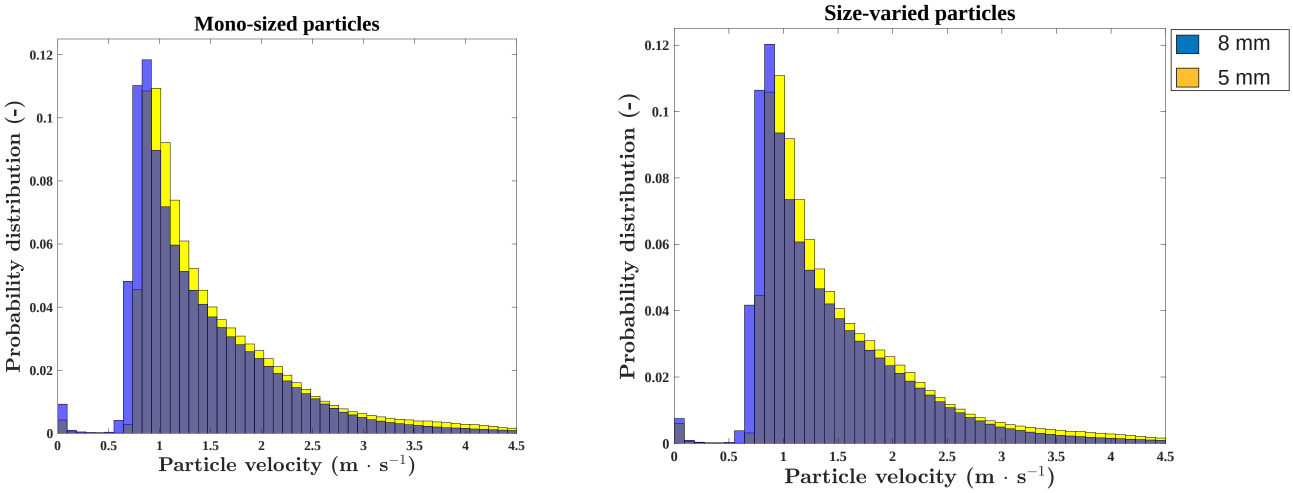

(a) (b)

Figure 21: Particle velocity distributions

In Figure 20a the potential energy of the 8-mm and 5-mm particles intersect. The 8-mm particle have a slight upwards slope with the 5-mm particles having a slight downwards slope. This is another indication of the *Brazilian nut effect* taking place. In this instance the 5-mm particles started filling available spaces that the impeller pins created, which further pushed the collective top particles upwards. Thus, the collective potential energy of the 5-mm particles is reduced while the collective 8-mm particles potential energy is increased.

Table 7: Estimated particle velocities captured between t = 2.90 s and t = 5.0 s

Velocities ($\mathrm{m \cdot s^{-1}}$)	5 mm		8 mm	
	MS	SV	MS	SV
Mean	1.4098	1.4171	1.5572	1.5545
Median	1.1714	1.1786	1.2882	1.2889
Mode	1.0350	1.0088	1.0608	1.0113

The estimated velocities indicated in Table 7, show that there was no significant or appreciable difference between the uniform-sized and size-varied particles. The estimated velocities in Table 7, as well as the velocity distribution in Figure 21, indicate that the 8 mm particles have the overall highest velocity speeds. The higher speeds, coupled with fewer particles with higher mass than that of the individual 5 mm particles, leads to a substantial increase in momentum and particle kinetic energies. One can then deduce that it is possible for the 8 mm particles to shape the particle motion in the dry system containing only the two sized particles.

It is necessary to approximate the relevance, or significance, of a particle or a class of particles to a system. The significance of a class of particles can be evaluated according to different criteria. The relevant class of particles can be approximated as the particles which dictate the flow and flow regime of the system, which particles contribute the most to collisions and energy dissipation of the system, which particles experienced the most interactions and was the most present at any given time, *etc.* Depending on the system and criteria, different conclusions can be made.

To further evaluate the relevance of the particles, a summary of their interactions at steady state is shown in Table 8. Inspecting Table 8 it can be seen that the 5 mm particles experienced the bulk of the collisions. Due to the 5 mm being present in most of the collisions it in turn dissipated more energy, and experienced more normal and tangential forces, than that of the 8 mm particles.

Table 8: Summation of particle experiences over 2.9 s and 5.0 s

	Mono-sized		Size-varied	
	5 mm	8 mm	5 mm	8 mm
Avg Normal Force	3.35 MN	1.47 MN	3.31 MN	1.50 MN
Avg Tangential Force	0.23 MN	0.15 MN	0.25 MN	0.15 MN
Total Energy Loss	2.21 kJ	1.94 kJ	2.22 kJ	1.93 kJ
Total no. of collisions	141.38×10^6	62.15×10^6	138.86×10^6	61.96×10^6
Collisions involving 5 mm	55.63 %	80.92 %	54.83 %	81.18 %
Collisions involving 8 mm	35.57 %	17.75 %	36.22 %	17.39 %
Impeller collisions	0.10 %	0.14 %	0.10 %	0.14 %
Environmental collisions (impeller + grinding chamber)	8.70 %	1.33 %	8.94 %	1.43 %
Total (5 mm + 8 mm + environmental collisions)	99.99 %	100.00 %	99.99 %	100.00 %

To further evaluate the collisions, the collision and energy loss profiles are illustrated in Figures 22 and 23. The collision frequency profiles are proportional to the particle occupation profiles shown in Figure 18. As seen in Figures 22 and 23, it appears that the majority of the collisions were facilitated at the top edges of the container. The colour streaks for the uniform-sized particles indicates that more collisions occurred in the mono-sized system as the concentrations of high frequency are darker than that of the size-varied simulation. This is due to there being more particles in the uniform-size simulation than in the size-varied simulation.

Inspecting the energy loss profile in Figures 22 and 23, it can be seen that the size-varied simulations facilitated more intense energy loss. Do note that the energy loss profiles, and force profiles, are proportional to one another. This is due to both the damping coefficients, C_n and C_t, and forces, F_n and F_t, being proportional to the spring stiffness coefficients, k_n and k_t. Thus, with the particles interacting in a turbulent manner, it appears that the size-varied simulations facilitated more intense collisions, and in turn more energy loss. The majority of the energy loss seems to be concentrated at the peripheries of the grinding chamber near the impeller pins.

There was a lack of energy loss or concentration above the impellers. The absence of energy loss at or near the top particle layer, illustrates that the region results in lacklustre collision events. Should particle segregation occur to a less severe degree, it is likely that the segregated particle layer would be reduced, resulting in the particles partaking in more active collisions.

The collision effectiveness may be further improved by confining the particles closer together. This can be achieved through the introduction of a liquid into the system.

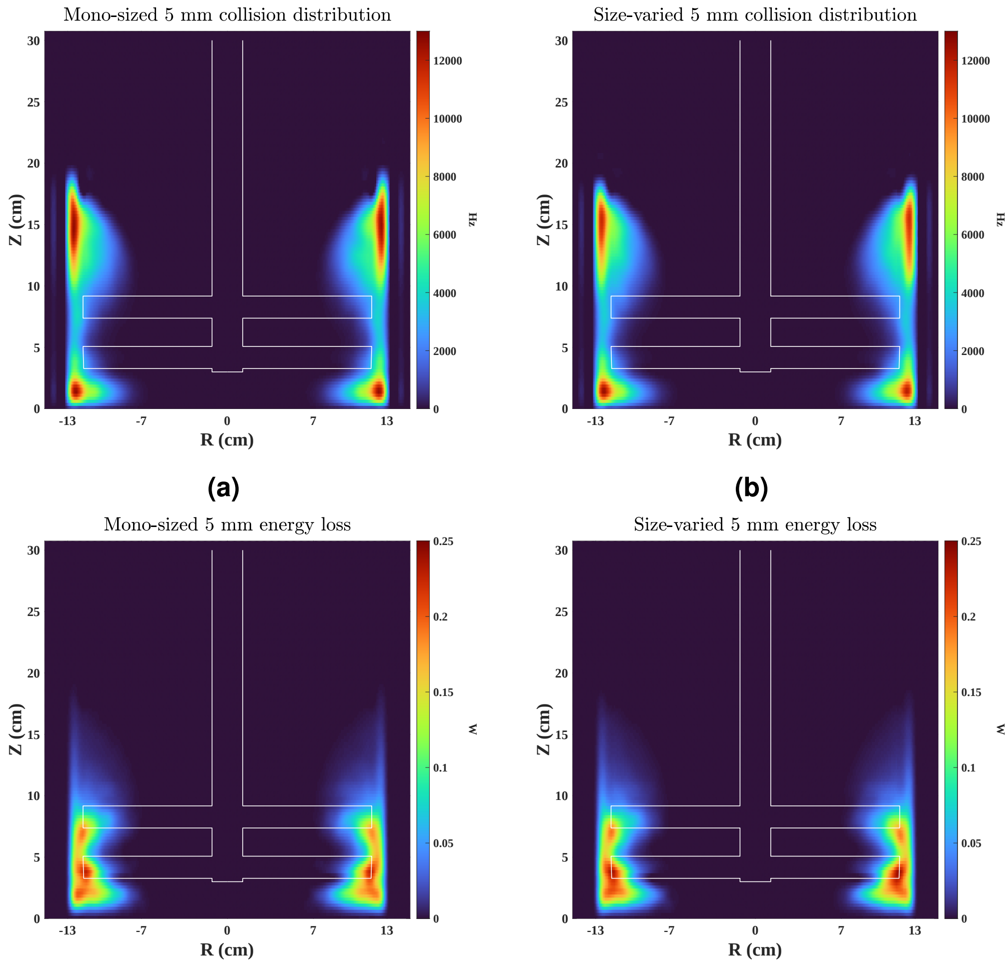

(a)

(b)

(c)

(d)

Figure 22: Time averaged 5 mm particle collisions (Hz) and energy loss data (W) between t = 4.75 s and t = 5.00 s

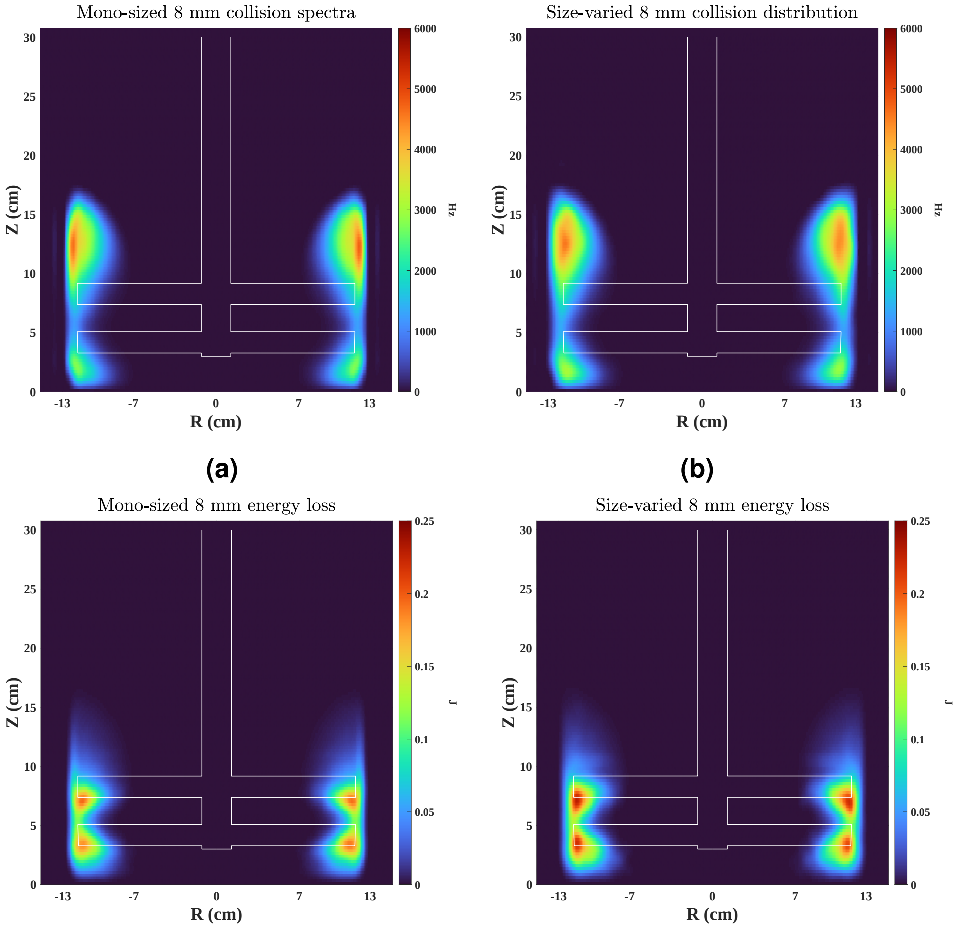

(a) (b)

(c) (d)

Figure 23: Time averaged 8 mm particle collisions (Hz) and energy loss data (W) between t = 4.75 s and t = 5.00 s

An attempt was made to define the particle interactions with that of the impeller. The degree to which the particles interact with the impeller is proportionate to the force, or resistance to movement, the particles impart on the impeller. This force is proportionate to the energy loss experienced by the relevant particulate medium imparted by the impeller. Thus, the particle interaction can be simplified to a ratio of the particle energy losses imparted by the impeller. This is shown in Equation 27.

$$\Upsilon = \frac{\sum |Total\ impeller\ energy\ loss\ 8\ mm|}{\sum |Total\ impeller\ energy\ loss\ 5\ mm|} \tag{27}$$

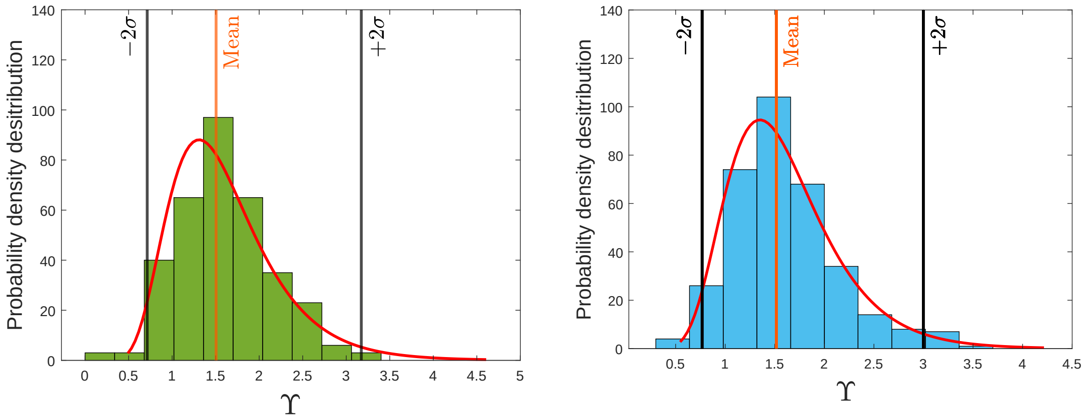

(a) Mono-sized distribution

(b) Size-varied distribution

Figure 24: Particle energy loss ratios relative to the impeller

Table 9: Estimated lognormal and normal distribution values for ratio of the 8 mm and 5 mm total energy loss relative to the impeller for the uniform and size-varied particulate systems

	Lognormal mean (u) mean (u)	Mean (e^u)	Lognormal variance (σ)	Normal mean (u)	Normal variance (σ)
Mono-sized	0.4087	1.5048	0.3730	1.6018	0.5374
Size-varied	0.4165	1.5167	0.3407	1.6053	0.5243

A histogram of the resulting ratios between t = 1.60 s and t = 5.00 s is shown. A lognormal and normal distribution was fitted for each system. The resulting values are shown in Table 9.

It can be seen from Figure 24 that a majority of the ratio values are larger than one. In Table 9 the mean for both systems was estimated to be around ≈1.50. This means that the larger particle experiences the majority of the intense collisions on the impeller, providing the most resistance to movement and in turn the more intense interactions.

Thus, given that the larger particles interact meaningfully with the impeller and have the highest momentum in the system, it is then plausible to say that the larger particles were, in turn, influencing the flow of the particles in this system.

4.1.4 Collisions

4.1.4.1 Force profile

The normal and tangential forces for the mono-sized and size-varied particle populations are shown in Figures 25 and 26. Inspecting the figures, it is observed that throughout all instances that the tangential energy loss was not as significant as the normal energy loss. This can be seen in the scales of Figure 25, as the normal forces are an order of magnitude larger than that of the tangential forces. Stirred mills are designed to improve and emphasise tangential based interactions in order to promote abrasion based breakages (Jankovic 2008; Francis 2014).

Other articles reviewed report the tangential energy loss to be equivalent as the (Sinnott et al. 2006; Morrison et al. 2009; Ndimande et al. 2019). This case, where the normal based energy is the dominant energy loss, was not fully representative of the system studied for this thesis.

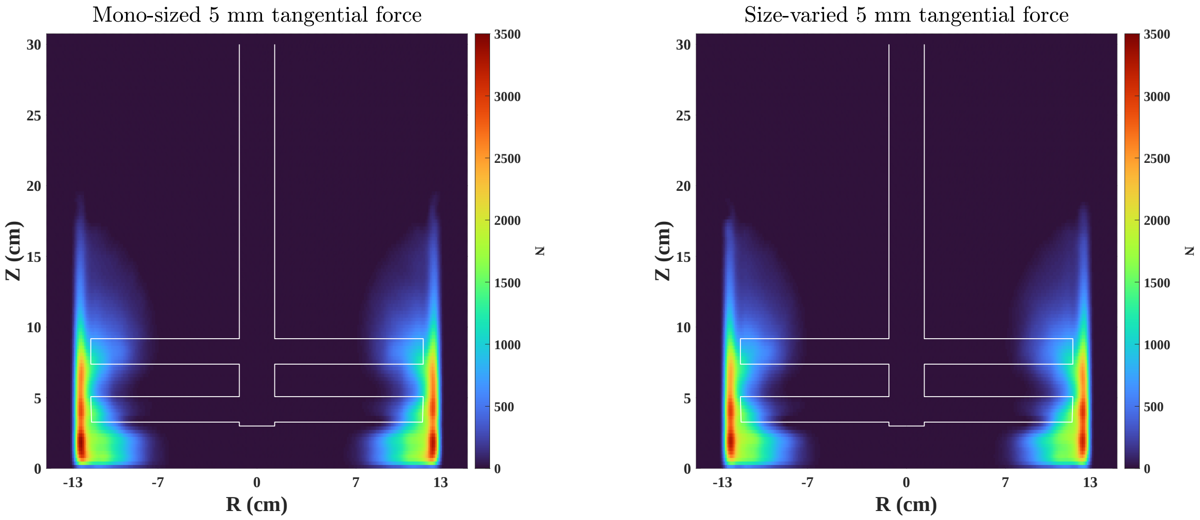

(a)

(b)

Figure 25: Time averaged 5 mm collision force data between t = 4.75 s and t = 5.00 s

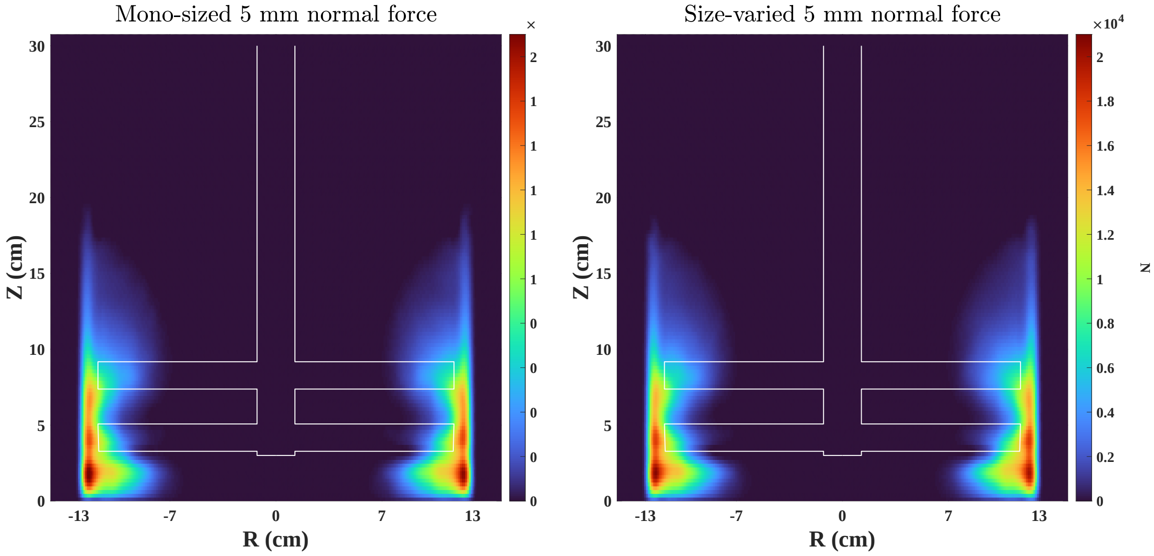

(c)

(d)

Figure 25: Time averaged 5 mm collision force data between t = 4.75 s and t = 5.00 s

In the experiment with the 5 mm particles, more intense forces were experienced at the edges of the container. The tangential forces were concentrated at the edges, whilst the normal forces were only slightly more evenly distributed. Additionally, the top particle layer that formed as shown in Figure 18a and 18b is not apparent here, further corroborating the statements that the formation of the top layer resulted in redundant collisions.

The experiment with the 8 mm particles gave forces that are more evenly distributed, with the tangential force being the weaker of the two forces. Furthermore, normal force was more evenly distributed throughout the system than that of the tangential force, indicating that fraction propagation and cleavage would be the dominant breaking force here.

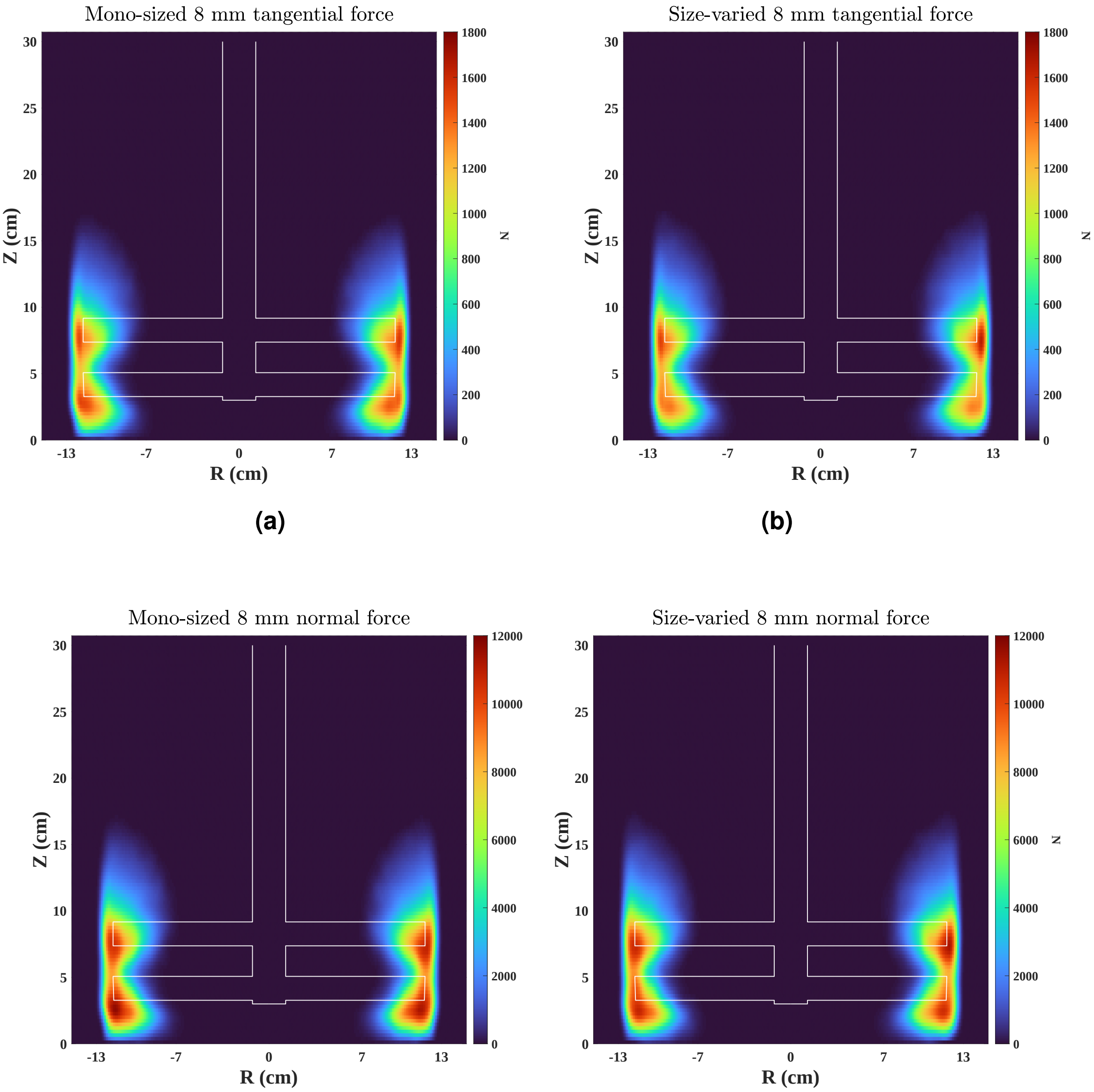

(a) (b)

(c) (d)

Figure 26: Time averaged 8 mm collision force data between t = 4.75 s and t = 5.00 s

4.1.4.2 Collision spectra

The collision spectra of the size-varied and uniform-sized simulations is illustrated in Figure 27.

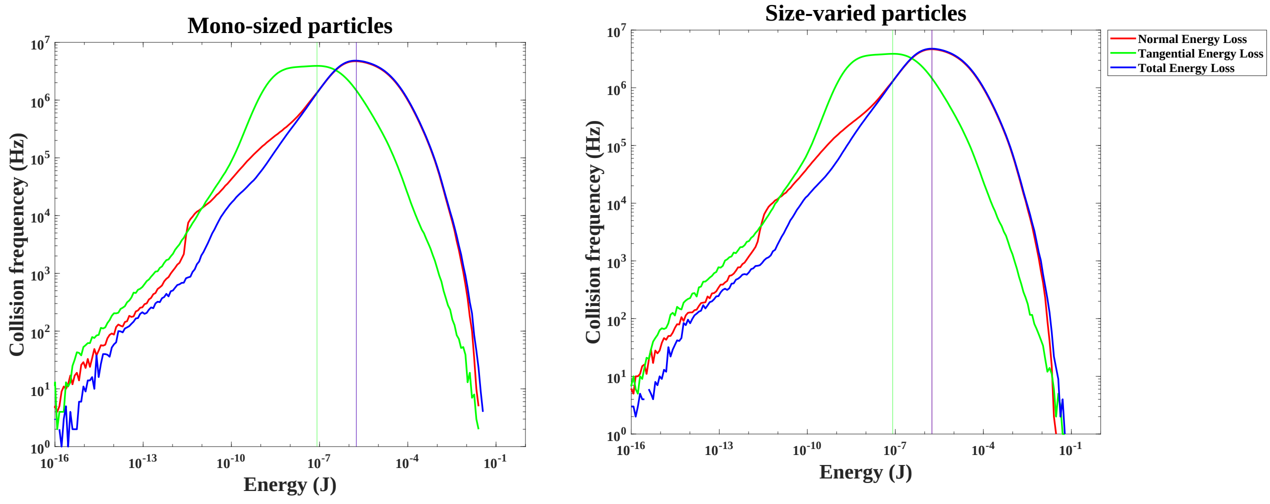

(a) **(b)**

Figure 27: Collision spectra of the mono-sized and size-varied simulations captured between t = 2.9 s and t = 5.0 s at 500 rpm

As seen in Figure 27, there are no significant differences between the two systems. A summary of the collision energy loss and collisions experienced by the particles can be found in Table 10. All evaluated energy losses are within a percent of one another with the uniform-sized particles often having the increased energy loss or collisions.

The normal energy loss was an order of magnitude larger than the tangential energy loss. This collision spectra does not follow the trends of other similar vertical stirred mill systems. Tangential energy loss is normally more prominent than normal based energy loss for both wet and dry systems for a stirred mill. Similiar vertical stirred mill grinding simulations can be found in Ndimande et al. (2019), and Oliveira et al. (2020). In these systems the tangential energy loss was more prominent than the normal energy loss. It is likely that the simulation model used does not properly account, or simulate, the tangential based interactions of the particles. This results in a reduced tangential force and energy loss.

As seen in Figure 27, even the collision intensities of the size-varied and uniform-sized particulate systems do not differ drastically. It was expected that the size varied systems would result in more intense collisions, it would allow for more turbulent flow of particles, which would result in a varied and increased range of normal and tangential based collisions.

Table 10: Size-varied simulation energy loss and collision summary between t = 2.9 s and t = 5.0 s at 500 rpm

	Mono-sized particles	Size-varied particles
Total energy lost	2962.86 J	2956.61 J
Normal energy lost	2828.89 J	2821.61 J
Tangential energy lost	133.96 J	135.00 J
Number of particles	22812	22604
5 mm particles	18335	18166
8 mm particles	4477	4438
Energy lost to particles	71.43 %	71.67 %
Energy lost to impeller	6.86 %	6.90 %
Energy lost to chamber	0.86 %	0.89 %

The collision modulus of the tangential energy loss was 81.67 nJ, whilst the normal and total energy loss share the same energy loss modulus of 1.771 μJ. These collision modulus values do not change according to the mono-sized and size-varied particles.

This could be due to there being insufficient variation of particles in the system to properly shift the most common collision intensity.

To further investigate the differences of the collision spectra of the mono-sized and size-varied systems the difference of collisions frequencies,ΔN_c, of specific collision energy losses were plotted. Equation 28 was used to estimate ΔN_c. In this equation $N_{c,MS}$ represents the mono-sized collision frequencies and $N_{c,SV}$ represents the size-varied collision frequencies.

$$\Delta N_c = N_{c,MS} - N_{c,SV}. \tag{28}$$

The resulting collision spectra is shown in Figure 28. This collision spectra indicates that there were significantly increased collisions for the uniform-sized particles, particularly around the collision modulus.

There is a discontinuity in the energy loss lines of Figure 28. The discontinuities are due to the size-varied collision intensities being more numerous than the mono-sized particles at the lower and higher collision intensities. The resulting collision frequencies are depicted in Figure **??** in Appendix A.2.

There are more particles in the mono-sized particle system than that of the size-varied particle system. Due to the increased particles, the amount of collision events increased.

The relation between the collision events and particles is shown in Equation 21.

Thus, the increased number of particles lead to increased collisions, which could lead to skewed or different collision intensities when evaluated over longer or different simulation times.

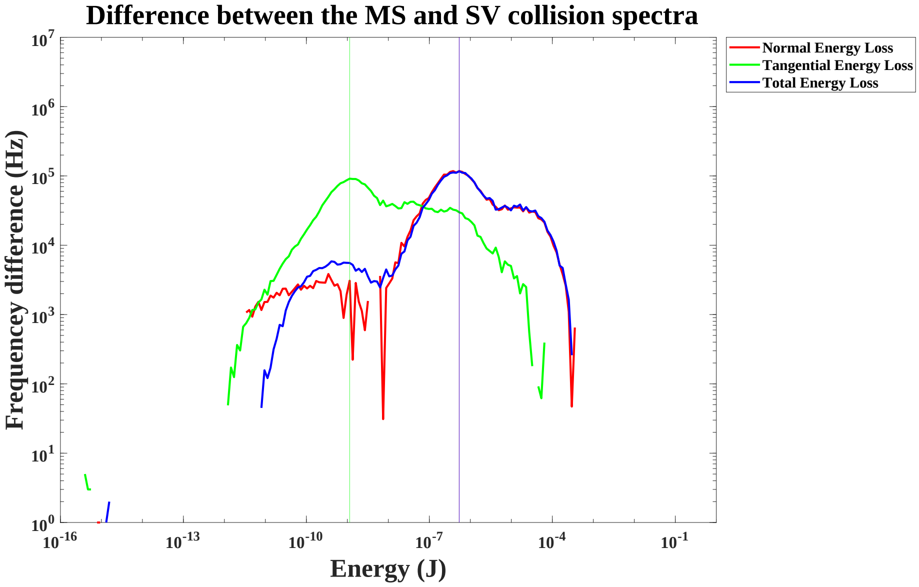

Figure 28: Collision spectra of the mono-sized and size-varied simulations captured between t = 2.9 s and t = 5.0 s at 500 rpm

4.1.5 Simulation artifacting

From the evaluated data and graphs of the previous sections, it can be concluded that the simulations experienced artifacting, among other inconsistencies.

The difference between the 5 mm particle occupations is illustrated in Figure 29. An increase in particle occupation is shown in the red regions of the occupation plot, while lower particle occupations are shown in the darker blue regions of the plot.

It is important to note that even though there are more particles in the mono-sized setup, the overall difference in particle occupation does not increase evenly. This is due to the particles collecting near the top edges of the mixture. This can be seen in the red region in Figure 29.

The layer of 5 mm particles forming on top of the mixture is an indication of simulation artifacting. In reality the agitation of the particles results in more sporadic movement. Simulation artifacts occur when the physics, simulation parameters or system interactions are not calibrated correctly (Barrett and Keat 2004). When this occurs the simulated system tends to reach a stable state that is note properly conducive of reality. These simulation artifacts can be mitigated by proper calibration of parameters and system interactions.

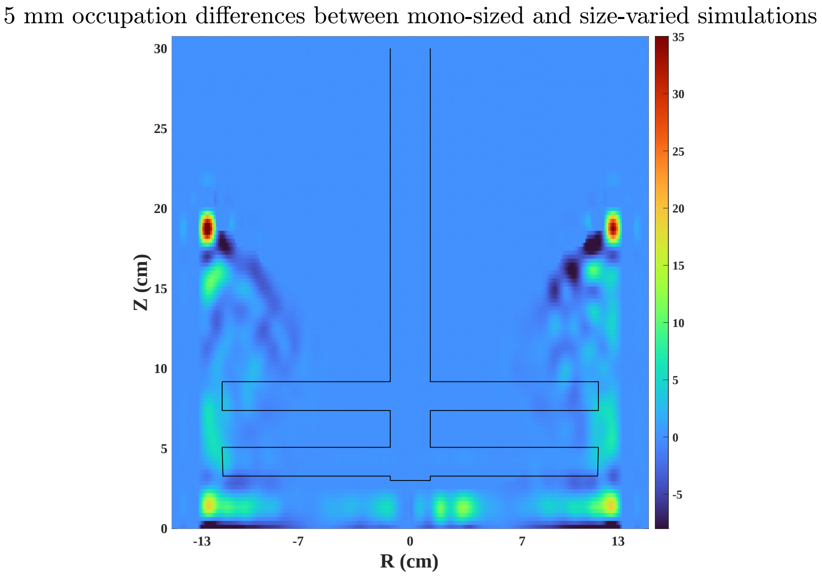

5 mm occupation differences between mono-sized and size-varied simulations

Figure 29: Difference between the size-varied and mono-sized particle occupation at steady state

For the collision spectra, the normal energy loss is the most prominent energy loss as opposed to the tangential energy loss. The tangential energy loss should be the dominant, or more prominent, energy loss, as stirred mills are designed to promote tangential based interactions (Jankovic 2008; Francis 2014). This is likely due to the DEM simulation software used in this instance, EDEM 2.5, not accounting for a prominent interaction relevant to tangential energy loss.

Both simulations appear to give similar results overall; however, minor differences exist. In the force profiles subsection the size-varied simulation showed increased force, which can be attributed to the slight increase in velocity for the size-varied systems shown in Section 4.1.3.3. Thus, the size-varied simulation leads to more pronounced collisions.

Though the simulations are an approximation of the real world, they cannot fully approximate every necessary and resulting detail. Thus, it is necessary to know that the phenomena observed in the simulations may be approximated as trends within the real world.

Moving forward, particle populations with size-deviations should be implemented to avoid accentuated results. Furthermore, the simulation software will be updated from EDEM 2.5 to EDEM 2022.3 to ensure that the collision interactions and models are up to date with modern standards.

4.1.6 Subsection summary

In Section 4.1 the tendency of simulation artifacting for a size-segregated system is investigated. This section serves as an introduction to how data will be illustrated in the following sections. A concern raised in this section was the degree to which particles tended to occupy the space above the bulk media, an indication of simulation artifacting, possibly emphasising particle segregation. Additionally, the spectra total, tangential and normal energy losses did not align with established trends. The normal energy loss was significantly larger than that of the tangential energy loss. The collision energy loss modal peaks did not drastically change according the mono-size and size-varied.

4.2 The influence of impeller speed on a size-segregated system

4.2.1 Initial setup

In this section the influence of impeller speed on particle collisions and movement are investigated.

Four impeller speeds were evaluated: 200 rpm, 350 rpm, 500 rpm and 700 rpm. These speeds were evaluated to investigate particle collisions and interactions when the grinding media was unfluidised, semi-fluidised and fully fluidised within the system.

Two particle populations were generated within the same environment over a time period of 2.00 seconds with randomised spawn locations. The random particle spawn locations allowed for an approximation of a well-mixed system. An illustration of a well-mixed particulate mixture is shown in Figure 16a in Section 4.1.1. Additionally, these particles were varied in size.

A sample of 160 particles was used to estimate the deviation of each particle population. A sample standard deviation of the population was estimated using Equation 29. x_i represents a sample of the collected data while $\bar{x}$ represents the overall mean of the data points. n represents the amount of data points.

$$\sigma = \sqrt{\frac{\sum_i^n (x_i - \bar{x})^2}{n-1}}. \tag{29}$$

The sample standard deviation can overestimate the population deviation, though with a sufficiently large sample the likelihood of this is diminished. A sample standard deviation of 35.14 μm was calculated for the 8 mm particles and 69.19 μm was calculated for the 5 mm particles. It was noted that in this instance there is a greater size variation for the smaller particles than for the larger particles. The probability density distribution of the 5 mm and 8 mm particles are shown in Figure 30.

A total of 3.25 kg of both particles were spawned into the simulations. This was done to ensure that the top impeller pins were covered when loading the grinding beads. This resulted in a system with 4 848 larger particles and 19 821 smaller particles.

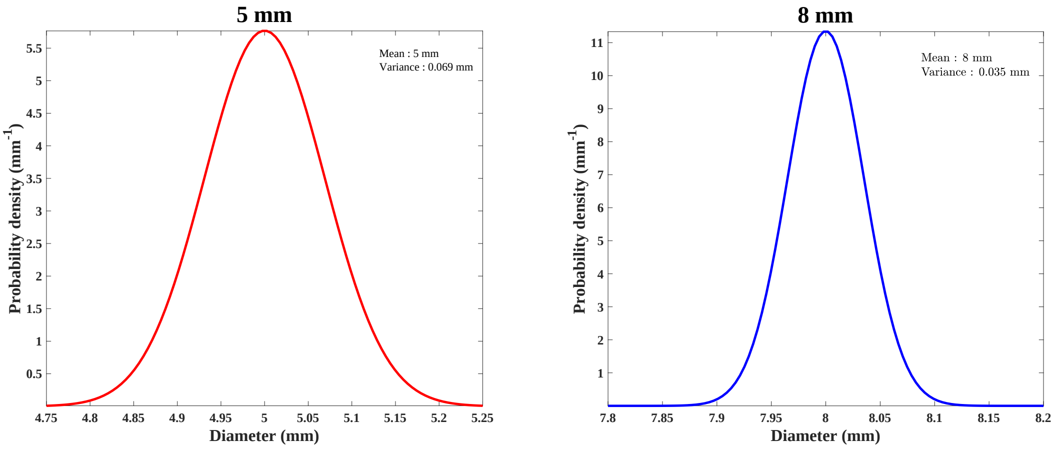

(a) **(b)**

Figure 30: Probability density distribution of the particle populations with their estimated variances

In the simulations, 2.00 seconds was dedicated to particle spawning and settling. Thereafter 1.00 second was dedicated to impeller acceleration. The acceleration over 1.00 second allows for a smooth establishment of steady state and particle dispersion. Different variable speeds were used in the simulations presented in this section. Different simulation durations were used to ensure that stability was reached and enough revolutions were attained for the data to sufficiently represent steady state conditions in the system.

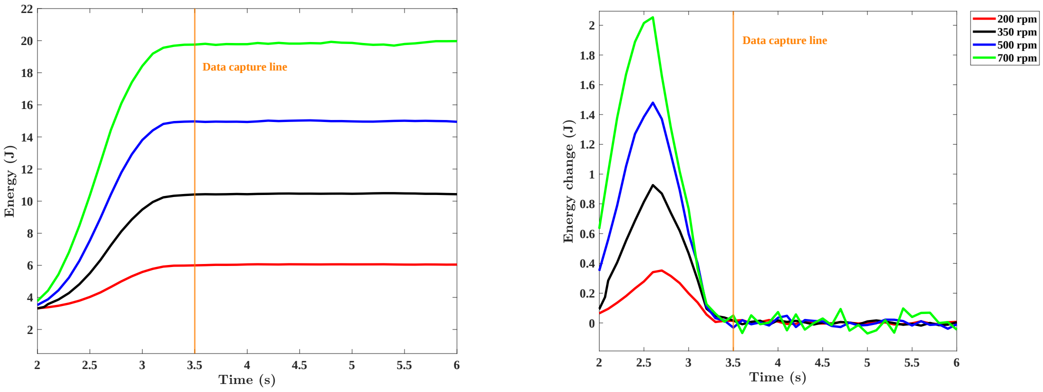

(a) Particle mechanical energy **(b)** Change in particle mechanical energy

Figure 31: Resulting particle mechanical energy

A total simulation time of 8.50 seconds was allowed for the 200 rpm simulation, with the remainder of the impeller speeds being defaulted to a 6.50 second duration. This was done to ensure that a minimum of 20 revolutions was obtained for each run.

Figure 31b shows that the change in total mechanical energy decreased to a stable value after 3.50 seconds. This indicates that steady state has been established. The total mechanical energy was estimated using Equation 24. The data illustrated in the following sequences has been captured or time averaged between t = 3.50 s and t = 6.50 s unless otherwise indicated.

4.2.2 Collision frequency

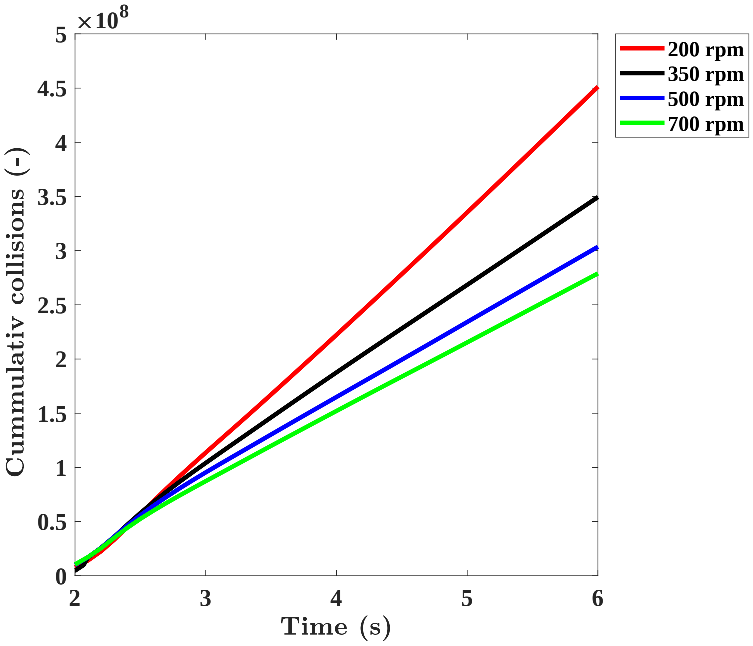

Figure 32: Cumulative collisions of the particles

In Figure 32 the cumulative collisions of particles at different impeller speeds are shown. It can be seen that the the total cumulative collisions of lower impeller speeds such as 200 rpm and 350 rpm, were higher than the higher impeller speeds, such as 500 rpm and 700 rpm. This can be seen with the summated final collision value at t = 6.00 s where the total collisions of 200 rpm is the most and the summated collisions for 700 rpm is the least.

It should be noted that the collision frequency does not follow the trend illustrated in Equation 21. This is likely due to the simulations experiencing artifacting. Artifacting is discussed in Section 4.1.5. The mechanisms by which this is facilitated is that a bulk of the particles collected just above the impeller pins, avoiding the pins that facilitated collisions. With an increased impeller speed more particles tended to collect above the impeller pins, further reducing the amount of collisions.

It should be stated that all simulations have the same starting point. Both the particle distribution, as well as the particle positions, remain consistent throughout each run.

4.2.3 Particles

4.2.3.1 Particle spatial distributions and segregation

In Figure 33 the time averaged particle occupation plot of the 5 mm and 8 mm particles are shown. The data is time averaged over t = 3.50 s and 6.50 s.

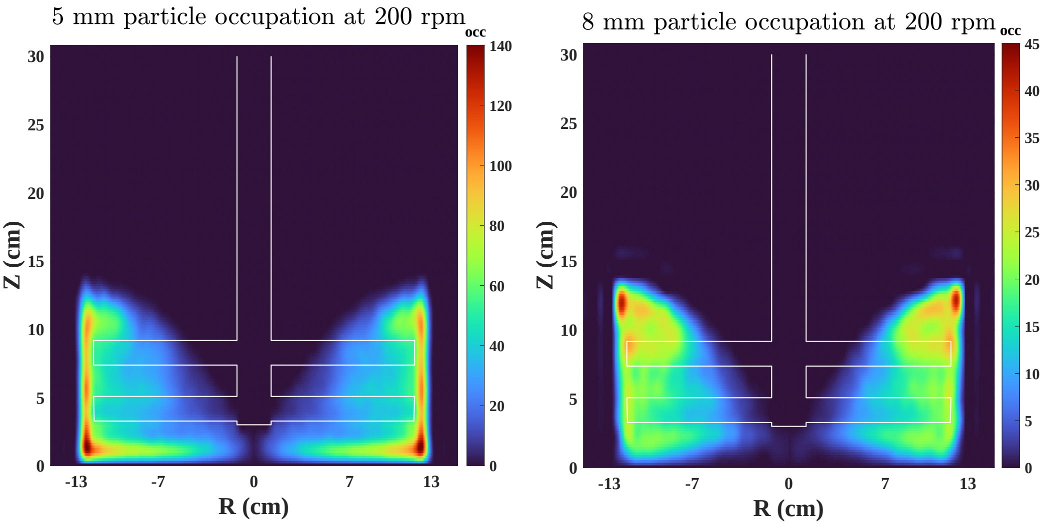

(a)

(b)

Figure 33: Particle occupation at different impeller speeds

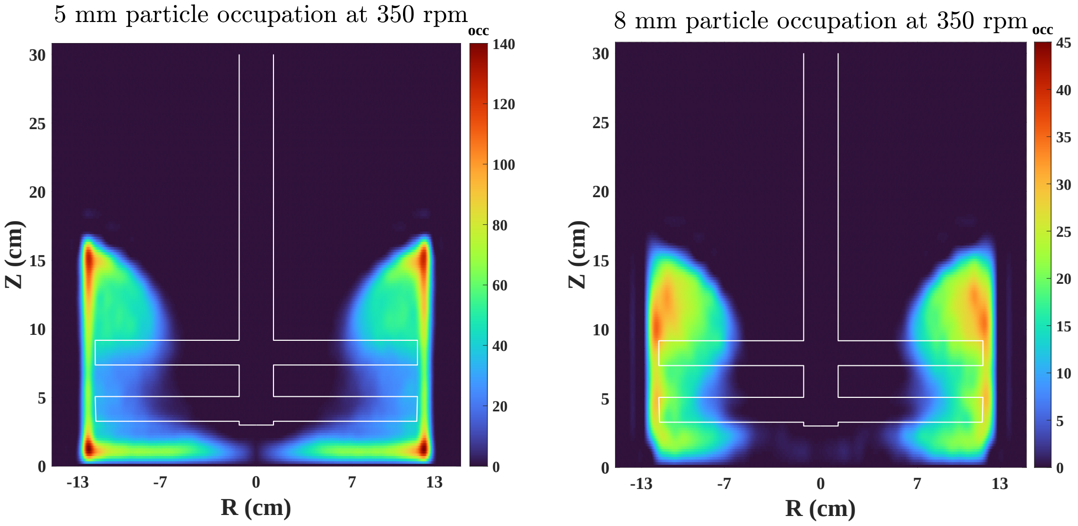

(c) **(d)**

Figure 33: Particle occupation at different impeller speeds

The simulation artifacting mentioned in Section 2.4.2.3 is present again in Figure 33, as a significant portion of the occupied the space above the bulk media at the top edges. As the impeller speed is increased, so too does the degree to which particles collect to the top edges. This results in increased particle segregation, as the particles tend to clump together.

Figure 33 shows the 5 mm and 8 mm particle occupation profiles at different impeller speeds. At 200 rpm the 5 mm particles, in Figure 33a, were predominantly located below the bottom impeller arm whilst the 8 mm particles, in Figure 33b, were located above the top impeller arm. With impeller speeds of 500 rpm and 700 rpm, seen in Figures 33c through to 33h , a collection of smaller particles tended to form a layer on top of the larger particles. At higher impeller speeds it appears that the majority of the 8 mm particles tended to collect above the impeller pins.

It is likely that the particles were experiencing the *Brazilian nut effect*, described in Section 2.7.3. This effect happens when the larger particles tend to rise to the top of a particulate media through mechanical agitation at low speeds. At higher speeds of mechanical agitation the smaller particles tend to rise to the top of the particulate media. The *Brazilian nut effect* can in turn increase particle segregation.

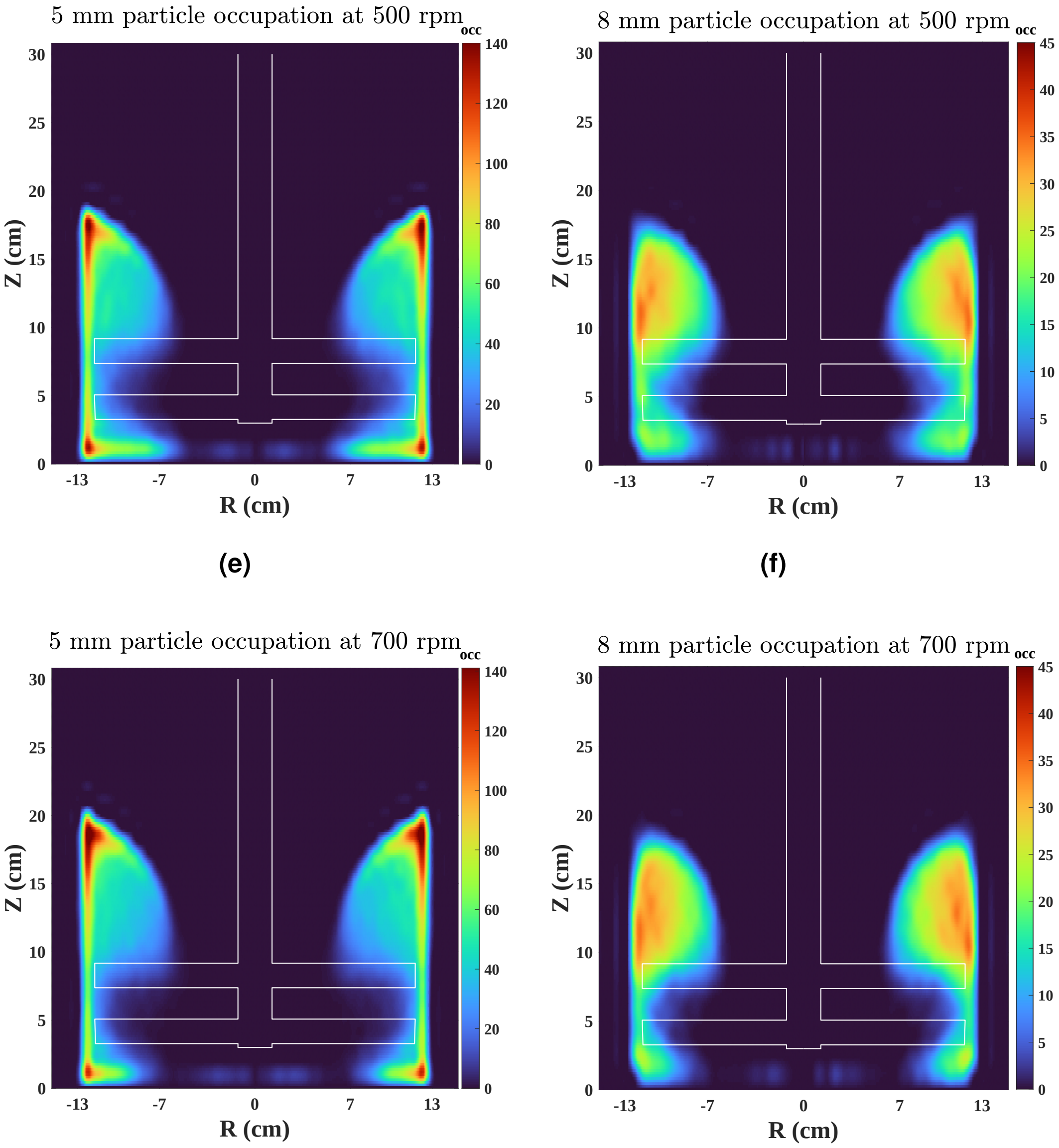

(e)

(f)

(g)

(h)

Figure 33: Particle occupation at different impeller speeds (continued)

Inspecting the final particle height distribution it can be seen that particle segregation increases with impeller speed. This is characterised by the increasing the 5 mm particle layer forming above the 8 mm particles at the end.

It is possible to inspect both the radial or axial motions of the particles.

Of these mechanisms radial dispersion is rapid while axial dispersion is time consuming (Sudah 2001; Arratia et al. 2006). For the purposes of this thesis, these mechanisms was evaluated using the change in particle concentrations inside a grid (Arratia et al. 2006). This grid is similar to the boxing method shown in Section 2.4.2.3.

It is possible to compute the degree of particle segregation using the sample standard deviation. The concentration deviation of particles was quantified using the box counting method and sample standard deviation shown in Equation 29 (Arratia et al. 2006). The particle concentrations, and deviation, in each grid cell is calculated.

å Both particles were taken into account when estimating the deviation, σ, as this leads to a more pronounced degree of segregation. A Cartesian grid was selected to be 14×14×12 with the grid cubes having a length of 19.84 mm.

Arratia et al. (2006) illustrates that particle segregating can be described by using the first-order formula in Equation 30. A indicates the severity of particles segregation, increasing as particle separation increases. Whilst β indicates the rate of segregation experienced by the system, increasing as the speed of particle segregation increases. n_{rev} is the amount of revolutions experienced. The symbol e is the natural exponent, also known as Euler's number or Napier's constant whose value is 2.71828.

$$\sigma = A(1 - e^{-n_{rev}\beta}) \tag{30}$$

Values for A and β were fitted according to the different impeller speeds. The resulting values can be found in Table 11. The data used to fit and obtain the values is shown in Figure 34. In Appendix A.1 the degree of segregation for the 5 mm and 8 mm particles can found in Figures A1a and A1c, while the degree of mixing for the particles can be found in Figures A1b and A1d.

Table 11: Fitted segregation values

	Speed	Asymptotic segregation limit (A)	Rate of segregation (β)
All	200 rpm	746.91	1.624
	350 rpm	1982.55	0.888
	500 rpm	2745.83	0.768
	700 rpm	3282.63	0.674
5 mm	200 rpm	482.52	2.018
	350 rpm	1518.81	0.891
	500 rpm	2068.39	0.833
	700 rpm	2458.27	0.755
8 mm	200 rpm	269.08	0.874
	350 rpm	463.96	0.875
	500 rpm	679.36	0.591
	700 rpm	825.17	0.511

An increase in impeller speed results in an increase the overall degree of particle segregation and a decrease in the rate of particle separation. This can be seen in the increase of the asymptotic segregation limit (A) and the decrease of the rate of segregation (β) accounting for all the particles when estimating σ. This is likely due to the particles fluidising or centrifuging outwards with the increased impeller speeds. At lower speeds more particles experience greater interaction with the impeller pins, as the particles were not dispersed either upwards or downwards to the collective of particles, as seen in Figures 33e and 33g.

With the increase in impeller pin interaction at lower speeds, the particles were able to disperse and mix more efficiently. With increased speeds particles tend to fluidise or centrifuge towards the outer edges of the container with the end result being a significant portion of particles occupying the space. The increase in impeller speeds allows less particles to interact with the impeller pins, thus it tends to collect either upwards or downwards with the rest of the particulate mixture. This in turn leads to increased particle separation.

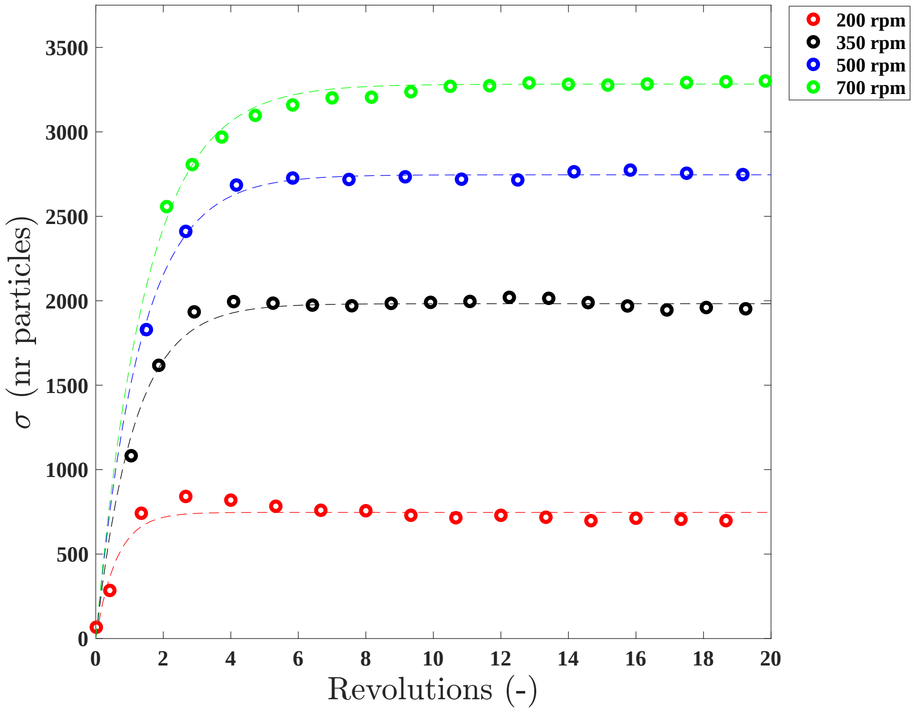

Figure 34: Segregation curves including both the small and large particles at different impeller agitation speeds

4.2.3.2 Particle motion

The quiver plots of the 5 mm and 8 mm at different impeller speeds are illustrated in Figure 35. The method by which the particle quiver plots are estimated is discussed in Section 4.1.3.2.

It should be noted that during acceleration, or activation of an agitator, that the particles' would likely imitate all the similar motions illustrated in Figure 35. Furthermore, the collective particle motion indicated here is the normalised vector fields of all the particles motions that have been collected at a specific point in space from t = 3.5 s and t = 6.5 s.

Inspecting the velocity profiles of the particles at 200 rpm, depicted in Figures 36a and 36b, it can be seen that their velocity deviations are less intense compared to the faster impeller speeds. This can be seen with the large and consistent coverage of the warm colours in the figures. This is due to the low impeller speed and is characterised by the distribution of the maximum velocity profile around the impeller pins. There were few differences between the velocity and motion profiles of the 5 mm and 8 mm particles at 200 rpm. Inspecting the particle motion of the 200 rpm impeller speed depicted in Figure 35, it can be seen that there is minor difference between the motion of the 5 mm and 8 mm particles. The particles were pushed upwards from the impeller pins to chamber edges. At the edges, the particles then proceed downwards. As smaller particles have increased flowability, it may be that the 5 mm particles could have saturated the available routes or motions for the 8 mm particles to travel downwards, resulting in the *Brazilian nut effect* where the larger particles tended to occupy the top of the bulk media. This is depicted in Figure 33b.

A vortex-like flow pattern starts to develop at 350 rpm and increases in height as impeller speed is increased. Here the particles were agitated and pushed upwards by the lower impeller pins, where it gets pushed to the edges of the container. At this point a particle can either flow upwards or downwards, where it then gets recycled back into the motion over an extended time frame. It is possible for the particle to collect at either the top or bottom of the particulate mixture, owing to the reduced velocity values there. The reduced velocity values can be seen above and below the impeller pins with the cold blue colours in Figures 37a through to 37f.

Figure 35: Particles motion at different impeller speeds

Impeller speed	5 mm particles	8 mm particles	Combined particle motion
200 rpm	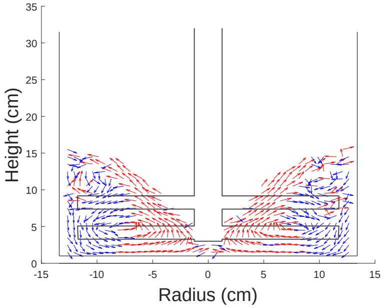	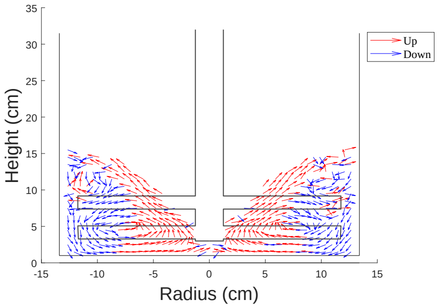	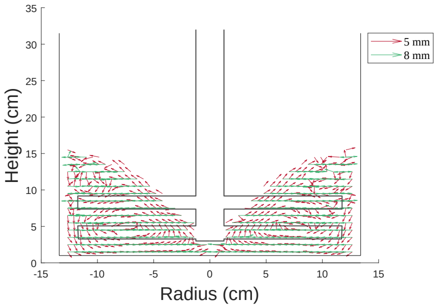
350 rpm	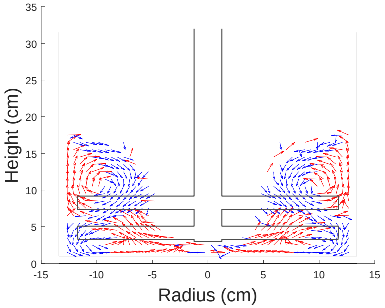	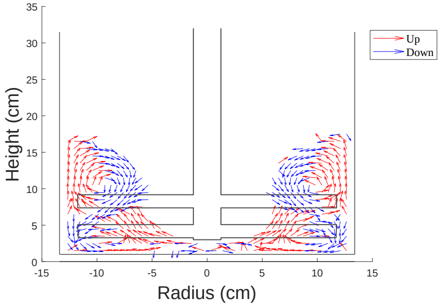	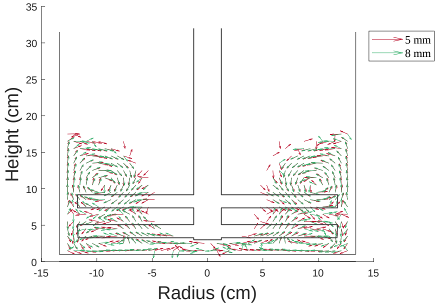

Figure 35: Particles motion at different impeller speeds (continued)

Impeller speed	5 mm particles	8 mm particles	Combined particle motion
500 rpm	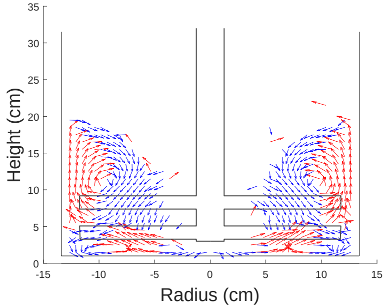	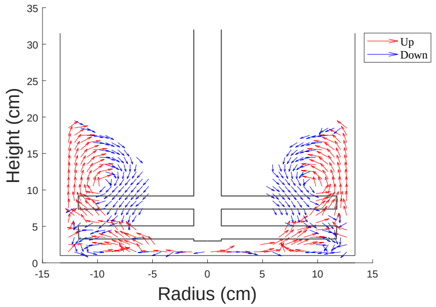	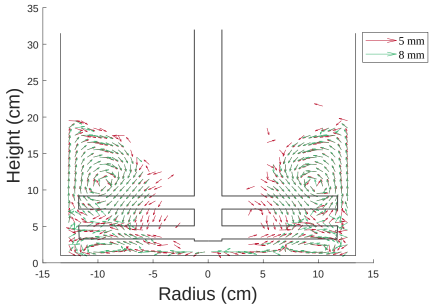
700 rpm	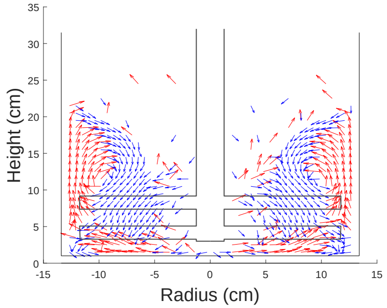	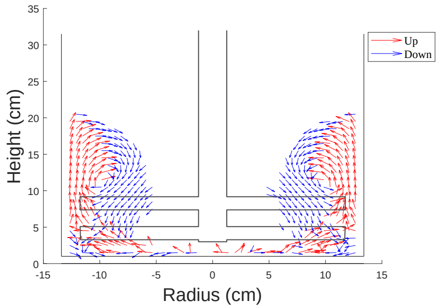	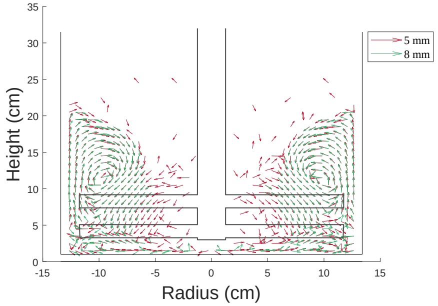

A more sporadic illustration of the particle flow pattern is established between 350 rpm and 700 rpm impeller speeds. It should be noted that the particle voidage at the centre of the impeller tends to increase with the impeller speed. This can be seen in the particle occupation and velocity profiles in Figures 33 and 36. The increase in the empty space is due to the particles that were fluidised, or centrifuged, outwards.

Furthermore, when inspecting the velocity profiles of the particles, it can be seen that the 8 mm particles tend to have a slightly increased velocity near the impeller pins. This is shown with the hot colours dominating the location near the impeller pins in the colour maps. This is likely due to a larger percentage of the 8 mm particles occupying the above region near the impeller pins. This is depicted in Figures 33f and 33h.

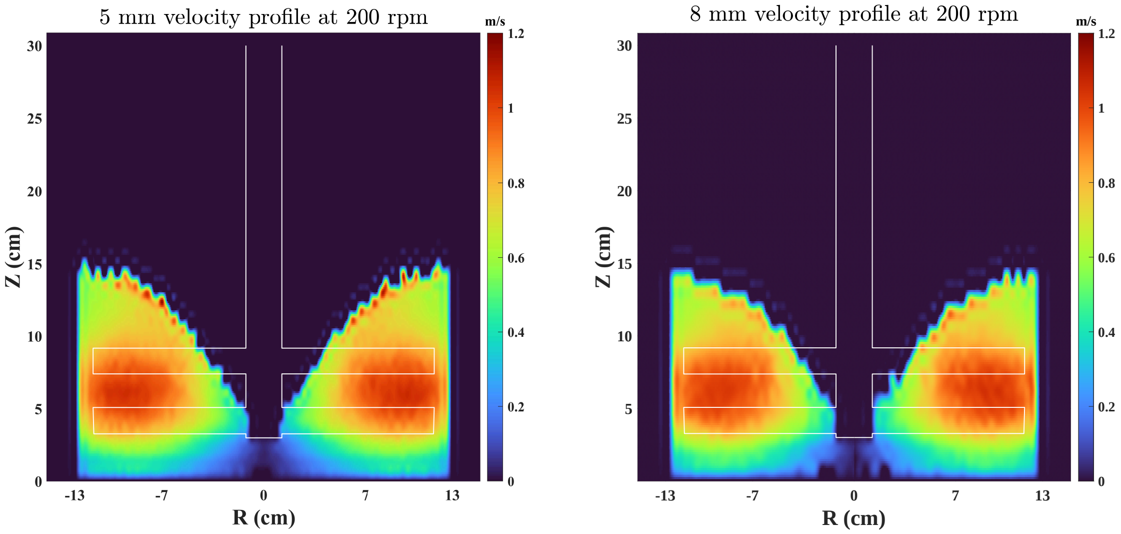

(a) (b)

Figure 36: Particle velocity profiles at different impeller speeds

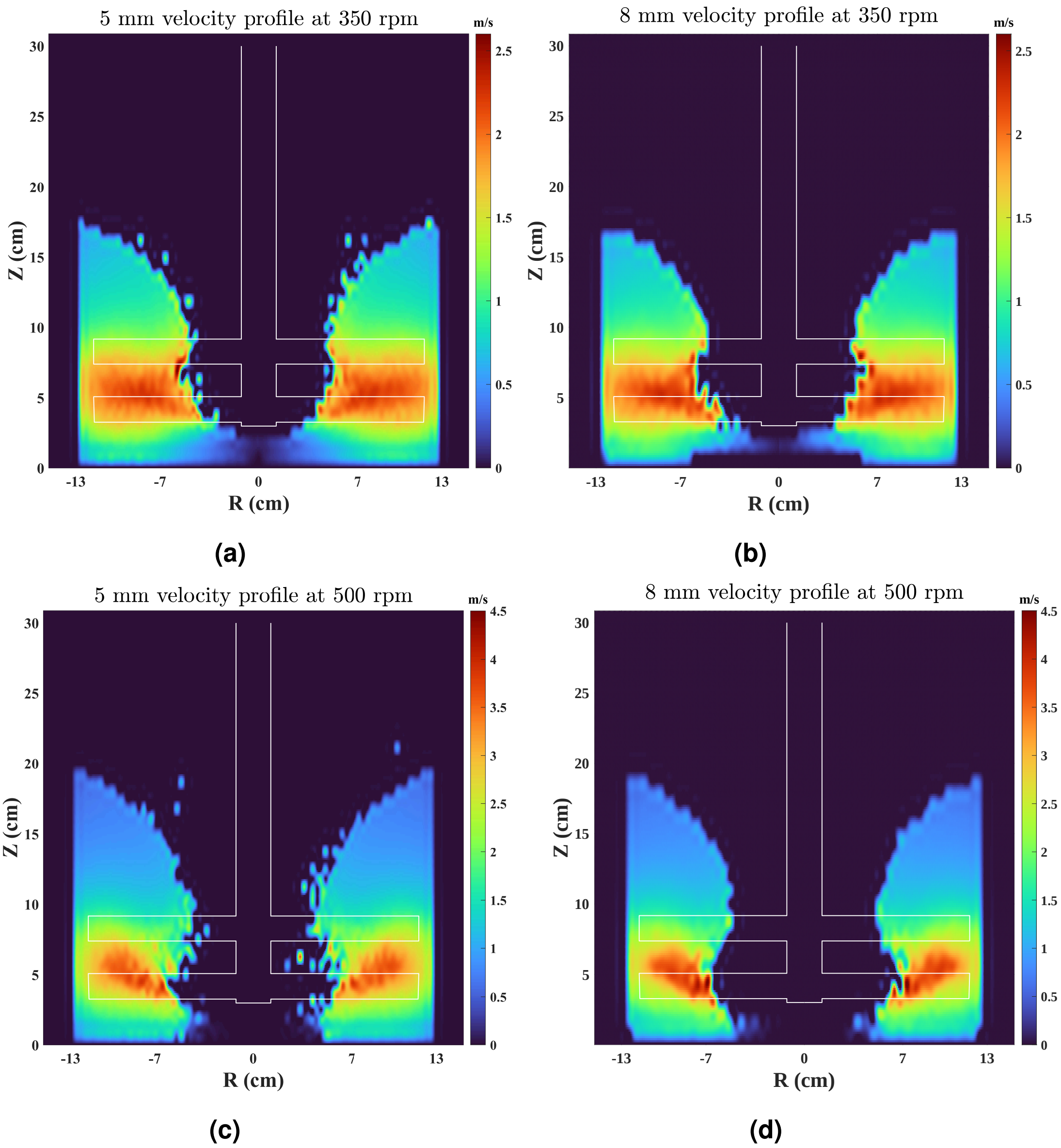

(a) (b)

(c) (d)

Figure 37: Particle velocity profiles at different impeller speeds

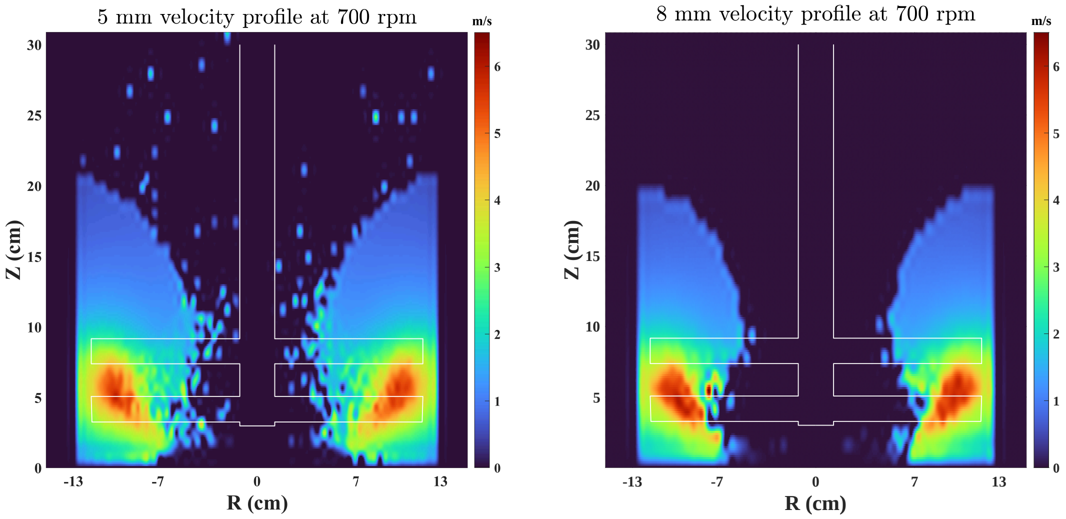

(e) (f)

Figure 37: Particle velocity profiles at different impeller speeds (continued)

4.2.3.3 Particle significance

In this section the particle dominances at different impeller speeds are evaluated, using the particle energy loss ratio, Υ, of Equation 27 in Section 4.1.3.3. The data used to evaluate the ratio is collected between t = 3.50 s and t = 6.50 s when steady state is established.

The ratio of particle energy loss relative to the impeller remains in favour of the 8 mm particles. The 8 mm particle population, or rather a significant portion of 8 mm particles occupies the region above the impeller pins.

This can be seen in Figure 33. This smaller population of 8 mm particles, coupled with the weight each particle has, allows for it to bear the brunt of the force of the impeller collisions. This in turn results in increased kinetic energy and momentum in an evenly weight distributed system. Increasing the impeller speed increases the mean of the ratio Υ, this can be seen in Figure 33. Thus, increasing the impeller speed increases the kinetic energy and momentum of the larger particle.

The particles tend to have the same motion and velocity profiles. This is shown in Figure 35 and in Figure 36. There are fewer 8 mm particles than 5 mm. This is due to 8 mm particles being equivalent to four 5 mm particles, based on mass. This can be seen in Equation 31.

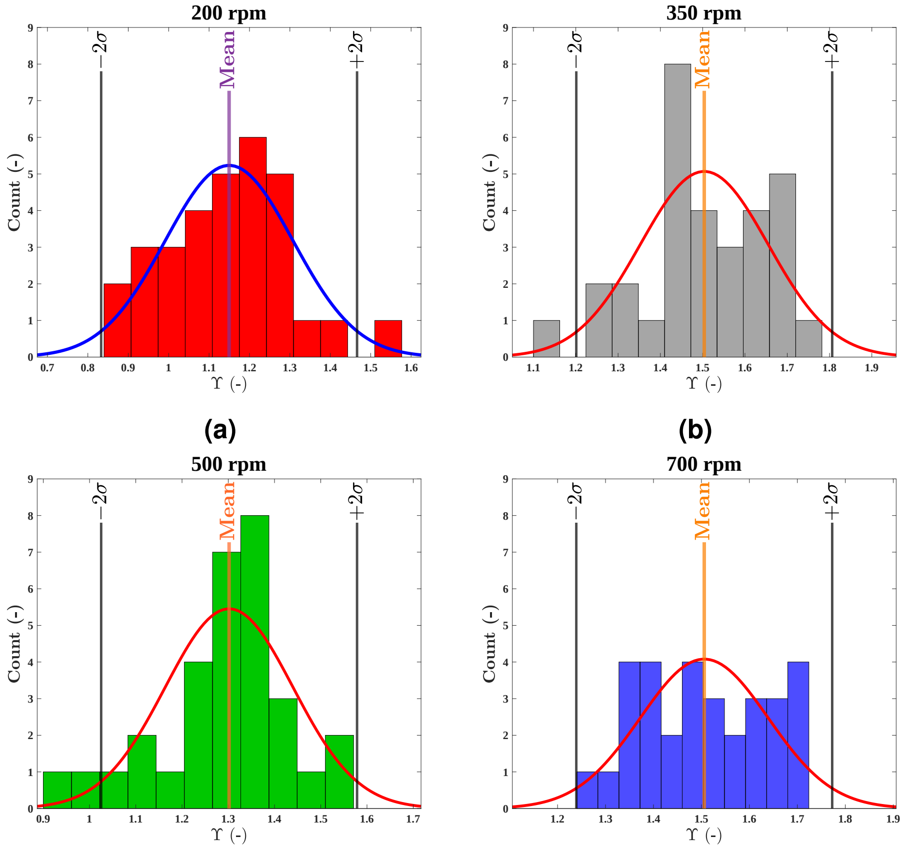

(a)

(b)

(c)

(d)

Figure 38: Particle energy loss ratios relative to the impeller

$$ratio\ 8\ to\ 5 = \frac{mass\ 8\ mm\ particle}{mass\ 5\ mm\ particle} = \frac{\frac{1}{6}\pi d_{p,8}^3 \rho_m}{\frac{1}{6}\pi d_{p,5}^3 \rho_m} = \frac{d_{p,8}^3}{d_{p,5}^3} = \frac{8^3}{5^3} = 4.096 \quad (31)$$

The 8 mm particles had more momentum and kinetic energy than that of the 5 mm particles. Thus, any deviations that a singular or multitude of 8 mm particles would have on the movement of the collective bulk media of the system, would be more significant than the 5 mm particles in a two particle size-mixed system. Thus, the larger particles in the context of an even weight distributed system, would have a more significant impact on the movement of the bulk media.

Table 12: Estimated normal distribution values for ratio of the 8 mm and 5 mm total energy loss relative to the impeller

	Normal mean (u)	Normal variance (σ)
200 rpm	1.150	0.158
350 rpm	1.504	0.151
500 rpm	1.302	0.138
700 rpm	1.509	0.133

4.2.4 Collision spectra

The collision spectra of the final revolution for the different impeller speeds are shown in Figure A3 in Appendix A.3. With an increase in impeller speed, both the range and intensity of collisions is increased. This can be seen in Table 13 where the 5th and 95th collision energy loss percentiles increase with the impeller speed.

Table 13: Range of collision intensities at various impeller speeds

Impeller speed	Average total collision intensity	5th percentile collision intensity	95th percentile collision intensity
200 rpm	1.35 μJ	5.05 nJ	2.53 μJ
350 rpm	5.77 μJ	9.43 nJ	11.69 μJ
500 rpm	13.11 μJ	12.73 nJ	27.96 μJ
700 rpm	25.67 μJ	10.16 nJ	55.40 μJ

In contrast to the collision spectra shown Section 4.1.4.2 in Figure 27, the tangential energy loss of the collision spectra in Figure A3 is more significant to the overall total energy loss. This is indicated by the total collision energy loss curve resembling the tangential energy loss curve at higher collision intensities. Collision spectra's are in line with Ndimande et al. (2019), and Oliveira et al. (2020), with tangential energy loss being more significant.

The reason for the discrepency of the tangential and total energy is due to using an updated EDEM simulation software. It is likely that the software takes into account a more nuanced, or prominent, shear based interactions that was not present in the previous version.

In Figure 39 the modal peak of different collision spectrums is depicted. The total collisions, shown in Figure 39a, depicts the modal peak involving all collisions *ie* particle-particle and environmental based collisions. The modal peaks, shown in Figure 39b, depicts the overall modal peaks collisions involving particle-particle collisions. The particle-particle collisions consisted of the small-small particle collisions, small-large particle collisions and large-large particle collisions. The individual aforementioned particle collisions are shown in Figure 39c - 39e.

The particle-environmental collisions, shown in Figure 39f, depicts the modal peak of collisions involving particles with the impeller and grinding chamber of the system.

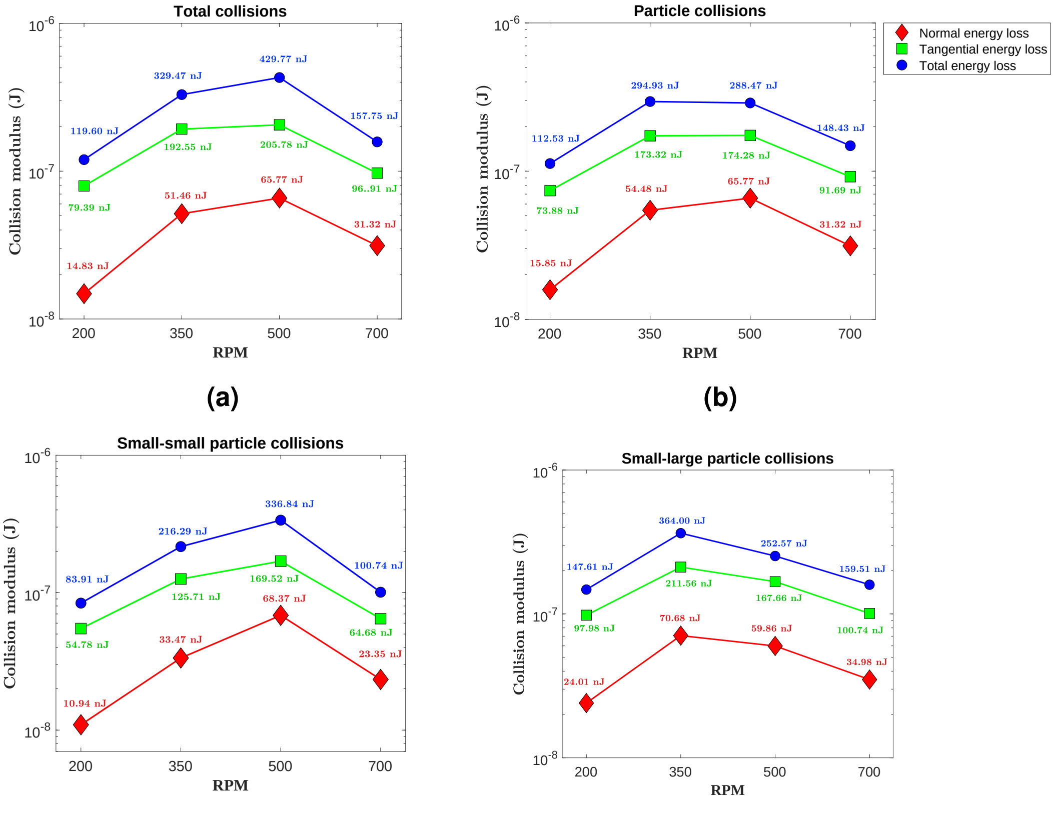

(a)

(b)

(c)

(d)

Figure 39: Modal peaks of collision data of (a) total collisions, (b) total particle collisions, (c) small-small particle collisions, (d) small-large particle collisions, (e) large-large particle collisions and (f) environmental collisions (impeller + grinding chamber collisions)

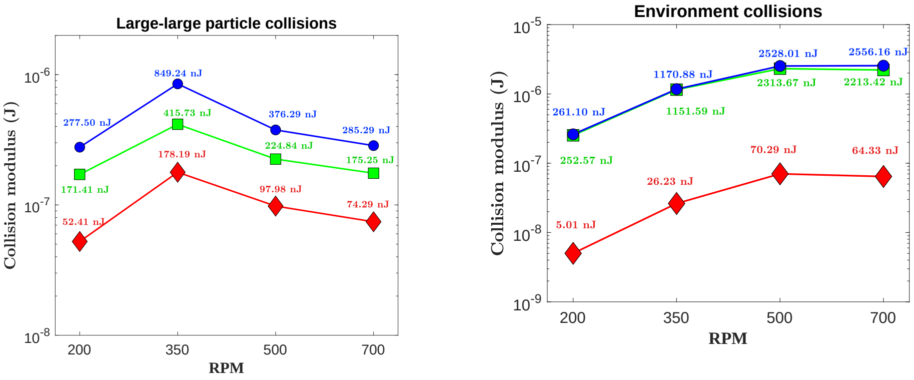

(e) **(f)**

Figure 39: Modal peaks of collision data of (a) total collisions, (b) total particle collisions, (c) small-small particle collisions, (d) small-large particle collisions, (e) large-large particle collisions and (f) environmental collisions (impeller + grinding chamber collisions)(continued)

The total collisions modal peaks, shown in Figure 39a, were largely dependent on the total particle collisions modal peaks, shown in Figure 39b, which in turn is largely influenced by the small-small particle collisions, depicted in Figure 39c. This is due to the modal peaks being dependent on the frequencies of the collision intensities. Thus, with the smaller particles being more numerous, they have a larger influence on the total collision energy loss.

The collision modulus for small-small particle collisions increased with rotational speed of the impeller from 200 rpm to 500 rpm. Further increase in rotational speed from 500 rpm to 700 rpm resulted in in a decrease of the collision modulus. For the small-large and large-large particle collisions the peak modulus can be seen in at 350 rpm. This decline of the collision modulus at higher impeller speeds indicates that excessive impeller speeds hinder the overall collision modulus. For effective breakage rates a substantive collision modulus is required.

For the particle-particle collisions, depicted in Figure 39b, the maximum collision modulus is estimated at 350 rpm whilst the maximum tangential and normal energy loss is estimated at 500 rpm. The difference between the collision intensities at 350 rpm and 500 rpm is not substantial. The increased collision intensity at 350 rpm can be attributed to small-large particle collisions. The collision intensity peak at 500 rpm can be attributed to the small-small particle collisions.

The large-large particle collisions were more intense than that of the smaller particles, thus their influence is at the higher end of the collision intensity spectrum. Thus, at the lower 350 rpm impeller speed, the large-large and small-large particle collisions were favoured, which can benefit the breaking of larger particles. At 500 rpm the small-small particle collisions were favoured which can be used to ground existing viable materials into a finer standard. At the highest impeller speed of 700 rpm, the collision moduli are reduced.

For the environmental collisions, the collision moduli increases as the impeller speed is increased. The collision moduli tended to stagnate between 500 rpm and 700 rpm. The environmental collisions are dictated by tangential collisions. This indicates that the impeller experiences increased drag as the speed is increased, resulting in increased equipment wear.

Increasing the impeller speed further reduced the collision frequency and also increased the particle separation. The reduced frequency is discussed in Section 4.2.2 and the increased particle separation is discussed at the end of Section 4.2.3.1. Excessive impeller speed, such as the 700 rpm speed, resulted in a reduction of particle-particle collision moduli. It is likely that the particles started to centrifuge outwards and upwards, avoiding impeller collisions which would reduce the intensity of collisions. The reduction of collision moduli can be seen in Figure 39. This indicates that excessive impeller speeds will not benefit consistent and effective breakage events. Thus, 350 rpm was considered the optimal grinding impeller speed, as it had suitable tangential and normal based collision modulii with better particle mixing.

The addition of a fluid into the simulation would have improved fine grinding performance of the mill, specifically the improvement of tangential based interactions(Gudin et al. 2006; Kotake et al. 2011). The addition of a fluid would further dampen compressive based interactions. The addition of a fluid would likely have upset the simulation artifacting by carrying, or moving, the additional particles above the impeller pins around in the chamber. With additional particles moving through the system, instead of collecting atop the particulate media, the amount of collisions, and in turn substantive collisions, forces would be increased.

Additional information and data of the collision modulii at different impeller speeds can be found in Appendix A.4.

4.2.4.1 Collision spectra - increased impeller speed

The reduction in modal collision intensities, observed at 700 rpm, was further investigated. Two additional simulations were performed with impeller speeds of 800 rpm and 900 rpm. The modal collision intensity for the final 0.50 seconds of each simulation is shown in Figure 40.

Increasing the impeller speed past 700 rpm did not result in any significant increase or decrease of the collision modulii. Any speed past 700 rpm resulted in most of the particle-particle collision moduli plateauing. For the impeller speeds of 700 rpm, 800 rpm and 900 rpm slight negligible decrease or increase of the moduli may be observed.

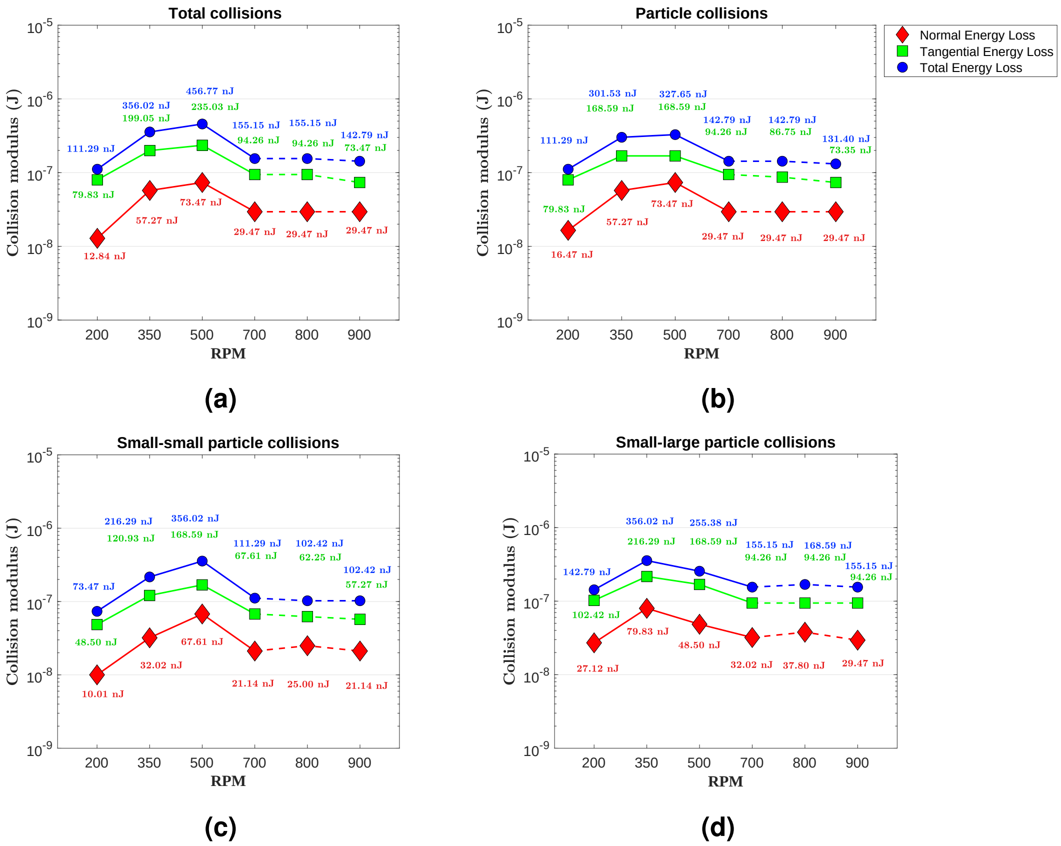

(a) (b)

(c) (d)

Figure 40: Modal peaks of collision with increased impeller speeds for (a) total collisions, (b) total particle collisions, (c) small-small particle collisions, (d) small-large particle collisions, (e) large-large particle collisions and (f) environmental collisions (impeller + grinding chamber collisions)

Overall the 800 rpm impeller did result in a slight increase in collision moduli at the elevated impeller speed, compared to 700 rpm. Furthermore, the 900 rpm impeller speed did result in the overall lowest collision moduli at the elevated impeller speeds. This general trend can be observed in Figures 40a through 40f.

It is likely that a significant portion of the particles are centrifuging outwards and upwards, avoiding the impeller pins. With a significant portion of the particles avoiding direct collisions with the impeller pins, less collision energy was transferred from the impeller pins to the particles, reducing the collision intensities.

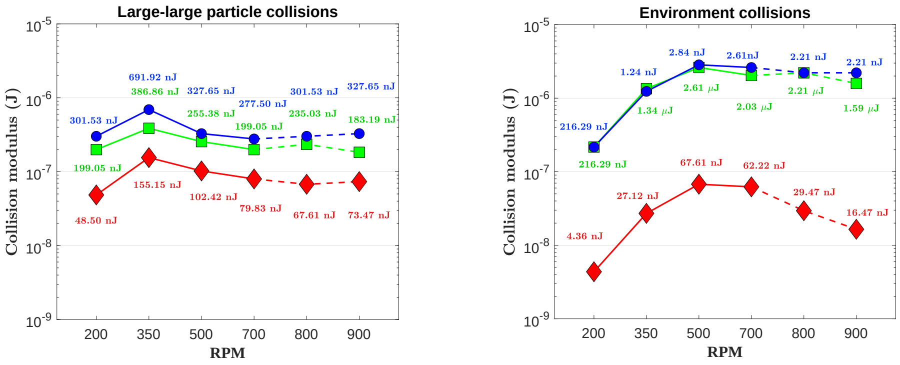

(e)

(f)

Figure 40: Modal peaks of collision with increased impeller speeds for (a) total collisions, (b) total particle collisions, (c) small-small particle collisions, (d) small-large particle collisions, (e) large-large particle collisions and (f) environmental collisions (impeller + grinding chamber collisions)(continued)

Increasing the impeller agitation speed further increased particle collision intensity ranges, as well as the power draw of the impeller. The power draw and effective breakage rate of a vertical stirred mill would need to be balanced for effective operation.

4.2.5 Power consumption

In this section the total torque experienced by the impeller, τ, is used with the angular speed, ω, to estimate the power draw. The power estimation is shown in Equation 32.

$$P = (\sum \tau_{impeller}) \cdot \omega \tag{32}$$

The power consumption values of the different impeller speeds were sporadic. This can be seen in Figure 41 where the power oscillates between different extreme values. This is due to the power being estimated by the simulated torque of the impeller.

The torque of the impeller varied from moment to moment. At any given point the torque was influenced by the amount of particles in contact with the impellers pins as well as the resistance to movement the collective particulate media provided at any given point. This resulted in different torque values being estimated at any given moment, as the amount of particles in contact with the impeller, and in turn resistance, would be significantly different (Faramarzi et al. 2020).

In order to mitigate the inconsistencies, a smoothed power draw was used to estimate power consumption. The energy consumed was estimated using Equation 33. The energy consumed was estimated between t = 3.50 s and t = 6.50 s.

$$\xi = \int_{t_i}^{t_f} P \, \mathrm{d}t. \tag{33}$$

The smoothing and filtering of the power is discussed in greater detail in Appendix A.5. The resulting power values are shown is in Table 14.

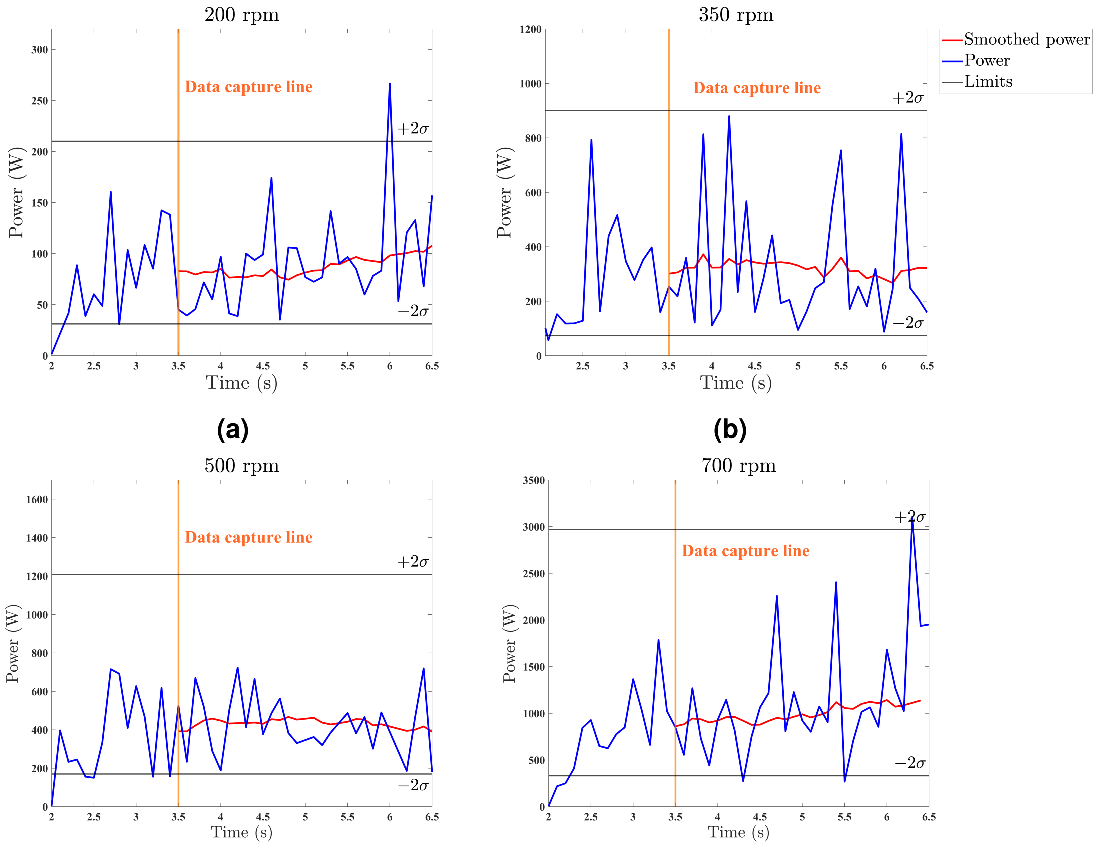

(a) **(b)** **(c)** **(d)**

Figure 41: Graphs of power values used to estimate energy consumption in Table 14

In Table 14 it can be seen that increasing the impeller speed increases the total power draw. The most substantial gains in energy consumed was seen between the impeller speeds 500 rpm and 700 rpm as well as 200 rpm and 350 rpm. The estimated log mean power increased with impeller speed. This can be seen in Table 14.

Table 14: Estimated power values for various impeller speeds for a 6.50 kg systems with a 50-50 weight distribution of 8- and 5-mm particles

	Lognormal mean power (e^u)(W)	Energy consumed (J)	Difference of mean power draw from previous impeller speed (W)	Estimated energy uncertainty (J)
200 rpm	80.76	268.53	–	± 3.28
350 rpm	257.26	1024.29	176.50	± 34.83
500 rpm	452.94	1516.79	195.68	± 127.90
700 rpm	991.68	3047.42	538.74	± 186.05

The substantive power draw of 700 rpm coupled with the reduced collision moduli, shown in Figure 39, reduces the inclination towards it being a reasonable or viable operating speed. It has a larger range of collisions, compared to the others, which should enable it to break tougher materials requiring more intense collisions. The range of collision intensities is shown in Table 13. The lower 200 rpm impeller speed resulted in a reduced range of collisions which may not be able to sufficiently break down potential materials. Its reduced range of collisions made it a less viable impeller speed, as it may not be able to viably facilitate breakage of a required material.

The impeller speeds of 350 rpm and 500 rpm have shown the best collision moduli. Each speed has its benefits, maximising either the small-small particle collisions for the 500 rpm speed, or the small-large and large-large particle collisions for the 350 rpm speed. The impeller speeds have increased collision ranges that should allow for improved breakages of tougher or coarser materials. The disparity, or increase, of energy consumed between the 350 rpm and 500 rpm impeller speeds is not as severe as the disparity between other impeller speeds. Increasing the impeller speed from 350 rpm to 500 rpm increased the energy consumed by $\approx$50 %. Increasing the impeller speed from 200 rpm to 350 rpm increased the energy consumed by $\approx$380 % percent. When increasing the impeller speed from 500 rpm to 700 rpm the energy consumed was increased by approximately 100 %. The non-linear nature of the power scaling can be attributed to the non-leaner nature and estimation of torque.

The collision energy proportions and distribution between t = 4.5 s and t = 6.5 s is illustrated in Figure 42. The proportions of the collision energy which is dedicated to large, small or environmental collisions is presented. The collision subjects are normalised to the respective total energy loss in the system. This is done using Equation 34. The total energy loss of collisions were normalised according to the maximum total energy loss of 700 rpm.

$$\epsilon_{prop,TOT} = \frac{\sum_{t_{begin}}^{t_{end}} e_{i,TOT}}{\sum_{t_{begin}}^{t_{end}} e_{ALL,TOT}} \times 100\ \% \tag{34}$$

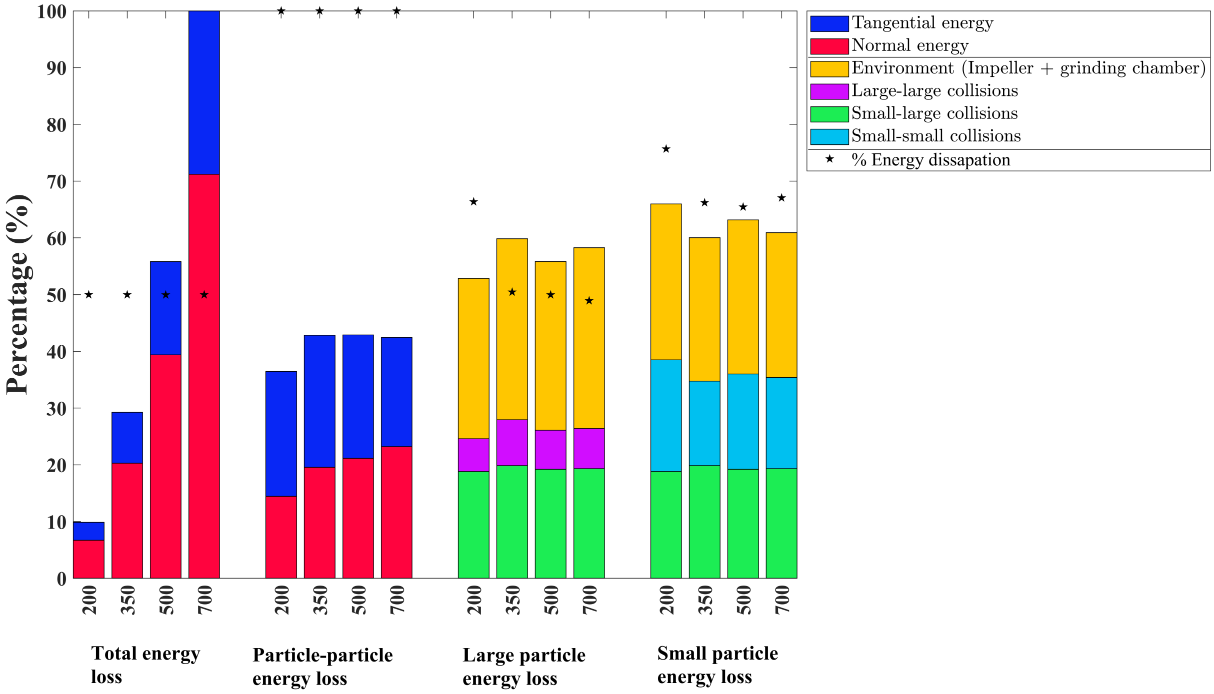

Figure 42: Accumulated power distribution between t = 4.5 s and t = 6.5 s. The total energy loss is normalised to the maximum energy loss whilst the rest of the energy loss subjects are normalised to their respective total energy loss

The specific percentage and numeric values depicted in the Figure 42 are available in Table 15. Additional data is further shown in Appendix A.6.

For the particle-particle collision energy loss, the disparity between 100 % and the depicted bar indicates the collisions between the particles and the environment. For the large and small particle energy loss, the disparity is due to the exclusion of collisions involving the other sized particle. The energy dissipation parameter shows what proportion of collisions result in energy loss. The higher the dissipation value, the higher the energy loss through collisions.

Table 15: Energy percentage breakdown of different impeller speeds, relevant to Figure 42

	200 rpm	350 rpm	500 rpm	700 rpm
Total energy loss	384.10 J	1139.94 J	2174.78 J	3895.09 J
Particle collisions	36.47 %	42.84 %	42.88 %	42.47 %
Environmental collisions (impeller + chamber)	55.73 %	57.16 %	57.13 %	57.54 %
Environmental collisions (impeller)	50.02 %	50.01 %	50.02 %	50.01 %
Large particles (environment + small)	52.84 %	59.83 %	55.82 %	58.27 %
Small particles (environment + large)	65.98 %	60.03 %	63.17 %	60.92 %
Large-large particle	5.77 %	8.08 %	6.88 %	7.09 %
Small-small particle	19.69 %	14.89 %	16.79 %	16.07 %
Small-large particle	18.82 %	19.87 %	19.21 %	19.32 %
Normal energy loss	251.02 J	769.31 J	1505.07 J	2743.62 J
Particle collisions	24.36 %	26.78 %	24.93 %	29.64 %
Environmental collisions (impeller + chamber)	75.64 %	73.09 %	62.60 %	70.36 %
Environmental collisions (impeller)	74.90 %	72.25 %	61.63 %	69.02 %
Large-large particle	3.27 %	4.99 %	4.08 %	4.98 %
Small-small particle	10.55 %	9.30 %	11.23 %	13.46 %
Small-large particle	10.55 %	12.50 %	9.62 %	11.19 %
Tangential energy loss	122.90 J	349.96 J	640.74 J	1122.08 J
Particle collisions	75.92 %	70.06 %	66.02 %	66.08 %
Environmental collisions (impeller + chamber)	23.65 %	29.94 %	29.83 %	33.92 %
Environmental collisions (impeller)	9.14 %	10.24 %	10.24 %	12.51 %
Large-large particle	9.49 %	13.33 %	10.43 %	10.95 %
Small-small particle	34.06 %	24.31 %	26.04 %	24.97 %
Small-large particle	32.12 %	32.49 %	29.55 %	30.16 %

Increasing the impeller speed increases the total collision energy loss in the system. This is shown in Figure 42, where the total energy loss bar increases with the impeller speed. As the total energy loss bar increases, so too does the normal and tangential energy loss. The total normal energy loss was larger than the tangential energy loss.

This can be seen as the blue proportion of the total energy loss bars in Figure 42 is less than the red portion, which illustrates the normal energy loss. This can also be seen in Table 15.

A large contributor to the direct collisions that promote the normal energy loss, is the collisions between the impeller and the particles. This can be seen in Table 15 under normal energy loss impeller collisions where the impeller collisions attribute to approximately 70 % of the energy of normal collisions. The direct impeller collisions, summated with the particle-particle collisions, results in a normal energy that is more than the tangential energy loss, which is largely promoted by particle-particle collisions. This can be seen in Table 15 under tangential energy loss where the particles account for approximately 70 % of the tangential energy loss.

The largest collision energy dissipation source for the particle collisions is the small-large particle collisions. This can be seen in Table 15 where it is ≈19 % of the total energy loss. This is then followed by the small-small particle collisions with ≈16 %. Finally the larger-larger particle collisions only account for ≈7 % of the total energy loss.

The smaller particles are responsible for the majority of the collision energy dissipation. This can be seen in Figure 42 where the energy dissipation of the smaller particles is larger than that of the larger particles. This can be seen in Table 15. This can be attributed to the cushioning effect being promoted, with each subsequent collision dissipating the remaining energy that can be used for effective breakages. Energy is lost with each particle collisions. The simulation parameter responsible for particle-particle energy loss is the coefficient of restitution discussed in Section 2.4.2.1.

Though the larger particles have higher kinetic and collision modulii, it dissipates less energy than the smaller particles. This is due to there being fewer larger particles, resulting in reduced collisions compared to the smaller particle.

The impeller promotes direct collisions. This can be seen in Table 16, where a majority of its experienced collision energies is normal based. The grinding chamber experiences drag with its mostly tangential energy loss. This can be seen in Table 16.

It is important to note the change the addition of fluid would do to simulated system. A prominent aspect the fluid would change is the total power draw of the system, as it would further increase the torque required to move the system. Additionally, the liquid for further reduce the impact of direct collision, further reducing the prominence of normal based collisions.

The addition of liquid would likely promote more tangential based forces and interactions in the simulation, further promoting fine grinding.

Table 16: Additional data that breaks down the proportions of the impeller speed tests

Subject	200 rpm (%)	350 rpm (%)	500 rpm (%)	700 rpm (%)
Proportion energy dissipation				
Total energy loss	49.98	49.97	49.95	49.97
Particle-particle energy loss (does not include impeller collisions)	99.99	99.99	99.99	99.99
Large particle energy loss (environment + large particle collisions)	66.36	50.44	49.96	48.92
Small particle energy loss (environment + small particle collisions)	75.67	66.20	65.44	67.05
Proportions of total energy loss[a]				
Tangential energy loss	32.87	31.27	29.85	29.03
Normal energy loss	67.13	68.73	70.15	70.97
Proportions of particle-particle collisions energy loss[a]				
Tangential energy loss	60.40	54.34	53.00	47.69
Normal energy loss	39.60	46.64	47.00	52.31
Particle total energy collision proportions[b]				
Large-large particle collisions	13.02	18.86	16.06	16.70
Small-small particle collisions	44.47	34.77	39.15	37.83
Large-small particle collisions	42.50	46.37	44.79	45.49
Particle normal energy collision proportions[b]				
Large-large particle collisions	13.44	18.63	16.37	16.81
Small-small particle collisions	43.30	34.71	45.03	45.41
Large-small particle collisions	43.28	46.66	38.60	37.77
Particle tangential energy collision proportions[b]				
Large-large particle collisions	12.82	19.01	15.61	16.57
Small-small particle collisions	44.87	34.67	39.45	37.79
Large-small particle collisions	42.30	46.33	44.76	45.64
Environmental energy collision proportions[a]				
Tangential energy loss (impeller)	5.64	6.05	6.77	6.90
Normal energy loss (impeller)	94.36	93.95	93.23	93.10
Tangential energy loss (grinding chamber)	90.65	90.24	89.48	86.71
Normal energy loss (grinding chamber)	9.35	9.76	10.52	13.29
Tangential energy loss (grinding chamber + impeller)	13.27	15.69	16.87	16.47
Normal energy loss (grinding chamber + impeller)	86.73	84.31	83.13	83.53

$$TE_{proportion,i} = \frac{\sum TE_i}{\sum TE_i + \sum NE_i} \tag{35}$$

$$\epsilon_{i,j} = \frac{\sum_i^n e_{i,j}}{\sum_i^n e_{particles,j}} \times 100\ \% \tag{36}$$

---

[a] This is estimated using Equation 35 and the data from Table A14.

[b] This is estimated using Equation 36 and the data from Table A14. Where *i* references the subject and *j* the collision type.

4.2.6 Particle and collision profile variations according to equipment height

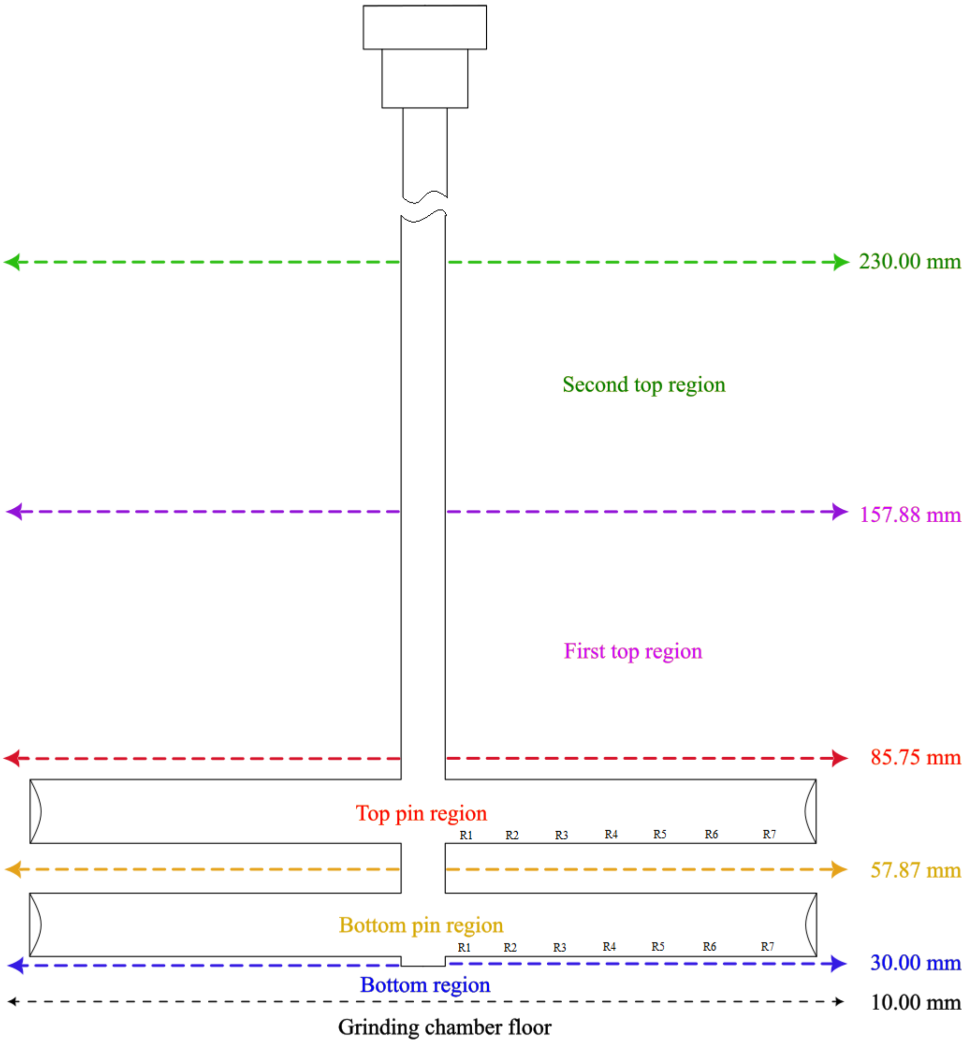

Figure 43: Height distribution of mill relative to the impeller

The force and energy loss profiles were evaluated according to the sections illustrated in Figure 43. These sections were selected to define the forces and interactions in regions of interest in the grinding chamber. These regions included the bottom region, where particles tended to occupy the grinding chamber floor. The top and bottom pins were defined as relevant areas so that their performance against one another could be compared.

A top region was defined with a height range of 85.75 mm to 230 mm. This region was selected to account for the particle layers that formed above the pins with the occupation plot shown in Figure 33 at 700 rpm. This top region was subsequently divided in half as not all particles tended to collect at the top point at lower impeller speeds.

Points of interest, along the radius of the regions, were defined to evaluate the forces. The collision data was collected between time t = 6.20 s and t = 6.50 s. The particle data was collected between t = 3.50 s and t = 6.50 s. These results can be seen in Figure 44 and 49.

Boxplots were used to illustrate the distribution of the energy and force of collisions in the regions of interest. It should be noted that the boxplots do not fully describe their distributions. The 10th and 90th percentiles of the relevant data were approximated as the maximum and minimum limits of the boxplots. The reason for this approximation is further elaborated on in Appendix B.1. Furthermore, the box edges then represents the 25th and 75th percentiles of the data, while the middle line represents the median value of the collisions.

4.2.6.1 Collision variations

The plots shown in Figure 44 through to Figure 49 illustrate the total energy losses as well as the normal and tangential force profiles of the collisions for each rotational speed. The radius is divided into eight different segments, similar to Sinnott et al. (2006). For the purposes of simplification, the final radius, r_7 = 12.21 cm, can be approximated as the grinding chamber wall along with the end of the impeller pin. The force profiles are proportional to the energy loss profiles. Logarithmic scales were used to illustrate the non-linear trends of the collision values.

Assorted colour schemes were used to group the impeller speeds. Blue-orange was used to indicate 200 rpm. Yellow-grey was used to indicate 350 rpm. Red and green was used to indicate 500 rpm. Brown-peach was used to indicate 700 pm. Different colours for the box edges were used to distinguish both the scale and variations of the box plots.

The second and first top regions force profiles and total energy loss is depicted in the figures in Figures 44 and 45. The collision distribution of 200 rpm is not present in the second top half region. This is due to its low impeller speed not enabling the particles to reach the second top half region. The magnitude and range of the boxplots suggests a chaotic motion in all cases.

Figure 44: Energy loss and force radial distributions for second top region between t = 6.20 s and t = 6.50 s

Impeller region	Total energy loss (J)	Average normal force (N)	Average tangential force (N)
Second top region	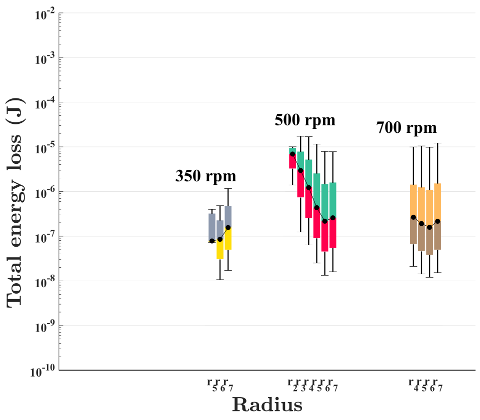	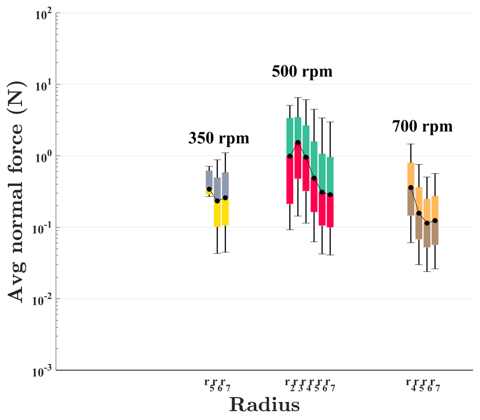	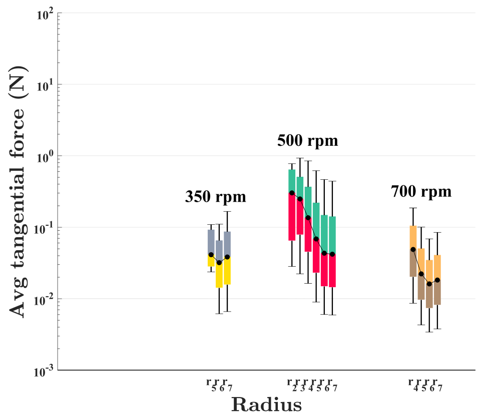

r_0 = 0.81 cm
r_1 = 2.44 cm
r_2 = 4.06 cm
r_3 = 5.69 cm
r_4 = 7.32 cm
r_5 = 8.95 cm
r_6 = 10.58 cm
r_7 = 12.21 cm

Figure 45: Energy loss and force radial distributions for first top region between t = 6.20 s and t = 6.50 s

Impeller region	Total energy loss (J)	Average normal force (N)	Average tangential force (N)
First top region	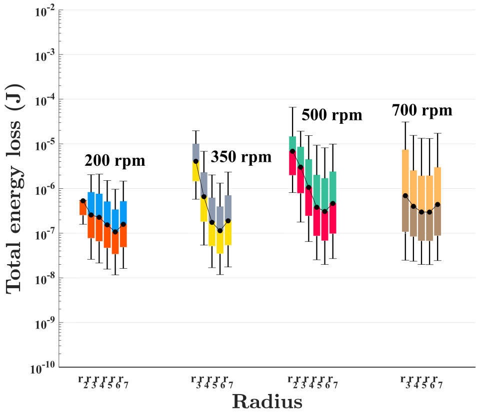	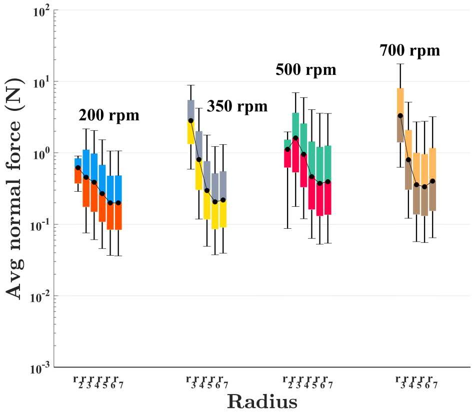	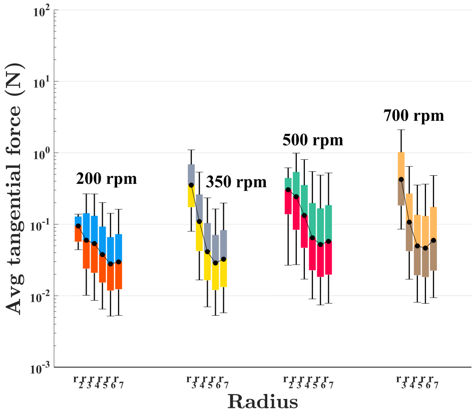

r_0 = 0.81 cm
r_1 = 2.44 cm
r_2 = 4.06 cm
r_3 = 5.69 cm
r_4 = 7.32 cm
r_5 = 8.95 cm
r_6 = 10.58 cm
r_7 = 12.21 cm

For the second top region, the 500 rpm impeller speed resulted in the most collisions, and in turn most particles, present there. This is more than the 700 rpm impeller speed, where the particles and collisions tended to spread more vertically than radially at the height section. Thus, the 700 rpm collisions have less radial coverage.

The total energy loss profiles of the second top region, show in the column in Figure 44, the energy loss distribution decreases along the radius for the 500 rpm and 700 rpm impeller speeds. For the 500 rpm impeller speed the a slight increases in energy loss can be seen. The overall range of values for the 350 rpm speed is incredibly low, between 10^{-8} and 10^{-6}. Thus, any slight variations to the low value collisions may seem larger. For the 500 rpm and 700 rpm impeller speeds nn increase in the total energy loss profiles is seen near the end of the radii at r_7 = 12.21 cm. This where the particles interact with the grinding chamber walls, promoting shear based breakages. The increase in total collision energy is due to the interaction with the grinding chamber walls.

The normal and tangential force profiles for the second top regions are shown in the second and third columns in Figure 44. The tangential forces have the same shape and trends as the normal forces; however, the tangential forces have reduced force values compared to the normal forces. The force profiles tended to decrease along the radius, only increasing at the end owing to the grinding chamber wall interactions. The 500 rpm had the largest range of collisions at the second top region. The 700 rpm profile indicated less intense collisions compared to the 500 rpm profile. The increased force profile range,for the 500 rpm, is owed to the radially distributed particles and the turbulent conditions that facilitated the collisions compared to the 700 rpm. For the 700 rpm, a significant portion of particles occupied the space above the bulk media, this is shown in Figure 33g. The significant portion of particles allowed for a cushioning effect to occur, dissipating energy and dampening the normal and tangential based interactions.

For the first top region the total energy loss is shown in the second column of Figure 45, with the normal and tangential forces being shown in the third and fourth columns. The force and total energy loss profile of the first top region follows the same trends as the second top region, as discussed in the paragraphs above. The only significant difference is that the first top region increased force and energy loss values when compared to the second top region.

For the 500 rpm profile, in both the first and second top region, there is an increase for the normal force at r_3 = 5.69 cm. This height region, between 8.58 cm and 15.79 cm, and the radius region, between 4.00 cm and 6.00 cm, coincides with where the particles motions change from moving inwards to outwards. This is shown in Figure 46 by means of a quiver plot. The increased values coincides with the beginning of the inflection line, shown in green in the figure, with the change in downward motion moving from inward to outward.

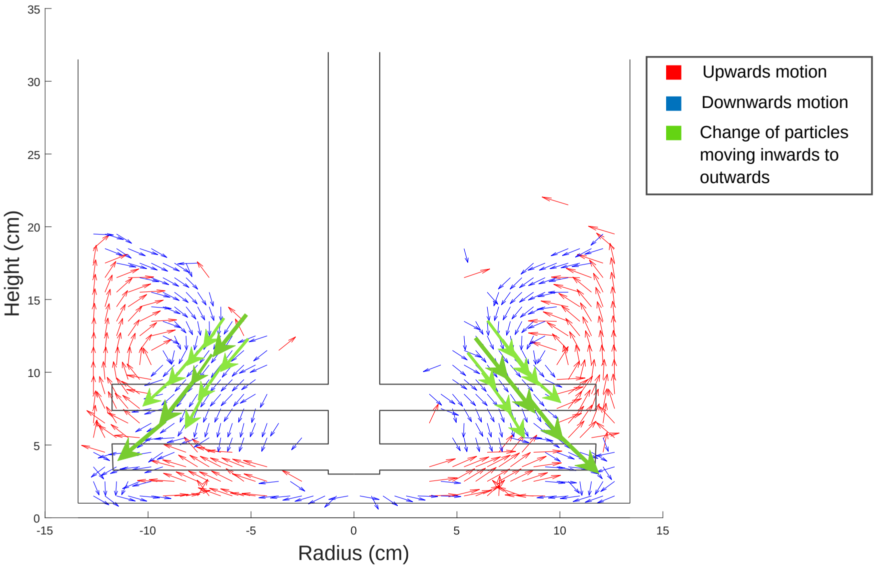

Figure 46: Illustration of particle motion changing from inwards to outwards

At this inflection line, particles above and below the line are moving inward and downward. The particles moving downward are likely to cause compressive and turbulent interactions.

The top pin total energy loss is shown in the second column of Figure 47. For 200 rpm the median total energy loss falls before rising. For the 350 rpm through to 700 rpm the energy loss distribution starts high before falling, only rising near the end due to the impeller pin end interactions and the grinding chamber wall. The 200 rpm energy ranges is consistent, indicating little turbulence. The 700 rpm energy ranges is far wider, indicating more turbulent and intensive collisions.

Both the 350 rpm and 500 rpm total energy loss follow a similiar pattern. The 350 rpm has a higher average median value than the 500 rpm, however, the 500 rpm has a wider range of collisions. The 350 rpm impeller speed presents a more consistent rate of energy loss.

The tangential and normal force profiles are shown in the third and fourth columns of Figure 47. Overall the normal forces have increased values compared to the tangential forces. For the 200 rpm impeller speed the force profiles follow a similiar trend as the energy loss profiles, falling before r_3 = 5.69 cm and rising afterwards. Similarly the 350 rpm force follows the same trend as the energy loss profile. A decrease in force values is seen along the radii before a rise at end. For 500 rpm the normal force profile follows sinusoidal pattern, rising at the initial radii values before falling and rising at the end of the radii values. The tangential force for 500 rpm follows a similiar pattern to the energy loss profile. For 700 rpm the normal and tangential force profiles followed a similiar shape dissimilar to the total energy loss. An arc like pattern is seen for the 700 rpm force profiles.

The highest force values for impeller speeds 350 rpm and 500 rpm can be found between r_3 = 5.69 cm and r_4 = 7.32 cm, around the initial values. This is due to the particles flowing downwards and colliding with the impeller pins, resulting in more intense collisions. Additionally, the velocity profile around the impeller pins, illustrated in Figure 37, is increased compared to the bulk media surrounding the pins. Thus, the velocity change further results in increased collision values owing to the agitation of the pins.

The total energy loss profiles for the bottom pin region can be seen in the second column of Figure 48. For the 200 rpm and initial reduction of the energy loss is seen before a consistent rise in energy loss after r_1 = 2.44 cm. For the total energy loss, the 350 rpm had the overall highest median values compared to the remainder of the impeller speeds. For the 350 rpm and 500 rpm the energy loss is decreases along the radii before before rising near the end. The 700 rpm energy loss follows a similiar trend barring an initial rise past the first radius. The increases length of the boxplots indicates turbulent particle collisions.

Figure 47: Energy loss and force radial distributions top pin region between t = 6.20 s and t = 6.50 s

Impeller region	Total energy loss (J)	Average normal force (N)	Average tangential force (N)
Top pin	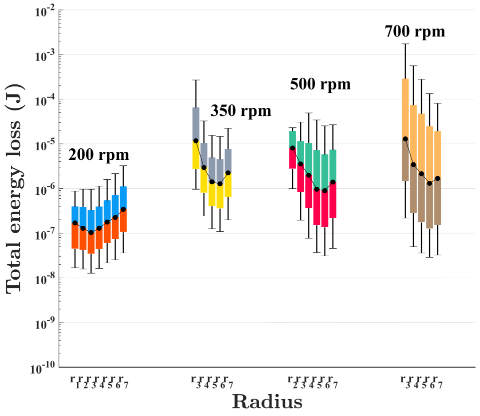	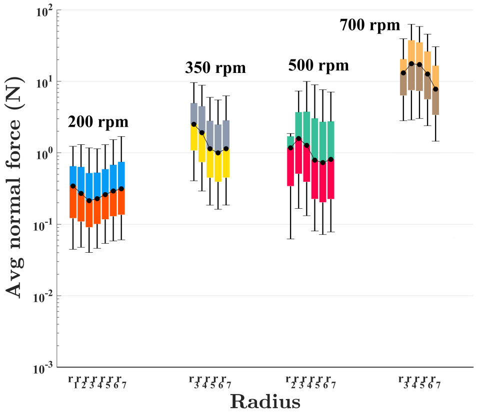	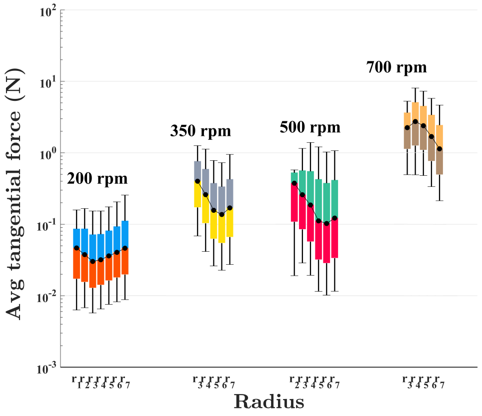
			r_0 = 0.81 cm r_1 = 2.44 cm r_2 = 4.06 cm r_3 = 5.69 cm r_4 = 7.32 cm r_5 = 8.95 cm r_6 = 10.58 cm r_7 = 12.21 cm

Figure 48: Energy loss and force radial distributions for bottom pin region between t = 6.20 s and t = 6.50 s

Impeller region	Total energy loss (J)	Average normal force (N)	Average tangential force (N)
Bottom pin	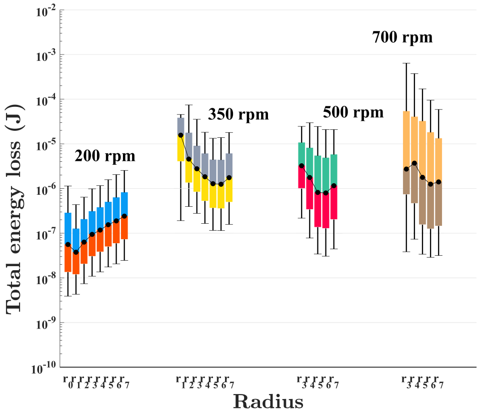	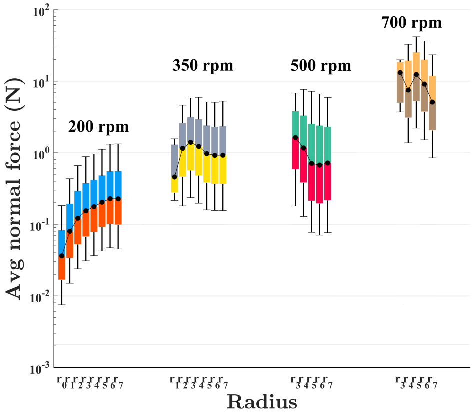	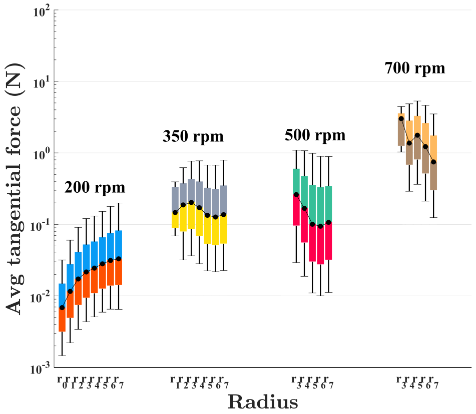

r_0 = 0.81 cm
r_1 = 2.44 cm
r_2 = 4.06 cm
r_3 = 5.69 cm
r_4 = 7.32 cm
r_5 = 8.95 cm
r_6 = 10.58 cm
r_7 = 12.21 cm

The normal and tangential force profiles for the bottom pin region can be seen in the third and fourth columns of Figure 48. The overall tangential force values are less than the normal values. The force profiles values for 200 rpm increases along the radius. The 350 rpm force profile values rises with an initial peak at r_3 = 5.69 cm before plateauing after r_5 = 8.95 cm. The 500 rpm force profile values follow a decrease in values before similarly plateauing past r_5 = 8.95 cm. For 350 rpm and 500 rpm, beyond r_5 = 8.95 cm the force and range of force values plateau, consistent collisions and grinding actions should be facilitated. For the 700 rpm a range of force values is seen. It shows increased force values compared to the remainder of the impeller speeds.

The median force values of 350 rpm, 500 rpm and 700 rpm peak around r_3 = 5.69 cm and r_4 = 7.32 cm. Inspecting the quiver plots shown in Figure 35 or in Figure 46, the radial region between r_3 = 5.69 cm and r_4 = 7.32 cm and axial region between 3.00 cm and 57.87 cm coincides where the upwards and downwards particle motions meet, resulting in increased collision values.

The top and bottom pins facilitate and promote the most intense forces of the regions owing to the pins' agitation. The top pin facilitated the overall highest median, Q3 and Q4 forces and energy losses. This indicates that it should have improved grinding, or breakage-action compared to that of the bottom pin.

The energy and force profiles for the bottom region can be seen in Figure 49. The 200 rpm and 350 rpm collision energy loss and force profiles follow the same trend, where the particles are centrifuged outward increasing normal and tangential forces. For the 500 rpm impeller speed a discrepancy in the maximum limit can be seen at r_2 = 4.06 cm. This is likely due to irregular compression occurring.

The normal force values are larger than that of the tangential force values. The increased values is due to the impeller pins forcing the particles downwards, which further compresses particles in the bottom region. The particles that are in turn forced downwards replace existing particles that occupied the space, which in turn moves upwards.

The 700 rpm profile has a transition region between r_0 = 0.871 cm and r_4 = 7.32 cm. This transition region indicates particles that do not experience any worthwhile collisions or compressive forces in the bottom region. The high speed of the 700 rpm impeller centrifuges particles outwards, which in turn results in inactive particles collecting below the impeller.

Figure 49: Energy loss and force radial distributions for bottom region between t = 6.20 s and t = 6.50 s

Impeller region	Total energy loss (J)	Average normal force (N)	Average tangential force (N)
Bottom region	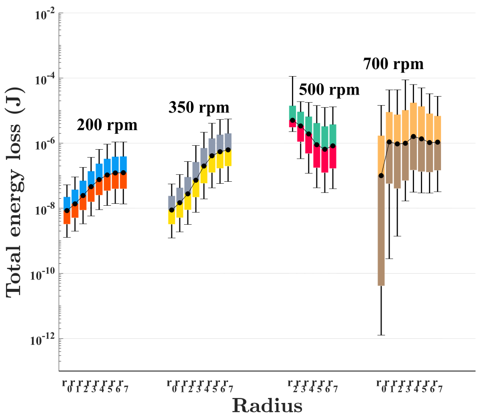	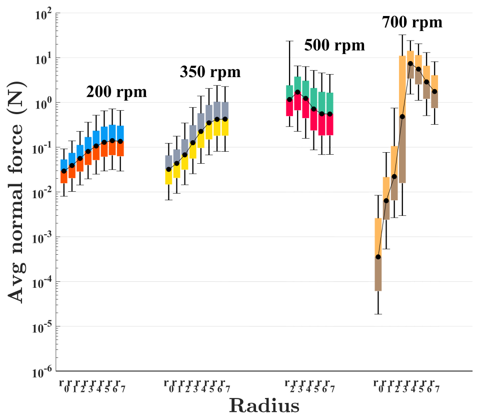	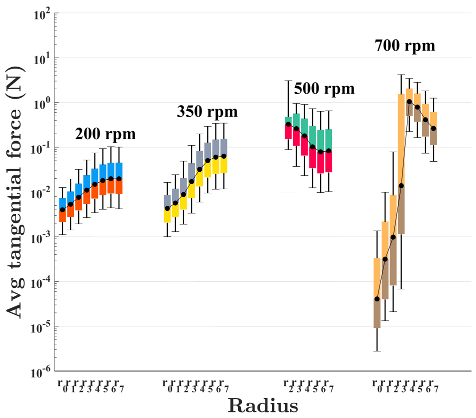

r_0 = 0.81 cm
r_1 = 2.44 cm
r_2 = 4.06 cm
r_3 = 5.69 cm
r_4 = 7.32 cm
r_5 = 8.95 cm
r_6 = 10.58 cm
r_7 = 12.21 cm

4.2.6.2 Particle variations

The axial velocities for the particle equipment height profiles are illustrated in Figures 50 and 54. In the axial velocity graphs, values above zero indicate particles rising upwards while values below zero indicate particles moving downwards.

Figures 50 and 51 show the axial velocity profiles for the large and small particles for the first and second top regions. The particles in the 200 rpm simulation did not disperse as high as the particles in the other impeller speed simulations. The large and small particle axial velocities are fairly similar for the first and second top regions. The smaller particles have a larger range of axial velocities in the first top region near the centre of the impeller between r_1 = 2.44 cm and r_2 = 4.06 cm for the 500 rpm and 700 rpm profiles. This large range is attributed to the dispersal of the particles moving downward from the second top region r_4 = 7.32 cm and r_6 = 10.58 cm. The overall median velocities are greater than those of the lower impeller speeds. The axial velocities at the top segments are lower compared to that of the lower pin values.

In Figures 52 and 53 the axial velocity for the large and small particles for the top and bottom pin segments are shown. For the 200 rpm profile, the median line remained consistently around the zero value. The similiar values for the box edges for the 200 rpm speed indicates a steady inflow and outflow of particles. At the radial end particles rapidly move upward. This is indicated in the particle motion in Figure 35. For the bottom pin the axial speed median values for the 350 rpm and 500 rpm were above zero, indicating a bulk media moving upward.

For the axial velocities for 350 rpm and 500 rpm profiles the top pin indicates particles being pushed downwards while the smaller particles indicates particles moving upwards. For the top pins the overall median line of the particles' axial velocities is below zero, indicating more than half of the particles moving downward. Near the radial end of the top axial velocities the medial values increases to zero.

Similarly the values for the Q1, Q3, minimum and maximum axial velocities for 200 rpm and 350 rpm can be seen in the top and bottom pin plots. This indicates an equivalent inflow and outflow of particles. A maximum value for the median value for the 200 rpm profile is seen at r_2 = 4.06 cm for the top pin segment. This coincides with upward particle motion in Figure 35.

Figure 50: Axial velocity distributions of large and small particles at different regions relative to the impeller

Impeller region	Small particles	Large particles
Second top region	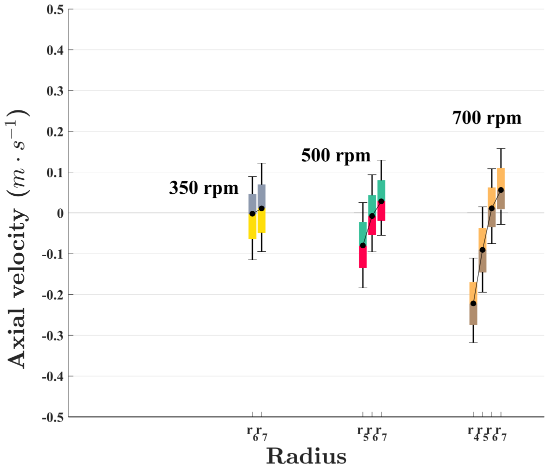	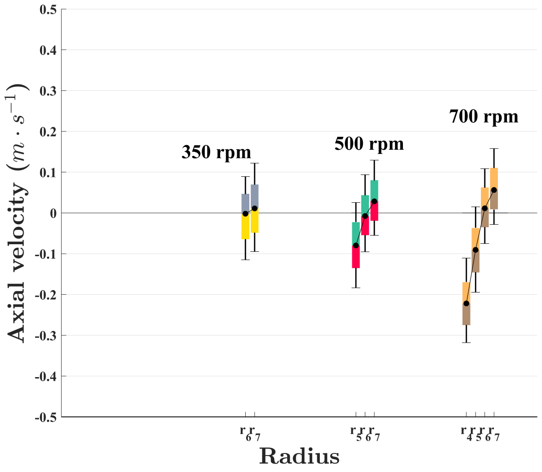
		r_0 = 0.81 cm r_1 = 2.44 cm r_2 = 4.06 cm r_3 = 5.69 cm r_4 = 7.32 cm r_5 = 8.95 cm r_6 = 10.58 cm r_7 = 12.21 cm

Figure 51: Axial velocity distributions of large and small particles at different regions relative to the impeller

Impeller region	Small particles	Large particles
First top region	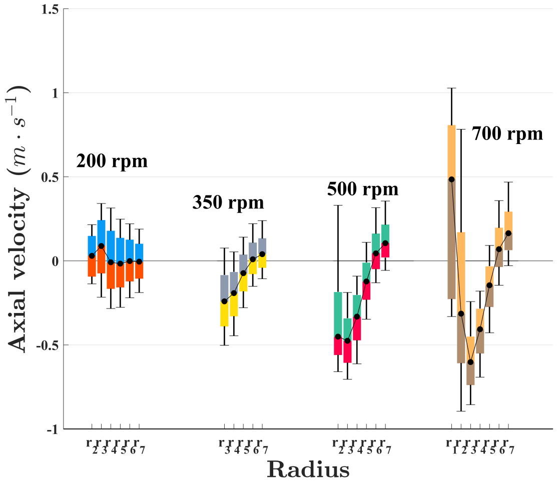	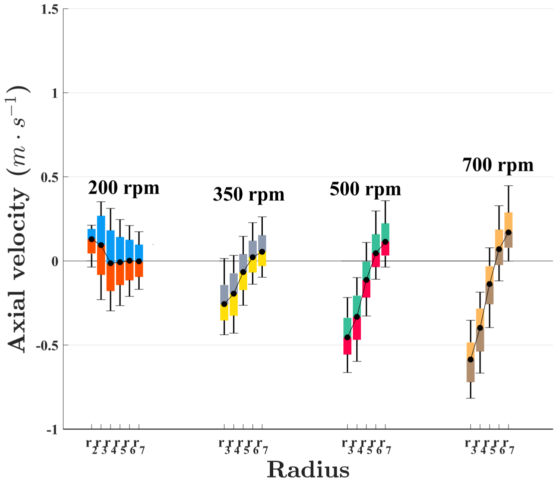 r_0 = 0.81 cm r_1 = 2.44 cm r_2 = 4.06 cm r_3 = 5.69 cm r_4 = 7.32 cm r_5 = 8.95 cm r_6 = 10.58 cm r_7 = 12.21 cm

Figure 52: Axial velocity distributions of large and small particles at different regions relative to the impeller

Impeller region	Small particles	Large particles
Top pin	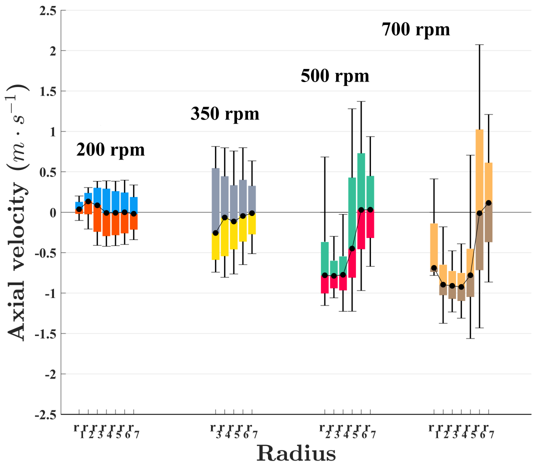	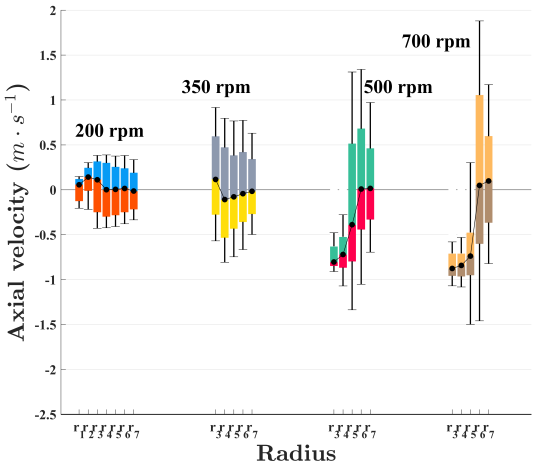 r_0 = 0.81 cm r_1 = 2.44 cm r_2 = 4.06 cm r_3 = 5.69 cm r_4 = 7.32 cm r_5 = 8.95 cm r_6 = 10.58 cm r_7 = 12.21 cm

Figure 53: Axial velocity distributions of large and small particles at different regions relative to the impeller

Impeller region	Small particles	Large particles
Bottom pin	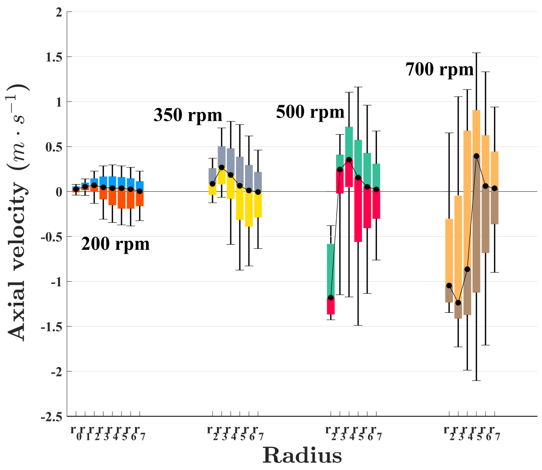	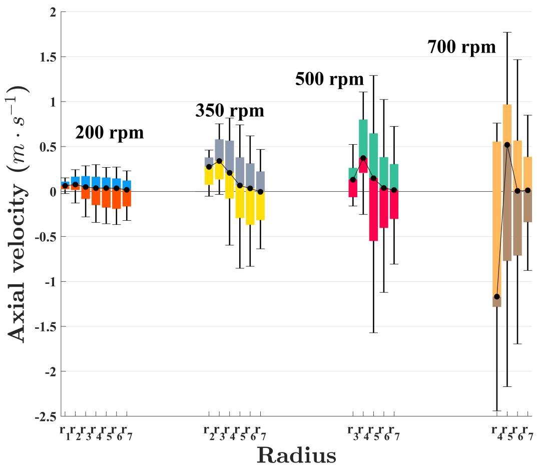 r_0 = 0.81 cm r_1 = 2.44 cm r_2 = 4.06 cm r_3 = 5.69 cm r_4 = 7.32 cm r_5 = 8.95 cm r_6 = 10.58 cm r_7 = 12.21 cm

The 700 rpm axial values for the top and bottom pin are incredibly sporadic, varying a lot while having a large range of values. Due the speed of 700 rpm, a large portion of the particles are centrifuged outwards. This gives rise to the increased range of axial velocities for the 700 rpm near the radial end. The increased impeller speed near the radial end promotes upwards motion of particles. Something similiar can also be seen for the 500 rpm with the increased range of axial values near the end of the impeller. The overall range of values for 500 rpm and 700 rpm indicates turbulent conditions.

In Figure 54 the axial velocity for the large and small particles for the bottom region is shown. For 200 rpm and 350 rpm the median axial remains close to zero whilst the Q1 and Q3 values remain equivalent, indicating a steady inflow and outflow of particles. For 500 rpm and 700 rpm the initial values between r$_0$ = 0.81 cm and r$_2$ = 4.06 cm remain close to zero, indicating particles that do not centrifuge outwards and participate in collisions. The maximum axial values are at r$_4$ = 7.32 cm where the particles transition from an upwards motion to a downwards motion in the quiver plot. Turbulent flow can be seen here, with the large range of axial velocities and varying median line. Thus, results in worthwhile collisions are facilitated.

Figure 54: Axial velocity distributions of large and small particles at different regions relative to the impeller

Impeller region	Small particles	Large particles
Bottom region	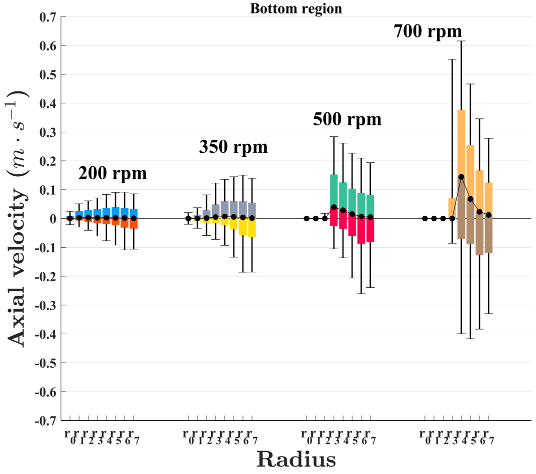	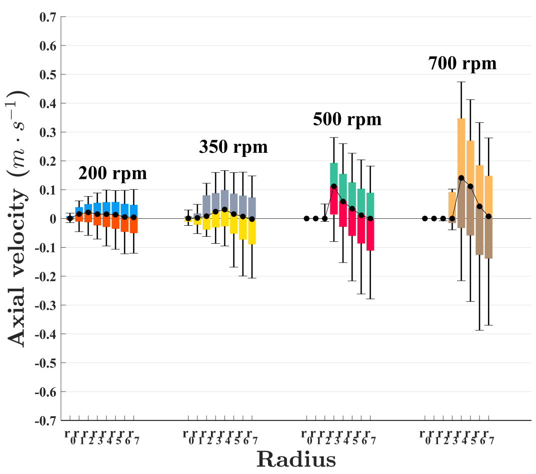
		r_0 = 0.81 cm r_1 = 2.44 cm r_2 = 4.06 cm r_3 = 5.69 cm r_4 = 7.32 cm r_5 = 8.95 cm r_6 = 10.58 cm r_7 = 12.21 cm

4.2.7 Subsection summary

In Section 4.2 the influence of the impeller speed on the particle motions and collisions was investigated. In the simulations the particles were susceptible to the *Brazilian nut effect* which reduced particle mixing and consequently collisions. Excessive impeller rotation speeds did not substantially benefit the particle-particle collision modulii as past 700 rpm the collision modulii for the particle-particle collision plateaued. Different impeller speeds, below 700 rpm, facilitated increased collision modulii for select particle-particle collisions. Additionally, regions of interest along the impeller radii were discussed.

4.3 Particle distribution influence on grinding performance

4.3.1 Initial setup

In this section the weight distribution of the 8 mm and 5 mm particles is varied to evaluate the grind characteristics. The percentage distribution, shown in the legend of Figure 55, indicates what weight percentage of the particles are 5 mm. The grinding characteristics were evaluated at 350 rpm. This impeller speed allowed for suitable collision modulii to be established with reduced particle segregation, compared to the higher impeller speeds.

The particle populations were spawned with the same normal deviations estimated in Section 4.2. For the 5 mm particle population the standard deviation was set to 69.19 μm. For the 8 mm particle population the standard deviation was set to 35.14 μm. A total of 6.5 kg was spawned for all systems.

In the following singular particle simulations, 2.00 seconds was dedicated to particle spawning and 1.00 second was dedicated to impeller acceleration. Afterwards 4.50 seconds of simulation time was dedicated for a steady state to be established. A total simulation duration of 6.50 seconds was facilitated for each system.

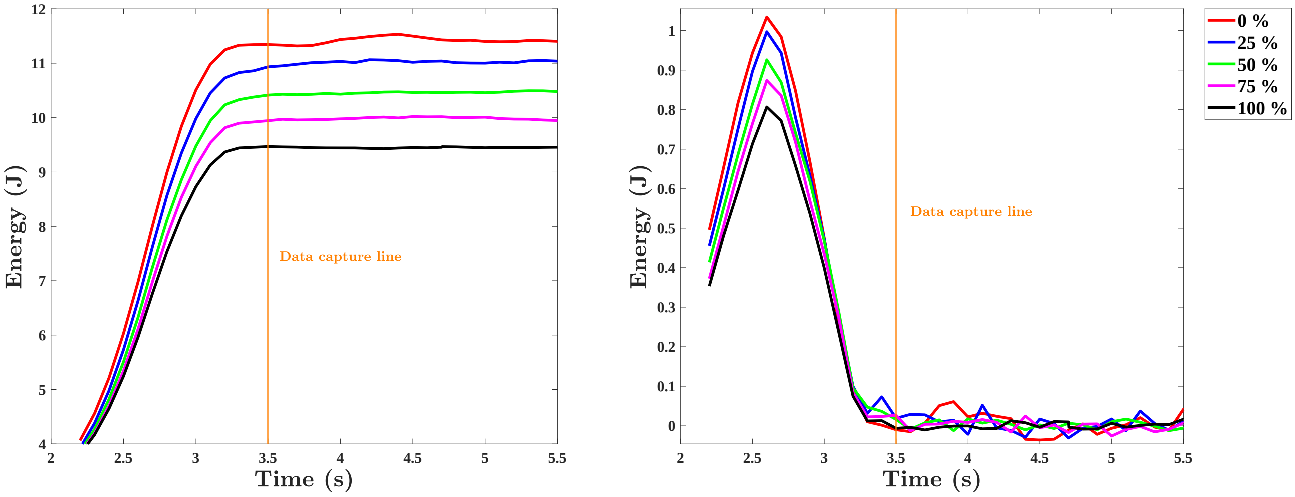

(a) Particle mechanical energy **(b)** Change in particle mechanical energy

Figure 55: Resulting particle mechanical energy

The total mechanical energy and change in total mechanical energy of the particulate system is shown in Figure 55. Any data discussed or plotted moving forward, without explicit time stamps, will be captured between t = 3.50 s and t = 5.50 s, as this is when steady state has been attained.

The 100 wt% 8 mm particles have the highest total mechanical energy. This is likely due to the impellers more effectively imparting energy onto the particles, as well as their size and collection near the impeller pins.

The 5 mm particles are more flowable than the 8 mm particles, which in turns facilitates a ”cushioning” effect where the smaller particles further dissipates energy that in turn dampens collisions. Furthermore, the increased flowability of the smaller particles allow for the particles to collect or occupy spaces that do not interact with the impellers. This in turn reduces the amount of energy imparted onto the particles from the impeller pins.

4.3.2 Collision spectra

Table 17 shows the range of collision energy loss values of the different weight distributions at 350 rpm. The addition of smaller particles further dampens the total range of collision energy loss values. This can be seen with both the reduction in median values, as well as the percentile values of the total energy loss values.

Table 17: Range of collision intensities and total energy draw of different weight distributions of 5 mm and 8 mm particles at 350 rpm and 6.5 kg

Weight % 5 mm particles	Median total collision energy loss	5^{th} percentile total collision energy loss	95^{th} percentile total collision intensity (J)
0 %	2.26 μJ	85.24 nJ	53.30 μJ
25 %	638.62 nJ	16.68 nJ	21.49 μJ
50 %	309.10 nJ	9.05 nJ	10.75 μJ
75 %	183.14 nJ	6.10 nJ	6.25 μJ
100 %	130.12 nJ	4.85 nJ	3.96 μJ

The collision modulus plots are shown in Figure 56. The logarithmic mean of the collision modulus of 15 revolutions is plotted in Figures 56. The mode collision values of the first 15 revolutions used can be found in Appendix A.7.

Increasing the quantity of smaller particles present in the system further reduces the overall modal peaks of particle-particle collisions. This can be seen in Figures 56a through to 56e where the collision modulus is inversely proportionate to the weight percentage of 5 mm particles. Increasing the quantity of smaller particles increases the amount of collisions. This relationship is shown in Equation 21. With increased particles the amount of energy dissipated and lost with each collision results in a cushioning effect being promoted. The loss of energy further reduces the amount of energy the particles can use to effectively grind.

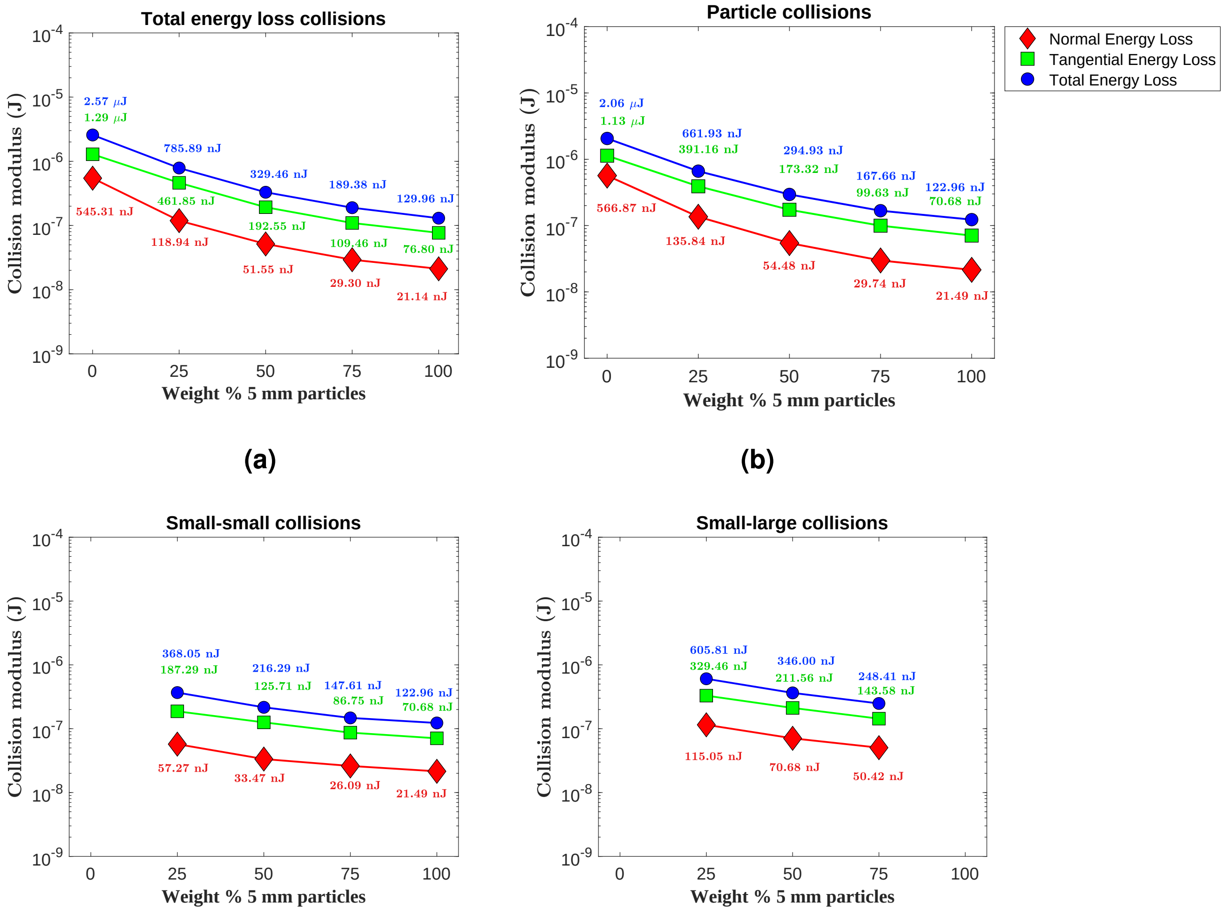

(a)

(b)

(c)

(d)

Figure 56: Modal peaks of collision data of (a) total collisions, (b) total particle collisions, (c) small-small particle collisions, (d) small-large particle collisions, (e) large-large particle collisions and (f) environmental collisions (impeller + grinding chamber collisions)

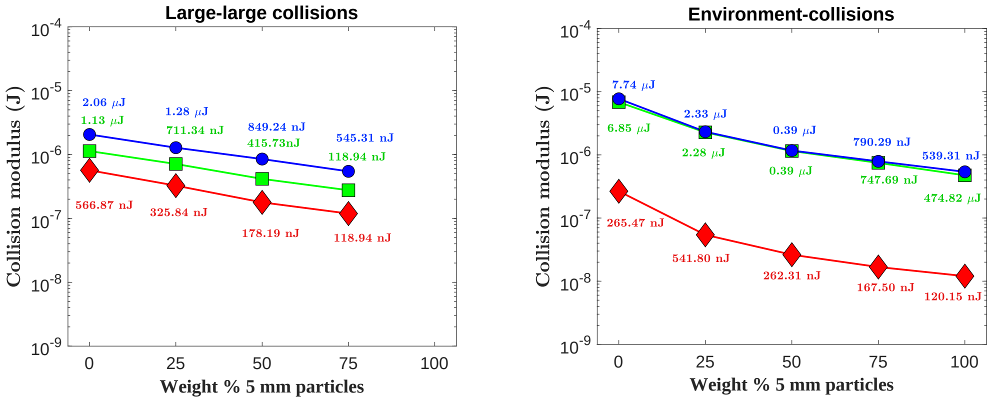

(e)

(f)

Figure 56: Modal peaks of collision data of (a) total collisions, (b) total particle collisions, (c) small-small particle collisions, (d) small-large particle collisions, (e) large-large particle collisions and (f) environmental collisions (impeller + grinding chamber collisions)(continued)

The addition of smaller particles reduces both the normal and tangential energy loss of collisions, and in turn the normal and tangential forces of collisions. The reduction in values further reduces the total energy loss and force. A decrease in the modal collision intensity indicates reduction of a big portion of collision intensities below the mode value. This is due to the logarithmic distribution of collision values. The rate at which the addition of smaller particles reduces the overall collision energy loss mode is non-linear. Furthermore, the total collision energy loss is dictated by tangential energy loss. This is true for the total collisions, shown in Figure 56a, as well as the overall particle-particle collisions shown in Figure 56b.

For the small-small particle collisions, shown in Figure 56c, the maximum collision intensities are achieved at 25 weight % of 5 mm particles. This is likely due to the dominance of the 8 mm particles, that have increased the total- and kinetic-energy, allowing for increased transfer of kinetic energy to the smaller particles. The increased total energy of the 8 mm particles can be seen in Figure 55a. It should be noted that the reduction of particle collision modes between 75 wt% and 100 wt% is less than the reductions between 25 wt% and 50 wt% and 50 wt% and 75 wt%. With this in mind, the addition of smaller particles past the 75 wt% mark does not result in any worthwhile increase or reduction of collision intensities.

The small-large particle collisions are depicted in Figure 56d. The addition of smaller particles reduces the small-large mode collision intensity. The intensity of the small-large energy loss is less than the large-large collisions and more than the small-small particle collisions.

The large-large particle collision intensities can be seen in Figure 56e. Similarly to the remainder of the particle collisions, the addition of smaller particles further dampens the large-large particle collision intensities.

The particle environmental collisions are shown in Figure 56f. The environmental modal collisions are dominated by tangential energy losses, which is similiar to the impeller speed tests in Section 4.2. Increasing the amount of smaller particles reduces the mode. This is due to the addition of smaller particles resulting in increased collisions, which in turn dissipates more of the available energy.

4.3.3 Particle energy dissipation

To evaluate the energy interactions with the different weight distributions, the total energy loss relative to the particles mass was analysed. The method used for this estimation is shown in Equation 37. The total energy loss estimated all energy involving all collisions of the relevant particle. This includes particle-particle collisions as well as particle-environmental collisions. The environmental collisions involves both the impeller and grinding chamber.

A collection of energy loss values between t = 3.50 s and t = 6.50 s, with a time step of t = 0.10 s, was used to estimate the ratio of energy loss relative to the mass. The resulting mean values, Θ, as well as the variances of the ratios are shown in Table 18. The resulting mean values are further illustrated in Figure 57. The data was captured at an impeller speed of 350 rpm.

$$\Theta = \frac{\sum_i^n Tot_{E,loss,i}}{\sum_i^n m_i} \tag{37}$$

Increasing the amount of smaller particles reduced the Θ ratio for the total particles. Furthermore, it appears that the amount of collision energy that the particles dissipate relative to their mass is inversely proportional to fraction of particles present in the system. This can be seen in Figure 57 where the maximum Θ ratios for the small and large particles are present when the particles are the least in the system.

Table 18: Values and variance of the Θ ratio's illustrated in Figure 57

Weight % 5 mm particles	0	25	50	75	100
	Total particles ($\mathrm{J \cdot kg^{-1}}$)				
Mean (μ)	7.509	7.713	7.284	6.806	5.852
Variance (σ)	0.149	0.122	0.080	0.092	0.040
	5 mm particles ($\mathrm{J \cdot kg^{-1}}$)				
Mean (μ)		10.024	8.730	7.333	5.852
Variance (σ)		0.474	0.218	0.132	0.040
	8 mm particles ($\mathrm{J \cdot kg^{-1}}$)				
Mean (μ)	7.509	8.635	8.750	8.835	
Variance (σ)	0.149	0.177	0.206	0.418	

In Figure 57 the highest value for the 8-mm Θ ratio is estimated at 75 wt% 5-mm particles. For the 5-mm Θ the maximum ratio is estimated at 25 wt% 5-mm particles. The high values are due to the non-linear nature of ratio of Θ in Equation 37. The rate at which the total energy loss scales, relative to the total mass of particles, is inversely proportionate as well as non-linear. The amount of energy a single particle can dissipate through collisions is reduced with more particles, as each collision dissipates energy. With more particles there are more collisions, this relationship is shown in Equation 20. However, the intensity of subsequent collisions after an initial particle collision is reduced compared to the initial intense collision. Thus, the additional particles do not scale adequately with collision energy loss intensities.

For the total particle Θ the maximum value is estimated at 25 wt% 5-mm particles.The 25 wt% exchange of 8-mm particles for 5-mm particles did not drastically dampen the collision energy loss of the larger Θ ratio. The smaller particles are more mobile and can more easily disperse throughout the system. This hindered the particles from clustering together and further dissipating the available collision energies.

It appears that a good particle weight distribution would be in favor of the larger particles. Between 0 wt% 5-mm particles and 50 wt% 5-mm particles. Between these weight distribution values is when the total- and small-Θ ratios are maximised. With more larger particles in a stirred mill the particles will be able to more effectively impart energy onto the limited smaller particles. This would result in more intense collisions for the small-small particles collisions. The increased values for the total energy loss and individual particles can be seen in Figure 57.

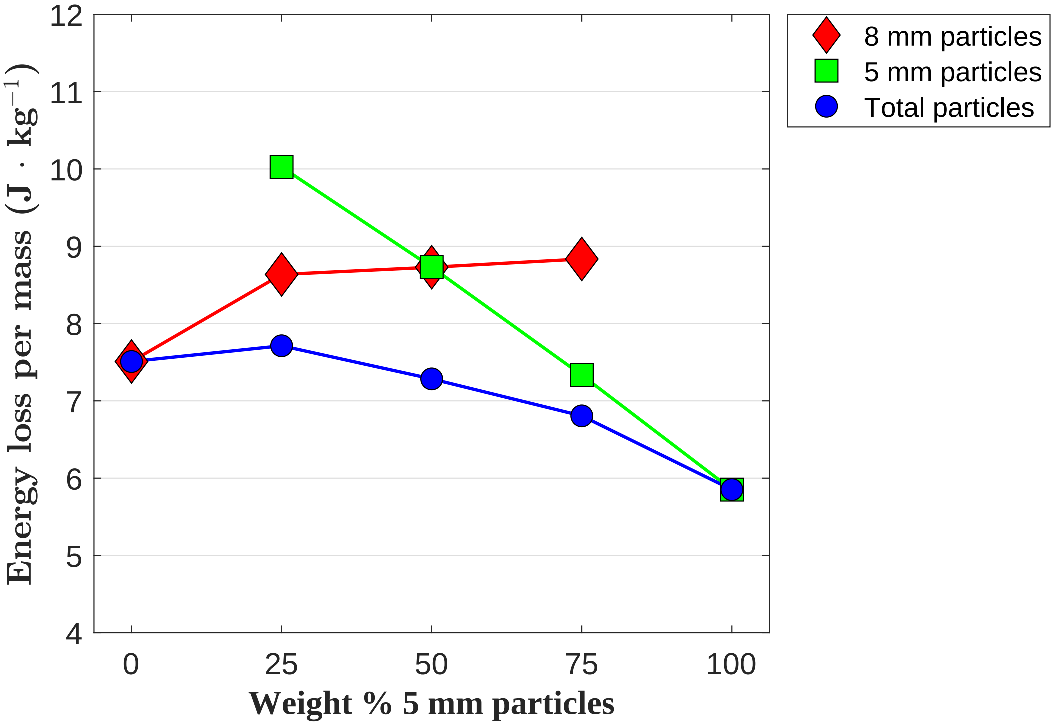

Figure 57: Energy loss relative to the weight distribution of the system at 350 rpm impeller speed

4.3.4 Subsection summary

In Section 4.3 the collision modulii of different particle weight distributions were evaluated. The addition of smaller particles reduced the collision modulii for all particle-particle collisions and collision types. However, the addition of smaller particles did slightly increase the total energy used for collision at 25 wt% 5 mm particles. Beyond the 25 wt% 5 mm particles the total energy used for collisions decreased.

4.4 Further particle segregation

4.4.1 Initial setup

To further investigate the tendency of particle segregation another simulation with 3 different particle sizes was conducted. First two particle sizes were the aforementioned 5-mm and 8-mm particles with their respective deviations of 69.19 μm and 35.14 μm. An additional third particle size of 3 mm was introduced with a deviation of 54.64 μm. The deviation was estimated from the average percentage deviation of the prior two particle sizes, relative to their radii.

To compare the degree of segregation of the 8 mm and 5 mm particles, the relative standard deviation (RSD) of particle spacial occupations, of different systems are compared to one another. The RSD is estimated by dividing sample standard deviation shown in Equation 29, σ, with the average of the measured value.

$$RSD = \frac{\sqrt{\frac{\sum_i^n (x_i - \bar{x})^2}{n-1}}}{\bar{x}} = \frac{\sigma}{\bar{x}} \tag{38}$$

The RSD is used as the indication of mixing in Arratia et al. (2006). A lower RSD indicates a system where the relevant particles are evenly distributed where they are present. A high RSD is due to a high sample standard deviation, σ, which indicates increased particle separation or accumulation throughout the occupied spaces.

For the purposes of comparing the particle separation of the 3 particles system to other particle systems, the mean of the average particle concentrations estimated at steady state with the box counting method, is used for the overall mean of the system. This ensures that the system is normalised, as they are not directly comparable with one another with different amounts of particles, sizes and weight distributions.

For the evaluated 3-particle sized system, an impeller speed of 350 rpm was used. A total mass of 6.5 kg was spawned into the set simulation. The weight distribution consisted of 33.33 wt % 3-mm particles, 33.33 wt % 5-mm particles with the remainder weight percentage being 8-mm particles. The mixing degree of different particle weight distributions, simulated in Section 4.3 is estimated and evaluated in the following section.

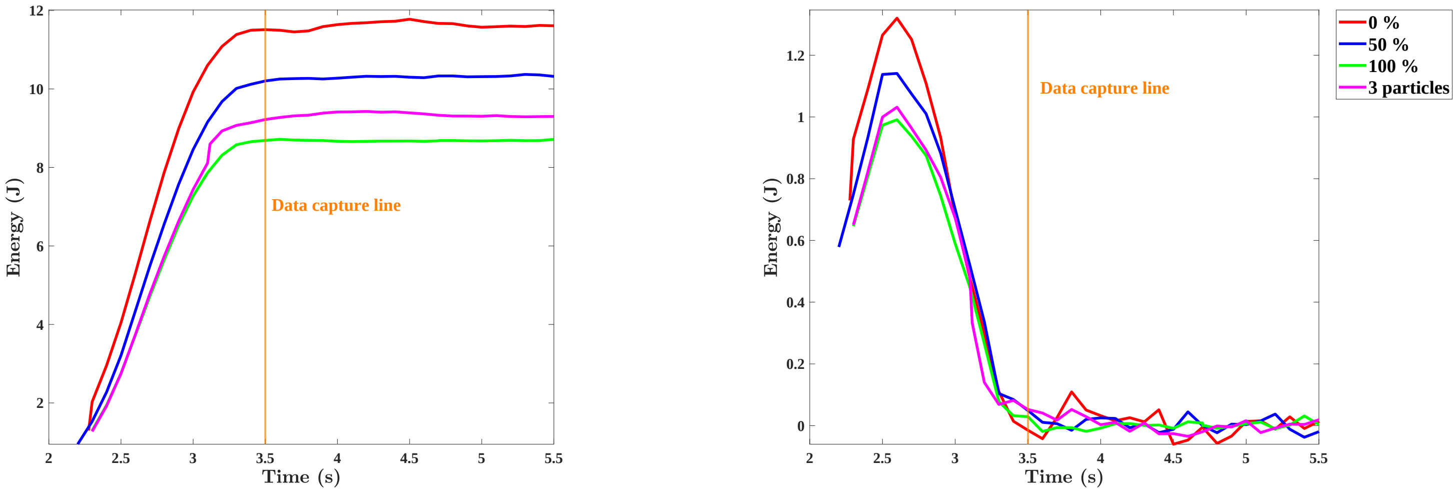

(a) Particle mechanical energy

(b) Change in particle mechanical energy

Figure 58: Resulting particle mechanical energy

The total particle mechanical energy, and change of mechanical energy, is illustrated in Figure 58. Steady state is properly established at 3.50 s. Thus, the average particle concentration was estimated using time values above t =3.50 s after steady state was achieved. The time frame for data capturing for the analysis in this section was defaulted to t = 3.50 s and t = 6.50 s. Any deviation from the default time frame is declared.

4.4.2 Degrees and tendencies of particle separation

Figure 59a, Figure 59b and Figure 59c show the relative particle spacial occupations by the 8 mm, 5 mm and 3 mm particles, respectively.

The 8 mm particles tended to dominate the space above the top impeller near the wall of the mill. This can be seen with the concentrated red and orange regions in Figure 59a. The 8 mm particles are well distributed throughout bulk media. This can be seen in the green regions surrounding the concentrated red regions in Figure 59a.

The 5 mm particles were dominantly near the grinding chamber wall which had some overlap with the 8 mm particles. This can be seen with the red and orange regions in Figure 59b. The introduction of the 3 mm particle reduced the available space that the 5 mm particle could occupy.

With the reduction of available space, the 5 mm particles tended to occupy he edges of the container. Furthermore, the 5 mm particles are reasonably distributed throughout the system. This can be seen with the consistent green regions occupying the available spaces throughout the bulk media.

The 3 mm particles did not show any areas of dominance and may have been distributed in all active regions with some high concentrations near the top along the wall of the active region and at the bottom area that doesn't experience fluidisation (Ndimande et al. 2019). The spacial occupation of the 3 mm particle is similiar to the particle spacial occupation of the 5 mm particles in Figure 33.

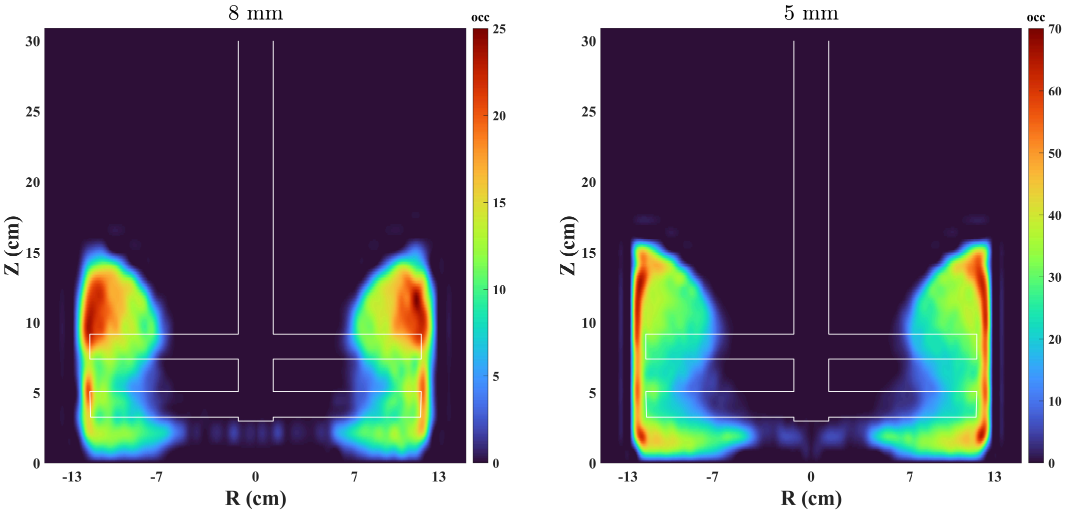

(a) **(b)**

Figure 59: Particle occupation profiles of 3 different particle sizes at 350 rpm time averaged between t = 3.50 s and t = 6.50 s

The 3 mm particle was susceptible to the *Reverse brazilian nut effect*, mentioned in Section 4.1.5. Smaller particles have improved flowability compared to larger particles. It requires less energy to move a small light particle compared to a large particles. This is owing to the inertia of the particles, and in turn their mass. The improved flowability of smaller particles allowed it to more effectively disperse towards the select regions, becoming the particle that collected atop the particulate media.

Thus, when the agitation speed is increased the lighter particles, in this case the 3 mm particle, experienced the *Reverse brazilian nut effect* (Breu et al. 2003; Garzó 2008).

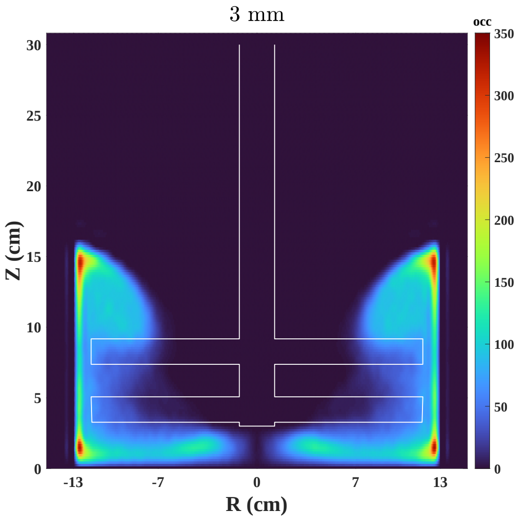

(c)

Figure 59: Particle occupation profiles of 3 different particle sizes at 350 rpm time averaged between t = 3.50 s and t = 6.50 s

In Figures 60 and 61 the percentage population occupation of the 8 mm and 5 mm particles are plotted. The figures depict the population percentage of a specific sized particle at a point in space. The percentage particle population, ϕ, is estimated using the number of particles at a specific point in space, N, of a specific particle size using Equation 39. The method by which particles spaces were estimated in Figures 60 and 61 is discussed at the end of Section 3.4.1. The particle weight distributions evaluated were sourced from the different weight distributions in Section 4.3.

$$\phi = \frac{N}{\sum N} \times 100.00\ \% \tag{39}$$

In Figure 60 the percentage occupation of the 8 mm is shown. At 100 wt % 8-mm, as shown in Figure 60a the particles are reasonably distributed throughout the system. A portion of the 8-mm particles occupied at the edges of the container. The collection of particles at the chamber edges is not present at 75 wt % 8-mm as shown in Figure 60b.

At 50 wt % the 8-mm particles are reasonably distributed throughout the system. A portion of the 8-mm particles tended to occupy the areas above and below the impeller pins in Figure 60c. This is shown by the slight yellow tinge above and below the impeller pins in Figure 60c. The collection of particles above and below the pins is further increased at 25 wt % 8-mm. This can be seen with the orange regions in Figure 60d.

The maximum collection of 8-mm particles is shown in Figure 60e with the 3-particle simulation. The addition of the smaller particle changes the dynamics and particle spatial occupations of the system. A large portion of the 5-mm particles tended to collect at the edges of the container. Due to this the larger 8-mm particle is unable to occupy the edge spaces. The 3-mm and 5-mm particles are distributed throughout the system. As such the smaller particles hinder movement for the 8-mm particles. Thus, the larger particles tended to clump together above, or at, the impeller pin ends.

In Figure 61 the percentage occupation of the 5 mm particles is shown. As the wt% of 5 mm particles is decreased, so too did the degree to which the particles tended to segregate increase. Similar trends to those discussed in the previous paragraphs are observed.

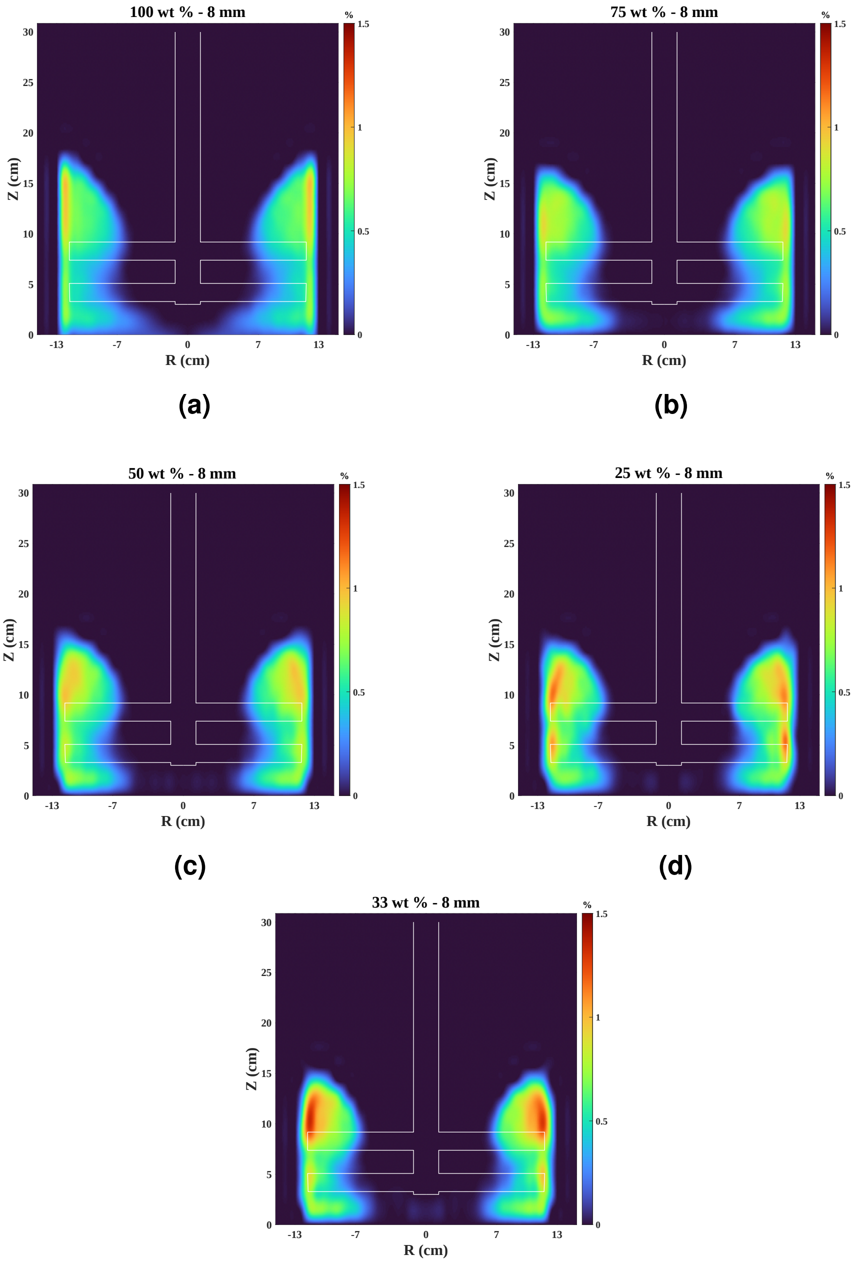

(a) (b)

(c) (d)

(e) [c]

Figure 60: The time averaged particle percentage occupation of the 8-mm particles at different weight distributions between t = 4.00 s and t = 6.50 s

---

[c] Note that the 3-particle system is not directly comparable to the other wt % systems. The wt % systems only contain 2 particles. The addition of another particle had shifted the particle occupations and dynamics.

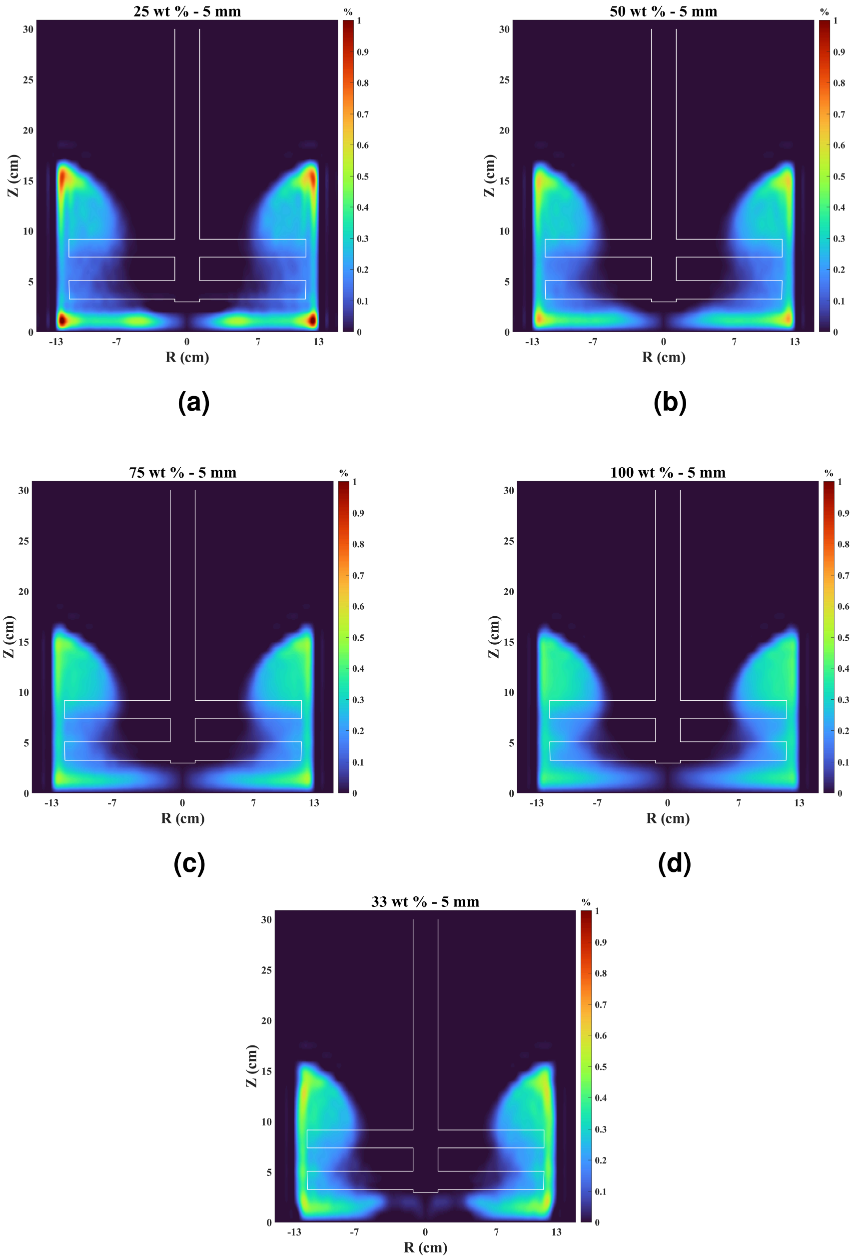

(a)

(b)

(c)

(d)

(e) c

Figure 61: The time averaged particle percentage occupation of the 5-mm particles at different weight distributions between t = 4.00 s and t = 6.50 s

The RSD values for different particle distributions are shown in Figure 62. Higher RSD values indicate increased particle segregation. Increased segregation indicates particles that are not properly mixed and dispersed throughout the bulk media.

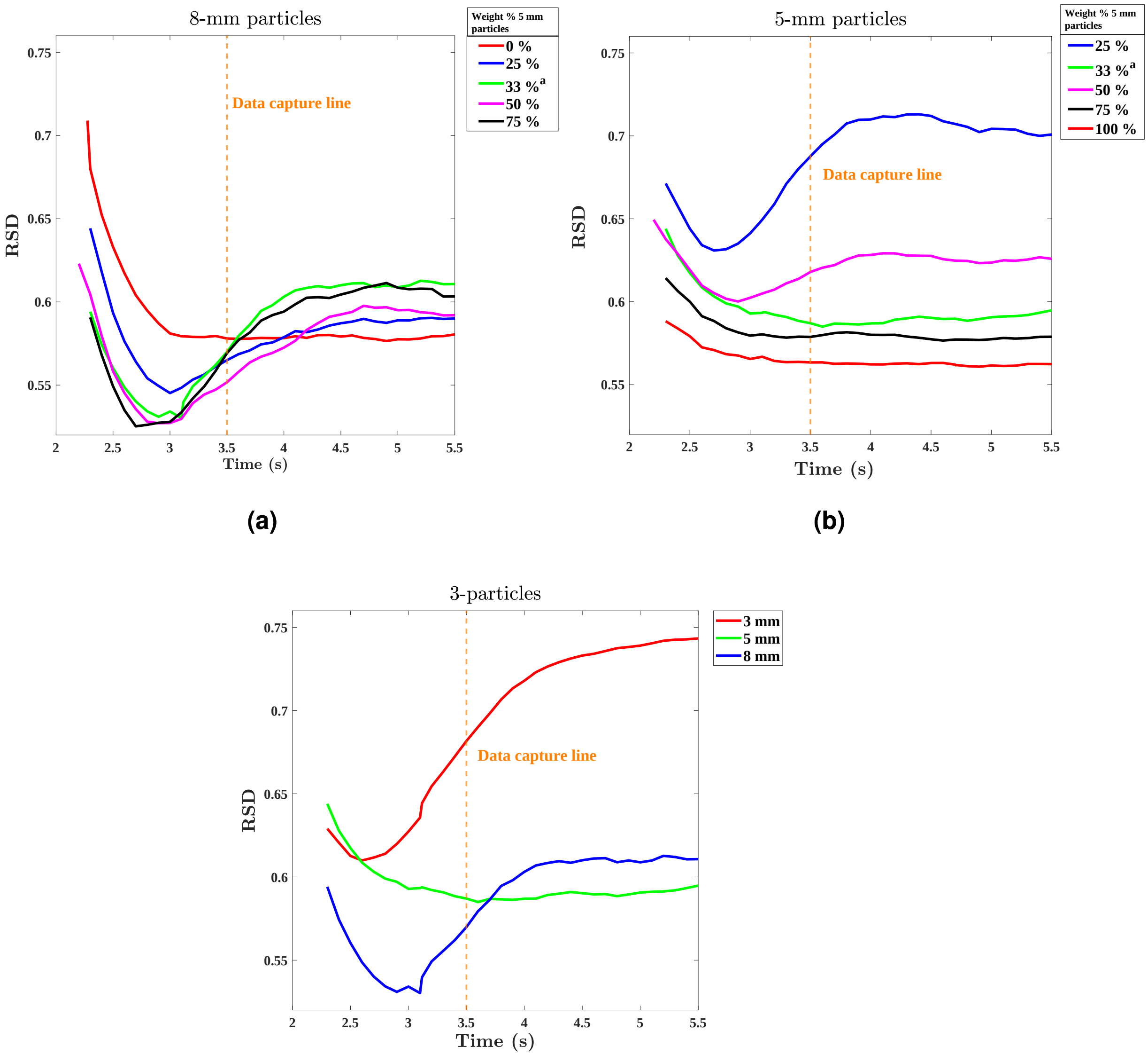

(a)

(b)

(c)

Figure 62: RSD values of particles with different weight distributions at an impeller rotation speed of 350 rpm

For the 3 particle system, shown in Figure 62c, it can be seen that the lighter 3 mm particle experienced the highest degree of particle segregation. This is then followed by the 8 mm and 5 mm particles.

The degree to which the 8 mm particle experienced segregation does not change drastically under different weight distributions. This can be seen in Figure 62a where the all the RSD$_{8mm}$ values stabilised around a value of 0.60. Thus, the degree to which the larger particle experience segregation does not drastically change. The reason for its tendencies could be that there is no sufficient alternative particle or media in the system that can properly displace and occupy it's space. The 8 mm particles can be considered the dominant particle in the system, shaping the flow collisions and, in turn, particles.

Compared to the 8 mm particles, the 5 mm particles experienced varying degrees of particle segregation. At lower concentrations the particles increased particle segregation. This can be seen in Figure 62 where the lower concentration of particles had increased RSD values. At a lower particle weight percentage, any tendencies of the particles to clump together or further disperse throughout the bulk media is emphasised, owing to how the RSD is estimated in Equation 38. As the amount of 5 mm particles increases, so too does the spaces the particles can occupy and saturate. This leads to situations where there is few significant deviations present in the particle concentration throughout the systems space. Thus, at lower weight distributions the particle experienced increased particle segregation.

In the 3-particle simulated system the 8-mm particles experienced increased separation compared to the 5-mm particles. This is shown in the RSD values for the 5-mm being lower than the 8-mm particles in Figure 62c. This is a consequence of how the RSD values is estimated using Equation 38. Any particle spacial occupations and deviations experienced in a lower particle population would be more significant than a larger particle population using Equation 38. Thus, the RSD$_{8mm}$ value is larger than the RSD$_{5mm}$ value, indicating reduced particle mixing.

The fewer particles there are of a certain species the more likely these particles are to experience increased separation by either clumping up together or not properly dispersing throughout the grinding system. This was observed in Figure 60 and 61, as well as the RSD estimations in Figure 62. The lighter particles of the system experience increased separation as opposed to the larger particles. This was observed in the RSD estimations of Figure 62. The larger particles tended to occupy the spaces above or below the impeller pin ends, not deviating drastically under different circumstances. It is likely that the larger particles would follow similar trends observed for the 5 mm particles, should a more dominant or heavier particle be introduced that contests the 8 mm particle.

4.4.3 Subsection summary

In Section 4.4 an additional simulation with 3 particle sizes was performed. Furthermore, the particle spatial distribution for different particle weight distributions was shown. It was observed that the lighter particle, at an elevated impeller speed, would be the most susceptible to the *Brazilian nut effect*. Additionally, the larger particles degree of mixing remained consistent at different weight distributions. The addition of the smaller particle did not significantly change its RSD value.

5 Conclusions and observations

The following observations were made:

- The size-mixed grinding media in a vertical stirred mill is susceptible to the *Brazilian nut effect*. At a lower impeller rotation speed the larger particles occupied the top region of the bulk media. At higher impeller rotation speeds, where the particles were fluidised, smaller particles occupied the top region of the bulk media. This further reduced the degree of particle mixing.
- Increased impeller rotation speeds, for a vertical stirred mill, did not substantially improve the collision modulii of the system. Instead the particle-particle collision modulii would tend to plateau after exceeding an impeller speed of 700 rpm.
- Furthermore, increasing the impeller rotation speed further increased both the range of collision values as well as the degree of particle segregation.
- The impeller speed that facilitated the maximum collision modulii for large-large and small-large collisions was facilitated at 350 rpm. The maximum collision modulii for small-small particle collisions was facilitated at 500 rpm.
- The addition of smaller particles reduced the overall collision modulus for all the particle-particle collision modulii. The addition of smaller particles further reduced the total energy used for collisions past the 25 wt% 5 mm particles .

Based on the aforementioned observations, the following conclusions were made with regards to the hypotheses:

1. With regards to the first hypothesis the high degree of particle mixing did not facilitate a maximised collision modulus. This disproves the initial hypothesis. The Optimal grinding was facilitated with a balance and trade-off between collision ranges, intensities and degree of particle mixing. The systems with intermediate mixing degrees, 350 rpm and 500 rpm, resulted in the maximised collision modulii.

2. With regards to the second hypothesis the optimal impeller rotation speed was verified. The impeller rotation speed of 350 rpm favoured small-large and large-large particle collision modulii. The impeller rotation speed of 500 rpm resulted in the maximum collision modulii for small-small particle collisions. Excessive impeller rotation speeds did not result in improved collision modulii. No one specific impeller speed maximised all the particle-particle collision modulii.
3. With regards to the third hypothesis the optimal size-mixed particle weight distribution was in favor of the larger particles. Increasing the weight percentage of smaller 5 mm particles beyond 25 % reduced the available energy applied to collisions. The addition of the smaller particle further reduced the overall collision modulii for a multitude of particle-particle collisions.

Based on the aforementioned conclusions, the following may be inferred for a grinding media's lifetime: as a new grinding media is introduced into a system, initial effective grinding action will be facilitated. As time continues, so too does the grinding media experience wear and tear, reducing grinding performance. As a consequence to the wear of media, the particles sizes are reduced. In turn larger objects or ores require more energy to break. A consequences of the smaller particles is that it would be more susceptible to segregation, further affecting grinding action.

If new grinding media is added to the system, and the size disparity is significant enough, new dynamics of a size-mixed grinding system can be expected. A specific consequence for such a system would be the introduction, or promotion, of the *Brazilian nut effect*. If a new impeller speed is facilitated, that reduces the consequence of the *Brazilian nut effect*, finer ore may be produced. The resulting weight distribution for effective breakage rates should be in favor of the larger, newer particles for improved grinding action.

5.1 Recommendations

The work done in this thesis made an exploratory attempt to evaluate if segregation occurs in a system with different sized particles. However, a more structured study with a wider range of particles sizes is recommended to further evaluate the extent of the effect and the implication on energy utilisation in such a system

Furthermore, the investigation of size-segregated media can be further expanded by introducing fluids and different sized media to the simulated systems. An increased variety of different sized particles in the system can lead to improved results, conclusions and tendencies to be evaluated. New phenomena or results may be observed when different grinding media materials are used in a mill.

Additionally, spherical particles are not the norm in industry, thus the mixing and collision tendencies of non-spherical, size-segregated, grinding media can be investigated with the methods presented in this thesis.

References

(2023). What are the system requirements for running edem?

Antonyuk, S., Khanal, M., Tomas, J., Heinrich, S., and Mörl, L. (2006). Impact breakage of spherical granules: experimental study and dem simulation. *Chemical Engineering and Processing: Process Intensification*, 45(10):838–856.

Arratia, P., Duong, N.-h., Muzzio, F., Godbole, P., and Reynolds, S. (2006). A study of the mixing and segregation mechanisms in the bohle tote blender via dem simulations. *Powder technology*, 164(1):50–57.

AZOMaterials (2022). Aisi 4140 alloy steel (uns g41400).

Barrett, J. F. and Keat, N. (2004). Artifacts in ct: recognition and avoidance. *Radiographics*, 24(6):1679–1691.

Bayel, D. K. (2019). The effect of grinding media performance on wet milling of calcite. *Selçuk Üniversitesi Mühendislik, Bilim Ve Teknoloji Dergisi*, 7(2):379–386.

Becker, M. and Schwedes, J. (1999). Comminution of ceramics in stirred media mills and wear of grinding beads. *Powder Technology*, 105(1-3):374–381.

Beinert, S., Fragniere, G., Schilde, C., and Kwade, A. (2015). Analysis and modelling of bead contacts in wet-operating stirred media and planetary ball mills with cfd–dem simulations. *Chemical Engineering Science*, 134:648–662.

Bilgili, E., Hamey, R., and Scarlett, B. (2004). Production of pigment nanoparticles using a wet stirred mill with polymeric media. *China Particuology*, 2(3):93–100.

Boikov, A., Savelev, R., and Payor, V. (2018). Dem calibration approach: Implementing contact model. In *Journal of Physics: Conference Series*, volume 1050, page 012014. IOP Publishing.

Bremner, S. (2016). A granular flow model of an annular shear cell.

Breu, A. P., Ensner, H.-M., Kruelle, C. A., and Rehberg, I. (2003). Reversing the brazil-nut effect: competition between percolation and condensation. *Physical review letters*, 90(1):014302.

Campbell, H. and Bauer, W. (1966). Cause and cure of demixing in solid-solid mixers. *Chem. Eng*, 73(19):129.

Cho, H., Waters, M., and Hogg, R. (1996). Investigation of the grind limit in stirred-media milling. *International Journal of Mineral Processing*, 44:607–615.

Cleary, P. W. (2004). Large scale industrial dem modelling. *Engineering Computations*.

Cleary, P. W., Sinnott, M., and Morrison, R. (2006). Analysis of stirred mill performance using dem simulation: Part 2–coherent flow structures, liner stress and wear, mixing and transport. *Minerals Engineering*, 19(15):1551–1572.

Cloos, U. (1983). Cylpebs: An alternative to balls as grinding media. *World Min.*, 36(10):59.

Cundall, P. A. and Strack, O. D. (1979). A discrete numerical model for granular assemblies. *geotechnique*, 29(1):47–65.

Ding, Y., Forster, R., Seville, J., and Parker, D. (2001a). Scaling relationships for rotating drums. *Chemical engineering science*, 56(12):3737–3750.

Ding, Y., Forster, R., Seville, J., and Parker, D. (2002). Segregation of granular flow in the transverse plane of a rolling mode rotating drum. *International Journal of Multiphase Flow*, 28(4):635–663.

Ding, Y., Seville, J., Forster, R., and Parker, D. (2001b). Solids motion in rolling mode rotating drums operated at low to medium rotational speeds. *Chemical Engineering Science*, 56(5):1769–1780.

Dominguez, A. and Valero, A. (2013). Global gold mining: Is technological learning overcoming the declining in ore grades. *J. Environ. Account. Manag*, 1(1):85–101.

Duran, J. and Mazozi, T. (1999). Granular boycott effect: How to mix granulates. *Physical Review E*, 60(5):6199.

EducativeTeam (2022). What is boolean indexing?

Edwards, G. C. (2016). Investigation of operating parameters in a vertical stirred mill. Master's thesis, University of Cape Town.

EIRICH, G. (2018). Eirich towermill vertical agitated media mill.

Eshuis, P., van der Weele, K., van der Meer, D., and Lohse, D. (2005). Granular leidenfrost effect: Experiment and theory of floating particle clusters. *Physical review letters*, 95(25):258001.

Fadhel, H. B. and Frances, C. (2001). Wet batch grinding of alumina hydrate in a stirred bead mill. *Powder Technology*, 119(2-3):257–268.

Faramarzi, L., Kheradmandian, A., and Azhari, A. (2020). Evaluation and optimization of the effective parameters on the shield tbm performance: torque and thrust—using discrete element method (dem). *Geotechnical and Geological Engineering*, 38:2745–2759.

Flavel, M. and Rimmer, H. (1981). Particle breakage study in an impact breakage environment. In *Reprint of paper presented at SME-AIME annual meeting, Chicago, USA, SME publication, Littleton, Ohio*.

Frances, C., Laguerie, C., Mazzarotta, B., and Veccia, T. (1996). On the analysis of fine wet grinding in a batch ball mill. *The Chemical Engineering Journal and The Biochemical Engineering Journal*, 63(3):141–147.

Francis, B. (2014). *Scale-up and operations of a vertical stirred mill*. PhD thesis, University of British Columbia.

Fruhstorfer, J., Schafföner, S., and Aneziris, C. G. (2014). Dry ball mixing and deagglomeration of alumina and zirconia composite fine powders using a bimodal ball size distribution. *Ceramics International*, 40(9):15293–15302.

Gao, M. and Forssberg, E. (1995). Prediction of product size distributions for a stirred ball mill. *Powder Technology*, 84(2):101–106.

Garzó, V. (2008). Brazil-nut effect versus reverse brazil-nut effect in a moderately dense granular fluid. *Physical Review E*, 78(2):020301.

Gaudin, A. and Malozemoff, P. (2002). Recovery by flotation of mineral particles of colloidal size. *The Journal of Physical Chemistry*, 37(5):597–607.

Graves, G. A. and Boehm, T. (2007). Mill media considerations for high energy mills. *Minerals engineering*, 20(4):342–347.

Gudin, D., Turczyn, R., Mio, H., Kano, J., and Saito, F. (2006). Simulation of the movement of beads by the dem with respect to the wet grinding process. *AIChE journal*, 52(10):3421–3426.

Hardware, T. (2022). Cpu benchmarks and hierarchy 2022: Intel and amd processors ranked.

He, M. and Forssberg, E. (2007). Influence of slurry rheology on stirred media milling of quartzite. *International Journal of Mineral Processing*, 84(1-4):240–251.

He, M., Wang, Y., and Forssberg, E. (2004). Slurry rheology in wet ultrafine grinding of industrial minerals: a review. *Powder technology*, 147(1-3):94–112.

Hromnik, M. (2013). A gpgpu implementation of the discrete element method applied to modeling the dynamic particulate environment inside a tumbling mill. Master's thesis, University of Cape Town.

Iordache, D.-A., Iordache, D.-A., Sterian, P., Sterian, A., and Pop, F. (2010). Complex computer simulations, numerical artifacts, and numerical phenomena. *Int. J. of Computers*, V:744–754.

IsaMill (2021). Isamill uses horizontal milling to secure better energy efficiency, product size and availability.

Jankovic, A. (2003). Variables affecting the fine grinding of minerals using stirred mills. *Minerals Engineering*, 16(4):337–345.

Jankovic, A. (2008). A review of regrinding and fine grinding technology-the facts and myths. *Metso Miner Process Technol Asia-Pac*.

Jankovic, A. and Sinclair, S. (2006). The shape of product size distributions in stirred mills. *Minerals Engineering*, 19(15):1528–1536.

Jayasundara, C. T., Yang, R., Guo, B., Yu, A., Govender, I., Mainza, A., van der Westhuizen, A., and Rubenstein, J. (2011). Cfd–dem modelling of particle flow in isamills–comparison between simulations and pept measurements. *Minerals engineering*, 24(3-4):181–187.

Kloss, C., Goniva, C., Hager, A., Amberger, S., and Pirker, S. (2012). Models, algorithms and validation for opensource dem and cfd–dem. *Progress in Computational Fluid Dynamics, an International Journal*, 12(2-3):140–152.

Kotake, N., Kuboki, M., Kiya, S., and Kanda, Y. (2011). Influence of dry and wet grinding conditions on fineness and shape of particle size distribution of product in a ball mill. *Advanced Powder Technology*, 22(1):86–92.

Kulya, C. (2008). Using discrete element modelling (dem) and breakage experiments to model the comminution action in a tumbling mill. Master's thesis, University of Cape Town.

Kwade, A. and Schwedes, J. (1997). Wet comminution in stirred media mills. *KONA Powder and Particle Journal*, 15:91–102.

Lameck, N., Kiangi, K., and Moys, M. (2006). Effects of grinding media shapes on load behaviour and mill power in a dry ball mill. *Minerals engineering*, 19(13):1357–1361.

Larson, M., Anderson, G., Morrison, R., and Young, M. (2011). Regrind mills: Challenges of scaleup. In *SME Annual Conference & Expo, Society for Mining, Metallurgy & Exploration*, pages 11–130.

Lichter, J. and Davey, G. (2006). Selection and sizing of ultrafine and stirred grinding mills. *Advances in comminution*, pages 69–85.

Lisso, M. (2013). Evaluating the effect of operating variables on energy consumption in stirred mills mussa lisso. Master's thesis, University of Cape Town.

Little, L. (2016). The development and demonstration of a practical methodology for fine particle shape characterisation in minerals processing.

Luding, S. (2008). Introduction to discrete element methods: basic of contact force models and how to perform the micro-macro transition to continuum theory. *European journal of environmental and civil engineering*, 12(7-8):785–826.

Ma, S.-j., Li, Z.-y., Yang, X.-j., Li, H.-j., Huo, X.-n., and Yang, J.-l. (2023). Grinding contribution and quantitative separation of impact and grinding mechanism in cylindrical mill. *Mining, Metallurgy & Exploration*, 40(5):1707–1717.

Malahe, M. (2012). A one-way coupled dem-cfd scheme to mode free-surface flows in tumbling mills. Master's thesis, University of Cape Town.

Maruf Hasan, M. (2016). *Process Modelling of Gravity Induced Stirred Mills*. PhD thesis, PHD thesis, University of Queensland, JKMRC, 211 pp. Brisbana, Australia.

Mazzinghy, D. B., Lichter, J., Schneider, C. L., Galéry, R., and Russo, J. F. C. (2017). Vertical stirred mill scale-up and simulation: Model validation by industrial samplings results. *Minerals Engineering*, 103:127–133.

Metso (2021a). Metso vertimills®.

Metso (2021b). Vertimill limeslaker.

Mindlin, R. D. (1949). Compliance of elastic bodies in contact.

Mindlin, R. D. and Deresiewicz, H. (1953). Elastic spheres in contact under varying oblique forces.

Mishra, B. (2003a). A review of computer simulation of tumbling mills by the discrete element method: Part i–contact mechanics. *International journal of mineral processing*, 71(1-4):73–93.

Mishra, B. (2003b). A review of computer simulation of tumbling mills by the discrete element method: Part ii–practical applications. *International journal of mineral processing*, 71(1-4):94–105.

Mishra, B. and Rajamani, R. K. (1992). The discrete element method for the simulation of ball mills. *Applied Mathematical Modelling*, 16(11):598–604.

Misra, A. and Cheung, J. (1999). Particle motion and energy distribution in tumbling ball mills. *Powder Technology*, 105(1-3):222–227.

Mkurazhizha, H. (2018). The effects of ore blending on comminution behaviour and product quality in a grinding circuit-svappavaara (lkab) case study.

Morrison, A., Govender, I., Mainza, A., and Parker, D. (2016). The shape and behaviour of a granular bed in a rotating drum using eulerian flow fields obtained from pept. *Chemical Engineering Science*, 152:186–198.

Morrison, R. and Cleary, P. W. (2004). Using dem to model ore breakage within a pilot scale sag mill. *Minerals Engineering*, 17(11-12):1117–1124.

Morrison, R. D., Cleary, P. W., and Sinnott, M. D. (2009). Using dem to compare the energy efficiency of pilot scale ball and tower mills. *Minerals Engineering*, 22(7-8):665–672.

Ndimande, C., Cleary, P., Mainza, A., and Sinnott, M. (2019). Using two-way coupled dem-sph to model an industrial scale stirred media detritor. *Minerals Engineering*, 137:259–276.

Neingo, P. and Tholana, T. (2016). Trends in productivity in the south african gold mining industry. *Journal of the Southern African Institute of Mining and Metallurgy*, 116(3):283–290.

Ntsele, C. and Allen, J. (2012). Technology selection of stirred mills for energy efficiency in primary and regrinding applications for the platinum industry. *The Southern African Institute of Mining and Metallurgy-Platinum*, 2012:781–808.

Oliveira, A., Rodriguez, V., De Carvalho, R., Powell, M., and Tavares, L. (2020). Mechanistic modeling and simulation of a batch vertical stirred mill. *Minerals Engineering*, 156:106487.

Orumwense, O. A. (1992). Kinetics of fine grinding in an annular ball mill. *Powder technology*, 73(2):101–108.

Pähtz, T., Durán, O., De Klerk, D. N., Govender, I., and Trulsson, M. (2019). Local rheology relation with variable yield stress ratio across dry, wet, dense, and dilute granular flows. *Physical review letters*, 123(4):048001.

Poux, M., Fayolle, P., Bertrand, J., Bridoux, D., and Bousquet, J. (1991). Powder mixing: some practical rules applied to agitated systems. *Powder Technology*, 68(3):213–234.

Radziszewski, P. and Allen, J. (2014). Towards a better understanding of stirred milling technologies-estimating power consumption and energy use. In *46th Annual Canadian Mineral Processors Operators Conference*, pages 55–66.

Rajamani, R., Mishra, B., Venugopal, R., and Datta, A. (2000). Discrete element analysis of tumbling mills. *Powder Technology*, 109(1-3):105–112.

Rule, C. (2011). Stirred milling-new comminution technology in the pgm industry. *Journal of the Southern African Institute of Mining and Metallurgy*, 111(2):101–107.

Santhanam, P. R. and Dreizin, E. L. (2012). Predicting conditions for scaled-up manufacturing of materials prepared by ball milling. *Powder Technology*, 221:403–411.

Scientific, H. (2012). A guidebook to particle size analysis. *Horiba Instruments, Inc*, pages 1–29.

Shi, F., Morrison, R., Cervellin, A., Burns, F., and Musa, F. (2009). Comparison of energy efficiency between ball mills and stirred mills in coarse grinding. *Minerals Engineering*, 22(7-8):673–680.

Shrivastava, A., Sakthivel, S., Pitchumani, B., and Rathore, A. (2011). A statistical approach for estimation of significant variables in wet attrition milling. *Powder technology*, 211(1):46–53.

Simba, K. P. and Moys, M. H. (2014). Effects of mixtures of grinding media of different shapes on milling kinetics. *Minerals Engineering*, 61:40–46.

Sinnott, M., Cleary, P. W., and Morrison, R. (2006). Analysis of stirred mill performance using dem simulation: Part 1–media motion, energy consumption and collisional environment. *Minerals Engineering*, 19(15):1537–1550.

Sinnott, M. D., Cleary, P. W., and Morrison, R. D. (2011). Is media shape important for grinding performance in stirred mills? *Minerals Engineering*, 24(2):138–151.

Somani, A., Nandi, T. K., Pal, S. K., and Majumder, A. K. (2017). Pretreatment of rocks prior to comminution–a critical review of present practices. *International journal of mining science and technology*, 27(2):339–348.

Soni, R. K. and Mishra, B. (2016). Understanding size segregation in tumbling mills. In *International Conference on Discrete Element Methods*, pages 1153–1168. Springer.

Soni, R. K., Mohanty, R., Mohanty, S., and Mishra, B. (2016). Numerical analysis of mixing of particles in drum mixers using dem. *Advanced Powder Technology*, 27(2):531–540.

Stender, H.-H., Kwade, A., and Schwedes, J. (2004). Stress energy distribution in different stirred media mill geometries. *International Journal of Mineral Processing*, 74:S103–S117.

Sudah, O. S. (2001). *Experimental and numerical investigation of mixing and segregation of free-flowing and cohesive powders in GEA Gallay tote blenders*. Rutgers The State University of New Jersey-New Brunswick.

Sun, Y., Dong, M., Mao, Y., and Fan, D. (2009). Analysis on grinding media motion in ball mill by discrete element method. *Manuf. Eng. Qual. Prod. Syst*, 1:227–231.

Szegvari, A., Yang, M., and Szegvari, A. (1999). Attritor grinding and dispersing equipment. *Union Process Inc., Akron, Ohio*.

Thornton, C. (2015). Granular dynamics, contact mechanics and particle system simulations. *A DEM study. Particle Technology Series*, 24.

UserBenchmark (2022). Amd ryzen 9 performance against intel xeon e5.

Varinot, C., Hiltgun, S., Pons, M.-N., and Dodds, J. (1997). Identification of the fragmentation mechanisms in wet-phase fine grinding in a stirred bead mill. *Chemical engineering science*, 52(20):3605–3612.

Vermeulen, LA & Howat, D. (1989). A sampling procedure validated. *Journal of the Southern African Institute of Mining and Metallurgy*, 89(12):365–370.

Walton, O. R. (1984). Application of molecular dynamics to macroscopic particles. *International Journal of Engineering Science*, 22(8-10):1097–1107.

Wang, Y. and Forssberg, E. (2007). Enhancement of energy efficiency for mechanical production of fine and ultra-fine particles in comminution. *China Particuology*, 5(3):193–201.

Weerasekara, N. S., Powell, M. S., Cleary, P., Tavares, L. M., Evertsson, M., Morrison, R., Quist, J., and Carvalho, R. (2013). The contribution of dem to the science of comminution. *Powder technology*, 248:3–24.

Wen, P., Zheng, N., Li, L., and Shi, Q. (2014). Symmetrically periodic segregation in a vertically vibrated binary granular bed. *Scientific reports*, 4(1):1–7.

Westpro (2021). Grinding mills: Ball mill.

Wills, B. A. and Finch, J. (2015). *Wills' mineral processing technology: an introduction to the practical aspects of ore treatment and mineral recovery*. Butterworth-Heinemann.

Yager, T. R. (2004). The mineral industry of south africa. *Energy*, pages 21–22.

Yang, R., Jayasundara, C., Yu, A., and Curry, D. (2006). Dem simulation of the flow of grinding media in isamill. *Minerals Engineering*, 19(10):984–994.

Zheng, J., Harris, C., and Somasundaran, P. (1995). Power consumption of stirred media mills. *Mining, Metallurgy & Exploration*, 12(1):34–40.

Appendices

A Data sets and graphs of relevant figures and tables

A.1 Degree of individual particle separation under different impeller speeds discussed in Section 4.2.3.1

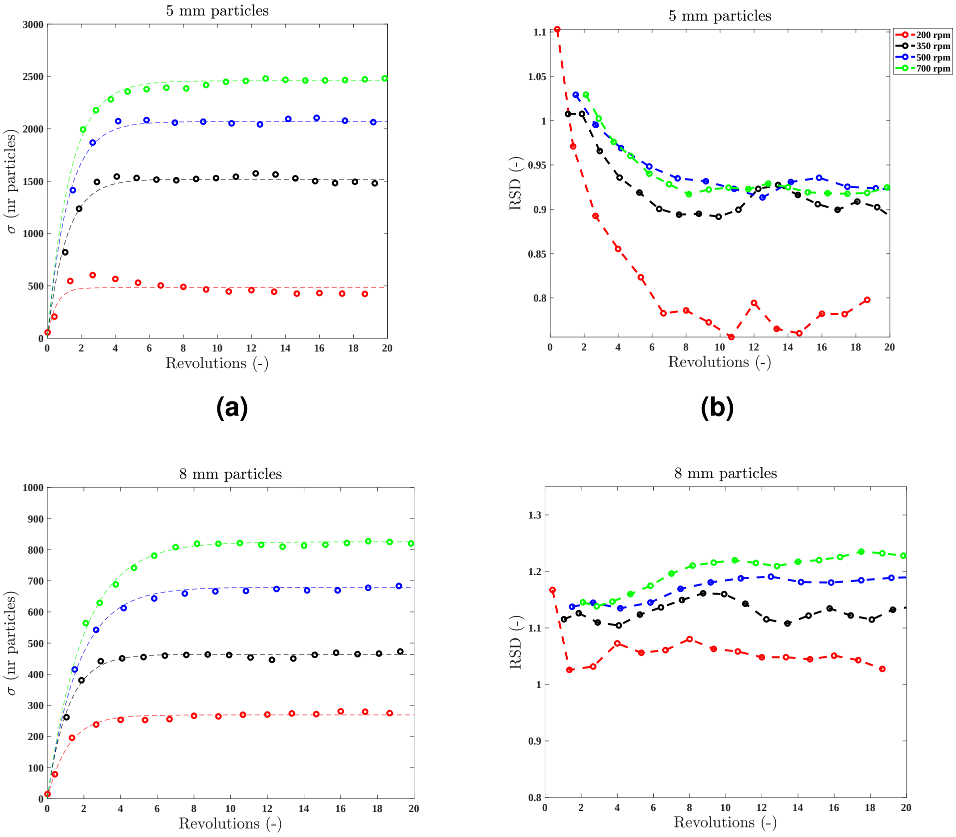

(a) (b) (c) (d)

Figure A1: Particle occupation at different impeller speeds (continued)

A.2 Collision spectra difference between size varied and mono-size particle populations

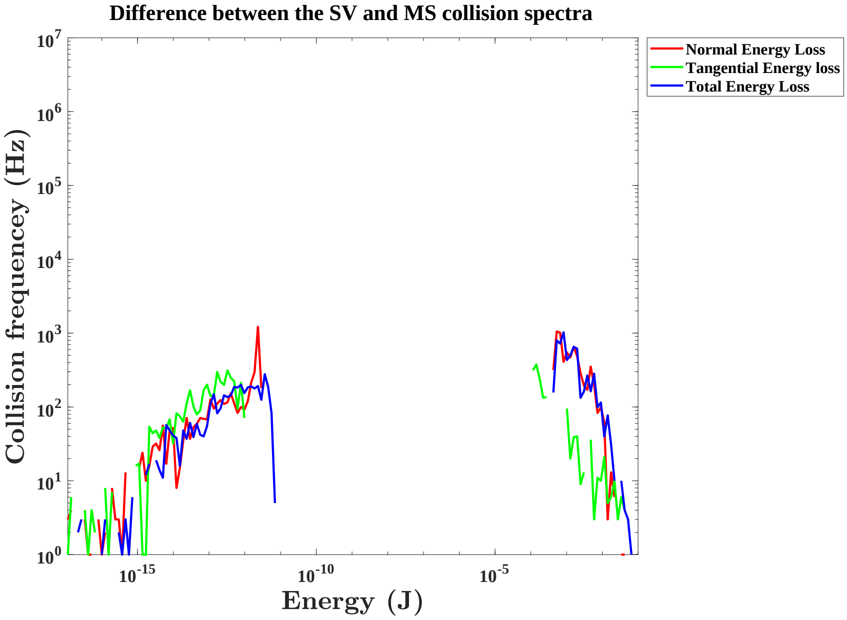

Figure A2: Collision spectra of the mono-sized and size-varied simulations captured between t = 2.9 s and t = 5.0 s at 500 rpm

A.3 Collision spectra of Section 4.2.4

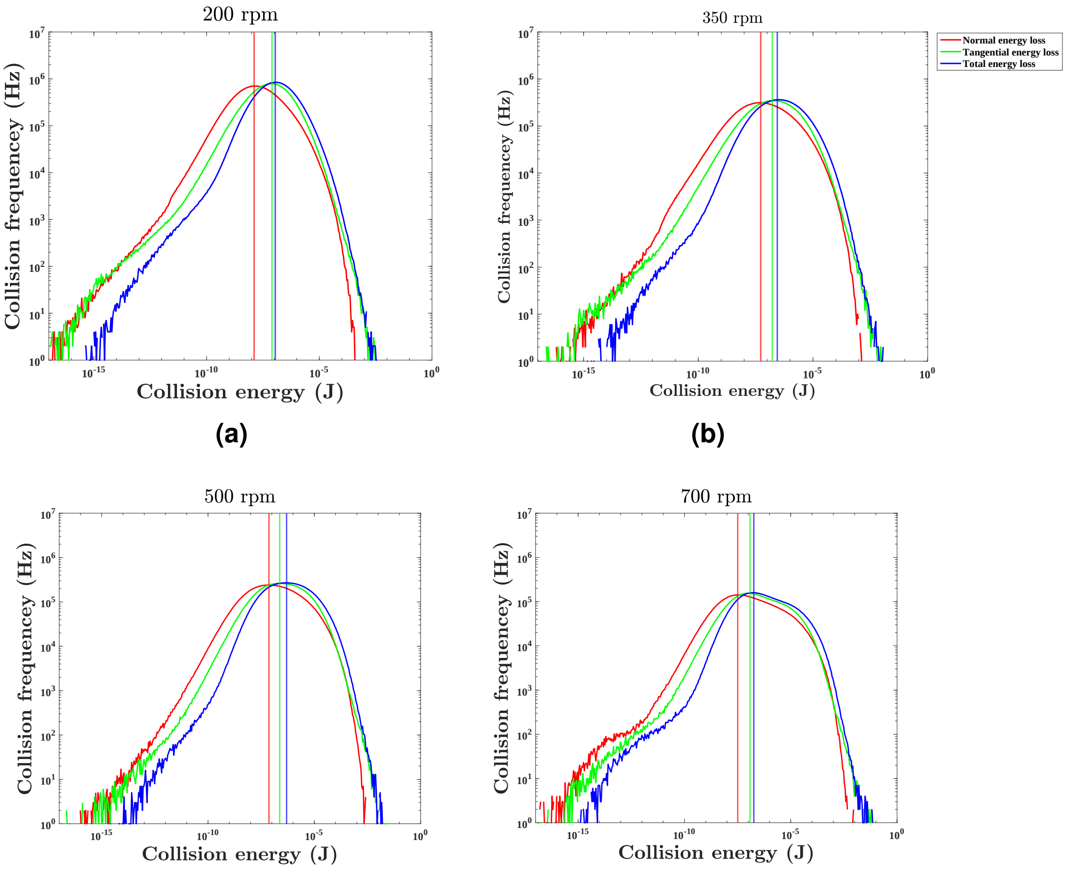

(a) **(b)** **(c)** **(d)**

Figure A3: Total energy loss collision spectra frequency plots between t = 3.0 s and t = 5.5 s for different impeller speeds

A.4 Collision modal intensities of different impeller speeds relevant to Figure 39

A.4.1 Total collisions

Table A1: Collision modal intensities for Total collisions at different impeller agitation speeds at different revolutions relevant to Figure 39a

	Normal energy loss (J)				Tangential energy loss (J)				Total energy loss (J)			
Revolution	200 rpm	350 rpm	500 rpm	700 rpm	200 rpm	350 rpm	500 rpm	700 rpm	200 rpm	350 rpm	500 rpm	700 rpm
1	1.647e-08	5.270e-08	6.761e-08	3.780e-08	7.983e-08	1.831e-07	1.685e-07	9.425e-08	1.209e-07	3.015e-07	3.868e-07	1.685e-07
2	1.647e-08	4.850e-08	6.222e-08	2.946e-08	7.983e-08	1.831e-07	1.990e-07	8.674e-08	1.314e-07	3.560e-07	3.560e-07	1.551e-07
3	1.516e-08	4.463e-08	6.222e-08	2.946e-08	7.983e-08	1.831e-07	1.990e-07	1.112e-07	1.209e-07	3.015e-07	4.203e-07	1.427e-07
4	1.516e-08	5.270e-08	5.726e-08	3.201e-08	7.983e-08	1.831e-07	1.831e-07	8.674e-08	1.209e-07	2.774e-07	4.567e-07	1.551e-07
5	1.647e-08	5.726e-08	6.222e-08	3.479e-08	7.983e-08	1.831e-07	2.162e-07	1.024e-07	1.314e-07	3.868e-07	3.868e-07	1.551e-07
6	1.516e-08	4.850e-08	6.222e-08	2.946e-08	7.983e-08	1.990e-07	1.831e-07	1.024e-07	1.314e-07	3.560e-07	3.868e-07	1.551e-07
7	1.516e-08	5.726e-08	7.346e-08	2.495e-08	7.346e-08	2.350e-07	1.831e-07	8.674e-08	1.112e-07	3.276e-07	4.567e-07	1.314e-07
8	1.516e-08	4.850e-08	6.222e-08	3.201e-08	7.983e-08	1.990e-07	2.162e-07	8.674e-08	1.314e-07	3.560e-07	4.567e-07	1.427e-07
9	1.395e-08	5.726e-08	6.222e-08	3.201e-08	7.983e-08	1.990e-07	1.990e-07	8.674e-08	1.112e-07	3.276e-07	3.560e-07	1.427e-07
10	1.516e-08	4.850e-08	6.222e-08	3.201e-08	8.674e-08	1.990e-07	2.350e-07	8.674e-08	1.112e-07	3.276e-07	4.567e-07	1.551e-07
11	1.516e-08	5.726e-08	6.761e-08	3.201e-08	7.983e-08	1.831e-07	2.350e-07	1.024e-07	1.112e-07	3.560e-07	5.860e-07	1.685e-07
12	1.395e-08	4.850e-08	7.346e-08	2.711e-08	7.983e-08	1.990e-07	2.350e-07	9.425e-08	1.314e-07	3.276e-07	4.567e-07	1.551e-07
13	1.284e-08	4.850e-08	7.346e-08	3.479e-08	7.346e-08	1.990e-07	2.162e-07	9.425e-08	1.112e-07	3.276e-07	3.868e-07	1.831e-07
14	1.395e-08	5.270e-08	6.761e-08	3.201e-08	7.983e-08	1.990e-07	1.990e-07	1.209e-07	1.112e-07	3.560e-07	4.567e-07	1.831e-07
15	1.284e-08	5.270e-08	7.346e-08	3.201e-08	7.983e-08	1.685e-07	2.350e-07	1.209e-07	1.112e-07	2.774e-07	4.963e-07	1.831e-07
Mean (e^{μ})	1.482e-08	5.154e-08	6.576e-08	3.131e-08	7.939e-08	1.925e-07	2.058e-07	9.691e-08	1.195E-07	3.294e-07	4.297e-07	1.577e-07
σ	0.079	0.079	0.081	0.101	0.038	0.077	0.107	0.120	0.076	0.096	0.134	0.100

Table A2: Collision modal peaks responsible for the most energy dissipation for the total collisions at different impeller agitation speeds at different revolutions relevant to Figure A4a

	Normal energy loss (J)				Tangential energy loss (J)				Total energy loss (J)			
Revolution	200 rpm	350 rpm	500 rpm	700 rpm	200 rpm	350 rpm	500 rpm	700 rpm	200 rpm	350 rpm	500 rpm	700 rpm
1	3.043E-03	2.056E-02	4.342E-02	3.677E-02	2.405E-06	1.165E-05	3.431E-05	1.010E-04	3.043E-03	1.741E-02	3.384E-02	6.577E-02
2	4.243E-03	1.249E-02	2.427E-02	6.577E-02	2.405E-06	1.376E-05	3.431E-05	9.296E-05	6.983E-03	1.357E-02	2.427E-02	6.577E-02
3	5.914E-03	1.249E-02	2.638E-02	2.638E-02	2.613E-06	1.495E-05	3.431E-05	1.193E-04	3.593E-03	1.058E-02	3.996E-02	3.384E-02
4	3.043E-03	1.058E-02	2.056E-02	2.427E-02	2.613E-06	1.376E-05	3.158E-05	1.193E-04	3.593E-03	1.475E-02	3.996E-02	6.577E-02
5	5.914E-03	1.475E-02	2.866E-02	7.765E-02	2.613E-06	1.495E-05	3.158E-05	1.098E-04	3.904E-03	9.735E-03	3.384E-02	6.577E-02
6	4.610E-03	9.735E-03	2.866E-02	4.718E-02	2.213E-06	1.165E-05	3.158E-05	1.010E-04	4.610E-03	1.249E-02	2.056E-02	3.996E-02
7	3.043E-03	1.058E-02	2.866E-02	4.718E-02	2.405E-06	1.165E-05	3.431E-05	1.010E-04	3.043E-03	1.058E-02	2.056E-02	7.146E-02
8	2.577E-03	1.741E-02	2.427E-02	5.126E-02	2.037E-06	1.765E-05	3.728E-05	1.010E-04	3.043E-03	2.427E-02	2.427E-02	5.126E-02
9	3.593E-03	8.959E-03	1.892E-02	5.126E-02	2.213E-06	1.266E-05	4.051E-05	1.010E-04	4.610E-03	1.249E-02	1.892E-02	5.126E-02
10	2.801E-03	1.058E-02	2.866E-02	4.718E-02	2.037E-06	1.625E-05	3.431E-05	9.296E-05	2.801E-03	8.959E-03	1.892E-02	4.342E-02
11	2.801E-03	9.735E-03	2.866E-02	4.718E-02	2.037E-06	1.625E-05	3.431E-05	1.098E-04	2.801E-03	2.638E-02	2.234E-02	4.342E-02
12	4.610E-03	1.249E-02	2.638E-02	9.963E-02	2.213E-06	1.165E-05	3.158E-05	1.098E-04	5.009E-03	2.056E-02	2.638E-02	9.168E-02
13	7.588E-03	1.249E-02	2.866E-02	9.963E-02	2.213E-06	1.165E-05	3.431E-05	9.296E-05	4.610E-03	2.056E-02	2.866E-02	1.083E-01
14	5.914E-03	1.741E-02	2.866E-02	5.126E-02	2.213E-06	1.165E-05	3.431E-05	1.010E-04	5.914E-03	2.056E-02	2.866E-02	5.126E-02
15	3.593E-03	1.058E-02	2.638E-02	4.718E-02	2.405E-06	1.376E-05	3.431E-05	1.098E-04	2.577E-03	1.058E-02	2.638E-02	5.126E-02
Mean (e^{μ})	3.992E-03	1.235E-02	2.697E-02	5.070E-02	2.301E-06	1.346E-05	3.412E-05	1.038E-04	3.840E-03	1.467E-02	2.638E-02	5.727E-02
σ	0.339	0.245	0.184	0.402	0.088	0.145	0.066	0.081	0.298	0.354	0.249	0.311

A.4.2 Particle collisions

Table A3: Collision modal intensities for a particle-particle particulate system at different impeller speeds at different revolutions relevant to Figure 39b

	Normal energy loss (J)				Tangential energy loss (J)				Total energy loss (J)			
Revolution	200 rpm	350 rpm	500 rpm	700 rpm	200 rpm	350 rpm	500 rpm	700 rpm	200 rpm	350 rpm	500 rpm	700 rpm
1	1.647E-08	5.270E-08	5.727E-08	3.780E-08	7.983E-08	1.552E-07	1.686E-07	8.675E-08	1.209E-07	2.554E-07	2.163E-07	1.314E-07
2	1.790E-08	4.850E-08	6.222E-08	2.947E-08	7.347E-08	1.686E-07	1.686E-07	8.675E-08	1.209E-07	2.775E-07	2.350E-07	1.552E-07
3	1.790E-08	5.727E-08	6.222E-08	2.947E-08	7.983E-08	1.832E-07	1.991E-07	8.675E-08	1.209E-07	2.775E-07	3.015E-07	1.428E-07
4	1.516E-08	5.270E-08	5.727E-08	3.202E-08	7.347E-08	1.832E-07	1.832E-07	8.675E-08	1.209E-07	2.775E-07	2.554E-07	1.428E-07
5	1.647E-08	5.727E-08	6.222E-08	3.479E-08	7.347E-08	1.832E-07	1.686E-07	1.024E-07	1.113E-07	2.775E-07	3.015E-07	1.552E-07
6	1.516E-08	4.850E-08	6.222E-08	2.947E-08	7.347E-08	1.832E-07	1.832E-07	1.024E-07	1.113E-07	3.015E-07	2.554E-07	1.314E-07
7	1.516E-08	5.727E-08	7.347E-08	2.496E-08	7.347E-08	1.686E-07	1.832E-07	8.675E-08	1.113E-07	3.276E-07	2.775E-07	1.314E-07
8	1.516E-08	5.270E-08	7.347E-08	3.202E-08	7.347E-08	1.991E-07	1.552E-07	8.675E-08	1.024E-07	2.775E-07	3.015E-07	1.428E-07
9	1.790E-08	5.727E-08	6.222E-08	3.202E-08	7.983E-08	1.552E-07	1.832E-07	8.675E-08	1.113E-07	3.276E-07	3.015E-07	1.428E-07
10	1.647E-08	5.727E-08	6.222E-08	3.202E-08	7.347E-08	1.686E-07	1.552E-07	8.675E-08	1.113E-07	3.015E-07	3.560E-07	1.552E-07
11	1.516E-08	5.727E-08	6.761E-08	3.202E-08	6.761E-08	1.832E-07	1.991E-07	1.024E-07	1.113E-07	3.015E-07	3.560E-07	1.552E-07
12	1.516E-08	5.727E-08	7.347E-08	2.712E-08	6.761E-08	1.552E-07	1.428E-07	9.426E-08	1.024E-07	3.276E-07	3.015E-07	1.552E-07
13	1.395E-08	5.727E-08	7.347E-08	3.479E-08	7.347E-08	1.552E-07	1.686E-07	9.426E-08	1.113E-07	3.276E-07	2.554E-07	1.552E-07
14	1.395E-08	5.270E-08	6.761E-08	3.202E-08	6.761E-08	1.991E-07	1.991E-07	9.426E-08	1.113E-07	3.015E-07	3.276E-07	1.832E-07
15	1.647E-08	5.270E-08	7.347E-08	3.202E-08	7.983E-08	1.686E-07	1.686E-07	9.426E-08	1.113E-07	2.775E-07	3.276E-07	1.552E-07
Mean (e^{μ})	1.585E-08	5.448E-08	6.577E-08	3.132E-08	7.388E-08	1.733E-07	1.743E-07	9.168E-08	1.125E-07	2.949E-07	2.885E-07	1.484E-07
σ	0.082	0.061	0.092	0.102	0.058	0.087	0.098	0.068	0.053	0.080	0.147	0.088

Table A4: Collision modal peaks responsible for the most energy dissipation for the particle collisions at different impeller agitation speeds at different revolutions relevant to Figure A4b

	Normal energy loss (J)				Tangential energy loss (J)				Total energy loss (J)			
Revolution	200 rpm	350 rpm	500 rpm	700 rpm	200 rpm	350 rpm	500 rpm	700 rpm	200 rpm	350 rpm	500 rpm	700 rpm
1	4.674E-06	1.918E-05	7.246E-05	2.133E-04	1.875E-06	9.871E-06	2.906E-05	7.873E-05	3.959E-06	2.265E-05	7.246E-05	2.133E-04
2	3.959E-06	1.625E-05	6.668E-05	1.807E-04	1.875E-06	9.871E-06	2.674E-05	9.296E-05	4.674E-06	2.085E-05	6.668E-05	1.963E-04
3	4.674E-06	2.265E-05	7.873E-05	1.963E-04	1.875E-06	9.084E-06	2.461E-05	9.296E-05	4.674E-06	2.265E-05	7.873E-05	2.519E-04
4	4.674E-06	1.918E-05	7.246E-05	1.963E-04	1.875E-06	1.165E-05	3.158E-05	8.555E-05	3.959E-06	2.265E-05	7.873E-05	2.133E-04
5	4.674E-06	2.674E-05	6.137E-05	2.519E-04	1.725E-06	1.073E-05	3.158E-05	8.555E-05	3.959E-06	2.265E-05	7.873E-05	2.133E-04
6	3.353E-06	2.265E-05	6.137E-05	1.663E-04	2.037E-06	9.084E-06	2.461E-05	7.873E-05	3.959E-06	2.461E-05	6.668E-05	1.963E-04
7	4.302E-06	1.918E-05	6.137E-05	2.133E-04	1.588E-06	1.165E-05	2.674E-05	7.873E-05	3.959E-06	2.085E-05	6.668E-05	1.963E-04
8	4.674E-06	2.085E-05	5.648E-05	2.133E-04	2.037E-06	9.871E-06	2.674E-05	7.873E-05	4.302E-06	2.265E-05	7.246E-05	2.318E-04
9	4.674E-06	1.765E-05	5.648E-05	2.133E-04	1.875E-06	9.084E-06	2.674E-05	7.873E-05	3.959E-06	2.674E-05	7.246E-05	2.318E-04
10	3.959E-06	1.918E-05	6.668E-05	1.807E-04	2.037E-06	9.084E-06	3.431E-05	9.296E-05	4.302E-06	2.461E-05	7.246E-05	1.963E-04
11	3.959E-06	1.765E-05	6.668E-05	1.807E-04	1.725E-06	1.073E-05	2.906E-05	9.296E-05	3.643E-06	2.906E-05	7.246E-05	2.318E-04
12	4.674E-06	1.918E-05	6.137E-05	1.963E-04	1.725E-06	9.871E-06	2.906E-05	8.555E-05	3.959E-06	2.674E-05	6.668E-05	2.318E-04
13	3.643E-06	1.918E-05	4.783E-05	1.963E-04	1.725E-06	9.871E-06	3.431E-05	6.668E-05	4.302E-06	2.674E-05	6.137E-05	2.318E-04
14	4.302E-06	1.625E-05	5.648E-05	1.963E-04	1.875E-06	1.165E-05	3.158E-05	9.296E-05	3.959E-06	2.265E-05	7.246E-05	1.963E-04
15	4.302E-06	2.085E-05	5.648E-05	2.133E-04	1.588E-06	9.084E-06	2.906E-05	7.873E-05	4.302E-06	2.461E-05	7.246E-05	1.963E-04
Mean (e^{μ})	4.278E-06	1.961E-05	6.240E-05	1.996E-04	1.823E-06	1.004E-05	2.890E-05	8.368E-05	4.115E-06	2.394E-05	7.127E-05	2.145E-04
σ	0.106	0.131	0.126	0.100	0.081	0.095	0.106	0.097	0.069	0.098	0.072	0.086

A.4.3 Small-small particle collisions

Table A5: Collision modal intensities for different impeller speeds at different revolutions for small-small particle collisions relevant to Figure 39c

	Normal energy loss (J)				Tangential energy loss (J)				Total energy loss (J)			
Revolution	200 rpm	350 rpm	500 rpm	700 rpm	200 rpm	350 rpm	500 rpm	700 rpm	200 rpm	350 rpm	500 rpm	700 rpm
1	1.395E-08	3.479E-08	6.222E-08	2.114E-08	6.761E-08	1.314E-07	1.428E-07	7.347E-08	9.426E-08	2.163E-07	2.350E-07	1.113E-07
2	1.284E-08	3.202E-08	4.850E-08	2.297E-08	6.222E-08	1.209E-07	1.552E-07	5.727E-08	9.426E-08	1.991E-07	2.163E-07	1.024E-07
3	1.284E-08	3.780E-08	6.761E-08	2.712E-08	5.727E-08	1.209E-07	1.991E-07	5.727E-08	9.426E-08	2.350E-07	3.276E-07	9.426E-08
4	1.284E-08	2.947E-08	7.983E-08	1.945E-08	5.727E-08	1.209E-07	1.428E-07	6.761E-08	9.426E-08	2.163E-07	2.554E-07	9.426E-08
5	1.088E-08	3.202E-08	6.222E-08	2.114E-08	6.222E-08	1.209E-07	1.314E-07	6.761E-08	8.675E-08	2.163E-07	3.869E-07	1.024E-07
6	1.088E-08	3.202E-08	5.727E-08	2.297E-08	6.222E-08	1.209E-07	1.552E-07	5.727E-08	8.675E-08	1.991E-07	3.869E-07	1.113E-07
7	1.001E-08	3.780E-08	7.347E-08	2.496E-08	5.270E-08	1.113E-07	1.552E-07	6.761E-08	9.426E-08	2.163E-07	3.560E-07	1.024E-07
8	1.001E-08	4.108E-08	7.347E-08	2.114E-08	5.270E-08	1.552E-07	1.552E-07	6.761E-08	7.347E-08	2.554E-07	3.015E-07	1.024E-07
9	1.088E-08	2.947E-08	7.983E-08	2.114E-08	5.270E-08	1.209E-07	1.991E-07	6.761E-08	7.983E-08	1.832E-07	3.015E-07	1.024E-07
10	1.088E-08	3.202E-08	5.270E-08	2.297E-08	5.270E-08	1.209E-07	1.832E-07	6.761E-08	7.983E-08	2.350E-07	3.276E-07	1.024E-07
11	1.001E-08	3.202E-08	8.675E-08	2.496E-08	5.727E-08	1.552E-07	1.991E-07	6.761E-08	7.983E-08	2.163E-07	3.560E-07	1.024E-07
12	9.211E-09	3.202E-08	7.347E-08	2.712E-08	4.850E-08	1.314E-07	2.350E-07	6.761E-08	7.347E-08	2.350E-07	4.568E-07	9.426E-08
13	1.001E-08	3.202E-08	7.347E-08	2.114E-08	4.850E-08	1.314E-07	1.314E-07	6.222E-08	7.347E-08	2.350E-07	3.869E-07	9.426E-08
14	1.001E-08	3.202E-08	6.761E-08	2.712E-08	4.463E-08	1.024E-07	1.991E-07	6.222E-08	8.675E-08	1.991E-07	3.560E-07	9.426E-08
15	1.001E-08	3.780E-08	7.983E-08	2.712E-08	4.850E-08	1.314E-07	1.991E-07	6.222E-08	7.347E-08	1.991E-07	5.393E-07	1.024E-07
Mean (e^{μ})	1.094E-08	3.347E-08	6.837E-08	2.335E-08	5.478E-08	1.257E-07	1.695E-07	6.468E-08	8.391E-08	2.163E-07	3.368E-07	1.007E-07
$sigma$	0.123	0.099	0.166	0.114	0.117	0.108	0.182	0.076	0.103	0.089	0.240	0.056

Table A6: Collision modal peaks responsible for the most energy dissipation for the small-small particle collisions at different impeller agitation speeds at different revolutions relevant to Figure A4c

	Normal energy loss (J)				Tangential energy loss (J)				Total energy loss (J)			
Revolution	200 rpm	350 rpm	500 rpm	700 rpm	200 rpm	350 rpm	500 rpm	700 rpm	200 rpm	350 rpm	500 rpm	700 rpm
1	3.086E-06	1.376E-05	4.402E-05	1.296E-04	1.461E-06	5.997E-06	2.085E-05	5.198E-05	2.840E-06	1.765E-05	5.198E-05	1.663E-04
2	2.840E-06	1.495E-05	3.728E-05	1.296E-04	1.588E-06	6.516E-06	2.085E-05	5.648E-05	2.613E-06	1.918E-05	4.051E-05	1.408E-04
3	3.353E-06	1.376E-05	3.728E-05	1.408E-04	1.725E-06	6.516E-06	2.085E-05	5.648E-05	3.086E-06	1.376E-05	4.402E-05	1.408E-04
4	3.353E-06	1.625E-05	4.051E-05	1.098E-04	1.461E-06	7.081E-06	1.918E-05	5.198E-05	3.086E-06	1.765E-05	4.402E-05	1.408E-04
5	3.086E-06	1.625E-05	3.728E-05	1.296E-04	1.461E-06	6.516E-06	1.918E-05	6.668E-05	3.086E-06	1.625E-05	4.783E-05	1.663E-04
6	3.353E-06	1.376E-05	4.402E-05	1.408E-04	1.345E-06	7.081E-06	2.085E-05	4.783E-05	2.405E-06	1.765E-05	4.051E-05	1.530E-04
7	3.959E-06	1.625E-05	4.051E-05	1.010E-04	1.238E-06	7.081E-06	2.085E-05	5.648E-05	2.840E-06	1.625E-05	4.783E-05	1.530E-04
8	3.643E-06	1.765E-05	3.728E-05	1.530E-04	1.345E-06	7.081E-06	1.765E-05	5.648E-05	2.613E-06	1.495E-05	5.198E-05	1.663E-04
9	3.643E-06	1.765E-05	4.783E-05	1.530E-04	1.238E-06	6.516E-06	1.918E-05	5.648E-05	3.086E-06	1.625E-05	5.198E-05	1.663E-04
10	3.353E-06	1.266E-05	3.728E-05	1.193E-04	1.238E-06	7.081E-06	1.918E-05	5.648E-05	2.613E-06	1.495E-05	5.198E-05	1.408E-04
11	2.405E-06	1.266E-05	4.402E-05	1.193E-04	1.345E-06	5.997E-06	1.918E-05	5.198E-05	2.840E-06	1.495E-05	4.783E-05	1.408E-04
12	3.086E-06	1.376E-05	4.402E-05	1.098E-04	1.238E-06	7.081E-06	2.085E-05	6.668E-05	2.840E-06	1.765E-05	4.051E-05	1.193E-04
13	2.840E-06	1.376E-05	4.051E-05	1.193E-04	1.461E-06	7.081E-06	1.918E-05	6.668E-05	2.840E-06	1.765E-05	4.783E-05	1.193E-04
14	2.840E-06	1.625E-05	3.431E-05	1.193E-04	1.345E-06	6.516E-06	1.765E-05	6.137E-05	2.840E-06	1.918E-05	4.402E-05	1.530E-04
15	2.840E-06	1.376E-05	3.728E-05	1.193E-04	1.588E-06	7.694E-06	1.765E-05	5.648E-05	2.613E-06	1.376E-05	4.402E-05	1.530E-04
Mean (e^{μ})	3.155E-06	1.479E-05	4.007E-05	1.254E-04	1.398E-06	6.774E-06	1.951E-05	5.711E-05	2.808E-06	1.643E-05	4.627E-05	1.472E-04
σ	0.127	0.113	0.093	0.121	0.103	0.069	0.064	0.099	0.076	0.108	0.093	0.108

A.4.4 Small-large particle collisions

Table A7: Collision modal intensities for different impeller speeds at different revolutions for small-large particle collisions relevant to Figure 39d

	Normal energy loss (J)				Tangential energy loss (J)				Total energy loss (J)			
Revolution	200 rpm	350 rpm	500 rpm	700 rpm	200 rpm	350 rpm	500 rpm	700 rpm	200 rpm	350 rpm	500 rpm	700 rpm
1	2.114E-08	6.761E-08	5.727E-08	3.780E-08	8.675E-08	1.991E-07	1.686E-07	9.426E-08	1.314E-07	3.015E-07	2.163E-07	1.314E-07
2	2.297E-08	6.761E-08	6.222E-08	2.947E-08	9.426E-08	1.686E-07	1.686E-07	8.675E-08	1.314E-07	3.869E-07	2.350E-07	1.686E-07
3	2.496E-08	7.347E-08	4.850E-08	4.108E-08	1.024E-07	1.991E-07	1.686E-07	1.113E-07	1.314E-07	3.276E-07	2.350E-07	1.552E-07
4	2.297E-08	6.222E-08	5.727E-08	3.202E-08	9.426E-08	2.554E-07	1.832E-07	1.113E-07	1.428E-07	3.869E-07	2.554E-07	1.552E-07
5	2.297E-08	5.727E-08	6.222E-08	4.108E-08	9.426E-08	1.832E-07	1.428E-07	1.024E-07	1.552E-07	3.869E-07	3.015E-07	1.552E-07
6	2.297E-08	7.347E-08	6.222E-08	3.780E-08	8.675E-08	2.350E-07	1.832E-07	1.024E-07	1.552E-07	3.560E-07	2.554E-07	1.552E-07
7	2.496E-08	5.727E-08	5.727E-08	2.947E-08	1.024E-07	2.350E-07	1.832E-07	9.426E-08	1.428E-07	4.568E-07	2.350E-07	1.552E-07
8	2.496E-08	7.347E-08	6.222E-08	3.202E-08	1.024E-07	2.163E-07	1.832E-07	1.024E-07	1.552E-07	3.869E-07	2.350E-07	1.428E-07
9	2.712E-08	9.426E-08	5.270E-08	3.202E-08	1.024E-07	2.163E-07	1.552E-07	1.024E-07	1.552E-07	4.204E-07	2.554E-07	1.428E-07
10	2.496E-08	7.983E-08	6.222E-08	4.108E-08	9.426E-08	2.163E-07	1.552E-07	8.675E-08	1.428E-07	3.276E-07	2.554E-07	1.686E-07
11	2.297E-08	8.675E-08	6.761E-08	3.780E-08	1.024E-07	1.991E-07	1.552E-07	1.113E-07	1.686E-07	3.560E-07	2.554E-07	1.686E-07
12	2.496E-08	6.761E-08	6.761E-08	3.479E-08	9.426E-08	2.350E-07	1.428E-07	1.024E-07	1.552E-07	3.276E-07	2.554E-07	1.552E-07
13	2.297E-08	6.761E-08	4.850E-08	3.202E-08	1.113E-07	2.350E-07	1.686E-07	9.426E-08	1.552E-07	3.276E-07	2.554E-07	1.832E-07
14	2.297E-08	6.761E-08	6.222E-08	3.202E-08	1.024E-07	1.991E-07	1.991E-07	9.426E-08	1.552E-07	3.560E-07	2.554E-07	1.832E-07
15	2.712E-08	7.347E-08	7.347E-08	3.780E-08	1.024E-07	1.991E-07	1.686E-07	1.209E-07	1.428E-07	3.869E-07	3.015E-07	1.832E-07
Mean (e^{μ})	2.401E-08	7.068E-08	5.986E-08	3.498E-08	9.798E-08	2.116E-07	1.677E-07	1.007E-07	1.476E-07	3.640E-07	2.526E-07	1.595E-07
σ	0.069	0.136	0.117	0.119	0.069	0.111	0.097	0.095	0.076	0.111	0.088	0.098

Table A8: Collision modal peaks responsible for the most energy dissipation for the small-large particle collisions at different impeller agitation speeds at different revolutions relevant to Figure A4d

	Normal energy loss (J)				Tangential energy loss (J)				Total energy loss (J)			
Revolution	200 rpm	350 rpm	500 rpm	700 rpm	200 rpm	350 rpm	500 rpm	700 rpm	200 rpm	350 rpm	500 rpm	700 rpm
1	5.519E-06	2.265E-05	8.555E-05	2.133E-04	2.213E-06	9.871E-06	3.431E-05	1.010E-04	3.959E-06	3.431E-05	9.296E-05	2.318E-04
2	5.997E-06	2.085E-05	6.668E-05	1.963E-04	2.405E-06	1.376E-05	3.431E-05	1.010E-04	4.674E-06	2.674E-05	8.555E-05	2.519E-04
3	5.519E-06	2.265E-05	7.873E-05	1.963E-04	2.037E-06	1.625E-05	3.158E-05	1.193E-04	4.674E-06	2.461E-05	1.010E-04	2.519E-04
4	5.519E-06	2.674E-05	7.246E-05	2.318E-04	2.405E-06	1.165E-05	3.728E-05	1.010E-04	5.079E-06	2.906E-05	7.873E-05	2.737E-04
5	5.519E-06	2.674E-05	7.246E-05	2.133E-04	2.213E-06	1.495E-05	3.158E-05	1.010E-04	5.079E-06	2.265E-05	7.873E-05	2.974E-04
6	6.516E-06	2.085E-05	6.137E-05	2.133E-04	2.037E-06	9.871E-06	3.158E-05	8.555E-05	5.519E-06	2.906E-05	6.668E-05	2.974E-04
7	5.519E-06	2.085E-05	6.137E-05	2.133E-04	2.037E-06	1.165E-05	3.158E-05	1.010E-04	4.674E-06	3.158E-05	8.555E-05	2.737E-04
8	4.674E-06	2.461E-05	7.246E-05	2.133E-04	2.037E-06	1.765E-05	3.431E-05	1.193E-04	4.302E-06	3.158E-05	9.296E-05	3.231E-04
9	4.674E-06	2.674E-05	6.668E-05	2.133E-04	2.213E-06	1.165E-05	3.431E-05	1.193E-04	5.997E-06	2.674E-05	9.296E-05	3.231E-04
10	5.519E-06	2.265E-05	7.873E-05	1.807E-04	2.037E-06	1.625E-05	3.431E-05	9.296E-05	5.079E-06	3.431E-05	8.555E-05	2.737E-04
11	4.302E-06	2.674E-05	6.668E-05	2.133E-04	2.037E-06	1.376E-05	3.431E-05	1.010E-04	5.519E-06	2.906E-05	9.296E-05	2.974E-04
12	6.516E-06	1.918E-05	6.137E-05	1.963E-04	2.405E-06	1.073E-05	3.158E-05	1.010E-04	5.079E-06	3.431E-05	9.296E-05	2.318E-04
13	5.079E-06	1.918E-05	5.198E-05	1.963E-04	2.405E-06	1.073E-05	4.402E-05	9.296E-05	5.997E-06	3.431E-05	1.010E-04	2.519E-04
14	4.674E-06	2.461E-05	8.555E-05	2.318E-04	1.875E-06	1.165E-05	3.158E-05	9.296E-05	5.079E-06	2.265E-05	1.010E-04	2.519E-04
15	4.674E-06	2.085E-05	8.555E-05	1.963E-04	2.405E-06	1.625E-05	3.158E-05	1.010E-04	5.519E-06	2.461E-05	7.246E-05	2.519E-04
Mean (e^{μ})	5.309E-06	2.290E-05	7.048E-05	2.075E-04	2.177E-06	1.288E-05	3.375E-05	1.016E-04	5.051E-06	2.874E-05	8.747E-05	2.707E-04
σ	0.125	0.121	0.146	0.068	0.084	0.197	0.090	0.097	0.115	0.150	0.123	0.108

A.4.5 Large-large particle collisions

Table A9: Collision modal intensities for different impeller speeds at different revolutions for large-large particle collisions relevant to Figure 39e

	Normal energy loss (J)				Tangential energy loss (J)				Total energy loss (J)			
Revolution	200 rpm	350 rpm	500 rpm	700 rpm	200 rpm	350 rpm	500 rpm	700 rpm	200 rpm	350 rpm	500 rpm	700 rpm
1	4.463E-08	1.552E-07	1.024E-07	6.222E-08	1.552E-07	4.568E-07	2.350E-07	2.163E-07	2.350E-07	1.048E-06	3.560E-07	2.554E-07
2	4.108E-08	1.832E-07	1.024E-07	7.347E-08	1.686E-07	4.963E-07	2.350E-07	1.428E-07	2.350E-07	8.877E-07	3.560E-07	3.015E-07
3	4.463E-08	1.686E-07	1.024E-07	7.347E-08	1.686E-07	4.204E-07	1.991E-07	1.686E-07	2.554E-07	8.170E-07	4.204E-07	2.775E-07
4	4.463E-08	1.832E-07	9.426E-08	8.675E-08	1.686E-07	4.568E-07	2.163E-07	1.686E-07	2.775E-07	9.646E-07	3.869E-07	2.775E-07
5	4.850E-08	1.991E-07	1.209E-07	9.426E-08	1.686E-07	3.869E-07	2.554E-07	1.832E-07	2.350E-07	8.877E-07	3.869E-07	4.204E-07
6	5.727E-08	1.552E-07	9.426E-08	7.983E-08	1.552E-07	3.560E-07	2.554E-07	1.686E-07	2.775E-07	6.368E-07	3.869E-07	3.276E-07
7	5.727E-08	1.552E-07	1.113E-07	6.761E-08	1.552E-07	3.276E-07	1.991E-07	2.163E-07	2.775E-07	8.877E-07	4.568E-07	3.015E-07
8	6.222E-08	1.686E-07	1.113E-07	6.761E-08	1.991E-07	3.869E-07	2.163E-07	1.686E-07	3.015E-07	8.170E-07	3.015E-07	3.015E-07
9	6.222E-08	1.686E-07	8.675E-08	6.761E-08	1.552E-07	3.560E-07	2.554E-07	1.686E-07	2.350E-07	6.919E-07	3.869E-07	3.015E-07
10	6.222E-08	1.991E-07	7.983E-08	7.983E-08	1.552E-07	3.869E-07	2.350E-07	2.163E-07	3.015E-07	7.518E-07	3.869E-07	2.554E-07
11	6.222E-08	1.552E-07	8.675E-08	8.675E-08	1.552E-07	3.869E-07	2.554E-07	1.552E-07	3.015E-07	6.919E-07	4.204E-07	2.554E-07
12	5.270E-08	1.832E-07	7.347E-08	6.222E-08	1.832E-07	4.568E-07	2.163E-07	1.552E-07	3.560E-07	1.048E-06	3.015E-07	2.350E-07
13	6.222E-08	1.832E-07	1.209E-07	6.222E-08	1.991E-07	4.568E-07	1.832E-07	1.552E-07	3.276E-07	1.048E-06	4.204E-07	2.775E-07
14	4.463E-08	2.350E-07	9.426E-08	7.983E-08	1.991E-07	4.963E-07	1.832E-07	1.832E-07	2.775E-07	8.877E-07	3.869E-07	2.775E-07
15	4.850E-08	1.991E-07	1.024E-07	7.983E-08	1.991E-07	4.568E-07	2.554E-07	1.832E-07	3.015E-07	8.170E-07	3.276E-07	2.554E-07
Mean (e^{μ})	5.241E-08	1.782E-07	9.798E-08	7.429E-08	1.714E-07	4.157E-07	2.248E-07	1.753E-07	2.775E-07	8.492E-07	3.763E-07	2.853E-07
σ	0.155	0.120	0.143	0.133	0.105	0.129	0.121	0.129	0.129	0.157	0.120	0.139

Table A10: Collision modal peaks responsible for the most energy dissipation for the large-large particle collisions at different impeller agitation speeds at different revolutions relevant to Figure A4e

	Normal energy loss (J)				Tangential energy loss (J)				Total energy loss (J)			
Revolution	200 rpm	350 rpm	500 rpm	700 rpm	200 rpm	350 rpm	500 rpm	700 rpm	200 rpm	350 rpm	500 rpm	700 rpm
1	7.694E-06	4.051E-05	1.807E-04	4.505E-04	3.959E-06	2.085E-05	8.555E-05	1.807E-04	9.084E-06	4.783E-05	1.663E-04	7.415E-04
2	9.084E-06	5.648E-05	1.530E-04	4.505E-04	3.353E-06	2.674E-05	6.137E-05	2.318E-04	8.360E-06	3.728E-05	1.663E-04	4.895E-04
3	5.997E-06	4.051E-05	1.663E-04	4.146E-04	3.353E-06	1.918E-05	5.198E-05	2.133E-04	6.516E-06	5.648E-05	2.318E-04	6.280E-04
4	9.871E-06	3.728E-05	1.663E-04	5.780E-04	4.302E-06	2.085E-05	7.873E-05	2.133E-04	1.165E-05	4.402E-05	2.318E-04	6.824E-04
5	7.081E-06	3.728E-05	1.530E-04	5.780E-04	4.674E-06	2.265E-05	7.873E-05	1.807E-04	7.081E-06	4.051E-05	1.098E-04	6.824E-04
6	9.871E-06	4.051E-05	1.296E-04	4.895E-04	5.079E-06	2.461E-05	7.246E-05	1.807E-04	8.360E-06	5.198E-05	1.963E-04	6.824E-04
7	9.871E-06	3.728E-05	1.296E-04	4.895E-04	2.840E-06	2.674E-05	7.246E-05	2.519E-04	7.694E-06	7.246E-05	1.530E-04	4.895E-04
8	7.694E-06	4.051E-05	1.193E-04	3.511E-04	3.353E-06	2.085E-05	1.010E-04	1.963E-04	7.694E-06	3.728E-05	1.530E-04	5.780E-04
9	9.084E-06	3.158E-05	1.663E-04	3.511E-04	3.086E-06	1.918E-05	6.668E-05	1.963E-04	7.694E-06	4.402E-05	1.663E-04	5.780E-04
10	9.084E-06	6.137E-05	1.807E-04	6.824E-04	2.840E-06	2.265E-05	6.668E-05	1.663E-04	7.081E-06	6.137E-05	1.663E-04	6.824E-04
11	9.084E-06	4.783E-05	1.296E-04	4.505E-04	4.302E-06	2.265E-05	1.098E-04	2.519E-04	7.081E-06	4.783E-05	1.663E-04	4.895E-04
12	7.694E-06	4.051E-05	1.408E-04	5.780E-04	3.353E-06	2.674E-05	6.137E-05	2.519E-04	8.360E-06	5.198E-05	1.663E-04	7.415E-04
13	1.073E-05	4.051E-05	1.408E-04	3.511E-04	3.353E-06	2.674E-05	5.648E-05	2.318E-04	9.084E-06	5.198E-05	1.530E-04	5.780E-04
14	9.871E-06	6.137E-05	2.133E-04	3.511E-04	3.086E-06	2.674E-05	5.648E-05	2.318E-04	9.871E-06	8.555E-05	1.807E-04	5.780E-04
15	8.360E-06	4.402E-05	1.408E-04	4.895E-04	2.213E-06	1.918E-05	4.783E-05	2.737E-04	5.519E-06	4.402E-05	1.663E-04	5.780E-04
Mean (e^{μ})	8.643E-06	4.306E-05	1.522E-04	4.606E-04	3.466E-06	2.290E-05	6.932E-05	2.145E-04	7.954E-06	5.028E-05	1.691E-04	6.075E-04
σ	0.156	0.192	0.158	0.212	0.217	0.133	0.235	0.152	0.180	0.232	0.178	0.143

A.4.6 Environmental collisions (impeller + grinding chamber)

Table A11: Collision modal intensities for different impeller speeds at different revolutions for environmental (impeller + grinding chamber) collisions relevant to Figure 39f

	Normal energy loss (J)				Tangential energy loss (J)				Total energy loss (J)			
Revolution	200 rpm	350 rpm	500 rpm	700 rpm	200 rpm	350 rpm	500 rpm	700 rpm	200 rpm	350 rpm	500 rpm	700 rpm
1	4.739E-09	2.947E-08	7.983E-08	4.850E-08	3.276E-07	1.461E-06	3.353E-06	2.613E-06	3.015E-07	1.139E-06	2.840E-06	3.643E-06
2	7.179E-09	2.712E-08	7.983E-08	3.479E-08	3.015E-07	1.139E-06	2.613E-06	2.213E-06	3.015E-07	1.139E-06	2.840E-06	2.405E-06
3	5.150E-09	2.297E-08	8.675E-08	3.479E-08	2.775E-07	1.238E-06	2.213E-06	2.213E-06	2.775E-07	1.238E-06	2.840E-06	3.086E-06
4	5.150E-09	2.712E-08	5.727E-08	3.479E-08	2.775E-07	1.139E-06	2.213E-06	2.405E-06	2.775E-07	1.139E-06	2.405E-06	3.086E-06
5	5.150E-09	2.496E-08	5.727E-08	5.727E-08	2.775E-07	1.048E-06	1.875E-06	2.037E-06	3.015E-07	1.139E-06	2.613E-06	3.086E-06
6	5.150E-09	2.114E-08	9.426E-08	5.727E-08	2.775E-07	1.048E-06	2.405E-06	1.875E-06	2.775E-07	1.048E-06	2.613E-06	3.086E-06
7	5.596E-09	2.496E-08	6.222E-08	4.850E-08	2.350E-07	1.048E-06	2.037E-06	2.213E-06	2.554E-07	1.139E-06	2.405E-06	2.213E-06
8	4.362E-09	3.202E-08	6.222E-08	1.024E-07	2.554E-07	1.238E-06	2.213E-06	2.037E-06	2.554E-07	1.238E-06	2.405E-06	2.213E-06
9	6.081E-09	2.712E-08	9.426E-08	1.024E-07	2.554E-07	1.048E-06	2.213E-06	2.037E-06	2.554E-07	1.048E-06	2.405E-06	2.213E-06
10	5.150E-09	2.496E-08	6.761E-08	1.686E-07	2.554E-07	9.646E-07	2.613E-06	2.037E-06	2.554E-07	1.345E-06	2.840E-06	2.405E-06
11	4.739E-09	2.712E-08	6.222E-08	7.983E-08	1.991E-07	1.238E-06	2.037E-06	2.213E-06	1.991E-07	1.238E-06	2.213E-06	2.213E-06
12	4.739E-09	2.947E-08	8.675E-08	4.850E-08	2.350E-07	1.345E-06	2.037E-06	2.213E-06	2.554E-07	1.139E-06	2.037E-06	2.213E-06
13	4.014E-09	2.947E-08	4.850E-08	4.850E-08	1.991E-07	1.345E-06	2.405E-06	2.405E-06	2.554E-07	1.139E-06	2.037E-06	2.213E-06
14	4.362E-09	2.297E-08	6.761E-08	1.113E-07	2.350E-07	8.877E-07	2.037E-06	2.405E-06	2.554E-07	1.238E-06	2.840E-06	2.405E-06
15	4.362E-09	2.496E-08	6.761E-08	1.113E-07	2.163E-07	1.238E-06	2.840E-06	2.405E-06	2.163E-07	1.238E-06	2.840E-06	2.405E-06
Mean (e^{μ})	5.009E-09	2.623E-08	7.029E-08	6.433E-08	2.526E-07	1.152E-06	2.314E-06	2.213E-06	2.611E-07	1.171E-06	2.528E-06	2.556E-06
σ	0.146	0.112	0.201	0.499	0.143	0.136	0.153	0.089	0.115	0.068	0.121	0.170

Table A12: Collision modal peaks responsible for the most energy dissipation for the environmental (impeller + grinding chamber) collisions at different impeller agitation speeds at different revolutions relevant to Figure A4f

	Normal energy loss (J)				Tangential energy loss (J)				Total energy loss (J)			
Revolution	200 rpm	350 rpm	500 rpm	700 rpm	200 rpm	350 rpm	500 rpm	700 rpm	200 rpm	350 rpm	500 rpm	700 rpm
1	3.04E-03	2.06E-02	4.34E-02	3.68E-02	7.69E-06	4.78E-05	1.30E-04	2.97E-04	3.04E-03	2.06E-02	3.38E-02	6.58E-02
2	4.24E-03	1.25E-02	2.43E-02	6.58E-02	5.52E-06	3.43E-05	1.10E-04	3.51E-04	6.98E-03	1.36E-02	2.43E-02	6.58E-02
3	5.91E-03	1.25E-02	2.64E-02	2.64E-02	6.00E-06	4.40E-05	1.41E-04	3.23E-04	3.59E-03	1.06E-02	4.00E-02	3.38E-02
4	3.04E-03	1.06E-02	2.06E-02	2.43E-02	1.18E-01	4.78E-05	1.53E-04	2.74E-04	3.59E-03	1.47E-02	4.00E-02	6.58E-02
5	5.91E-03	1.47E-02	2.87E-02	7.77E-02	1.18E-01	5.65E-05	1.30E-04	3.23E-04	3.90E-03	9.74E-03	3.38E-02	4.00E-02
6	4.61E-03	9.74E-03	2.87E-02	4.72E-02	5.08E-06	4.78E-05	1.01E-04	4.15E-04	3.59E-03	1.25E-02	2.06E-02	4.00E-02
7	3.04E-03	1.06E-02	2.87E-02	4.72E-02	8.36E-06	6.14E-05	9.30E-05	2.74E-04	3.04E-03	1.06E-02	2.06E-02	7.15E-02
8	2.58E-03	1.74E-02	2.43E-02	5.13E-02	1.18E-01	3.73E-05	1.01E-04	2.74E-04	3.04E-03	2.43E-02	2.43E-02	5.13E-02
9	3.59E-03	8.96E-03	1.89E-02	5.13E-02	6.52E-06	3.43E-05	1.10E-04	2.74E-04	4.61E-03	1.25E-02	2.43E-02	5.13E-02
10	2.80E-03	1.06E-02	2.87E-02	4.72E-02	5.52E-06	4.78E-05	1.10E-04	2.74E-04	2.80E-03	8.96E-03	1.89E-02	4.34E-02
11	2.80E-03	9.74E-03	2.87E-02	4.72E-02	5.52E-06	4.78E-05	1.01E-04	2.97E-04	2.80E-03	2.64E-02	2.23E-02	4.34E-02
12	4.61E-03	1.25E-02	2.64E-02	9.96E-02	6.52E-06	6.67E-05	7.25E-05	2.97E-04	5.01E-03	2.06E-02	2.64E-02	9.17E-02
13	7.59E-03	1.25E-02	2.87E-02	9.96E-02	7.69E-06	6.67E-05	1.19E-04	3.23E-04	4.61E-03	2.06E-02	2.87E-02	1.08E-01
14	5.91E-03	1.74E-02	2.87E-02	5.13E-02	9.08E-06	4.05E-05	1.19E-04	2.13E-04	5.91E-03	2.06E-02	2.87E-02	5.13E-02
15	3.59E-03	1.06E-02	2.64E-02	4.72E-02	1.28E-01	3.73E-05	9.30E-05	2.97E-04	2.58E-03	1.06E-02	2.64E-02	5.13E-02
Mean (e^{μ})	3.99E-03	1.24E-02	2.70E-02	5.07E-02	8.99E-05	4.68E-05	1.10E-04	2.97E-04	3.78E-03	1.48E-02	2.68E-02	5.54E-02
σ	0.339	0.245	0.184	0.402	4.495	0.221	0.187	0.147	0.294	0.363	0.233	0.322

A.4.7 Energy dissipation collision modulii

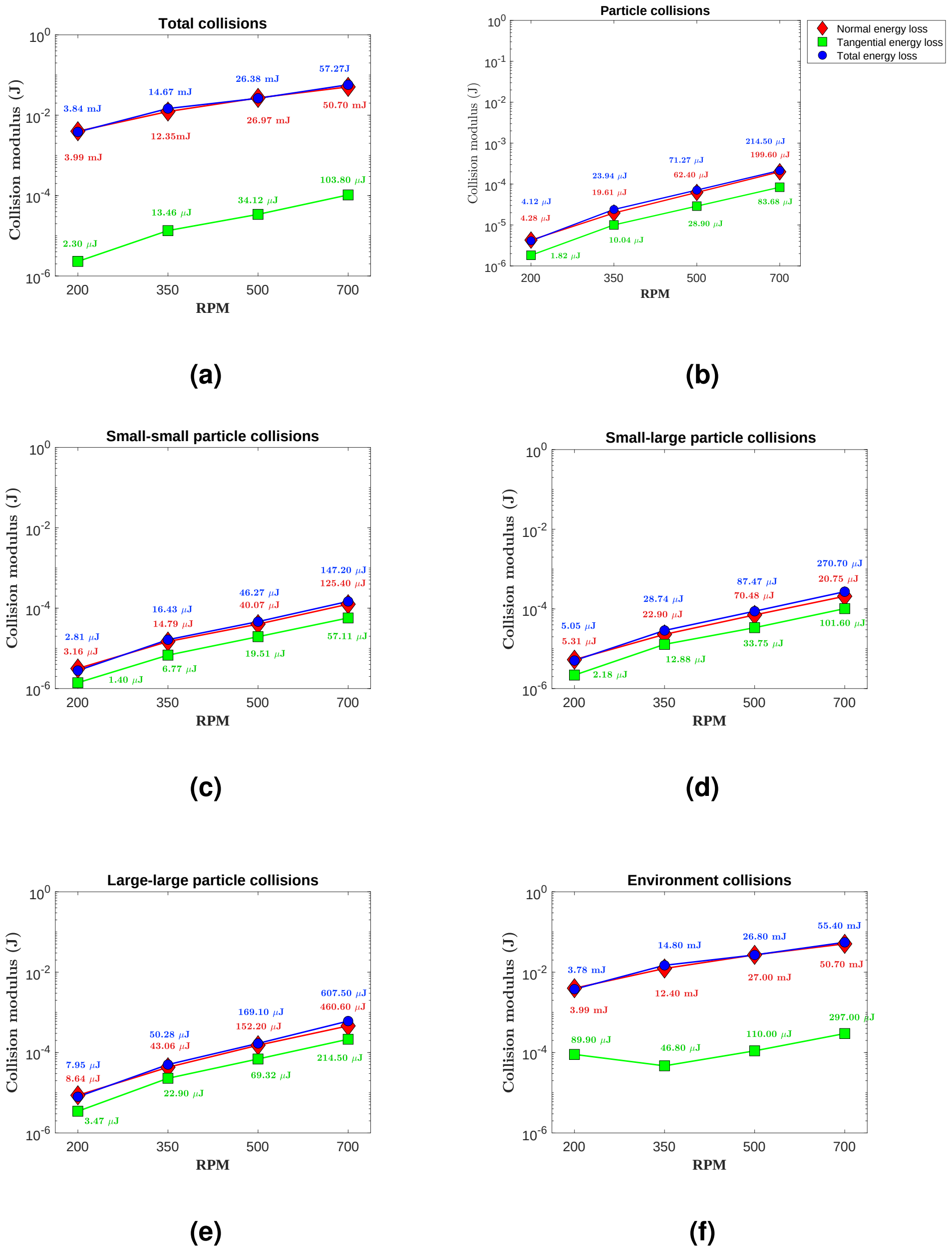

(a)

(b)

(c)

(d)

(e)

(f)

Figure A4: Modal peaks of the most energy dissipation intensities of the (a) total collisions, (b) total particle collisions, (c) small-small particle collisions, (d) small-large particle collisions, (e) large-large particle collisions and (f) environmental collisions (impeller + grinding chamber collisions) at different impeller speeds

A.4.8 Additional discussion of energy dissipation modulii

The logarithmic mean collision modal intensities of the first fifteen revolutions, for the different impeller speeds, are depicted in Figure 39. The collision modal values for the first fifteen revolutions are shown in Tables A1 and A11. Both the lognormal mean and deviation are reported in the tables. As can be seen in these tables, the collision moduli of the slower impeller speeds showed less deviation than that of the faster impeller speeds.

The method used to estimate this modulii is shown in Section 3.4.2. The resulting moduli are illustrated in Appendix A.8. Increasing the impeller speeds increased the collisions modulus that dissipated the most energy. Collision intensities have a logarithmic distribution, thus the more intense collisions are an order of magnitude larger than the bulk of collisions. It should be noted that the collisions that in turn dissipated the most energy are dictated by normal collisions. This is likely due to the impeller promoting direct collisions to the particles. The impeller in turn facilitates the most intense collisions, whilst further propagating the other types of particle-particle collisions.

A.5 Power filtering values at different impeller speeds

Power, P, at time, t_i, is estimated using

$$P_{unsmoothed,t_i} = \sum(\tau_{impeller,t_i}) \cdot \omega_{t_i}. \tag{40}$$

A histogram, with a lognormal distribution fitted to it, is shown in Figure A5. The upper and lower limits of the distribution is used to filter out any outliers in the data.

Afterwards, the filtered data is smoothed using a moving average. The energy consumed during the simulation is then estimated using

$$\xi = \int_{t_0}^{t_n} P_{smoothed}\, dt. \tag{41}$$

Finally, the uncertainty of the power consumption is estimated using

$$\hat{P} = \int_{t_0}^{t_n} (P_{unsmoothed} - P_{smoothed})\, dt. \tag{42}$$

Table A13: Estimated power values for various impeller speeds for a 6.50 kg systems with a 50-50 weight distribution of 8- and 5-mm particles

	Mean power (e^u)(W)	Lognormal variance (σ)	Min limit (W)	Max limit (W)	Energy consumed (J)	Estimated energy uncertainty (J)
200 rpm	80.76	0.478	31.06	209.97	268.53	± 3.28
350 rpm	257.26	0.627	73.47	900.80	1024.29	± 34.83
500 rpm	452.94	0.491	169.82	1208.08	1516.79	± 127.90
700 rpm	991.68	0.548	331.24	2968.74	3047.42	± 186.05

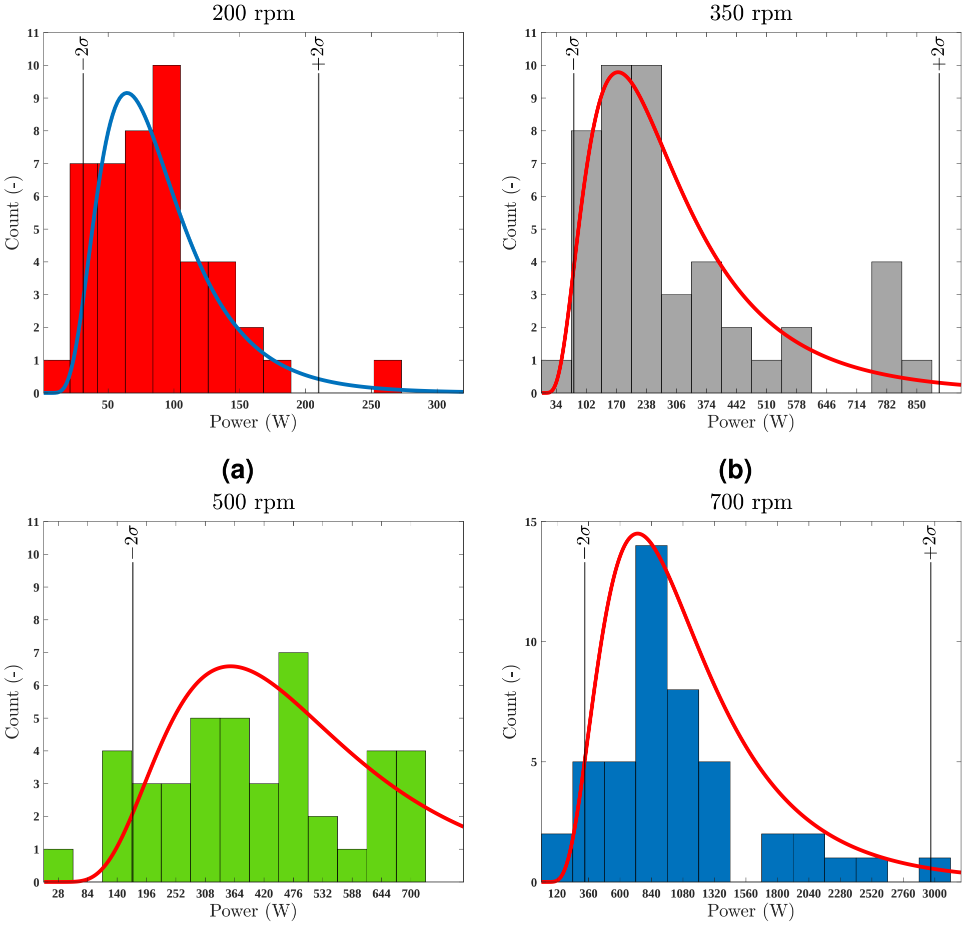

Figure A5: Histogram of power values between t = 2.00 s and t = 6.50 s with lognormal deviations estimated by the steady state power values between t = 3.50 s and t = 6.50 s

A.6 Additional and relations of Figure 42

Table A14: Summated energy proportions between t = 4.5 s and t = 6.5 s as used in Figure 42

	200 rpm	350 rpm	500 rpm	700 rpm
Total energy loss (J)	384.10	1139.94	2174.78	3895.09
Particle collisions	170.06	488.31	932.47	1654.13
Environmental collisions (impeller + chamber)	214.04	651.63	1242.48	2241.10
Environmental collisions (impeller)	192.12	570.09	1087.80	1948.02
Total collisions involving large particles	202.94	682.07	1213.89	2269.63
Total collisions involving small particles	253.43	684.36	1373.86	2372.93
Large-large particle	22.15	92.08	149.73	276.25
Small-small particle	75.63	169.77	365.05	625.79
Small-large particle	72.28	226.46	417.69	752.44
Normal energy loss (J)	251.02	769.31	1505.07	2743.62
Particle collisions	61.16	206.03	375.21	813.12
Environmental collisions (impeller + chamber)	189.86	563.29	942.15	1930.50
Environmental collisions (impeller)	188.02	555.83	927.60	1893.67
Large-large particle	8.22	38.39	61.42	136.70
Small-small particle	26.48	71.51	168.95	369.30
Small-large particle	26.47	96.13	144.84	307.12
Tangential energy loss (J)	122.90	349.96	640.74	1122.08
Particle collisions	93.30	245.17	423.03	741.45
Environmental collisions (impeller + chamber)	29.06	104.79	191.14	380.64
Environmental collisions (impeller)	11.23	35.82	67.41	140.41
Large-large particle	11.96	46.60	66.82	122.85
Small-small particle	41.86	84.99	166.88	280.18
Small-large particle	39.47	113.58	189.33	338.41

A.7 Collision modal intensities of the first 15 revolutions, when steady state had been reached, of different size-segregated weight distributions relevant to Figure 56

A.7.1 Total collisions

Table A15: Collision modal intensities for particle weight distributions at different revolutions for total collision energy losses relevant to Figure 56a

	Normal energy loss (J)					Tangential energy loss (J)					Total energy loss (J)				
Revolution	0 %	25 %	50 %	75 %	100 %	0 %	25 %	50 %	75 %	100 %	0 %	25 %	50 %	75 %	100 %
1	4.568E-07	1.024E-07	5.270E-08	2.947E-08	1.945E-08	1.345E-06	4.204E-07	1.552E-07	1.024E-07	7.347E-08	2.613E-06	8.170E-07	2.554E-07	1.991E-07	1.314E-07
2	6.368E-07	1.314E-07	4.850E-08	3.202E-08	2.297E-08	1.461E-06	4.204E-07	1.686E-07	1.113E-07	7.347E-08	2.613E-06	7.518E-07	2.775E-07	1.991E-07	1.314E-07
3	4.963E-07	1.024E-07	5.727E-08	2.947E-08	2.297E-08	1.238E-06	3.869E-07	1.832E-07	1.113E-07	7.347E-08	2.840E-06	7.518E-07	2.775E-07	1.832E-07	1.314E-07
4	5.860E-07	1.113E-07	5.270E-08	2.712E-08	1.945E-08	1.139E-06	4.204E-07	1.832E-07	1.113E-07	7.983E-08	2.840E-06	7.518E-07	2.775E-07	1.991E-07	1.314E-07
5	5.860E-07	1.024E-07	5.727E-08	3.202E-08	1.945E-08	1.345E-06	4.568E-07	1.832E-07	9.426E-08	7.983E-08	2.840E-06	8.877E-07	2.775E-07	1.686E-07	1.209E-07
6	6.368E-07	1.209E-07	4.850E-08	2.947E-08	2.114E-08	1.139E-06	4.568E-07	1.832E-07	1.024E-07	7.347E-08	2.405E-06	7.518E-07	3.015E-07	1.991E-07	1.314E-07
7	4.963E-07	1.209E-07	5.727E-08	2.712E-08	2.297E-08	1.238E-06	4.963E-07	1.686E-07	1.024E-07	7.347E-08	2.613E-06	8.877E-07	3.276E-07	1.832E-07	1.314E-07
8	4.963E-07	1.209E-07	5.270E-08	2.712E-08	2.114E-08	1.345E-06	5.393E-07	1.991E-07	1.209E-07	7.983E-08	2.840E-06	8.170E-07	2.775E-07	1.991E-07	1.314E-07
9	4.963E-07	1.428E-07	5.727E-08	2.947E-08	2.297E-08	1.238E-06	4.963E-07	1.552E-07	1.209E-07	7.983E-08	2.613E-06	7.518E-07	3.276E-07	1.832E-07	1.314E-07
10	4.568E-07	1.428E-07	5.727E-08	2.947E-08	2.114E-08	1.048E-06	4.963E-07	1.686E-07	1.113E-07	7.347E-08	2.613E-06	7.518E-07	3.015E-07	1.832E-07	1.314E-07
11	6.368E-07	1.209E-07	5.727E-08	2.947E-08	2.114E-08	1.345E-06	5.393E-07	1.832E-07	1.209E-07	7.983E-08	2.037E-06	7.518E-07	3.015E-07	2.163E-07	1.209E-07
12	6.919E-07	1.209E-07	5.727E-08	2.947E-08	1.945E-08	1.345E-06	4.568E-07	1.552E-07	1.024E-07	7.983E-08	2.613E-06	7.518E-07	3.276E-07	2.163E-07	1.209E-07
13	5.860E-07	1.209E-07	5.727E-08	3.202E-08	2.297E-08	1.725E-06	4.568E-07	1.552E-07	1.024E-07	7.983E-08	2.840E-06	8.877E-07	3.276E-07	1.832E-07	1.428E-07
14	5.860E-07	1.314E-07	5.270E-08	2.947E-08	1.945E-08	1.461E-06	4.568E-07	1.991E-07	1.113E-07	7.983E-08	2.213E-06	7.518E-07	3.015E-07	1.686E-07	1.314E-07
15	4.204E-07	1.024E-07	5.270E-08	2.712E-08	2.114E-08	1.048E-06	4.568E-07	1.686E-07	1.209E-07	7.347E-08	2.213E-06	7.518E-07	2.775E-07	1.686E-07	1.314E-07
Mean (e^u)	5.453E-07	1.189E-07	5.448E-08	2.930E-08	2.114E-08	1.286E-06	4.619E-07	1.733E-07	1.095E-07	7.680E-08	2.570E-06	7.859E-07	2.949E-07	1.894E-07	1.300E-07
σ	0.150	0.114	0.061	0.058	0.070	0.133	0.093	0.087	0.078	0.043	0.105	0.069	0.080	0.082	0.043

Table A16: Collision modal intensities for the most energy dissipation at different particle weight distributions at different revolutions for total collision energy losses

	Normal energy loss (J)					Tangential energy loss (J)					Total energy loss (J)				
Revolution	0 %	25 %	50 %	75 %	100 %	0 %	25 %	50 %	75 %	100 %	0 %	25 %	50 %	75 %	100 %
1	3.677E-02	1.892E-02	2.056E-02	7.588E-03	5.914E-03	4.402E-05	2.461E-05	9.871E-06	7.694E-06	4.302E-06	2.427E-02	1.149E-02	1.741E-02	8.959E-03	5.914E-03
2	5.126E-02	1.357E-02	1.249E-02	8.959E-03	4.243E-03	4.402E-05	2.461E-05	9.871E-06	7.694E-06	4.674E-06	3.677E-02	1.149E-02	1.058E-02	8.959E-03	5.914E-03
3	3.384E-02	2.234E-02	1.249E-02	1.149E-02	5.443E-03	4.402E-05	2.461E-05	1.165E-05	8.360E-06	4.674E-06	2.427E-02	3.114E-02	1.058E-02	1.058E-02	4.243E-03
4	1.149E-02	1.602E-02	1.058E-02	8.245E-03	3.904E-03	4.783E-05	2.265E-05	1.165E-05	7.081E-06	4.674E-06	3.114E-02	1.249E-02	1.475E-02	8.959E-03	3.904E-03
5	2.866E-02	3.114E-02	1.475E-02	9.735E-03	2.801E-03	4.783E-05	2.461E-05	1.073E-05	7.081E-06	5.079E-06	1.892E-02	1.602E-02	9.735E-03	8.959E-03	3.904E-03
6	2.234E-02	2.056E-02	9.735E-03	9.735E-03	3.593E-03	4.051E-05	3.431E-05	1.165E-05	8.360E-06	4.302E-06	7.588E-03	1.357E-02	1.249E-02	9.735E-03	3.904E-03
7	5.570E-02	2.056E-02	1.058E-02	8.245E-03	5.914E-03	4.051E-05	2.906E-05	1.165E-05	8.360E-06	4.302E-06	1.602E-02	2.056E-02	1.058E-02	7.588E-03	5.914E-03
8	1.602E-02	2.638E-02	1.741E-02	5.443E-03	4.243E-03	4.051E-05	2.906E-05	9.871E-06	9.084E-06	4.674E-06	1.602E-02	1.249E-02	2.427E-02	5.443E-03	4.610E-03
9	1.602E-02	1.892E-02	8.959E-03	1.058E-02	4.610E-03	4.783E-05	2.674E-05	9.084E-06	7.694E-06	5.519E-06	2.056E-02	1.149E-02	1.249E-02	6.983E-03	4.610E-03
10	2.866E-02	1.149E-02	1.058E-02	1.249E-02	3.593E-03	4.051E-05	2.461E-05	9.084E-06	7.694E-06	5.079E-06	2.866E-02	8.959E-03	8.959E-03	8.245E-03	3.043E-03
11	3.114E-02	2.427E-02	9.735E-03	7.588E-03	3.904E-03	4.402E-05	2.906E-05	1.073E-05	8.360E-06	3.959E-06	3.384E-02	8.959E-03	2.638E-02	7.588E-03	3.904E-03
12	1.249E-02	1.357E-02	1.249E-02	5.443E-03	3.904E-03	4.783E-05	1.918E-05	9.871E-06	8.360E-06	5.079E-06	1.357E-02	2.056E-02	2.056E-02	5.914E-03	3.307E-03
13	1.149E-02	1.357E-02	1.249E-02	1.357E-02	4.610E-03	5.198E-05	3.158E-05	9.871E-06	8.360E-06	5.079E-06	1.249E-02	1.741E-02	2.056E-02	1.475E-02	4.243E-03
14	2.427E-02	2.056E-02	1.741E-02	8.245E-03	3.904E-03	4.051E-05	2.265E-05	1.165E-05	9.084E-06	3.959E-06	2.234E-02	2.056E-02	2.056E-02	7.588E-03	5.443E-03
15	1.058E-02	1.892E-02	1.058E-02	6.427E-03	3.904E-03	3.728E-05	2.265E-05	1.165E-05	8.360E-06	4.674E-06	2.234E-02	1.741E-02	1.058E-02	6.427E-03	3.904E-03
Mean (e^u)	2.271E-02	1.871E-02	1.235E-02	8.619E-03	4.219E-03	4.378E-05	2.573E-05	1.055E-05	8.087E-06	4.648E-06	2.033E-02	1.475E-02	1.442E-02	8.200E-03	4.362E-03
σ	0.547	0.277	0.245	0.273	0.200	0.091	0.150	0.095	0.076	0.097	0.421	0.348	0.364	0.246	0.207

A.7.2 Particle collisions

Table A17: Collision modal intensities for particle weight distributions at different revolutions for total collision energy losses relevant to Figure 56b

	Normal energy loss (J)					Tangential energy loss (J)					Total energy loss (J)				
Revolution	0 %	25 %	50 %	75 %	100 %	0 %	25 %	50 %	75 %	100 %	0 %	25 %	50 %	75 %	100 %
1	4.568E-07	1.024E-07	5.270E-08	2.947E-08	1.945E-08	1.345E-06	4.204E-07	1.552E-07	1.024E-07	6.761E-08	1.875E-06	5.860E-07	2.554E-07	1.686E-07	1.209E-07
2	6.368E-07	1.314E-07	4.850E-08	3.202E-08	2.297E-08	9.646E-07	4.204E-07	1.686E-07	9.426E-08	7.347E-08	2.213E-06	5.860E-07	2.775E-07	1.991E-07	1.209E-07
3	5.860E-07	1.552E-07	5.727E-08	2.947E-08	2.297E-08	1.139E-06	3.276E-07	1.832E-07	9.426E-08	7.347E-08	2.213E-06	5.860E-07	2.775E-07	1.552E-07	1.113E-07
4	5.860E-07	1.113E-07	5.270E-08	2.712E-08	2.297E-08	1.139E-06	3.276E-07	1.832E-07	1.113E-07	7.983E-08	1.875E-06	5.860E-07	2.775E-07	1.552E-07	1.209E-07
5	5.860E-07	1.024E-07	5.727E-08	3.202E-08	1.945E-08	1.139E-06	4.568E-07	1.832E-07	9.426E-08	6.761E-08	2.405E-06	6.919E-07	2.775E-07	1.552E-07	1.209E-07
6	6.368E-07	1.686E-07	4.850E-08	2.947E-08	2.114E-08	9.646E-07	4.568E-07	1.832E-07	9.426E-08	7.347E-08	2.213E-06	6.919E-07	3.015E-07	1.552E-07	1.314E-07
7	4.963E-07	1.209E-07	5.727E-08	2.712E-08	2.297E-08	1.238E-06	3.869E-07	1.686E-07	1.024E-07	7.347E-08	1.875E-06	6.368E-07	3.276E-07	1.552E-07	1.314E-07
8	4.963E-07	1.209E-07	5.270E-08	2.947E-08	2.114E-08	1.345E-06	3.869E-07	1.991E-07	9.426E-08	7.347E-08	1.875E-06	7.518E-07	2.775E-07	1.686E-07	1.209E-07
9	4.963E-07	1.428E-07	5.727E-08	2.947E-08	2.297E-08	1.048E-06	3.560E-07	1.552E-07	1.113E-07	6.761E-08	2.213E-06	7.518E-07	3.276E-07	1.832E-07	1.209E-07
10	5.393E-07	1.428E-07	5.727E-08	2.947E-08	2.114E-08	1.048E-06	3.560E-07	1.686E-07	1.113E-07	6.761E-08	1.875E-06	5.860E-07	3.015E-07	1.686E-07	1.209E-07
11	6.368E-07	1.552E-07	5.727E-08	2.947E-08	2.114E-08	1.238E-06	3.869E-07	1.832E-07	9.426E-08	6.761E-08	2.037E-06	7.518E-07	3.015E-07	1.686E-07	1.209E-07
12	6.919E-07	1.428E-07	5.727E-08	2.947E-08	1.945E-08	1.139E-06	4.568E-07	1.552E-07	9.426E-08	6.761E-08	2.037E-06	7.518E-07	3.276E-07	1.686E-07	1.209E-07
13	5.860E-07	1.686E-07	5.727E-08	3.202E-08	2.297E-08	1.139E-06	3.869E-07	1.552E-07	9.426E-08	6.761E-08	2.037E-06	6.368E-07	3.276E-07	1.832E-07	1.209E-07
14	5.860E-07	1.552E-07	5.270E-08	2.947E-08	2.114E-08	1.139E-06	3.869E-07	1.991E-07	1.113E-07	6.761E-08	2.037E-06	6.919E-07	3.015E-07	1.686E-07	1.314E-07
15	5.393E-07	1.428E-07	5.270E-08	3.202E-08	2.114E-08	1.048E-06	3.869E-07	1.686E-07	9.426E-08	7.347E-08	2.213E-06	6.919E-07	2.775E-07	1.686E-07	1.314E-07
Mean (e^u)	5.669E-07	1.358E-07	5.448E-08	2.979E-08	2.149E-08	1.133E-06	3.912E-07	1.733E-07	9.963E-08	7.068E-08	2.060E-06	6.619E-07	2.949E-07	1.677E-07	1.230E-07
σ	0.117	0.166	0.061	0.053	0.064	0.102	0.108	0.087	0.075	0.053	0.082	0.103	0.080	0.073	0.047

Table A18: Collision modal intensities for the most energy dissipation at different particle weight distributions at different revolutions for particle-particle collision energy losses

	Normal energy loss (J)					Tangential energy loss (J)					Total energy loss (J)				
Revolution	0 %	25 %	50 %	75 %	100 %	0 %	25 %	50 %	75 %	100 %	0 %	25 %	50 %	75 %	100 %
1	7.246E-05	4.051E-05	1.918E-05	1.376E-05	7.694E-06	3.158E-05	1.765E-05	9.871E-06	6.516E-06	3.959E-06	8.555E-05	3.728E-05	2.265E-05	1.625E-05	9.084E-06
2	6.668E-05	3.728E-05	1.625E-05	1.376E-05	7.694E-06	3.728E-05	1.625E-05	9.871E-06	6.516E-06	3.959E-06	6.668E-05	5.198E-05	2.085E-05	1.376E-05	1.073E-05
3	5.648E-05	3.728E-05	2.265E-05	1.495E-05	7.081E-06	2.906E-05	1.625E-05	9.084E-06	5.997E-06	3.643E-06	7.246E-05	5.198E-05	2.265E-05	1.376E-05	8.360E-06
4	6.137E-05	3.431E-05	1.918E-05	1.266E-05	7.081E-06	3.158E-05	1.625E-05	1.165E-05	5.997E-06	3.643E-06	7.246E-05	4.783E-05	2.265E-05	1.376E-05	9.084E-06
5	6.137E-05	3.431E-05	2.674E-05	1.266E-05	7.081E-06	3.431E-05	1.625E-05	1.073E-05	5.997E-06	3.959E-06	7.246E-05	4.783E-05	2.265E-05	1.376E-05	9.084E-06
6	6.137E-05	2.906E-05	2.265E-05	1.266E-05	8.360E-06	3.431E-05	1.625E-05	9.084E-06	5.997E-06	4.302E-06	6.668E-05	4.051E-05	2.461E-05	1.376E-05	8.360E-06
7	5.198E-05	2.906E-05	1.918E-05	1.376E-05	7.694E-06	2.906E-05	1.625E-05	1.165E-05	5.997E-06	4.302E-06	6.668E-05	4.783E-05	2.085E-05	1.765E-05	9.871E-06
8	6.668E-05	4.051E-05	2.085E-05	1.266E-05	9.084E-06	3.431E-05	1.625E-05	9.871E-06	6.516E-06	3.959E-06	6.668E-05	4.783E-05	2.265E-05	1.376E-05	8.360E-06
9	5.648E-05	3.158E-05	1.765E-05	1.165E-05	9.084E-06	3.158E-05	1.765E-05	9.084E-06	6.516E-06	3.959E-06	6.668E-05	3.728E-05	2.674E-05	1.376E-05	8.360E-06
10	4.783E-05	3.158E-05	1.918E-05	1.266E-05	8.360E-06	3.158E-05	2.085E-05	9.084E-06	7.081E-06	3.959E-06	8.555E-05	4.402E-05	2.461E-05	1.376E-05	9.871E-06
11	5.198E-05	3.158E-05	1.765E-05	1.165E-05	9.084E-06	3.431E-05	1.918E-05	1.073E-05	5.997E-06	3.959E-06	7.873E-05	4.402E-05	2.906E-05	1.376E-05	8.360E-06
12	5.198E-05	3.728E-05	1.918E-05	1.165E-05	7.081E-06	3.431E-05	1.918E-05	9.871E-06	6.516E-06	3.959E-06	7.873E-05	4.402E-05	2.674E-05	1.376E-05	9.084E-06
13	5.198E-05	3.431E-05	1.918E-05	1.266E-05	9.084E-06	3.158E-05	1.918E-05	9.871E-06	5.997E-06	3.959E-06	9.296E-05	4.402E-05	2.674E-05	1.625E-05	9.871E-06
14	6.137E-05	4.051E-05	1.625E-05	1.266E-05	8.360E-06	3.158E-05	2.085E-05	1.165E-05	5.997E-06	3.959E-06	8.555E-05	4.402E-05	2.265E-05	1.625E-05	9.871E-06
15	6.137E-05	4.051E-05	2.085E-05	1.266E-05	7.694E-06	3.158E-05	2.085E-05	9.084E-06	5.519E-06	3.643E-06	8.555E-05	4.402E-05	2.461E-05	1.376E-05	9.871E-06
Mean (e^u)	5.839E-05	3.508E-05	1.961E-05	1.281E-05	7.998E-06	3.246E-05	1.785E-05	1.004E-05	6.200E-06	3.937E-06	7.574E-05	4.476E-05	2.394E-05	1.446E-05	9.185E-06
σ	0.117	0.119	0.131	0.069	0.099	0.068	0.103	0.095	0.061	0.049	0.117	0.100	0.098	0.088	0.082

A.7.3 Small-small particle collisions

Table A19: Collision modal intensities for particle weight distributions at different revolutions for small-small particle collision energy losses relevant to Figure 56c

	Normal energy loss (J)					Tangential energy loss (J)					Total energy loss (J)				
Revolution	0 %	25 %	50 %	75 %	100 %	0 %	25 %	50 %	75 %	100 %	0 %	25 %	50 %	75 %	100 %
1		6.761E-08	3.479E-08	2.947E-08	1.945E-08		2.163E-07	1.314E-07	8.675E-08	6.761E-08		4.568E-07	2.163E-07	1.428E-07	1.209E-07
2		6.222E-08	3.202E-08	2.947E-08	2.297E-08		1.552E-07	1.209E-07	9.426E-08	7.347E-08		3.276E-07	1.991E-07	1.428E-07	1.209E-07
3		5.270E-08	3.780E-08	2.496E-08	2.297E-08		1.832E-07	1.209E-07	7.347E-08	7.347E-08		3.869E-07	2.350E-07	1.428E-07	1.113E-07
4		4.463E-08	2.947E-08	2.496E-08	2.297E-08		1.686E-07	1.209E-07	7.347E-08	7.983E-08		3.560E-07	2.163E-07	1.428E-07	1.209E-07
5		5.727E-08	3.202E-08	2.712E-08	1.945E-08		1.686E-07	1.209E-07	9.426E-08	6.761E-08		2.775E-07	2.163E-07	1.314E-07	1.209E-07
6		6.222E-08	3.202E-08	2.496E-08	2.114E-08		1.832E-07	1.209E-07	9.426E-08	7.347E-08		2.554E-07	1.991E-07	1.552E-07	1.314E-07
7		6.222E-08	3.780E-08	2.496E-08	2.297E-08		1.686E-07	1.113E-07	8.675E-08	7.347E-08		3.560E-07	2.163E-07	1.552E-07	1.314E-07
8		7.347E-08	4.108E-08	2.496E-08	2.114E-08		1.686E-07	1.552E-07	8.675E-08	7.347E-08		3.560E-07	2.554E-07	1.428E-07	1.209E-07
9		7.347E-08	2.947E-08	2.712E-08	2.297E-08		1.832E-07	1.209E-07	8.675E-08	6.761E-08		4.204E-07	1.832E-07	1.428E-07	1.209E-07
10		4.108E-08	3.202E-08	2.712E-08	2.114E-08		1.991E-07	1.209E-07	7.983E-08	6.761E-08		4.204E-07	2.350E-07	1.686E-07	1.209E-07
11		4.108E-08	3.202E-08	2.496E-08	2.114E-08		1.991E-07	1.552E-07	7.983E-08	6.761E-08		3.869E-07	2.163E-07	1.552E-07	1.209E-07
12		4.108E-08	3.202E-08	2.712E-08	1.945E-08		1.991E-07	1.314E-07	9.426E-08	6.761E-08		3.869E-07	2.350E-07	1.552E-07	1.209E-07
13		7.347E-08	3.202E-08	2.496E-08	2.297E-08		2.350E-07	1.314E-07	9.426E-08	6.761E-08		3.560E-07	2.350E-07	1.428E-07	1.209E-07
14		6.761E-08	3.202E-08	2.496E-08	2.114E-08		1.991E-07	1.024E-07	8.675E-08	6.761E-08		4.963E-07	1.991E-07	1.428E-07	1.314E-07
15		5.727E-08	3.780E-08	2.496E-08	2.114E-08		1.991E-07	1.314E-07	9.426E-08	7.347E-08		3.560E-07	1.991E-07	1.552E-07	1.314E-07
Mean (e^u)		5.727E-08	3.347E-08	2.609E-08	2.149E-08		1.873E-07	1.257E-07	8.675E-08	7.068E-08		3.680E-07	2.163E-07	1.476E-07	1.230E-07
σ		0.217	0.099	0.062	0.064		0.111	0.108	0.089	0.053		0.171	0.089	0.061	0.047

Table A20: Collision modal intensities for the most energy dissipation values at different particle weight distributions at different revolutions for small-small particle collision energy losses

	Normal energy loss (J)					Tangential energy loss (J)					Total energy loss (J)				
Revolution	0 %	25 %	50 %	75 %	100 %	0 %	25 %	50 %	75 %	100 %	0 %	25 %	50 %	75 %	100 %
1		1.918E-05	1.376E-05	9.084E-06	7.694E-06		7.694E-06	5.997E-06	5.079E-06	3.959E-06		1.918E-05	1.765E-05	1.165E-05	9.084E-06
2		2.265E-05	1.495E-05	1.073E-05	7.694E-06		7.081E-06	6.516E-06	4.674E-06	3.959E-06		1.918E-05	1.918E-05	1.376E-05	1.073E-05
3		1.625E-05	1.376E-05	1.165E-05	7.081E-06		8.360E-06	6.516E-06	4.674E-06	3.643E-06		1.918E-05	1.376E-05	1.376E-05	8.360E-06
4		2.461E-05	1.625E-05	1.165E-05	7.081E-06		6.516E-06	7.081E-06	5.079E-06	3.643E-06		2.085E-05	1.765E-05	1.376E-05	9.084E-06
5		1.765E-05	1.625E-05	1.266E-05	7.081E-06		8.360E-06	6.516E-06	5.519E-06	3.959E-06		1.495E-05	1.625E-05	1.376E-05	9.084E-06
6		1.765E-05	1.376E-05	1.266E-05	8.360E-06		8.360E-06	7.081E-06	5.997E-06	4.302E-06		1.625E-05	1.765E-05	1.266E-05	8.360E-06
7		1.625E-05	1.625E-05	1.266E-05	7.694E-06		8.360E-06	7.081E-06	4.674E-06	4.302E-06		1.625E-05	1.625E-05	1.073E-05	9.871E-06
8		1.625E-05	1.765E-05	1.266E-05	9.084E-06		7.694E-06	7.081E-06	5.997E-06	3.959E-06		1.918E-05	1.495E-05	1.376E-05	8.360E-06
9		2.085E-05	1.765E-05	1.165E-05	9.084E-06		7.694E-06	6.516E-06	5.079E-06	3.959E-06		1.918E-05	1.625E-05	1.376E-05	8.360E-06
10		2.265E-05	1.266E-05	1.266E-05	8.360E-06		8.360E-06	7.081E-06	4.674E-06	3.959E-06		1.918E-05	1.495E-05	1.376E-05	9.871E-06
11		1.266E-05	1.266E-05	1.073E-05	9.084E-06		6.516E-06	5.997E-06	5.997E-06	3.959E-06		1.495E-05	1.495E-05	1.266E-05	8.360E-06
12		1.376E-05	1.376E-05	1.165E-05	7.081E-06		6.516E-06	7.081E-06	5.079E-06	3.959E-06		1.918E-05	1.765E-05	1.376E-05	9.084E-06
13		1.165E-05	1.376E-05	1.266E-05	9.084E-06		7.694E-06	7.081E-06	4.674E-06	3.959E-06		1.495E-05	1.765E-05	1.376E-05	9.871E-06
14		1.495E-05	1.625E-05	1.073E-05	8.360E-06		7.694E-06	6.516E-06	5.519E-06	3.959E-06		1.765E-05	1.918E-05	1.165E-05	9.871E-06
15		1.376E-05	1.376E-05	1.266E-05	7.694E-06		7.694E-06	7.694E-06	5.519E-06	3.643E-06		1.918E-05	1.376E-05	1.165E-05	9.871E-06
Mean (e^u)		1.698E-05	1.479E-05	1.172E-05	7.998E-06		7.609E-06	6.774E-06	5.193E-06	3.937E-06		1.785E-05	1.643E-05	1.295E-05	9.185E-06
σ		0.224	0.113	0.097	0.099		0.093	0.069	0.097	0.049		0.113	0.108	0.086	0.082

A.7.4 Small-large particle collisions

Table A21: Collision modal intensities for particle weight distributions at different revolutions for small-large particle collision energy losses relevant to Figure 56d

	Normal energy loss (J)					Tangential energy loss (J)					Total energy loss (J)				
Revolution	0 %	25 %	50 %	75 %	100 %	0 %	25 %	50 %	75 %	100 %	0 %	25 %	50 %	75 %	100 %
1		1.024E-07	6.761E-08	3.780E-08			2.775E-07	1.991E-07	1.552E-07			5.860E-07	3.015E-07	2.554E-07	
2		1.314E-07	6.761E-08	5.270E-08			2.775E-07	1.686E-07	1.686E-07			5.860E-07	3.869E-07	2.554E-07	
3		9.426E-08	7.347E-08	4.850E-08			3.015E-07	1.991E-07	1.428E-07			5.393E-07	3.276E-07	2.554E-07	
4		9.426E-08	6.222E-08	4.463E-08			3.015E-07	2.554E-07	1.314E-07			5.860E-07	3.869E-07	2.554E-07	
5		9.426E-08	5.727E-08	4.463E-08			3.015E-07	1.832E-07	1.314E-07			4.963E-07	3.869E-07	2.554E-07	
6		1.113E-07	7.347E-08	4.850E-08			3.276E-07	2.350E-07	1.552E-07			4.963E-07	3.560E-07	2.554E-07	
7		1.113E-07	5.727E-08	5.270E-08			3.276E-07	2.350E-07	1.552E-07			6.368E-07	4.568E-07	2.775E-07	
8		1.209E-07	7.347E-08	5.727E-08			3.869E-07	2.163E-07	1.314E-07			6.368E-07	3.869E-07	2.350E-07	
9		1.428E-07	9.426E-08	4.850E-08			3.560E-07	2.163E-07	1.209E-07			7.518E-07	4.204E-07	1.991E-07	
10		1.428E-07	7.983E-08	4.850E-08			3.276E-07	2.163E-07	1.428E-07			5.860E-07	3.276E-07	2.554E-07	
11		1.428E-07	8.675E-08	5.727E-08			3.276E-07	1.991E-07	1.428E-07			5.860E-07	3.560E-07	2.775E-07	
12		1.209E-07	6.761E-08	5.727E-08			3.276E-07	2.350E-07	1.314E-07			6.919E-07	3.276E-07	2.350E-07	
13		1.209E-07	6.761E-08	5.727E-08			3.869E-07	2.350E-07	1.209E-07			6.919E-07	3.276E-07	2.554E-07	
14		1.113E-07	6.761E-08	5.270E-08			3.869E-07	1.991E-07	1.686E-07			6.919E-07	3.560E-07	2.350E-07	
15		1.024E-07	7.347E-08	5.270E-08			3.560E-07	1.991E-07	1.686E-07			5.860E-07	3.869E-07	2.350E-07	
Mean (e^u)		1.151E-07	7.068E-08	5.042E-08			3.295E-07	2.116E-07	1.436E-07			6.058E-07	3.640E-07	2.484E-07	
σ		0.150	0.136	0.117			0.111	0.111	0.115			0.121	0.111	0.081	

Table A22: Collision modal intensities for the most energy dissipation values at different particle weight distributions at different revolutions for small-large particle collision energy losses

	Normal energy loss (J)					Tangential energy loss (J)					Total energy loss (J)				
Revolution	0 %	25 %	50 %	75 %	100 %	0 %	25 %	50 %	75 %	100 %	0 %	25 %	50 %	75 %	100 %
1		2.674E-05	2.265E-05	2.265E-05			1.765E-05	9.871E-06	8.360E-06			3.158E-05	3.431E-05	2.085E-05	
2		3.158E-05	2.085E-05	2.265E-05			1.625E-05	1.376E-05	9.871E-06			3.728E-05	2.674E-05	2.085E-05	
3		3.728E-05	2.265E-05	1.918E-05			1.625E-05	1.625E-05	9.871E-06			3.158E-05	2.461E-05	2.085E-05	
4		3.431E-05	2.674E-05	1.765E-05			1.625E-05	1.165E-05	8.360E-06			3.728E-05	2.906E-05	2.085E-05	
5		2.674E-05	2.674E-05	1.918E-05			1.625E-05	1.495E-05	7.694E-06			4.051E-05	2.265E-05	2.461E-05	
6		2.906E-05	2.085E-05	1.918E-05			1.625E-05	9.871E-06	9.084E-06			4.051E-05	2.906E-05	2.265E-05	
7		2.265E-05	2.085E-05	2.085E-05			1.625E-05	1.165E-05	9.871E-06			4.783E-05	3.158E-05	2.265E-05	
8		2.906E-05	2.461E-05	2.461E-05			1.376E-05	1.765E-05	9.084E-06			4.402E-05	3.158E-05	2.674E-05	
9		2.461E-05	2.674E-05	1.918E-05			1.376E-05	1.165E-05	7.694E-06			3.728E-05	2.674E-05	2.674E-05	
10		3.431E-05	2.265E-05	2.265E-05			1.376E-05	1.625E-05	1.266E-05			3.728E-05	3.431E-05	2.085E-05	
11		3.158E-05	2.674E-05	1.918E-05			1.495E-05	1.376E-05	8.360E-06			3.728E-05	2.906E-05	2.085E-05	
12		2.461E-05	1.918E-05	1.625E-05			1.918E-05	1.073E-05	8.360E-06			3.431E-05	3.431E-05	2.461E-05	
13		2.461E-05	1.918E-05	2.461E-05			1.918E-05	1.073E-05	8.360E-06			3.158E-05	3.431E-05	2.906E-05	
14		2.906E-05	2.461E-05	1.918E-05			1.376E-05	1.165E-05	9.084E-06			3.728E-05	2.265E-05	3.158E-05	
15		4.051E-05	2.085E-05	1.495E-05			1.376E-05	1.625E-05	1.266E-05			3.431E-05	2.461E-05	1.918E-05	
Mean (e^u)		2.938E-05	2.290E-05	1.994E-05			1.572E-05	1.288E-05	9.185E-06			3.708E-05	2.874E-05	2.329E-05	
σ		0.169	0.121	0.143			0.117	0.197	0.153			0.119	0.150	0.146	

A.7.5 Large-large particle collisions

Table A23: Collision modal intensities for particle weight distributions at different revolutions for large-large particle collision energy losses relevant to Figure 56e

	Normal energy loss (J)					Tangential energy loss (J)					Total energy loss (J)				
Revolution	0 %	25 %	50 %	75 %	100 %	0 %	25 %	50 %	75 %	100 %	0 %	25 %	50 %	75 %	100 %
1	4.568E-07	3.276E-07	1.552E-07	7.347E-08		1.345E-06	6.368E-07	4.568E-07	3.560E-07		1.875E-06	1.139E-06	1.048E-06	4.568E-07	
2	6.368E-07	2.775E-07	1.832E-07	1.832E-07		9.646E-07	8.877E-07	4.963E-07	3.276E-07		2.213E-06	1.139E-06	8.877E-07	8.170E-07	
3	5.860E-07	2.775E-07	1.686E-07	1.832E-07		1.139E-06	6.368E-07	4.204E-07	3.560E-07		2.213E-06	1.345E-06	8.170E-07	4.204E-07	
4	5.860E-07	3.276E-07	1.832E-07	1.832E-07		1.139E-06	6.368E-07	4.568E-07	3.276E-07		1.875E-06	1.238E-06	9.646E-07	6.368E-07	
5	5.860E-07	3.015E-07	1.991E-07	1.209E-07		1.139E-06	6.368E-07	3.869E-07	3.560E-07		2.405E-06	1.588E-06	8.877E-07	8.877E-07	
6	6.368E-07	3.276E-07	1.552E-07	1.552E-07		9.646E-07	8.877E-07	3.560E-07	2.554E-07		2.213E-06	1.139E-06	6.368E-07	4.568E-07	
7	4.963E-07	3.560E-07	1.552E-07	1.209E-07		1.238E-06	8.170E-07	3.276E-07	3.015E-07		1.875E-06	1.345E-06	8.877E-07	7.518E-07	
8	4.963E-07	3.560E-07	1.686E-07	9.426E-08		1.345E-06	8.170E-07	3.869E-07	2.775E-07		1.875E-06	1.588E-06	8.170E-07	5.393E-07	
9	4.963E-07	3.276E-07	1.686E-07	9.426E-08		1.048E-06	6.919E-07	3.560E-07	2.775E-07		2.213E-06	1.345E-06	6.919E-07	5.860E-07	
10	5.393E-07	3.869E-07	1.991E-07	1.209E-07		1.048E-06	6.368E-07	3.869E-07	2.163E-07		1.875E-06	1.238E-06	7.518E-07	5.860E-07	
11	6.368E-07	3.276E-07	1.552E-07	7.983E-08		1.238E-06	6.368E-07	3.869E-07	2.554E-07		2.037E-06	1.238E-06	6.919E-07	3.276E-07	
12	6.919E-07	3.276E-07	1.832E-07	1.209E-07		1.139E-06	6.368E-07	4.568E-07	1.686E-07		2.037E-06	1.139E-06	1.048E-06	3.869E-07	
13	5.860E-07	3.560E-07	1.832E-07	1.113E-07		1.139E-06	7.518E-07	4.568E-07	2.775E-07		2.037E-06	1.139E-06	1.048E-06	4.963E-07	
14	5.860E-07	2.775E-07	2.350E-07	1.024E-07		1.139E-06	7.518E-07	4.963E-07	2.163E-07		2.037E-06	1.588E-06	8.877E-07	5.860E-07	
15	5.393E-07	3.560E-07	1.991E-07	1.113E-07		1.048E-06	6.919E-07	4.568E-07	2.554E-07		2.213E-06	1.139E-06	8.170E-07	5.393E-07	
Mean (e^u)	5.669E-07	3.258E-07	1.782E-07	1.189E-07		1.133E-06	7.113E-07	4.157E-07	2.760E-07		2.060E-06	1.279E-06	8.492E-07	5.453E-07	
σ	0.117	0.102	0.120	0.288		0.102	0.128	0.129	0.214		0.082	0.129	0.157	0.275	

Table A24: Collision modal intensities for the most energy dissipation values at different particle weight distributions at different revolutions for large-large particle collision energy losses

	Normal energy loss (J)					Tangential energy loss (J)					Total energy loss (J)				
Revolution	0 %	25 %	50 %	75 %	100 %	0 %	25 %	50 %	75 %	100 %	0 %	25 %	50 %	75 %	100 %
1	7.25E-05	5.20E-05	4.05E-05	2.91E-05		3.16E-05	2.46E-05	2.08E-05	2.46E-05		8.56E-05	7.25E-05	4.78E-05	4.40E-05	
2	6.67E-05	4.78E-05	5.65E-05	4.05E-05		3.73E-05	2.46E-05	2.67E-05	2.67E-05		6.67E-05	7.25E-05	3.73E-05	2.46E-05	
3	5.65E-05	4.40E-05	4.05E-05	9.30E-05		2.91E-05	2.08E-05	1.92E-05	1.50E-05		7.25E-05	7.25E-05	5.65E-05	2.27E-05	
4	6.14E-05	4.78E-05	3.73E-05	2.91E-05		3.16E-05	2.46E-05	2.08E-05	1.92E-05		7.25E-05	6.67E-05	4.40E-05	4.05E-05	
5	6.14E-05	4.40E-05	3.73E-05	3.43E-05		3.43E-05	2.46E-05	2.27E-05	1.17E-05		7.25E-05	6.67E-05	4.05E-05	3.73E-05	
6	6.14E-05	6.14E-05	4.05E-05	4.05E-05		3.43E-05	2.91E-05	2.46E-05	1.62E-05		6.67E-05	7.25E-05	5.20E-05	7.87E-05	
7	5.20E-05	7.25E-05	3.73E-05	4.40E-05		2.91E-05	2.91E-05	2.67E-05	1.62E-05		6.67E-05	7.25E-05	7.25E-05	4.78E-05	
8	6.67E-05	5.20E-05	4.05E-05	4.78E-05		3.43E-05	2.91E-05	2.08E-05	1.38E-05		6.67E-05	6.14E-05	3.73E-05	4.05E-05	
9	5.65E-05	5.20E-05	3.16E-05	3.43E-05		3.16E-05	2.91E-05	1.92E-05	3.16E-05		6.67E-05	7.25E-05	4.40E-05	3.16E-05	
10	4.78E-05	6.14E-05	6.14E-05	8.56E-05		3.16E-05	2.91E-05	2.27E-05	2.27E-05		8.56E-05	8.56E-05	6.14E-05	2.67E-05	
11	5.20E-05	6.67E-05	4.78E-05	4.05E-05		3.43E-05	2.91E-05	2.27E-05	2.27E-05		7.87E-05	7.87E-05	4.78E-05	3.43E-05	
12	5.20E-05	5.20E-05	4.05E-05	3.16E-05		3.43E-05	2.91E-05	2.67E-05	3.73E-05		7.87E-05	6.67E-05	5.20E-05	4.05E-05	
13	5.20E-05	4.40E-05	4.05E-05	3.16E-05		3.16E-05	2.91E-05	2.67E-05	2.27E-05		9.30E-05	6.67E-05	5.20E-05	5.20E-05	
14	6.14E-05	4.05E-05	6.14E-05	2.91E-05		3.16E-05	2.91E-05	2.67E-05	1.62E-05		8.56E-05	6.67E-05	8.56E-05	5.20E-05	
15	6.14E-05	5.20E-05	4.40E-05	2.08E-05		3.16E-05	3.16E-05	1.92E-05	1.92E-05		8.56E-05	6.67E-05	4.40E-05	3.73E-05	
Mean (e^u)	5.84E-05	5.20E-05	4.31E-05	3.88E-05		3.25E-05	2.73E-05	2.29E-05	2.01E-05		7.57E-05	7.05E-05	5.03E-05	3.88E-05	
σ	0.117	0.166	0.192	0.397		0.068	0.111	0.133	0.318		0.117	0.081	0.232	0.320	

A.7.6 Environmental collisions (impeller + grinding chamber)

Table A25: Collision modal intensities for different particle weight distributions at different revolutions for environmental (impeller + grinding chamber) collisions relevant to Figure 56f

	Normal energy loss (J)					Tangential energy loss (J)					Total energy loss (J)				
Revolution	0 %	25 %	50 %	75 %	100 %	0 %	25 %	50 %	75 %	100 %	0 %	25 %	50 %	75 %	100 %
1	3.015E-07	4.463E-08	5.319E-04	1.516E-08	8.477E-09	6.516E-06	2.213E-06	4.051E-05	8.877E-07	4.204E-07	8.360E-06	2.405E-06	4.228E-07	8.170E-07	4.963E-07
2	2.163E-07	4.463E-08	4.895E-04	1.945E-08	8.477E-09	6.516E-06	2.405E-06	4.051E-05	6.919E-07	4.204E-07	9.871E-06	2.405E-06	4.594E-07	7.518E-07	5.860E-07
3	2.163E-07	4.463E-08	5.780E-04	1.284E-08	1.284E-08	7.081E-06	2.405E-06	2.906E-05	7.518E-07	4.204E-07	6.516E-06	2.037E-06	3.033E-07	8.170E-07	5.393E-07
4	2.554E-07	6.761E-08	5.780E-04	1.647E-08	1.182E-08	7.081E-06	2.405E-06	3.728E-05	7.518E-07	4.568E-07	9.084E-06	2.405E-06	4.228E-07	8.170E-07	4.568E-07
5	2.163E-07	6.761E-08	5.319E-04	1.647E-08	1.647E-08	7.081E-06	1.875E-06	5.648E-05	8.877E-07	4.963E-07	7.081E-06	2.037E-06	3.581E-07	8.877E-07	5.393E-07
6	4.568E-07	5.270E-08	3.815E-04	1.647E-08	1.395E-08	8.360E-06	2.213E-06	3.158E-05	8.170E-07	4.963E-07	7.694E-06	1.875E-06	3.581E-07	8.170E-07	5.393E-07
7	3.276E-07	5.270E-08	5.780E-04	1.516E-08	1.182E-08	7.081E-06	2.037E-06	3.431E-05	6.919E-07	5.393E-07	8.360E-06	2.213E-06	3.891E-07	8.170E-07	5.393E-07
8	3.276E-07	5.727E-08	3.815E-04	1.516E-08	1.395E-08	5.519E-06	2.405E-06	5.198E-05	8.170E-07	4.963E-07	7.081E-06	2.840E-06	4.594E-07	6.919E-07	5.860E-07
9	2.775E-07	4.850E-08	3.815E-04	1.516E-08	1.182E-08	5.519E-06	2.213E-06	3.728E-05	8.170E-07	4.963E-07	7.694E-06	2.037E-06	3.581E-07	9.646E-07	4.963E-07
10	3.015E-07	6.222E-08	6.824E-04	1.790E-08	1.182E-08	7.081E-06	2.213E-06	4.783E-05	6.919E-07	4.963E-07	8.360E-06	2.213E-06	2.791E-07	6.919E-07	5.393E-07
11	2.554E-07	6.222E-08	5.319E-04	1.945E-08	1.395E-08	8.360E-06	2.613E-06	3.728E-05	6.919E-07	4.204E-07	8.360E-06	2.840E-06	2.791E-07	6.919E-07	5.393E-07
12	2.775E-07	6.222E-08	5.319E-04	1.647E-08	1.284E-08	7.081E-06	2.613E-06	4.051E-05	7.518E-07	4.963E-07	7.081E-06	2.840E-06	4.228E-07	8.170E-07	5.860E-07
13	2.554E-07	4.850E-08	5.319E-04	1.790E-08	1.284E-08	7.081E-06	2.037E-06	4.051E-05	7.518E-07	4.568E-07	7.694E-06	2.405E-06	4.228E-07	8.170E-07	5.860E-07
14	1.832E-07	5.270E-08	3.511E-04	1.945E-08	1.088E-08	6.516E-06	2.213E-06	4.051E-05	6.919E-07	5.860E-07	6.516E-06	2.213E-06	4.228E-07	8.170E-07	5.860E-07
15	2.163E-07	5.270E-08	5.780E-04	1.945E-08	1.088E-08	6.516E-06	2.405E-06	3.158E-05	5.860E-07	4.568E-07	7.081E-06	2.405E-06	4.228E-07	6.919E-07	4.963E-07
Mean (e^u)	2.655E-07	5.418E-08	5.005E-04	1.675E-08	1.202E-08	6.849E-06	2.276E-06	3.919E-05	7.477E-07	4.748E-07	7.737E-06	3.912E-05	5.348E-04	7.903E-07	5.393E-07
σ	0.228	0.146	0.197	0.122	0.178	0.117	0.092	0.183	0.111	0.099	0.119	0.129	0.214	0.098	0.077

Table A26: Collision modal peaks responsible for the most energy dissipation for the environmental (impeller + grinding chamber) collisions at different particle weight distributions at different revolutions

	Normal energy loss (J)					Tangential energy loss (J)					Total energy loss (J)				
Revolution	0 %	25 %	50 %	75 %	100 %	0 %	25 %	50 %	75 %	100 %	0 %	25 %	50 %	75 %	100 %
1	3.677E-02	1.892E-02	2.056E-02	7.588E-03	5.914E-03	1.807E-04	7.873E-05	4.505E-04	3.158E-05	5.648E-05	2.427E-02	1.149E-02	2.056E-02	8.959E-03	5.914E-03
2	5.126E-02	1.357E-02	1.249E-02	8.959E-03	4.243E-03	1.807E-04	7.873E-05	5.319E-04	2.674E-05	2.265E-05	3.677E-02	1.149E-02	1.058E-02	8.959E-03	5.914E-03
3	3.384E-02	2.234E-02	1.249E-02	1.149E-02	5.443E-03	1.296E-04	7.246E-05	4.146E-04	2.906E-05	1.765E-05	2.427E-02	3.114E-02	1.058E-02	1.058E-02	4.243E-03
4	1.149E-02	1.602E-02	1.058E-02	8.245E-03	3.904E-03	1.296E-04	1.098E-04	5.780E-04	3.158E-05	2.461E-05	1.892E-02	1.249E-02	1.475E-02	8.959E-03	3.904E-03
5	2.866E-02	3.114E-02	1.475E-02	9.735E-03	2.801E-03	1.193E-04	1.098E-04	4.146E-04	3.728E-05	3.158E-05	2.866E-02	1.602E-02	9.735E-03	8.959E-03	3.904E-03
6	2.234E-02	2.056E-02	9.735E-03	9.735E-03	3.593E-03	1.530E-04	1.098E-04	7.415E-04	3.728E-05	1.765E-05	7.588E-03	1.357E-02	1.249E-02	9.735E-03	3.904E-03
7	5.570E-02	2.056E-02	1.058E-02	8.245E-03	5.914E-03	1.530E-04	9.296E-05	1.176E-01	3.158E-05	2.085E-05	1.602E-02	2.056E-02	1.058E-02	5.009E-03	5.914E-03
8	1.602E-02	2.638E-02	1.741E-02	5.443E-03	4.243E-03	1.530E-04	9.296E-05	1.389E-01	2.461E-05	4.051E-05	1.602E-02	1.249E-02	2.427E-02	5.443E-03	4.610E-03
9	1.602E-02	1.892E-02	8.959E-03	1.058E-02	4.610E-03	1.296E-04	1.193E-04	1.782E-01	2.461E-05	2.461E-05	2.056E-02	1.149E-02	1.249E-02	6.983E-03	4.610E-03
10	2.866E-02	1.149E-02	1.058E-02	1.249E-02	3.593E-03	1.530E-04	7.873E-05	1.782E-01	3.431E-05	1.495E-05	2.866E-02	8.959E-03	8.959E-03	8.245E-03	3.307E-03
11	3.114E-02	2.427E-02	9.735E-03	7.588E-03	3.904E-03	1.530E-04	9.296E-05	1.389E-01	3.431E-05	2.461E-05	3.384E-02	8.959E-03	2.638E-02	7.588E-03	3.904E-03
12	1.249E-02	1.357E-02	1.249E-02	5.443E-03	3.904E-03	1.408E-04	7.873E-05	8.057E-04	3.431E-05	2.906E-05	1.357E-02	2.056E-02	2.056E-02	5.443E-03	3.307E-03
13	1.149E-02	1.357E-02	1.249E-02	1.357E-02	4.610E-03	1.663E-04	7.246E-05	8.057E-04	2.906E-05	1.376E-05	1.249E-02	1.741E-02	2.056E-02	1.475E-02	4.243E-03
14	2.427E-02	2.056E-02	1.741E-02	8.245E-03	3.904E-03	1.193E-04	7.246E-05	8.057E-04	2.674E-05	2.674E-05	2.234E-02	2.056E-02	2.056E-02	7.588E-03	5.443E-03
15	1.058E-02	1.892E-02	1.058E-02	6.427E-03	3.904E-03	1.193E-04	7.246E-05	4.146E-04	2.286E-01	1.083E-01	2.234E-02	1.741E-02	1.058E-02	6.427E-03	3.904E-03
Mean (e^u)	2.271E-02	1.871E-02	1.235E-02	8.619E-03	4.219E-03	1.440E-04	8.747E-05	3.653E-03	5.555E-05	4.258E-05	2.022E-02	1.475E-02	1.458E-02	7.932E-03	4.386E-03
σ	0.547	0.277	0.245	0.273	0.2	0.142	0.179	2.723	2.306	2.2	0.416	0.348	0.373	0.284	0.198

A.8 Estimation and filtering of torque values to consider for power consumption for Table 17, the steps discussed in Section 4.2.5 are applied here

Table A27: Torque lognormal values and estimated power consumption for various particle weight distributions for a 6.50 kg system at 350 rpm

	Mean (e^u)(W)	Lognormal variance (σ)	Min limit ($e^{u-2\sigma}$)(W)	Max limit ($e^{u+2\sigma}$)(W)	Energy consumed from torque (J)	Estimated energy uncertainty (J)
0 %	242.16	0.510	87.26	672.01	886.24	± 74.76
25 %	265.62	0.547	88.97	793.01	877.69	± 31.39
50 %	257.26	0.627	73.47	900.80	1024.29	± 34.83
75 %	249.40	0.610	73.66	844.42	972.22	± 116.62
100 %	223.73	0.354	110.13	454.51	642.51	± 22.67

The methods used to estimate power consumed is discussed in Appendix A.5. The 50 wt% data was estimated in Appendix A.5 as the 350 rpm impeller speed.

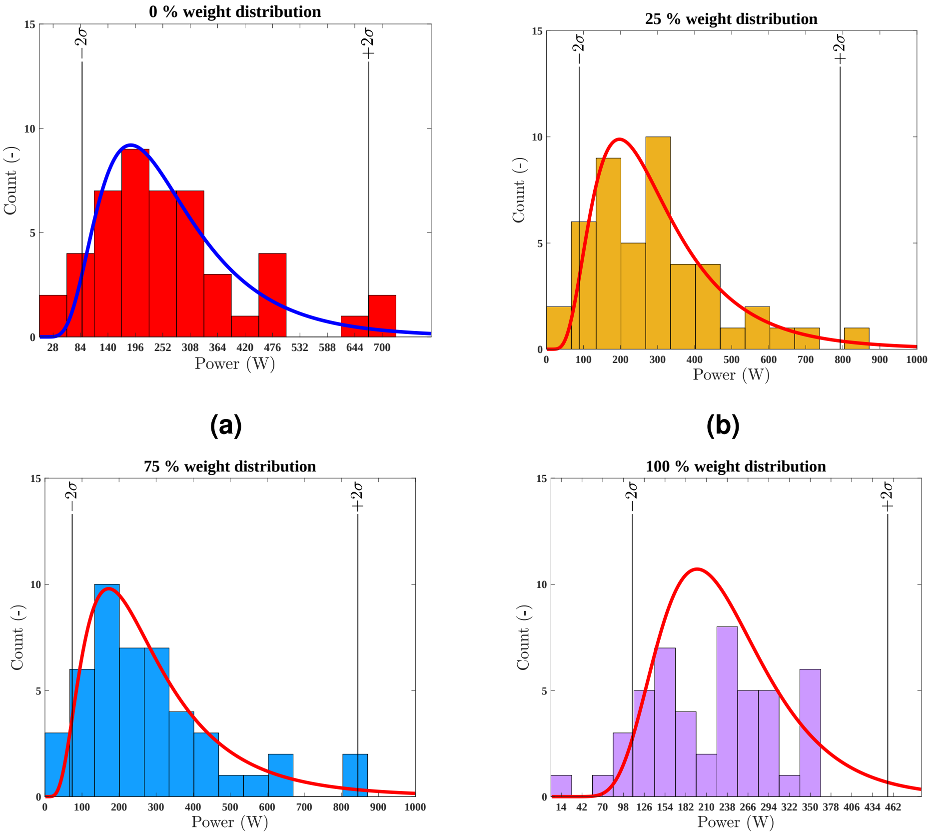

(a) **(b)**

(c) **(d)**

Figure A6: Power data of various particle weight distributions speeds from t = 2.00 s to t = 6.50 s

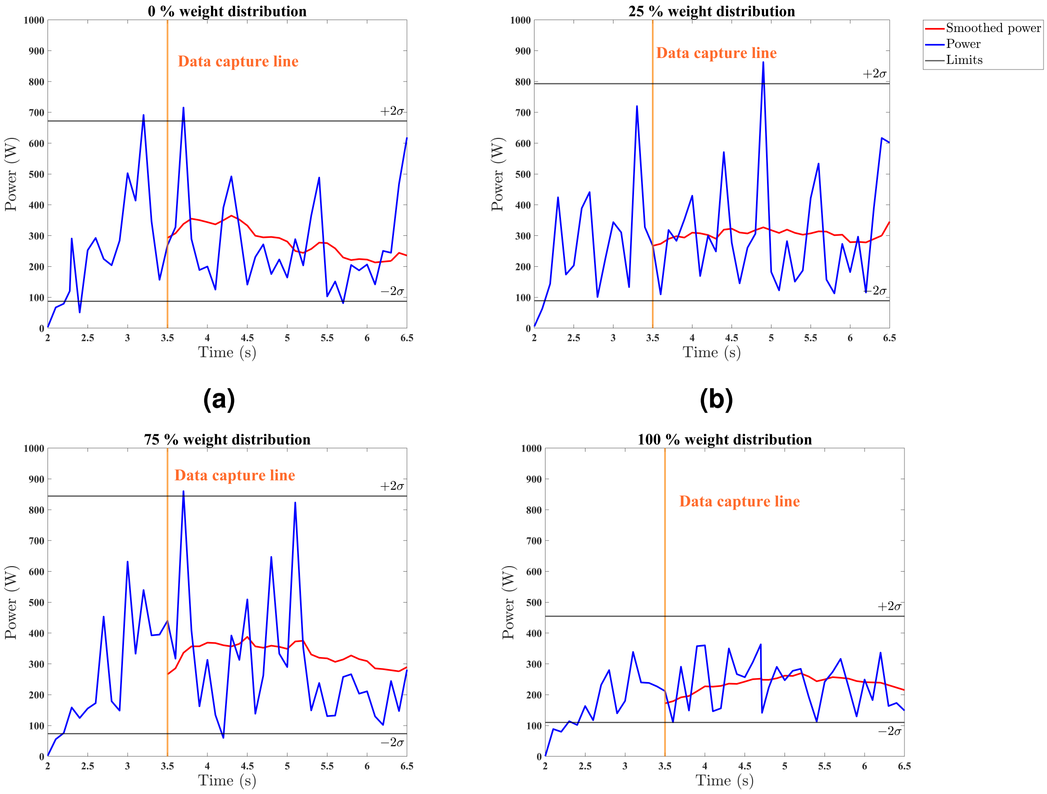

(a)

(b)

(c)

(d) 75 % - 5 mm + 25 % - 8 mm

Figure A7: Torque data of various particle weight distributions speeds

A.9 Angular velocity ranges for particles at different impeller speeds

Table A28: Angular velocity distributions of large and small particles at different regions relative to the impeller

Impeller region	Small particles	Large particles	
Second top region	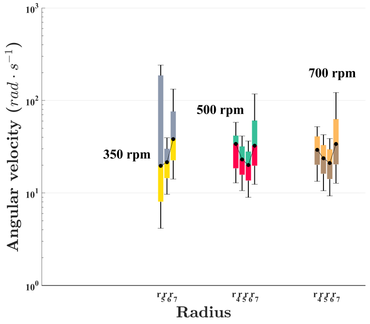	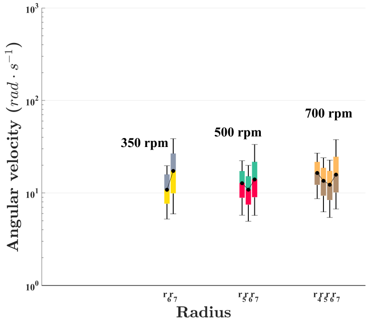	r_0 = 0.81 cm r_1 = 2.44 cm r_2 = 4.06 cm r_3 = 5.69 cm r_4 = 7.32 cm r_5 = 8.95 cm r_6 = 10.58 cm r_7 = 12.21 cm
First top region	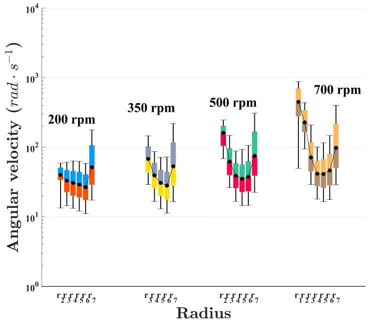	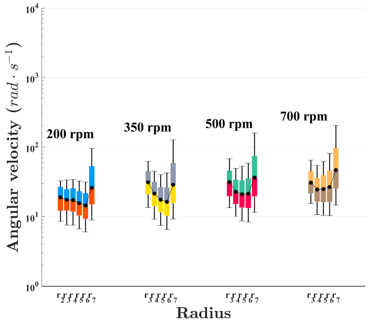	r_0 = 0.81 cm r_1 = 2.44 cm r_2 = 4.06 cm r_3 = 5.69 cm r_4 = 7.32 cm r_5 = 8.95 cm r_6 = 10.58 cm r_7 = 12.21 cm

Table A28: Angular velocity distributions of large and small particles at different regions relative to the impeller

Impeller region	Small particles	Large particles	
Top pin	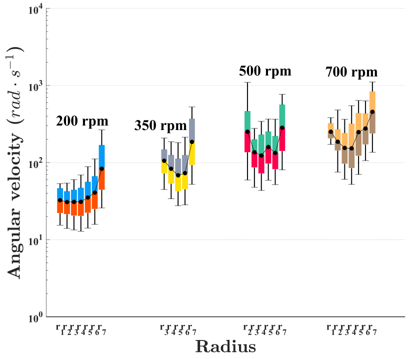	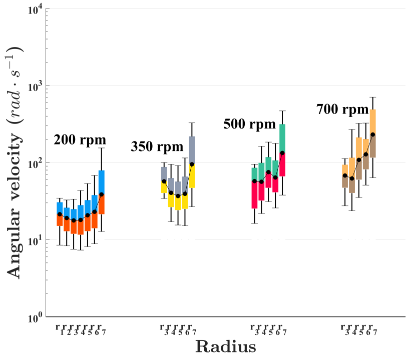	r_0 = 0.81 cm r_1 = 2.44 cm r_2 = 4.06 cm r_3 = 5.69 cm r_4 = 7.32 cm r_5 = 8.95 cm r_6 = 10.58 cm r_7 = 12.21 cm
Bottom pin	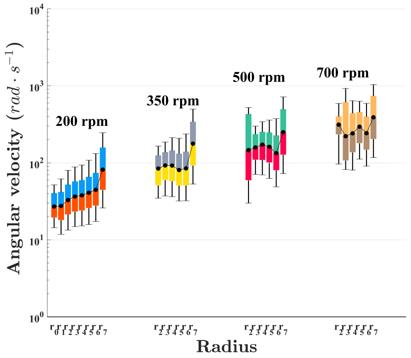	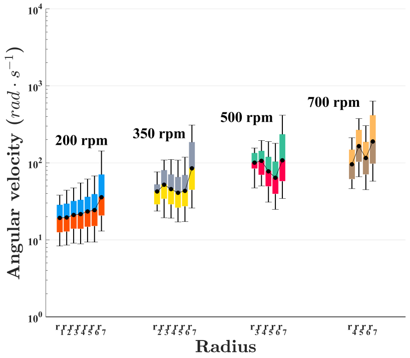	r_0 = 0.81 cm r_1 = 2.44 cm r_2 = 4.06 cm r_3 = 5.69 cm r_4 = 7.32 cm r_5 = 8.95 cm r_6 = 10.58 cm r_7 = 12.21 cm

Table A28: Angular velocity distributions of large and small particles at different regions relative to the impeller

Impeller region	Small particles	Large particles	
Bottom region	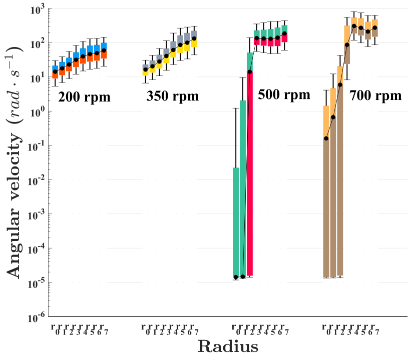	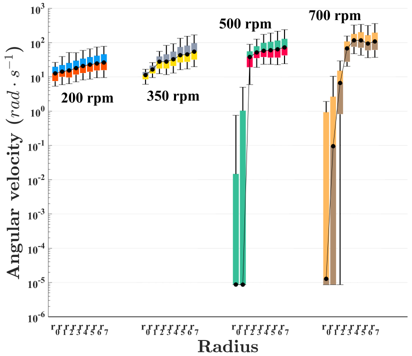	r_0 = 0.81 cm r_1 = 2.44 cm r_2 = 4.06 cm r_3 = 5.69 cm r_4 = 7.32 cm r_5 = 8.95 cm r_6 = 10.58 cm r_7 = 12.21 cm

Table A28: Angular velocity distributions of large and small particles at different regions relative to the impeller

Impeller region	Small particles	Large particles	
Top pin	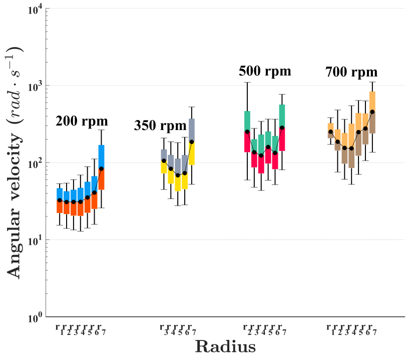	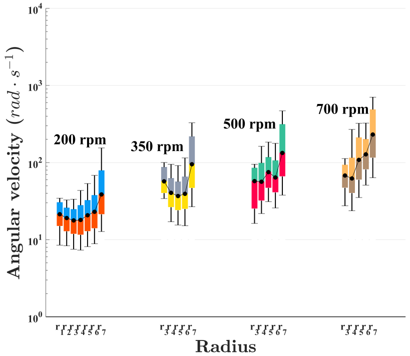	r_0 = 0.81 cm r_1 = 2.44 cm r_2 = 4.06 cm r_3 = 5.69 cm r_4 = 7.32 cm r_5 = 8.95 cm r_6 = 10.58 cm r_7 = 12.21 cm
Bottom pin	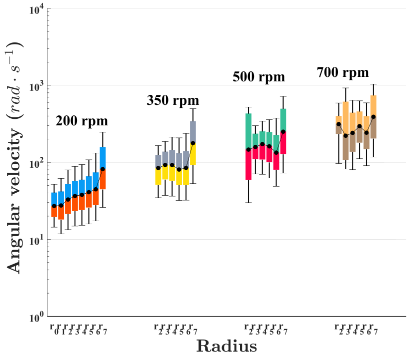	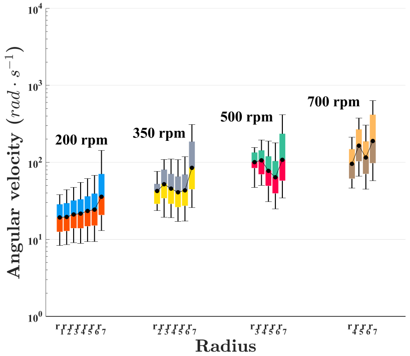	r_0 = 0.81 cm r_1 = 2.44 cm r_2 = 4.06 cm r_3 = 5.69 cm r_4 = 7.32 cm r_5 = 8.95 cm r_6 = 10.58 cm r_7 = 12.21 cm

Table A28: Angular velocity distributions of large and small particles at different regions relative to the impeller

Impeller region	Small particles	Large particles	
Bottom region	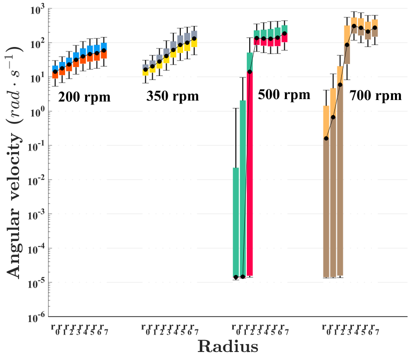	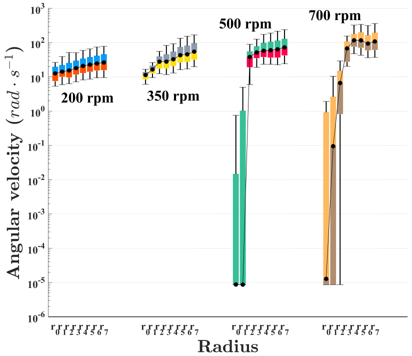	r_0 = 0.81 cm r_1 = 2.44 cm r_2 = 4.06 cm r_3 = 5.69 cm r_4 = 7.32 cm r_5 = 8.95 cm r_6 = 10.58 cm r_7 = 12.21 cm

B Reasons for certain decisions

B.1 Outlier compromise data in Section 4.2.6

Collision data has what can be best described as a lognormal or left-skewed distribution. In order to estimate outliers of such a skewed data an $Nc \times Nc$ matrix needs to be evaluated for the limits. Here Nc is the number of collision data points needed to be evaluated. This approach is computationally intensive when working with large sets of data. Working with the provided hardware specifications outlined in Sections 3.1, the $Nc \times Nc$ computation matrix exceeded the hardware's capabilities. Thus, the maximum and minimum values were approximated using upper and lower bound percentile values of 90th and 10th percentiles. The estimation of a percentile is not as computationally intensive as the $Nc \times Nc$ matrix.